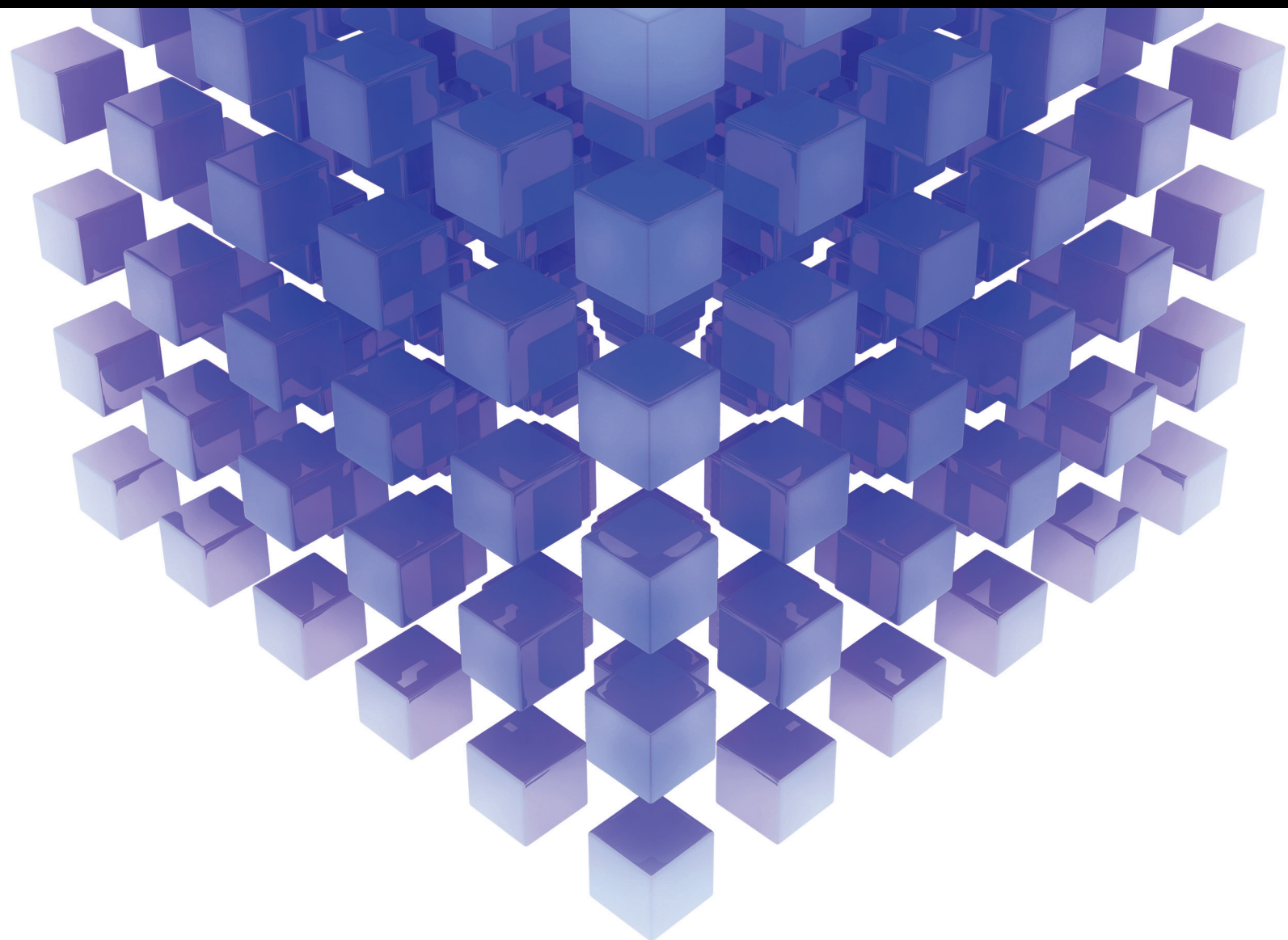


Mathematical Problems in Engineering

# Advanced Mesh-Based and Particle-Based Numerical Methods for Engineering and Applied Mathematics Problems

Guest Editors: Cheng-Tang Wu, Lihua Wang, Bernard Bonello, Leevan Ling, Ninshu Ma, and Marc A. Schweitzer





---

**Advanced Mesh-Based and Particle-Based  
Numerical Methods for Engineering and  
Applied Mathematics Problems**

Mathematical Problems in Engineering

---

**Advanced Mesh-Based and Particle-Based  
Numerical Methods for Engineering and  
Applied Mathematics Problems**

Guest Editors: Cheng-Tang Wu, Lihua Wang, Bernard Bonello,  
Leevan Ling, Ninshu Ma, and Marc A. Schweitzer



Copyright © 2017 Hindawi Publishing Corporation. All rights reserved.

This is a special issue published in “Mathematical Problems in Engineering.” All articles are open access articles distributed under the Creative Commons Attribution License, which permits unrestricted use, distribution, and reproduction in any medium, provided the original work is properly cited.

## Editorial Board

- Mohamed Abd El Aziz, Egypt  
Farid Abed-Meraim, France  
José Ángel Acosta, Spain  
Paolo Addresso, Italy  
Claudia Adduce, Italy  
Ramesh Agarwal, USA  
Juan C. Agüero, Australia  
R Aguilar-López, Mexico  
Tarek Ahmed-Ali, France  
Hamid Akbarzadeh, Canada  
Muhammad N. Akram, Norway  
Guido Ala, Italy  
Mohammad-Reza Alam, USA  
Salvatore Alfonzetti, Italy  
Francisco Alhama, Spain  
Mohammad D. Aliyu, Canada  
Juan A. Almendral, Spain  
Lionel Amodeo, France  
Sebastian Anita, Romania  
Renata Archetti, Italy  
Felice Arena, Italy  
Sabri Arik, Turkey  
Alessandro Arsie, USA  
Edoardo Artioli, Italy  
Fumihiko Ashida, Japan  
Hassan Askari, Canada  
Mohsen Asle Zaeem, USA  
Romain Aubry, USA  
Matteo Aureli, USA  
Francesco Aymerich, Italy  
Seungik Baek, USA  
Khaled Bahlali, France  
Laurent Bako, France  
Stefan Balint, Romania  
Alfonso Banos, Spain  
Roberto Baratti, Italy  
Azeddine Beghdadi, France  
Denis Benasciutti, Italy  
Ivano Benedetti, Italy  
Elena Benvenuti, Italy  
Jamal Berakdar, Germany  
Michele Betti, Italy  
Jean-Charles Beugnot, France  
Simone Bianco, Italy  
Gennaro N. Bifulco, Italy
- David Bigaud, France  
Antonio Bilotta, Italy  
Jonathan N. Blakely, USA  
Paul Bogdan, USA  
Alberto Borboni, Italy  
Paolo Boscariol, Italy  
Daniela Boso, Italy  
Guillermo Botella-Juan, Spain  
Abdel-Ouahab Boudraa, France  
Fabio Bovenga, Italy  
Francesco Braghin, Italy  
Michael J. Brennan, UK  
Maurizio Brocchini, Italy  
Julien Bruchon, France  
Michele Brun, Italy  
Javier Buldu&apos;, Spain  
Tito Busani, USA  
Raquel Caballero-Águila, Spain  
Pierfrancesco Cacciola, UK  
Salvatore Caddemi, Italy  
Jose E. Capilla, Spain  
F. Javier Cara, Spain  
Ana Carpio, Spain  
Carmen Castillo, Spain  
Inmaculada T. Castro, Spain  
Gabriele Cazzulani, Italy  
Luis Cea, Spain  
M. Chadli, France  
Gregory Chagnon, France  
Ching-Ter Chang, Taiwan  
Michael J. Chappell, UK  
Kacem Chehdi, France  
Peter N. Cheimets, USA  
Xinkai Chen, Japan  
Francisco Chicano, Spain  
Hung-Yuan Chung, Taiwan  
Joaquim Ciurana, Spain  
John D. Clayton, USA  
Giuseppina Colicchio, Italy  
Mario Cools, Belgium  
Sara Coppola, Italy  
Jean-Pierre Corriou, France  
J.-C. Cortés, Spain  
Carlo Cosentino, Italy  
Paolo Crippa, Italy
- Andrea Crivellini, Italy  
Erik Cuevas, Mexico  
Peter Dabnichki, Australia  
Luca D'Acerno, Italy  
Weizhong Dai, USA  
Andrea Dall'Asta, Italy  
Purushothaman Damodaran, USA  
Farhang Daneshmand, Canada  
Fabio De Angelis, Italy  
Pietro De Lellis, Italy  
Stefano de Miranda, Italy  
Filippo de Monte, Italy  
Maria do Rosário de Pinho, Portugal  
Xavier Delorme, France  
Frédéric Demoly, France  
Luca Deseri, USA  
Angelo Di Egidio, Italy  
Ramón I. Diego, Spain  
Yannis Dimakopoulos, Greece  
Zhengtao Ding, UK  
M. Djemai, France  
Alexandre B. Dolgui, France  
Florent Duchaine, France  
George S. Dulikravich, USA  
Bogdan Dumitrescu, Romania  
Horst Ecker, Austria  
Ahmed El Hajjaji, France  
Fouad Erchiqui, Canada  
Anders Eriksson, Sweden  
R. Emre Erkmen, Australia  
Andrea L. Facci, Italy  
Giovanni Falsone, Italy  
Hua Fan, China  
Yann Favennec, France  
Fiorenzo A. Fazzolari, UK  
Giuseppe Fedele, Italy  
Roberto Fedele, Italy  
Jose R. Fernandez, Spain  
Jesus M. Fernandez Oro, Spain  
Eric Feulvarch, France  
Barak Fishbain, Israel  
Simme Douwe Flapper, Netherlands  
Thierry Floquet, France  
Eric Florentin, France  
Jose M. Framinan, Spain

Francesco Franco, Italy  
Elisa Francomano, Italy  
Leonardo Freitas, UK  
Tomonari Furukawa, USA  
Mohamed Gadala, Canada  
Matteo Gaeta, Italy  
Mauro Gaggero, Italy  
Zoran Gajic, Iraq  
Erez Gal, Israel  
Ugo Galvanetto, Italy  
Akemi Gálvez, Spain  
Rita Gamberini, Italy  
Maria L. Gandarias, Spain  
Arman Ganji, Canada  
Xin-Lin Gao, USA  
Zhong-Ke Gao, China  
Giovanni Garcea, Italy  
Fernando García, Spain  
Jose M. Garcia-Aznar, Spain  
Alessandro Gasparetto, Italy  
Vincenzo Gattulli, Italy  
Oleg V. Gendelman, Israel  
Mergen H. Ghayesh, Australia  
Agathoklis Giaralis, UK  
Anna M. Gil-Lafuente, Spain  
Ivan Giorgio, Italy  
Alessio Gizzi, Italy  
Hector Gómez, Spain  
David González, Spain  
Francisco Gordillo, Spain  
Rama S. R. Gorla, USA  
Oded Gottlieb, Israel  
Nicolas Gourdain, France  
Kannan Govindan, Denmark  
Antoine Grall, France  
Fabrizio Greco, Italy  
Jason Gu, Canada  
Federico Guarracino, Italy  
José L. Guzmán, Spain  
Quang Phuc Ha, Australia  
Zhen-Lai Han, China  
Thomas Hanne, Switzerland  
Xiao-Qiao He, China  
Sebastian Heidenreich, Germany  
Luca Heltai, Italy  
Alfredo G. Hernández-Díaz, Spain  
Rafael M. Herrera, Spain  
M.I. Herreros, Spain

Eckhard Hitzer, Japan  
Jaromir Horacek, Czech Republic  
Muneo Hori, Japan  
András Horváth, Italy  
Gordon Huang, Canada  
Nicolas Hudon, Canada  
Sajid Hussain, Canada  
Asier Ibeas, Spain  
Orest V. Iftime, Netherlands  
Giacomo Innocenti, Italy  
Emilio Insfran, Spain  
Nazrul Islam, USA  
Benoit Jung, France  
Benjamin Ivorra, Spain  
Payman Jalali, Finland  
Reza Jazar, Australia  
Khalide Jbilou, France  
Linni Jian, China  
Bin Jiang, China  
Zhongping Jiang, USA  
Ningde Jin, China  
Grand R. Joldes, Australia  
Dylan F. Jones, UK  
Tamas Kalmar-Nagy, Hungary  
Tomasz Kapitaniak, Poland  
Haranath Kar, India  
Konstantinos Karamanos, Belgium  
Jean-Pierre Kenne, Canada  
Chaudry M. Khalique, South Africa  
Do Wan Kim, Republic of Korea  
Nam-Il Kim, Republic of Korea  
Oleg Kirillov, Germany  
Manfred Krafczyk, Germany  
Frederic Kratz, France  
Petr Krysl, USA  
Jurgen Kurths, Germany  
Kyandoghere Kyamakya, Austria  
Davide La Torre, Italy  
Risto Lahdelma, Finland  
Hak-Keung Lam, UK  
Jimmy Lauber, France  
Antonino Laudani, Italy  
Aimé Lay-Ekuakille, Italy  
Nicolas J. Leconte, France  
Marek Lefik, Poland  
Yaguo Lei, China  
Stefano Lenci, Italy  
Roman Lewandowski, Poland

Panos Liatsis, UAE  
Anatoly Lisnianski, Israel  
Peide Liu, China  
Peter Liu, Taiwan  
Wanquan Liu, Australia  
Alessandro Lo Schiavo, Italy  
Jean Jacques Loiseau, France  
Paolo Lonetti, Italy  
Sandro Longo, Italy  
Rosana R. López, Spain  
Sebastian López, Spain  
Luis M. López-Ochoa, Spain  
Vassilios C. Loukopoulos, Greece  
Valentin Lychagin, Norway  
Antonio Madeo, Italy  
J. María Maestre, Spain  
Fazal M. Mahomed, South Africa  
N. Manamanni, France  
Didier Maquin, France  
Damijan Markovic, France  
F. Marotti de Sciarra, Italy  
Benoit Marx, France  
Franck Massa, France  
Paolo Massioni, France  
G. A. Maugin, France  
Alessandro Mauro, Italy  
Michael Mazilu, UK  
Driss Mehdi, France  
Roderick Melnik, Canada  
Pasquale Memmolo, Italy  
Xiangyu Meng, Canada  
Jose Merodio, Spain  
Alessio Merola, Italy  
Luciano Mescia, Italy  
Laurent Mevel, France  
Y. V. Mikhlin, Ukraine  
Aki Mikkola, Finland  
Hiroyuki Mino, Japan  
Pablo Mira, Spain  
Vito Mocella, Italy  
Roberto Montanini, Italy  
Gisele Mophou, France  
Marco Morandini, Italy  
Simone Morganti, Italy  
Aziz Moukrim, France  
Emiliano Mucchi, Italy  
Josefa Mula, Spain  
Domenico Mundo, Italy

Jose J. Muñoz, Spain  
Giuseppe Muscolino, Italy  
Marco Mussetta, Italy  
Hakim Naceur, France  
Hassane Naji, France  
Keivan Navaie, UK  
Dong Ngoduy, UK  
Tatsushi Nishi, Japan  
Xesús Nogueira, Spain  
Ben T. Nohara, Japan  
Mohammed Nouari, France  
Mustapha Nourelfath, Canada  
Roger Ohayon, France  
Mitsuhiro Okayasu, Japan  
Calogero Orlando, Italy  
Javier Ortega-Garcia, Spain  
A. Ortega-Moñux, Spain  
Naohisa Otsuka, Japan  
Erika Ottaviano, Italy  
Arturo Pagano, Italy  
Alkis S. Paipetis, Greece  
Alessandro Palmeri, UK  
Anna Pandolfi, Italy  
Elena Panteley, France  
Achille Paolone, Italy  
Xosé M. Pardo, Spain  
Manuel Pastor, Spain  
P. N. Pathirana, Australia  
Francesco Pellicano, Italy  
Marcello Pellicciari, Italy  
Haipeng Peng, China  
Mingshu Peng, China  
Zhike Peng, China  
Marzio Pennisi, Italy  
Maria Patrizia Pera, Italy  
Matjaz Perc, Slovenia  
Francesco Pesavento, Italy  
Dario Piga, Italy  
Antonina Pirrotta, Italy  
Marco Pizzarelli, Italy  
Vicent Pla, Spain  
Javier Plaza, Spain  
Sébastien Poncet, Canada  
J.-C. Ponsart, France  
Mauro Pontani, Italy  
Stanislav Potapenko, Canada  
C. Pretty, New Zealand  
Carsten Proppe, Germany

Luca Pugi, Italy  
Giuseppe Quaranta, Italy  
Dane Quinn, USA  
Vitomir Racic, Italy  
Jose Ragot, France  
K. Ramamani Rajagopal, USA  
Gianluca Ranzi, Australia  
Alain Rassineux, France  
S.S. Ravindran, USA  
Alessandro Reali, Italy  
Oscar Reinoso, Spain  
Nidhal Rezg, France  
Ricardo Riaza, Spain  
Gerasimos Rigatos, Greece  
Francesco Ripamonti, Italy  
Eugenio Roanes-Lozano, Spain  
Bruno G. M. Robert, France  
José Rodellar, Spain  
Ignacio Rojas, Spain  
Alessandra Romolo, Italy  
Carla Roque, Portugal  
Debashish Roy, India  
Gianluigi Rozza, Italy  
R. Ruiz García, Spain  
Antonio Ruiz-Cortes, Spain  
Ivan D. Rukhlenko, Australia  
Mazen Saad, France  
Kishin Sadarangani, Spain  
Mehrhad Saif, Canada  
Miguel A. Salido, Spain  
Roque J. Salterén, Spain  
F. J. Salvador, Spain  
Alessandro Salvini, Italy  
Maura Sandri, Italy  
Miguel A. F. Sanjuan, Spain  
Juan F. San-Juan, Spain  
Roberta Santoro, Italy  
I. Ferreira Santos, Denmark  
J. A. Sanz-Herrera, Spain  
Nickolas S. Sapidis, Greece  
E. J. Sapountzakis, Greece  
Andrey V. Savkin, Australia  
Thomas Schuster, Germany  
Mohammed Seaid, UK  
Lotfi Senhadji, France  
Joan Serra-Sagrasta, Spain  
Gerardo Severino, Italy  
Ruben Sevilla, UK

Leonid Shaikhet, Ukraine  
Hassan M. Shanechi, USA  
Bo Shen, Germany  
Suzanne M. Shontz, USA  
Babak Shotorban, USA  
Zhan Shu, UK  
Dan Simon, Greece  
Luciano Simoni, Italy  
Christos H. Skiadas, Greece  
Alba Sofi, Italy  
Francesco Soldovieri, Italy  
Raffaele Solimene, Italy  
Jussi Sopanen, Finland  
Marco Spadini, Italy  
Ruben Specogna, Italy  
Sri Sridharan, USA  
Ivanka Stamova, USA  
Salvatore Strano, Italy  
Yakov Strelniker, Israel  
Sergey A. Suslov, Australia  
Thomas Svensson, Sweden  
Andrzej Swierniak, Poland  
Yang Tang, Germany  
Alessandro Tasora, Italy  
Sergio Teggi, Italy  
Alexander Timokha, Norway  
Gisella Tomasini, Italy  
Francesco Tornabene, Italy  
Antonio Tornambe, Italy  
Irina N. Trendafilova, UK  
George Tsiatas, Greece  
Antonios Tsourdos, UK  
Vladimir Turetsky, Israel  
Mustafa Tutar, Spain  
Ilhan Tuzcu, USA  
Efstratios Tzirtzilakis, Greece  
Filippo Ubertini, Italy  
Francesco Ubertini, Italy  
Hassan Ugail, UK  
Giuseppe Vairo, Italy  
Kuppalapalle Vajravelu, USA  
Robertt A. Valente, Portugal  
Eusebio Valero, Spain  
Pandian Vasant, Malaysia  
Marcello Vasta, Italy  
M. E. Vázquez-Méndez, Spain  
Josep Vehi, Spain  
K. C. Veluvolu, Republic of Korea



---

Fons J. Verbeek, Netherlands  
Franck J. Vernerey, USA  
Georgios Veronis, USA  
Anna Vila, Spain  
R.-J. Villanueva-Micó, Spain  
U. E. Vincent, UK  
Mirko Viroli, Italy  
Michael Vynnycky, Sweden  
Shuming Wang, China  
Yan-Wu Wang, China

Yongqi Wang, Germany  
Roman Wendner, Austria  
Desheng D. Wu, Sweden  
Yuqiang Wu, China  
Guangming Xie, China  
Xuejun Xie, China  
Gen Q. Xu, China  
Hang Xu, China  
Joseph J. Yame, France  
Xinggang Yan, UK

Luis J. Yebra, Spain  
Peng-Yeng Yin, Taiwan  
Qin Yuming, China  
Vittorio Zampoli, Italy  
Ibrahim Zeid, USA  
Huaguang Zhang, China  
Qingling Zhang, China  
Jian G. Zhou, UK  
Quanxin Zhu, China  
Mustapha Zidi, France

# Contents

---

**Advanced Mesh-Based and Particle-Based Numerical Methods for Engineering and Applied Mathematics Problems**

Cheng-Tang Wu, Lihua Wang, Bernard Bonello, Leevan Ling, Ninshu Ma, and Marc A. Schweitzer  
Volume 2017, Article ID 1273017, 2 pages

**Multisensors Cooperative Detection Task Scheduling Algorithm Based on Hybrid Task Decomposition and MBPSO**

Changyun Liu, Xiangke Guo, Zhihui Li, Yingying Wang, and Gang Wei  
Volume 2017, Article ID 3453589, 11 pages

**A Meshless Radial Basis Function Based on Partition of Unity Method for Piezoelectric Structures**

Sen Li, Linqun Yao, Shichao Yi, and Wei Wang  
Volume 2016, Article ID 7632176, 17 pages

**A Novel Multiobjective Quantum-Behaved Particle Swarm Optimization Based on the Ring Model**

Di Zhou, Yajun Li, Bin Jiang, and Jun Wang  
Volume 2016, Article ID 4968938, 15 pages

**Model Test Research on the End Bearing Behavior of the Large-Diameter Cast-in-Place Concrete Pile for Jointed Rock Mass**

Jingwei Cai, Aiping Tang, Xincheng Yin, Xiaxin Tao, and Shibo Tao  
Volume 2016, Article ID 4860143, 15 pages

**A New Method to Solve Numeric Solution of Nonlinear Dynamic System**

Min Hu and Fengjun Li  
Volume 2016, Article ID 1485759, 8 pages

**The Application of Nonordinary, State-Based Peridynamic Theory on the Damage Process of the Rock-Like Materials**

X. B. Gu and Q. H. Wu  
Volume 2016, Article ID 9794605, 9 pages

**An Efficient Approach for Real-Time Prediction of Rate of Penetration in Offshore Drilling**

Xian Shi, Gang Liu, Xiaoling Gong, Jialin Zhang, Jian Wang, and Hongning Zhang  
Volume 2016, Article ID 3575380, 13 pages

**Using EVT for Geological Anomaly Design and Its Application in Identifying Anomalies in Mining Areas**

Feilong Qin, Bingli Liu, and Ke Guo  
Volume 2016, Article ID 3436192, 11 pages

**An Improved Ant Colony Algorithm for Solving the Path Planning Problem of the Omnidirectional Mobile Vehicle**

Jiang Zhao, Dingding Cheng, and Chongqing Hao  
Volume 2016, Article ID 7672839, 10 pages

**Low Model Analysis and Synchronous Simulation of the Wave Mechanics**

Wenyuan Duan, Heyuan Wang, and Meng Kan  
Volume 2016, Article ID 2850651, 13 pages



---

**A Numerical Method Based on Daubechies Wavelet Basis and B-Spline Patches for Elasticity Problems**

Yanan Liu and Keqin Din

Volume 2016, Article ID 2549213, 11 pages

**Flow Simulation of Suspension Bridge Cable Based on Lattice-Boltzmann Method**

Liang Huang, Yuhan Deng, and Bo Wang

Volume 2016, Article ID 2537581, 7 pages

## Editorial

# Advanced Mesh-Based and Particle-Based Numerical Methods for Engineering and Applied Mathematics Problems

**Cheng-Tang Wu,<sup>1</sup> Lihua Wang,<sup>2</sup> Bernard Bonello,<sup>3</sup> Leevan Ling,<sup>4</sup>  
Ninshu Ma,<sup>5</sup> and Marc A. Schweitzer<sup>6,7</sup>**

<sup>1</sup>Livermore Software Technology Corporation (LSTC), Livermore, CA 94551, USA

<sup>2</sup>School of Aerospace Engineering and Applied Mechanics, Tongji University, Shanghai 200092, China

<sup>3</sup>Institut des NanoSciences de Paris, Université Pierre et Marie Curie, 75005 Paris, France

<sup>4</sup>Department of Mathematics, Hong Kong Baptist University, Kowloon Tong, Hong Kong

<sup>5</sup>Center of Computational Welding Science, Osaka University, Osaka 5650871, Japan

<sup>6</sup>Institute for Numerical Simulation, University of Bonn, 53115 Bonn, Germany

<sup>7</sup>Fraunhofer Institute for Algorithms and Scientific Computing SCAI, 53754 Sankt Augustin, Germany

Correspondence should be addressed to Cheng-Tang Wu; [ctwu@lstc.com](mailto:ctwu@lstc.com)

Received 22 February 2017; Accepted 22 February 2017; Published 19 March 2017

Copyright © 2017 Cheng-Tang Wu et al. This is an open access article distributed under the Creative Commons Attribution License, which permits unrestricted use, distribution, and reproduction in any medium, provided the original work is properly cited.

Thanks for the rapid progress of computing resources, many advanced numerical methods have undergone extensive developments and led to widespread applications in interdisciplinary sciences and engineering. The title of this special issue is a topic that significant research efforts have been spent on over the past decade. The development of powerful mesh-based and particle-based numerical methods for both routine and sophisticated engineering problems with complete solutions has been recognized by most researchers to benefit the industry as a whole, while creating new avenues for further research and spearheading of pioneering efforts within the field of computation and industrial applications. The objective of this special issue is to present the state-of-the-art and prospective directions of those advanced numerical methods from the research areas to computation and application fields for engineering and applied mathematical problems.

This special issue contains 12 peer-reviewed papers. Different from the use of traditional computational methods, L. Huang et al. consider the Lattice-Boltzmann method for a flow simulation of suspension bridge cable. F. Qin et al. conduct a geological anomaly design using an extreme value theory. W. Duan et al. study the internal wave dynamic problems using the low model analysis. X. Shi et al. predict the rate of penetration in drilling problems using an efficient

machine learning approach. Y. Liu and K. Din propose a numerical method based on Daubechies wavelet basis and B-spline patches for elasticity problems. J. Zhao et al. present an improved ant colony algorithm for solving the path planning problem for omnidirectional mobile vehicle. X. B. Gu and Q. H. Wu apply the nonordinary state-based peridynamic theory for the damage process of rock materials. J. Cai et al. apply the discrete element method for the analysis of large-diameter cast-in-place concrete piles. C. Liu et al. developed a multisensor scheduling algorithm based on the hybrid task decomposition and a modified binary particle swarm optimization. A new numerical method based on cubic spline function is developed by M. Hu and F. Li for solving the nonlinear dynamics problems. A new multiobjective algorithm based the quantum-behaved particle swarm optimization is proposed by D. Zhou et al. Finally, a meshless radial basis function based on the partition of unity method is developed by S. Li et al. for the analysis of piezoelectric structures.

## Acknowledgments

We would like to thank all who kindly contributed their papers to this special issue. We are also indebted to the

reviewers and publishing team for their assistance during the preparation and publication of this special issue.

*Cheng-Tang Wu*  
*Lihua Wang*  
*Bernard Bonello*  
*Leevan Ling*  
*Ninshu Ma*  
*Marc A. Schweitzer*

## Research Article

# Multisensors Cooperative Detection Task Scheduling Algorithm Based on Hybrid Task Decomposition and MBPSO

Changyun Liu,<sup>1</sup> Xiangke Guo,<sup>1,2</sup> Zhihui Li,<sup>1</sup> Yingying Wang,<sup>1</sup> and Gang Wei<sup>1</sup>

<sup>1</sup>*Air and Missile Defense College, Air Force Engineering University, Xi'an 710051, China*

<sup>2</sup>*College of Electronic and Information Engineering, Beijing University of Aeronautics and Astronautics, Beijing 100191, China*

Correspondence should be addressed to Changyun Liu; [icemissile@sina.com](mailto:icemissile@sina.com)

Received 14 July 2016; Revised 8 October 2016; Accepted 26 October 2016; Published 12 February 2017

Academic Editor: Cheng-Tang Wu

Copyright © 2017 Changyun Liu et al. This is an open access article distributed under the Creative Commons Attribution License, which permits unrestricted use, distribution, and reproduction in any medium, provided the original work is properly cited.

A multisensor scheduling algorithm based on the hybrid task decomposition and modified binary particle swarm optimization (MBPSO) is proposed. Firstly, aiming at the complex relationship between sensor resources and tasks, a hybrid task decomposition method is presented, and the resource scheduling problem is decomposed into subtasks; then the sensor resource scheduling problem is changed into the match problem of sensors and subtasks. Secondly, the resource match optimization model based on the sensor resources and tasks is established, which considers several factors, such as the target priority, detecting benefit, handover times, and resource load. Finally, MBPSO algorithm is proposed to solve the match optimization model effectively, which is based on the improved updating means of particle's velocity and position through the doubt factor and modified Sigmoid function. The experimental results show that the proposed algorithm is better in terms of convergence velocity, searching capability, solution accuracy, and efficiency.

## 1. Introduction

The early warning detection system of the ballistic missile defense system is composed of the space-based satellite, the ground radar, the sea-based radar, and so on. Due to the early warning equipment deployment and sensor detecting capability, multitactical ballistic missile (TBM) emerging randomly cannot be tracked by a single early warning equipment stably and continuously in the entire trajectory of TBM.

The goal of the multisensors cooperative detection is to ascertain the detection sequence and the detection time about TBM under the constraint of limited sensor resources and visualization period and to achieve the optimized match of sensor resources and detecting tasks, so that the optimum detecting profit is obtained.

Many researchers have done lots of researches on the resource scheduling of the early warning satellites in depth. In [1, 2], the parallel tabu genetic algorithm and improved particle swarm optimization algorithm are used, respectively, to resolve early warning satellites scheduling problems. A variable neighborhood heuristic algorithm for the dynamic

task planning of the Low Earth Orbit warning system is studied in [3]. The task decomposition method for early warning satellites scheduling is studied in [4, 5]. The above researches on the early warning satellites task scheduling is focused on the method of numerical solution and task decomposition, while the sensor resources schedule in BMDS should be the combined schedule containing the early warning satellites and ground radars and so on. Aiming at antimissile resource scheduling, the multitarget optimization model including many factors is established in [6], but the task decomposition method is different from the practical problem and the difference between early warning satellites and radars is not reflected in its scheduling model.

Sensor resources scheduling is a nonlinear multitarget combination optimization problem in essence. Because of the high velocity of TBM, it is vital to resolve the sensor scheduling problem in real time. Particle swarm optimization (PSO) [7–9] is easy and effective to use, so it has been widely applied in the sensor resources scheduling and the weapon-target allocation (WTA) [10]. Aiming at the optimization problems of the binary representations solution, BPSO is

proposed by Kennedy and Eberhart in [11]. And many improved BPSO algorithms aiming at the shortcomings of BPSO are presented in literature [12–15]. Among them, BPSO algorithm is modified in generation mechanism, update mechanism, and selection mechanism for multiobjective resource allocation problem in [13]. And a memetic binary particle swarm optimization algorithm is introduced in [15] to improve the local and global search performance.

Multisensors task scheduling is not only a nonlinear multitarget combination optimization problem, but also a real-time algorithm, so a multisensors task scheduling algorithm based on hybrid task decomposition and modified binary particle swarm optimization (MBPSO) is proposed. Aiming at the complex relationship between sensor resources and tasks, a hybrid task decomposition method is presented, so that the resource scheduling problem is decomposed into subtasks, and then the sensor resource scheduling problem is changed into the match problem of sensors and subtasks. Through the analysis of subtasks, the resource match optimization model based on the sensor resources and tasks is established, which contains several factors, such as the target priority, detecting benefit, handover times, and resource load. For the purpose of global optimization and real-time calculation, a match optimization model for MBPSO algorithm is proposed, which is based on the improved updating means of particle's through the doubt factor and modified Sigmoid function, multisensors cooperative detecting tasks optimization, and real-time solving are realized.

## 2. Cooperative Detecting Task Decomposition Based on Hybrid Task Decomposition

Antimissile multisensors cooperative detecting task has the following characteristics:

- (1) There are many different kinds of sensor resources in the ballistic missile defense system, so the visualization relationship between sensors and targets is complex when there are many TBM.
- (2) The flight range of the ballistic target is large, and it is easy to be out of the visual field of one sensor and enters into the visual field of another sensor.
- (3) The ballistic target has a low possibility to maneuver in the midcourse flight, so its motion trajectory can be predicted precisely.
- (4) The emergence time, position, number, and type of ballistic targets are difficult to predict, so the cooperative detecting tasks are random and dynamic.
- (5) The threat degree of multiple ballistic targets is different, so the priority of cooperative detection tasks is also different.

It can be concluded from the above task characteristics that one single cooperative detection task cannot be involved independently in the scheduling, the cooperative detection task should be decomposed into subtasks, and these subtasks can be used in scheduling.

*2.1. Task Decomposition's Requirements.* Through the task decomposition, the multisensors cooperative detecting tasks are decomposed into many basic and independent subtasks, which cannot be decomposed any longer. Some requirements to subtasks are as follows:

- (1) Completeness: cooperative detecting tasks are decomposed into many subtasks, and the sum of subtasks is equal to the cooperative detecting tasks.
- (2) Independence: the subtasks cannot be replaced by each other.
- (3) Granularity: the length of subtasks should be moderate. If the length of the subtasks is too long, it will occupy a sensor resource for a long time, which does not meet the requirement for optimization. If the length of subtasks is too short, it will not meet the requirements of estimation and prediction, which improves the complexity of optimization. Assume that the longest subtask is  $D_{\max}$  and the shortest is  $D_{\min}$ .
- (4) Interval: a certain interval is allowed among subtasks. If the interval is too long, it increases the trajectory prediction error and is more difficult for sensors to capture the target in the next subtask's time. So the interval cannot exceed the upper limit value.

*2.2. Method of Hybrid Task Decomposition.* The basic methods [4–6] of task decomposition include “the longest observation time” decomposition method, “evenly split” decomposition method, and “start-stop time” decomposition method. The characteristics of these methods are mainly as follows:

- (1) “The longest observation time” decomposition method: a sensor will be occupied for a long time, which not only decreases the detection efficiency of sensor resources but also increases the resource conflict.
- (2) “Evenly split” decomposition method: it is difficult to determine the length of subtasks. If the length of subtasks is too long, some tasks will not be completed by proper sensors, and if the length of subtasks is too short, the handover of sensors will be frequent.
- (3) “Start-stop time” decomposition method: a sensor detects the same target for a long time, which reduces the detection efficiency, and the number of subtasks would increase significantly with the increasing number of targets.

Due to the characteristics of the above task decomposition methods, the subtasks in a single task decomposition method would conflict each other, which results in the local optimization of resource scheduling, so the single task decomposition method cannot meet the requirement of task decomposition. Then combining “evenly split” decomposition method with “start-stop time” decomposition method, a hybrid task decomposition method for multisensors detecting multitarget is designed. Its main idea is as follows: firstly, using the “start-stop time” decomposition method, the whole task is decomposed into many subtasks according to the visualization start time and end time of all sensors

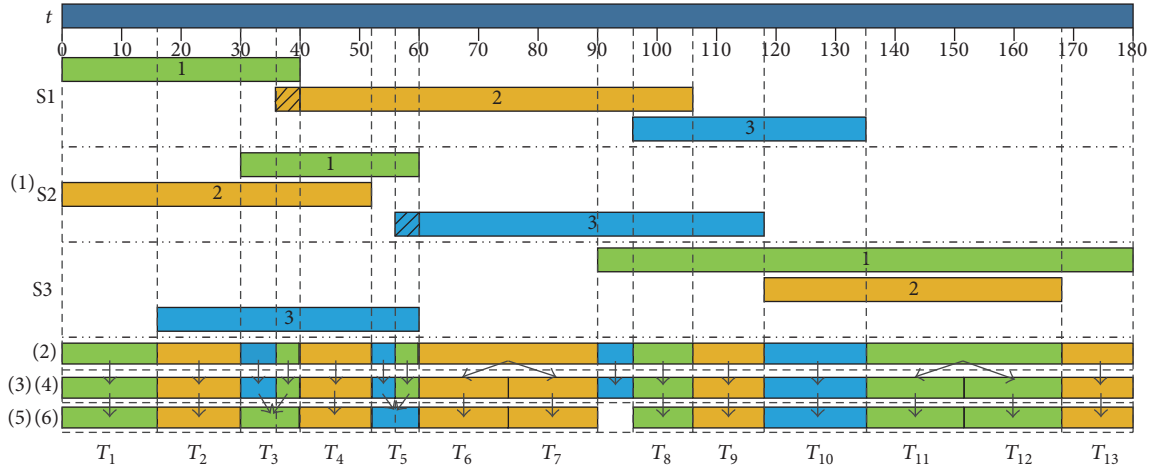


FIGURE 1: Process of hybrid task decomposition.

to all targets; secondly, using “evenly split” decomposition method, the subtasks are selected according to the constraint condition, if the length of subtasks is too long, it will continue to be split again, and if the length of subtasks is too short, it will be integrated. The specific diagram of hybrid task decomposition method is shown in Figure 1.

In Figure 1, S1 denotes sensor 1, S2 denotes sensor 2, S3 denotes sensor 2, and T1 to T13 denote subtask 1 to subtask 13, respectively. Green-1, orange-2, and blue-3 denote the interval of time; that is, target-1, target-2, and target-3 are in the detecting area of different sensor, respectively. For example, the green-1 in the area of S1 means that the interval of time of the target-1 in the sensor 1 detection area is from zero seconds to forty seconds, which denotes  $[0, 40]$ . The hybrid task decomposition is the basis of the match optimization model.

The detailed steps of hybrid task decomposition method are as follows.

*Step 1* (calculating). According to the visual relationship between all sensors and all ballistic targets, the visualization interval of sensors and targets is determined.

*Step 2* (sorting). The start time and end time in visualization interval of all sensors to all targets are marked, and the marked time is sorted in time from small to large, and then the two adjacent moments are synthesized into an interval; as a result, the whole tasks are decomposed into subtasks.

*Step 3* (selecting). According to the third constraint condition of task decomposition, the subtasks between  $D_{\max}$  and  $D_{\min}$  are selected. If the length of subtasks is longer than  $D_{\max}$ , go to Step 4.

*Step 4* (splitting). If the length of subtasks is longer than  $D_{\max}$ , the subtasks would be split continually, so the length of subtasks is in  $[D_{\min}, D_{\max}]$ . It is supposed that the length of subtasks is  $M$ , the task is split into  $N$  subtasks whose length

is  $D_z$ , the detailed method is as follows:

$$N = \begin{cases} \lceil M/D_{\min} \rceil & \text{if } M \bmod D_{\min} \neq 0 \\ M/D_{\min} & \text{if } M \bmod D_{\min} = 0 \end{cases} \quad (1)$$

$$D_z = M/N,$$

where  $\lceil M/D_{\min} \rceil$  denotes the largest integer beyond  $M/D_{\min}$ .

*Step 5*. If the length of subtasks is less than  $D_{\min}$ , the processing step is as follows: (1) if the subtask is in existence independently, namely, the subtask length of the previous, and next subtask exceeds  $D_{\min}$ , the subtask would be deleted; (2) if the number of adjacent subtasks is more than two, it is supposed that the start time and the end time of  $i$ th subtask are  $t_{\text{start}}^i$  and  $t_{\text{end}}^i$ , respectively, and the time of the integrated subtask is  $t_{\text{start}}$  and  $t_{\text{end}}$ , respectively. So the integration method is as follows:

- (1) initialize:  $t_{\text{start}} = t_{\text{start}}^1$ ,  $i = 2$ ;
- (2) if  $(t_{\text{end}}^i - t_{\text{start}}) \notin [D_{\min}, D_{\max}]$ , go to (3); otherwise, go to (4);
- (3)  $i = ++$ , go to (2);
- (4)  $k = i$ , the  $k$  adjacent subtasks are integrated, and the visual interval of the integrated subtask whose length is less than  $D_{\min}$  would be deleted, as it be shown in slash part of Figure 1.

*Step 6* (deleting). After subtasks are processed by Steps 4 and 5, the subtasks whose length cannot meet the third constraint condition is deleted.

### 3. Match Optimization Model of Resources and Subtasks

After the task is decomposed, the implementation of multi-sensor cooperative detecting task is transformed into the

implementation of its subtasks. In the interval of each subtask, there are two relationships between sensors and targets: (1) whether the target is in the visualization interval or not; (2) if the target is in the visualization interval of sensors, whether it is detected by the corresponding sensors or not. The multitargets subtasks optimization of multisensors resource is resolved through establishing the match optimization model of sensor resources and subtasks.

**3.1. Description of the Problem.** In order to facilitate the description of the problem, the following definitions are given.

**Definition 1** (subtask detection matrix  $D^k$ ). The subtask detection matrix denotes the matrix whose component denotes whether the target can be detected by sensor or not in the subtask interval of sensor, one denotes that the target can be detected by sensor, and zero denotes that the target cannot be detected by sensor.

**Definition 2** (subtask scheduling matrix  $E^k$ ). The subtask scheduling matrix denotes the matrix whose component denotes whether the detecting task of sensor is implemented or not in the subtask interval of sensor at the basis of subtask detection matrix, zero denotes that the sensor is to detect target, and zero denotes that the sensor is not to detect target.

It is supposed that, in  $[T_s, T_e]$ , the number of ballistic targets is  $m$ , in addition, the number of LEO satellites is  $n_1$ , and the number of ground radars is  $n_2$  in BMDS. After the task is decomposed,  $TN$  subtasks are obtained in time sequence, and the  $k$ th subtask is in  $[ST^k, ET^k]$ , so the subtask detection matrix  $D^k$  and subtask scheduling matrix  $E^k$  are as follows:

$$\begin{aligned} D^k &= (d_{ij}^k)_{(n_1+n_2)m}, \\ E^k &= (e_{ij}^k)_{(n_1+n_2)m}. \end{aligned} \quad (2)$$

In  $[ST^k, ET^k]$ , if the  $j$ th ballistic target is in the visualization interval of the  $i$ th sensor, then  $d_{ij}^k = 1$ ; otherwise  $d_{ij}^k = 0$ . In like manner, in  $[ST^k, ET^k]$ , if the  $i$ th ballistic target is detected by the  $j$ th sensor, then  $e_{ij}^k = 1$ ; otherwise  $e_{ij}^k = 0$  and  $0 \leq e_{ij}^k \leq d_{ij}^k$ .

In the scheduling interval  $[T_s, T_e]$ , the whole detection matrix  $D$  and the whole scheduling matrix  $E$ , respectively, are

$$D = [D^1, \dots, D^k, \dots, D^{TN}] \quad (3)$$

$$E = [E^1, \dots, E^k, \dots, E^{TN}]. \quad (4)$$

So the solution to the whole scheduling problem is to determine the value of each element in the whole scheduling matrix  $E$ .

**3.2. Objective Function.** The goal of multisensors cooperative detecting is to detect ballistic target stably and continuously. When the cooperative detecting task is scheduled, not only the property of targets but also the feasibility of detecting task to target is considered. So when the match optimiza-

tion objective function between sensors and subtasks is established, such factors as the target priority, detecting benefit, handover times, and resource load are considered comprehensively.

(1) *Target Priority.*  $Pr_j$  denotes the priority of the  $j$ th target and  $0 \leq Pr_j \leq 1$ .

(2) *Detection Benefit of Sensor to Target [16].* Detection benefit includes two factors: one is the distance of target to sensor, the closer the distance between sensor and the target is, the more advantage the target is detected by sensor; the other is detection angle of sensor to target, there is the optimal detection angle, and the larger the difference between the detection angle and the best detection angle is, the poorer the detection efficiency is. The distance detection benefit  $A_{ij}^k$  and angle detection benefit  $P_{ij}^k$  of the  $i$ th sensor to the  $j$ th target in the interval of the  $k$ th subtask are defined, respectively, as follows:

$$A_{ij}^k = \frac{D_{\max}^i - \bar{D}_{ij}^k}{D_{\max}^i} \quad (5)$$

$$P_{ij}^k = \frac{\max\{\theta_{\text{opt}}^i - \bar{\theta}_{ij}^k\} - (\theta_{\text{opt}}^i - \bar{\theta}_{ij}^k)}{\max\{\theta_{\text{opt}}^i - \bar{\theta}_{ij}^k\}}, \quad (6)$$

where  $D_{\max}^i$  is the maximum detection distance of the  $i$ th sensor,  $\bar{D}_{ij}^k$  is the average detection distance of the  $i$ th sensor to the  $j$ th target in the  $[ST^k, ET^k]$ ,  $\theta_{\text{opt}}^i$  is the best detection angle of the  $i$ th sensor, and  $\bar{\theta}_{ij}^k$  is the average detection angle of the  $i$ th sensor to the  $j$ th target in the  $[STime^k, ETime^k]$ .

The normalized distance detection benefit  $A$  and normalized angle detection benefit  $P$  are as follows:

$$A = \frac{\sum_{i=1}^{(n_1+n_2)} \sum_{j=1}^m \sum_{k=1}^{TN} A_{ij}^k \cdot e_{ij}^k}{\sum_{i=1}^{(n_1+n_2)} \sum_{j=1}^m \sum_{k=1}^{TN} d_{ij}^k} \quad (7)$$

$$P = \frac{\sum_{i=1}^{(n_1+n_2)} \sum_{j=1}^m \sum_{k=1}^{TN} P_{ij}^k \cdot e_{ij}^k}{\sum_{i=1}^{(n_1+n_2)} \sum_{j=1}^m \sum_{k=1}^{TN} d_{ij}^k},$$

where  $0 \leq A \leq 1, 0 \leq P \leq 1$ .

(3) *Handover Rate of Sensor.* In the scheduling interval, the larger the number of total handover is, the more frequent the handover is, which would cause the loss of target more easily. The whole resources scheduling matrix (namely,  $E$ )'s corresponding element of adjacent subtask is calculated by "XOR," and then the number of "1" is added up as the total number of handover. The handover rate in the scheduling interval is defined as

$$B = \frac{\sum_{i=1}^{(n_1+n_2)} \sum_{j=1}^m \sum_{k=1}^{TN-1} e_{ij}^k \oplus e_{ij}^{k+1}}{(n_1 + n_2) \cdot m \cdot (TN - 1)}, \quad (8)$$

where  $0 \leq B \leq 1$ .

(4) *The Total Load Rate of Resource* [17]. The total load rate of sensor resource is defined as the ratio of total detection time and total visualization time of sensor to target in the [Time<sub>s</sub>, Time<sub>e</sub>], which is marked as  $L$ .

$$L = \frac{\sum_{i=1}^{n_1+n_2} \sum_{j=1}^m \sum_{k=1}^{TN} (ET^k - ST^k) e_{ij}^k}{\sum_{i=1}^{n_1+n_2} \sum_{j=1}^m \sum_{k=1}^{TN} (ET^k - ST^k) d_{ij}^k}, \quad (9)$$

where  $0 \leq L \leq 1$ ; the smaller  $L$  is, the lighter the load of sensor resource is.

It is known from the above analysis that the matching optimization model of resources and subtasks contains such several factors as  $Pr_j$ ,  $A$ ,  $P$ ,  $B$ , and  $L$ . Then the objective function is established through linear weighting of these factors:

$$Z = \alpha_1 Pr_j + \alpha_2 A + \alpha_3 P - \alpha_4 B - \alpha_5 L, \quad (10)$$

where  $\alpha_1, \alpha_2, \alpha_3, \alpha_4$ , and  $\alpha_5$  are the weight coefficient, which are adjusted adaptively, and  $\alpha_1 + \alpha_2 + \alpha_3 + \alpha_4 + \alpha_5 = 1$ .

**3.3. Constraint Condition Analysis.** The factors of matching optimization objective function in (10) include the target, sensor resource, and subtask. In the course of optimization solution of the objective function, it must be subject to the corresponding constraint conditions. So analysis of constraint conditions is the prerequisite for the optimization solution of objective function.

- (1) The tracking target capacity constraint of sensor.

The tracking target capacity of sensors is

$$\sum_{j=1}^m e_{ij}^k \leq R_i, \quad \forall i, k, \quad (11)$$

where  $R_i$  denotes the tracking target capacity of the  $i$ th sensor.

- (2) Binary detection constraint of LEO satellites.

The TBM must be detected by two satellites at the same time; namely,

$$\sum_{i=1}^{n_1} e_{ij}^k = \{0, 2, 4, \dots\}, \quad \forall j, k. \quad (12)$$

- (3) The number constraint of sensor.

$$\left\{ r_j^{s1} \leq \sum_{i=1}^{n_1} e_{ij}^k \leq r_j^{e1} \right\} \cap \left\{ r_j^{s2} \leq \sum_{i=n_1}^{(n_1+n_2)} e_{ij}^k \leq r_j^{e2} \right\}, \quad (13)$$

$\forall j, k$ ,

where  $r_j^{s1}$  and  $r_j^{e1}$  are the lower limit and upper limit of the satellites, respectively, and  $r_j^{s2}$  and  $r_j^{e2}$  are the lower limit and upper limit of the radars, respectively.

- (4) Feasibility constraint.

$$0 \leq e_{ij}^k \leq d_{ij}^k, \quad \forall i, j, k. \quad (14)$$

- (5) Solution space constraint.

$$\begin{aligned} d_{ij}^k &= \{0, 1\} \\ e_{ij}^k &= \{0, 1\}. \end{aligned} \quad (15)$$

## 4. Fast Computation for Resource Matching Model Based on MBPSO

In order to realize fast computation for the match optimization model, two more steps are involved:

- (1) For the optimization process of objective function is affected by the above constraints, these five constraints should be processed further to eliminate the corresponding effect.
- (2) A modified binary particle swarm optimization (MBPSO) is devised by modifying the updates on particle's velocity and position. On one hand, the modified update on particle's velocity is used to solve the problem that particle is easily trapped into local optimum in BPSO; on the other hand, the modified updates on particle's position are used to solve the problem that particles in BPSO cannot converge to the optimal solution.

### 4.1. Processing of Constraint Condition

**4.1.1. Binary Matrix Encoding.** The mapping relationship between solution matrix  $E$  and particle's position  $X$  is established according to resource matching model. A 0-1 binary matrix is built by binary encoding matrix  $E$ , whose dimension is  $C \times (TN \cdot m)$  (where  $C = R_1 + R_2 + \dots + R_{n_1+n_2}$ ). The encoding process is shown in Figure 2.

This encoding structure transforms the sensor with multitargets detecting capability into several sensors with the single-target detecting capability. The particle's position is  $X = (x_{ij})_{C \times (TN \cdot m)}$  (if  $x_{ij}$  is equal to 1, this denotes that the  $j$ th target is detected by the  $i$ th sensor in the interval of subtask, while if  $x_{ij}$  is equal to 0, this denotes that the  $j$ th target is not detected by sensor  $i$ th sensor). The particles created with this encoding method are very intuitive, which are the one-to-one mapping relationship with total scheduling matrix  $E$  and denote the scheduling results directly without decoding computation.

The analysis shows that this binary matrix encoding will satisfy the constraint conditions (1) and (5) of resources optimization objective function.

**4.1.2. Further Processing of Constraint Condition.** In order to eliminate the influence of constraint condition (2), (3), and (4) to objective function, these three constraints should be further processed, respectively.

Target Sensor		1	...	$m$	...	$(j-1)m+1$	...	$j-m$	...	$(TN-1)m+1$	...	$TN-m$
		0	...	1	...	1	...	0	...	1	...	0
S1	1	0	...	1	...	1	...	0	...	1	...	0
	⋮	⋮	⋮	⋮	⋮	⋮	⋮	⋮	⋮	⋮	⋮	⋮
⋮	R1	1	...	0	...	...	1	0	...	0	...	1
	⋮	⋮	⋮	⋮	⋮	⋮	⋮	⋮	⋮	⋮	⋮	⋮
C	1	...	1	...	0	...	1	...	0	...	1	

FIGURE 2: Encoding process of particle.

- (1) *Processing the Constraint (2)*. The deployment location of satellites is considered, the two satellites whose location are close to each other are integrated as one sensor, and the target capacity of combined satellites is the minimum of the two satellites.
- (2) *Processing the Constraint (4)*. The penalty function method is adopted, which is to check the position where the element is equal to 0 in total detection matrix  $D$ , and then the corresponding position' value in the distance detection benefit matrix and angle detection benefit matrix is set zero, which can eliminate the infeasible solution.
- (3) *Processing the Constraint (3)*. In the course of encoding and updating the particle, constraint (3) is inspected, if it is not conformed to constraint (3), then particle will be modified, and the modified steps are as follows.

*Step 1.* The number of "1" in the column of particle is added up, which is defined as  $N$ .

*Step 2.* If  $N < (r_j^{s1} + r_j^{s2})$ , the value of  $(r_j^{s1} + r_j^{s2}) - N$  in this column is set to zero randomly, and then Step 4 is run; if  $N \geq (r_j^{s1} + r_j^{s2})$ , Step 3 is run.

*Step 3.* If  $N > (r_j^{e1} + r_j^{e2})$ , the value of  $N - (r_j^{e1} + r_j^{e2})$  in this column is set to zero randomly.

*Step 4.* If all columns of particle are corrected, the step is jumped to Step 1; otherwise, the modified step is completed.

#### 4.2. Modified BPSO Algorithm

*4.2.1. Modified Method for Particle Velocity Updating Means.* The particle velocity updating means in basic BPSO is as

follows:

$$v_{ij}^{k+1} = \omega v_{ij}^k + c_1 r_1 (p_{ij}^k - x_{ij}^k) + c_2 r_2 (p_{gj}^k - x_{ij}^k), \quad (16)$$

where  $k$  is the  $k$ th iteration,  $\omega$  is the inertia weight,  $c_1$  and  $c_2$  are the cognition learning rate and social learning rate, respectively,  $r_1$  and  $r_2$  are random number between 0 and 1,  $P_{ibest} = [p_{i1}, p_{i2}, \dots, p_{iD}]$  is the optimal value of personal, and  $P_{gbest} = [p_{g1}, p_{g2}, \dots, p_{gD}]$  is the swarm optimal value.

The useful information is not made full use of in the iterative process of basic BPSO; namely, such factors as the particle's velocity, personal optimal solution, and global optimal solution are contained. The whole swarm would fall into local optima, when global optimal solution is invalid at a certain moment or global optimal solution is trapped into local optima. The personal optimal solution and global optimal solution are doubted through introducing the doubt factor  $-\omega^k r_3 [p_{ij}^k + p_{gj}^k]$ , which is to reduce the probability of the premature convergence when particle is fallen into local optima. And the modified velocity updating means is as follows:

$$v_{ij}^{k+1} = \omega^k v_{ij}^k + c_1 r_1 (p_{ij}^k - x_{ij}^k) + c_2 r_2 (p_{gj}^k - x_{ij}^k) - \omega^k r_3 (p_{ij}^k + p_{gj}^k), \quad (17)$$

where  $r_3$  is random number between 0 and 1.

The modified velocity updating means of the particle are shown in Figure 3.

*4.2.2. Modified Method of Particle Position Updating Means.* The particle position updating means in basic BPSO are as

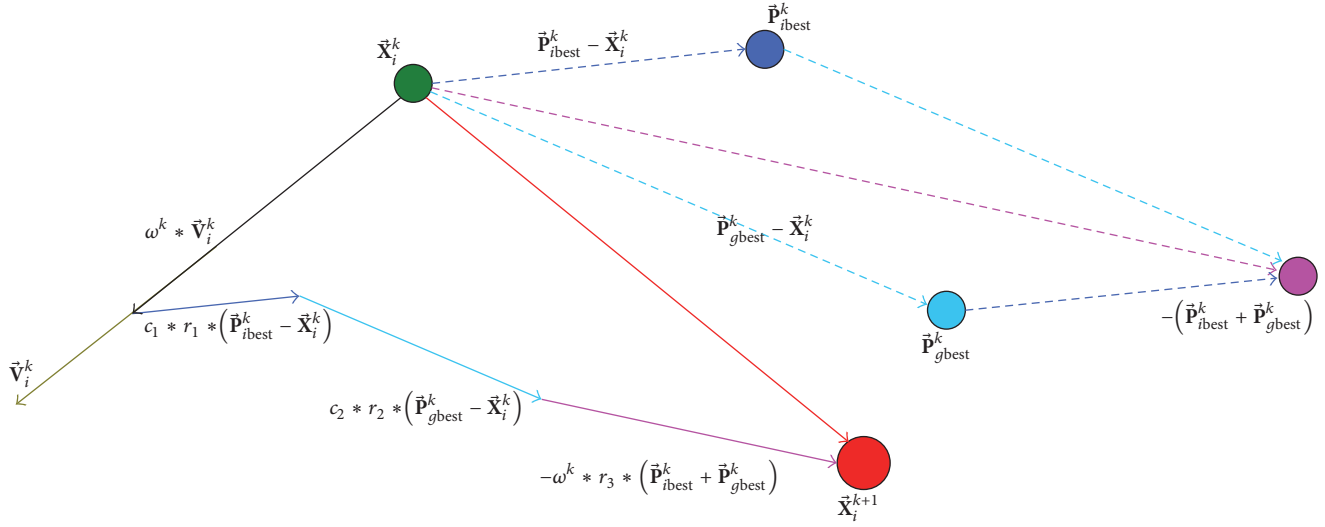


FIGURE 3: Graphical representation of the particle updating.

follows:

$$x_{ij}^{k+1} = \begin{cases} 1, & a < S(v_{ij}^{k+1}) \\ 0, & \text{otherwise,} \end{cases} \quad (18)$$

where  $a$  is random number between 0 and 1 and  $S(v_{ij}^{k+1})$  denotes a Sigmoid fuzzy function (where  $S(v_{ij}^{k+1}) = 1/1 + \exp(-v_{ij}^{k+1})$ ).  $v_{ij}^{k+1} \in [v_{\min}, v_{\max}]$  denotes the probability of  $x_{ij}^{k+1}$  whose value is 1 or 0.

Sigmoid function is modified referring methods in [15], and the contrast diagram of the basic Sigmoid function and modified Sigmoid function is shown in Figure 4.

Analysis of Figure 4 shows that, in the Sigmoid function of BPSO, the particle velocity is larger and positive, which means that probability of 1 for the particle position is large; in the same way, the particle velocity is less and negative, which means that probability of 0 for the particle position is large, and the particle velocity is 0, which means that the probability of 0 and 1 for particle position is 0.5. While there is no difference between positive velocity and negative velocity in the modified Sigmoid function, a large absolute value of velocity means that the current particle's position is not suitable and a great movement is required to make the particle reach the optimal position. Also, a small absolute value of the velocity indicates that the current particle's position is close to the optimal position.

So the modified Sigmoid function is used to update particle's position in MBPSO algorithm; the modified velocity updating means is

$$S(v_{ij}^{k+1}) = E + (1 - E) \times |\tanh(v_{ij}^{k+1})| \quad (19)$$

$$x_{ij}^{k+1} = \begin{cases} \bar{x}_{ij}^k, & a < S(v_{ij}^{k+1}) \\ x_{ij}^k, & \text{other,} \end{cases} \quad (20)$$

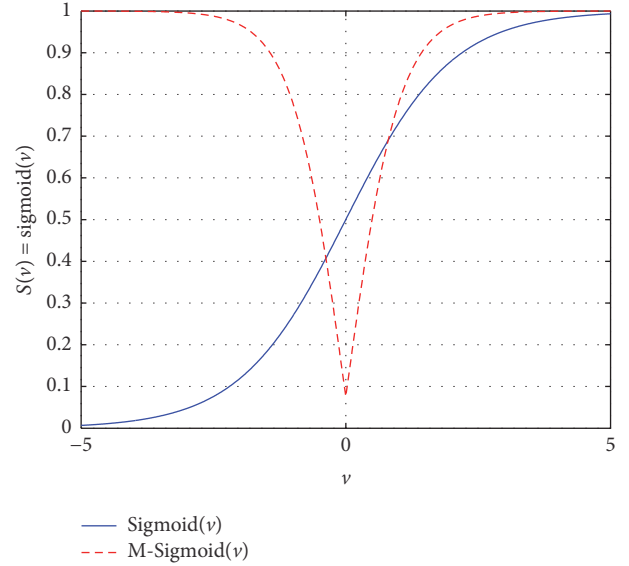


FIGURE 4: The contrast diagram of the basic Sigmoid function and modified Sigmoid function.

where  $E = \text{erf}(NF/T^t) = (2/\sqrt{\pi}) \int_0^{NF/T^t} e^{-t^2} dt$  is a small value. If the optimal position of particles is not changed in several sequential iterations,  $E$  is added to accelerate the convergence rate and to escape from a local optima.  $NF$  is the number of generations that the optimal position is not changed in the sequential iterations,  $T^t$  is a time constant, and  $\bar{x}_{ij}^k$  is the complement of  $x_{ij}^k$ .

**4.3. Algorithm Process.** MBPSO algorithm process is as follows.

*Step 1.* Set parameter. Set  $\omega$ ,  $c_1$ ,  $c_2$ ,  $c_3$ , the largest number of iterations  $\text{Iter}_{\max}$ ,  $NF$ ,  $T^t$ , population size, particle's dimension, and so on.

TABLE 1: Relevant parameters of TBM.

TBM	Launch time	Flight time (s)	Maximum height (km)	Priority
TBM1	18:00:00	930	551	2
TBM2	18:00:00	1032	615	1
TBM3	18:00:00	879	529	4
TBM4	18:00:00	911	543	3

*Step 2.* Initialize the particle swarm, the current personal optimal fitness value, and global optimal fitness value. The position and velocity of initial swarm are generated randomly and  $k = 1$ .

*Step 3.* Judge whether the particle meets constraint (3) or not; if constraint (3) is met, the processing step is gone to Step 4; otherwise, the particle is modified with the modified method.

*Step 4.* The fitness value of each particle is calculated by (10), then  $P_{ibest}$  and  $P_{gbest}$  are updated.

*Step 5.* The velocity of particle is updated by (17), and the position is updated by (19) and (20); then it is judged that whether the particle meets constraint (3) or not, if it meets, the process step is gone to Step 6; otherwise, the particle is modified with the modified method.

*Step 6.* If  $k < \text{Iter}_{\max}$ , then  $k = k + 1$ , and the process step is gone to Step 4; otherwise, the process step is gone to Step 7.

*Step 7.* Output  $P_{gbest}$ . The optimal scheduling matrix scheme is obtained; then the algorithm is ended.

## 5. Simulation Analysis

*5.1. Simulation Conditions.* In order to validate efficiency of the resources match model and MBPSO algorithm proposed in this paper, simulation scenario is supposed as follows:

- (1) Command and control system received early warning information of 4 TBMs at 18:00:30. Relevant information is shown in Table 1.
- (2) Two LEO satellites and three ground radars are deployed in early warning system. LEO satellite's parameters are as follows: orbit altitude is 1600 km, detection range is as far as 1400 km, field size is  $20^\circ \times 10^\circ$ , the best detection angle is  $90^\circ$ , target capacity is 2. Ground radar's parameters are as follows: two works on  $P$ -band, one works on  $X$ -band, and the detection range of three radars are, respectively, 3000 km, 4000 km, and 2000 km, the area of azimuth-angle is  $\pm 60^\circ$ , the area of pitch-angle is  $1\text{--}90^\circ$ , the best detection angle is  $45^\circ$ ,  $60^\circ$ , and  $80^\circ$ , respectively, and target capacity of the radar is 3, 4, and 8, respectively.

Task scheduling time is from 18:06:30 to 18:08:30, in which sensors will detect targets and provide subsequent intercepting with significant instructions of TBM. The visualization interval of sensor to target is shown in Table 2.

TABLE 2: Visualization interval of sensor to TBM.

	TBM1	TBM2	TBM3	TBM4
Sat1	[0, 85]	[0, 102]	[0, 68]	[0, 89]
Sat2	[0, 120]	[0, 120]	[0, 120]	[0, 120]
PR1	[0, 85]	[0, 89]	[0, 72]	[0, 83]
PR2	[40, 120]	[46, 120]	[24, 120]	[29, 120]
XR1	[97, 120]	[110, 120]	[72, 120]	[83, 120]

*5.2. Simulation Process.* Assume  $D_{\max}$  is 20 s,  $D_{\min}$  is 10 s, and  $\text{MacLong}$  is 15 s. Nine subtasks are obtained by the task decomposition method proposed in this paper, whose corresponding interval, respectively, is [0, 12], [12, 24], [29, 40], [46, 57], [57, 68], [72, 83], [83, 97], [97, 110], and [110, 120]. Meanwhile, subtasks' detection matrix is as follows:

$$D^1 = \begin{pmatrix} 1 & 1 & 1 & 1 \\ 1 & 1 & 1 & 1 \\ 1 & 1 & 1 & 1 \\ 0 & 0 & 0 & 0 \\ 0 & 0 & 0 & 0 \end{pmatrix}$$

$$D^2 = \begin{pmatrix} 1 & 1 & 1 & 1 \\ 1 & 1 & 1 & 1 \\ 1 & 1 & 1 & 1 \\ 0 & 0 & 0 & 0 \\ 0 & 0 & 0 & 0 \end{pmatrix}$$

$$D^3 = \begin{pmatrix} 1 & 1 & 1 & 1 \\ 1 & 1 & 1 & 1 \\ 1 & 1 & 1 & 1 \\ 0 & 0 & 1 & 1 \\ 0 & 0 & 0 & 0 \end{pmatrix}$$

$$D^4 = \begin{pmatrix} 1 & 1 & 1 & 1 \\ 1 & 1 & 1 & 1 \\ 1 & 1 & 1 & 1 \\ 1 & 1 & 1 & 1 \\ 0 & 0 & 0 & 0 \end{pmatrix}$$

$$D^5 = \begin{pmatrix} 1 & 1 & 1 & 1 \\ 1 & 1 & 1 & 1 \\ 1 & 1 & 1 & 1 \\ 1 & 1 & 1 & 1 \\ 0 & 0 & 0 & 0 \end{pmatrix}$$

$$\begin{aligned}
 D^6 &= \begin{pmatrix} 1 & 1 & 0 & 1 \\ 1 & 1 & 1 & 1 \\ 1 & 1 & 0 & 1 \\ 1 & 1 & 1 & 1 \\ 0 & 0 & 1 & 0 \end{pmatrix} & D^4 &= \begin{pmatrix} 1 & 1 & 0 & 0 \\ 1 & 1 & 0 & 0 \\ 1 & 1 & 0 & 1 \\ 1 & 1 & 1 & 1 \\ 0 & 0 & 0 & 0 \end{pmatrix} \\
 D^7 &= \begin{pmatrix} 0 & 1 & 0 & 0 \\ 1 & 1 & 1 & 1 \\ 0 & 0 & 0 & 0 \\ 1 & 1 & 1 & 1 \\ 0 & 0 & 1 & 1 \end{pmatrix} & D^5 &= \begin{pmatrix} 1 & 1 & 0 & 0 \\ 1 & 1 & 0 & 0 \\ 1 & 1 & 0 & 1 \\ 1 & 1 & 1 & 1 \\ 0 & 0 & 0 & 0 \end{pmatrix} \\
 D^8 &= \begin{pmatrix} 0 & 0 & 0 & 0 \\ 1 & 1 & 1 & 1 \\ 0 & 0 & 0 & 0 \\ 1 & 1 & 1 & 1 \\ 1 & 0 & 1 & 1 \end{pmatrix} & D^6 &= \begin{pmatrix} 1 & 1 & 0 & 0 \\ 1 & 1 & 0 & 0 \\ 1 & 1 & 0 & 1 \\ 1 & 1 & 1 & 1 \\ 0 & 0 & 1 & 0 \end{pmatrix} \\
 D^9 &= \begin{pmatrix} 0 & 0 & 0 & 0 \\ 1 & 1 & 1 & 1 \\ 0 & 0 & 0 & 0 \\ 1 & 1 & 1 & 1 \\ 1 & 1 & 1 & 1 \end{pmatrix}. & D^7 &= \begin{pmatrix} 0 & 1 & 0 & 0 \\ 0 & 1 & 0 & 0 \\ 0 & 0 & 0 & 0 \\ 1 & 1 & 1 & 1 \\ 0 & 0 & 1 & 1 \end{pmatrix}
 \end{aligned}$$

(21)

Assume that  $\text{Iter}_{\max} = 50$ ,  $NF = 5$ ,  $c_1 = c_2 = c_3 = 2.05$ ,  $T^l = 20$ , swarm size is 30, weight coefficient  $\alpha_1 = 0.3$ ,  $\alpha_2 = 0.25$ ,  $\alpha_3 = 0.2$ ,  $\alpha_4 = 0.15$ ,  $\alpha_5 = 0.1$ ,  $r_j^{s1} + r_j^{s2} = 1$ , and  $r_j^{e1} + r_j^{e2} = 4$ . According to resources match model in Section 2, the total scheduling matrix is solved by MBPSO algorithm. So subtasks' scheduling matrix is as follows:

$$\begin{aligned}
 D^1 &= \begin{pmatrix} 1 & 1 & 0 & 0 \\ 1 & 1 & 0 & 0 \\ 1 & 1 & 0 & 1 \\ 0 & 0 & 0 & 0 \\ 0 & 0 & 0 & 0 \end{pmatrix} & D^8 &= \begin{pmatrix} 0 & 0 & 0 & 0 \\ 0 & 0 & 0 & 0 \\ 0 & 0 & 0 & 0 \\ 1 & 1 & 1 & 1 \\ 1 & 0 & 1 & 1 \end{pmatrix} \\
 D^2 &= \begin{pmatrix} 1 & 1 & 0 & 0 \\ 1 & 1 & 0 & 0 \\ 1 & 1 & 0 & 1 \\ 0 & 0 & 0 & 0 \\ 0 & 0 & 0 & 0 \end{pmatrix} & D^9 &= \begin{pmatrix} 0 & 0 & 0 & 0 \\ 0 & 0 & 0 & 0 \\ 0 & 0 & 0 & 0 \\ 1 & 1 & 1 & 1 \\ 1 & 1 & 1 & 1 \end{pmatrix}.
 \end{aligned}$$

(22)

### 5.3. Simulation Conclusion

**5.3.1. Optimizing Scheduling Scheme.** The total scheduling matrix  $D$  is transformed, and then the optimal match scheme is obtained, as shown in Figure 5.

Analysis of Figure 5 shows the following:

- (1) The optimal scheduling scheme meets the constraint of total detection matrix.
- (2) It is guaranteed that there is at least one sensor to detect each TBM, in addition to TBM3 which is not detected in period  $[0, 29]$ . Under the constraint of

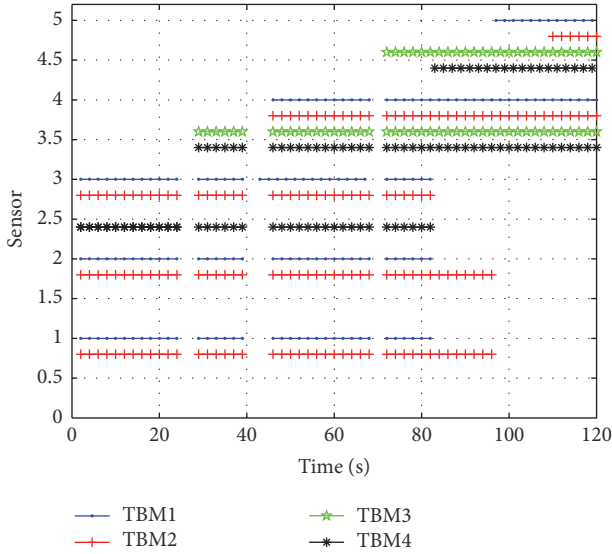


FIGURE 5: Optimal scheduling scheme of multisensor for four-TBM detection.

TABLE 3: Performance contrast of algorithms.

Algorithm	Average convergence iteration	Average computation time/s
BPSO	16	2.5382
NBPSO	32	3.0759
MBPSO-2	22	2.5968
MBPSO	18	2.6125

binary satellite detection, the TBM is detected by sensor 1 and sensor 2 for the meantime.

- (3) More sensors are needed to detect TBM2, 4 sensors at the most time, while less sensors are needed to detect TBM3, 2 at the most time. That is, TBM2's priority is the highest, and TBM3's priority is the lowest.
- (4) Besides intervals [24, 29] and [40, 46], detection of each sensor to TBM is not interrupted, which denotes that detection to TBM is continuous and has fewer handover times.

5.3.2. *Algorithm Performance Contrast.* The algorithm is verified in MATLAB R2013a on Pentium 3.2 GHz platform. The above match optimization model is solved by BPSO [11], NBPSO [18], MBPSO-2, respectively, and the proposed algorithm, and the performance of each algorithm is compared through calculating 100 times. MBPSO-2 is the algorithm which is obtained by improving the particle's velocity updating means in BPSO.

The optimum fitness value contrast of four kinds of algorithm is shown in Figure 6.

The performance contrast of four kinds of algorithm is shown in Table 3.

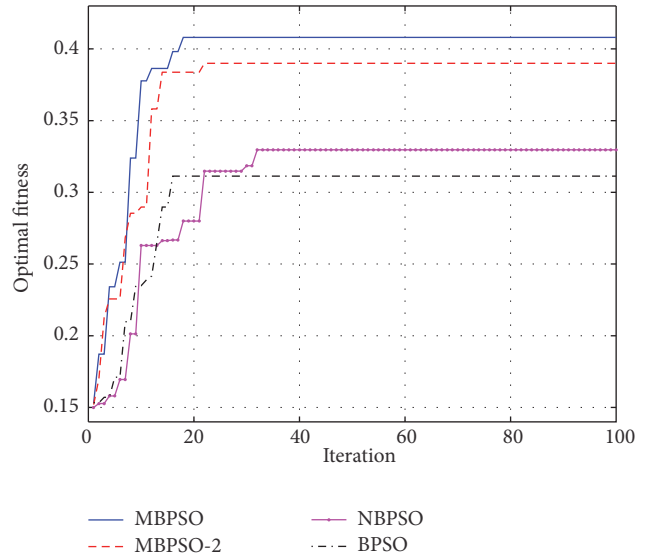


FIGURE 6: Contrast of optimal fitness value curves.

It can be analyzed from Figure 6 and Table 3 that the optimal fitness value of the MBPSO algorithm is better than that of the other three algorithms, and the iteration number of MBPSO is the least, which is 18, while the iteration number of MBPSO-2 and NBPSO is 22 and 32, respectively, which suggest that the real time of the MBPSO algorithm is the best among the BPSO, NBPSO, MBPSO-2, and MBPSO.

On one hand, the Sigmoid function in NBPSO is modified, and the optimal fitness value of NBPSO is better than BPSO, but NBPSO still easily traps into local optima due to its velocity updating means. On the other hand, the velocity updating means in MBPSO-2 are modified, and the optimal fitness value of MBPSO-2 is greatly improved, but the particle cannot be converged to the best solution because of the problem of basic Sigmoid function. With both the velocity and position updating means of particle modified in MBPSO, which makes it easier for particle to jump out of local optima, the convergence speed and search capability of MBPSO are better than those of the other three algorithms.

## 6. Conclusions

The resources scheduling problem for the multisensor cooperative detecting the ballistic target is researched in this paper. The multisensor cooperative detecting task is decomposed as many subtasks by hybrid task decomposition method. Then the resource match optimization model based on the resources and tasks is established. Finally, MBPSO algorithm is proposed to solve the match optimization model efficiently. Simulation results show that the proposed algorithm is better in terms of convergence velocity, searching capability, solution accuracy, and efficiency.

## Competing Interests

The authors declare that there is no conflict of interests regarding the publication of this paper.

## Authors' Contributions

Changyun Liu and Xiangke Guo have contributed equally to this paper.

## Acknowledgments

This paper is supported by National Natural Science Fund of China (61503408) and Doctoral Foundation of Air Force Engineering University under Grant (KGD080914002).

## References

- [1] Y. Zhi-Wei, N. Yi-Feng, and L. Han-Ling, "Study of sensor scheduling for early warning satellite based on parallel tabu genetic algorithm (PTGA)," *Journal of Astronautics*, vol. 24, no. 6, pp. 598–603, 2003.
- [2] T. Shao-Xun, Y. Xian-Qing, and L. Xue-Shan, "An Improved particle swarm optimization algorithm for early warning satellites scheduling problems," *Systems Engineering*, vol. 30, no. 1, pp. 116–121, 2012.
- [3] P. Jian, P. Zou, and W. Xiong, "Heuristic algorithm for dynamic task planning of early warning system of Low Earth Orbit," *Journal of Electronics and Information Technology*, vol. 35, no. 10, pp. 2438–2444, 2013.
- [4] F. Ming-Yue, L. Guo-Hui, and Y. Xian-Qing, "Rule-based scheduling method for sensors on early warning satellites basing on task analysis," *Computer Applications*, vol. 27, no. 12, pp. 3095–3098, 2007.
- [5] M. Feng, G. Liu, and X. Yi, "Sensor scheduling method for space-based early warning system," *Computer Engineering and Applications*, vol. 45, no. 2, pp. 225–228, 2009.
- [6] X.-S. Zhao, H.-X. Wang, and Y.-C. Cai, "Resource scheduling method in antimissile early warning campaign," *Systems Engineering and Electronics*, vol. 37, no. 6, pp. 1300–1305, 2015.
- [7] W.-L. Guan, Y.-H. Tan, H.-X. Zhang, and J.-L. Song, "Distribution system feeder reconfiguration considering different model of DG sources," *International Journal of Electrical Power & Energy Systems*, vol. 68, pp. 210–221, 2015.
- [8] M. Yusoff, J. Ariffin, and A. Mohamed, "DPSO based on a min-max approach and clamping strategy for the evacuation vehicle assignment problem," *Neurocomputing*, vol. 148, pp. 30–38, 2015.
- [9] L. Zhang, Y. Tang, C. Hua, and X. Guan, "A new particle swarm optimization algorithm with adaptive inertia weight based on Bayesian techniques," *Applied Soft Computing Journal*, vol. 28, pp. 138–149, 2015.
- [10] Y.-J. Zheng, H.-F. Ling, J.-Y. Xue, and S.-Y. Chen, "Population classification in fire evacuation: a multiobjective particle swarm optimization approach," *IEEE Transactions on Evolutionary Computation*, vol. 18, no. 1, pp. 70–81, 2014.
- [11] J. Kennedy and R. C. Eberhart, "Discrete binary version of the particle swarm algorithm," in *Proceedings of the 1997 IEEE International Conference on Systems, Man, and Cybernetics*, pp. 4104–4108, Orlando, Fla, USA, October 1997.
- [12] A. H. El-Maleh, A. T. Sheikh, and S. M. Sait, "Binary particle swarm optimization (BPSO) based state assignment for area minimization of sequential circuits," *Applied Soft Computing*, vol. 13, no. 12, pp. 4832–4840, 2013.
- [13] K. Fan, W. You, and Y. Li, "An effective modified binary particle swarm optimization (mBPSO) algorithm for multi-objective resource allocation problem (MORAP)," *Applied Mathematics and Computation*, vol. 221, pp. 257–267, 2013.
- [14] B. Wei and J. Zhao, "Haplotype inference using a novel binary particle swarm optimization algorithm," *Applied Soft Computing*, vol. 21, pp. 415–422, 2014.
- [15] Z. Beheshti, S. M. Shamsuddin, and S. Hasan, "Memetic binary particle swarm optimization for discrete optimization problems," *Information Sciences*, vol. 299, pp. 58–84, 2015.
- [16] R. Jun-Liang, X. Qing-Hua, L. Qiang, and J. Zhe, "Resource scheduling method of missile defense early warning system based on self-adaptive probability particle swarm optimization," *Journal of Air Force Engineering University*, vol. 15, no. 6, pp. 45–48, 2014.
- [17] W. Bo, A. Wei, X. Kai et al., "Multi-object tracking sensor scheduling for Low Earth Orbit constellation based on multi-model," *Acta Aeronautica et Astronautica Sinica*, vol. 31, no. 5, pp. 946–957, 2010.
- [18] M. Rostami-Shahrbabak and H. Nezamabadi-Pour, "New approach to binary PSO algorithm," in *Proceedings of the 14th Iranian Conference on Electrical Engineering*, pp. 1–6, Tehran, Iran, May 2006.

## Research Article

# A Meshless Radial Basis Function Based on Partition of Unity Method for Piezoelectric Structures

Sen Li,<sup>1</sup> Linqun Yao,<sup>2</sup> Shichao Yi,<sup>3</sup> and Wei Wang<sup>2</sup>

<sup>1</sup>*School of Mathematical Sciences, Soochow University, Suzhou 215006, China*

<sup>2</sup>*School of Urban Rail Transportation, Soochow University, Suzhou 215006, China*

<sup>3</sup>*School of Mathematics and Physics, Jiangsu University of Science and Technology, Zhenjiang 212003, China*

Correspondence should be addressed to Linqun Yao; [lqyao@suda.edu.cn](mailto:lqyao@suda.edu.cn)

Received 27 August 2016; Accepted 20 October 2016

Academic Editor: Lihua Wang

Copyright © 2016 Sen Li et al. This is an open access article distributed under the Creative Commons Attribution License, which permits unrestricted use, distribution, and reproduction in any medium, provided the original work is properly cited.

A meshless radial basis function based on partition of unity method (RBF-PUM) is proposed to analyse static problems of piezoelectric structures. The methods of radial basis functions (RBFs) possess some merits: the shape functions have high order continuity;  $h$ -adaptivity is simpler than mesh-based methods; the shape functions are easily implemented in high dimensional space. The partition of unity method (PUM) easily constructs local approximation. The character of local approximate space can be varied and regarded as  $p$ -adaptivity. Considering the good properties of the two methods, the RBFs are used for local approximation and the local supported weight functions are used in the partition of unity method. The system equations of the RBF-PUM are derived using the variational principle. The field variables are approximated using the RBF-PUM shape functions which inherit all the advantages of the RBF shape functions such as the delta function property. The boundary conditions can be implemented easily. Numerical examples of piezoelectric structures are investigated to illustrate the efficiency of the proposed method and the obtained results are compared with analytical solutions and available numerical solutions. The behaviors of some parameters that probably influenced numerical results are also studied in detail.

## 1. Introduction

Piezoelectric material is a new advanced material which can be used for developing smart structures with self-controlling and self-monitoring capabilities. The essential feature of piezoelectric material is the capability of energy transformation between electrical energy and mechanical energy. Hence, piezoelectric materials have been widely used as intelligent control devices such as sensors, actuators, ultrasonic transducers, and active damping devices.

Due to the complicated properties of piezoelectric materials, various approaches including analytical and numerical methods have been proposed to deal with the problems involving piezoelectric materials. However, the analytical solutions are rather restricted in general and difficult to find unless some geometry and boundary are relatively simple. Accurate, efficient, and robust numerical methods are required to simulate piezoelectric problems. Some numerical methods have been proposed to analyse piezoelectric

problems such as the finite element method (FEM) [1–4], the boundary element method (BEM) [5–7], and the smoothed FEM [8]. Among them, the FEM is considered to be an effective method for mechanical and electromechanical coupling problems. Since the FEM is a mesh-based method, the FEM may lead to large errors when mesh distortion appears or low quality meshes are adopted. Mesh distortion may occur in the problems of large deformation, crack propagation, and so forth. An alternative method is called meshless method which can eliminate mesh-based problems. In the meshless method, only a set of scattered nodes is required to represent problem domain and boundary and therefore the adaptivity is simpler than mesh-based methods.

The initial ideal of meshless method dates back to the smooth particle hydrodynamics (SPH) method proposed by Lucy [9] and Gingold and Monaghan [10] for modeling astrophysical phenomena. Then several meshless methods including the diffuse element method (DEM) [11], the element-free Galerkin (EFG) method [12], the reproducing

kernel particle method (RKPM) [13], the  $h$ - $p$  clouds method [14], the point interpolation method (PIM) [15–17], the radial basis function point interpolation method (RPIM) [18, 19], the moving Kriging (MK) meshless method [20], and the meshless local Petrov-Galerkin (MLPG) method [21–25] have been proposed to solve partial differential equations and mechanical problems. Most of these methods are carried out based on weak form equations and a set of background cells or local subdomains is required to implement numerical integration. In the MLPG method, the moving least square (MLS) approach [26] is used to construct approximate functions and the major drawback is that the MLS shape functions lack interpolation property. The boundary conditions cannot be imposed directly and some methods should be proposed to overcome this problem, such as the Lagrange multiplier method [12] and the penalty function method [18]. In the RPIM, radial basis functions (RBFs) are used to construct the shape functions. The variable is only related to the distance between interpolation point and node and therefore the method is easily implemented in high dimension space. The behaviors of radial basis functions [27–32] have been widely investigated. Radial basis functions are also used in the meshless collocation method [33–35] which is based on the strong form equations. These methods based on the RBFs have obtained high accurate solutions and have been shown excellent interpolation property.

Some methods coupling with the partition of unity method (PUM) [36, 37] have also been investigated in mechanical problems in recent years. The main advantages of the PUM are the flexibility in choosing the local approximation which can be used the approaches of the MLS, the PIM, and the RPIM. Rajendran and Zhang [38] developed a new “FE-Meshfree” method using the concepts of partition of unity method. In this method, the FEM shape functions are used for weight functions and the meshless approach is used to construct local approximation. Some of important works including Q4-LSPIM [38, 39], Q4-RPIM [40], and T3-RPIM [41] have been presented for static and vibration analysis of mechanical problems and obtained very accurate results.

In this paper, a meshless radial basis function based on partition of unity method (RBF-PUM) is proposed to analyse 2D piezoelectric structures. The RBFs are used for local approximation and Shepard’s method [44] is used for the construction of weight functions in the partition of unity method. The RBF-PUM method has been studied by Wendland [45] and Fasshauer [29] and successfully applied in the convection diffusion equations [46] using the collocation method. The field variables are approximated using the RBF-PUM shape functions which inherits all good advantages of the PUM and RBFs. The performance of the RBF-PUM shape functions will be discussed in detail.

The rest of this paper is organized as follows. The formulation of the RBF-PUM method is presented in Section 2. The governing equations and variational equations for 2D piezoelectric problems are given in Section 3. Numerical examples are considered to verify the effectiveness of the proposed method in Section 4. Finally, we end this paper with some conclusions in Section 5.

## 2. The Formulation of the RBF-PUM Method

*2.1. The Partition of Unity Method.* This section recalls briefly the partition of unity method for 2D problem. Let  $\Omega \subset \mathbf{R}^2$  be a problem domain and  $\{\Omega_i\}_{i=1}^M$  be an open cover of  $\Omega$  satisfying some mild overlapping conditions such that

$$\forall \mathbf{x} \in \Omega \quad I(\mathbf{x}) = \{i \mid \mathbf{x} \in \Omega_i\}, \quad 1 \leq \text{card}(I(\mathbf{x})) \leq M, \quad (1)$$

where  $I(\mathbf{x})$  is an index set of the patches in which the interpolation point  $\mathbf{x}$  locates and  $M$  is the total number of all patches.

For every patch  $\Omega_i$ , we construct a local approximation  $u_i(\mathbf{x})$ . According to the concept of the partition of unity method, the global approximation function  $u^h(\mathbf{x})$  can be expressed as

$$u^h(\mathbf{x}) = \sum_{i=1}^M w_i(\mathbf{x}) u_i(\mathbf{x}), \quad (2)$$

where  $\{w_i(\mathbf{x})\}_{i=1}^M$  are weight functions. The weight functions are compactly supported, nonnegative, and continuous and satisfy the partition of unity:

$$\begin{aligned} \text{supp}(w_i(\mathbf{x})) &= \Omega_i \quad i = 1, \dots, M, \\ \sum_{i=1}^M w_i(\mathbf{x}) &= 1 \quad \text{on } \Omega. \end{aligned} \quad (3)$$

Equation (3) shows that  $w_i(\mathbf{x}) = 0$  for  $i \notin I(\mathbf{x})$ . Therefore, (2) can be rewritten as

$$u^h(\mathbf{x}) = \sum_{i \in I(\mathbf{x})} w_i(\mathbf{x}) u_i(\mathbf{x}). \quad (4)$$

*2.2. Construction of Weight Functions with Partition of Unity Property.* For the partition of unity method, the patch can be of any shape, such as square, circular, spherical, or hyperspherical. The basic requirement for all patch domains is that they cover problem domain and boundary. In this paper, the circular patch is used for the analysis in the PUM.

Let  $\{X_i\}_{i=1}^M$  be a set of central points of patches  $\{\Omega_i\}_{i=1}^M$  and  $\{r_i\}_{i=1}^M$  be the radiuses as shown in Figure 1. Nonnegative and compactly supported weight functions  $\{w_i\}_{i=1}^M$  can be constructed using Shepard’s method [44] as follows:

$$w_i(\mathbf{x}) = \frac{\varphi_i(\mathbf{x})}{\sum_{k=1}^M \varphi_k(\mathbf{x})}, \quad i = 1, \dots, M, \quad (5)$$

where function  $\varphi_i(\mathbf{x})$  is given by

$$\varphi_i(\mathbf{x}) = \varphi\left(\frac{\|\mathbf{x} - X_i\|}{r_i}\right). \quad (6)$$

In the present study, Wendland function [47] is used for function  $\varphi(r)$ :

$$\varphi(r) = \begin{cases} (1-r)^4(1+4r) & 0 \leq r \leq 1, \\ 0 & r > 1, \end{cases} \quad (7)$$

in which

$$r = \frac{\|\mathbf{x} - X_i\|}{r_i}. \quad (8)$$

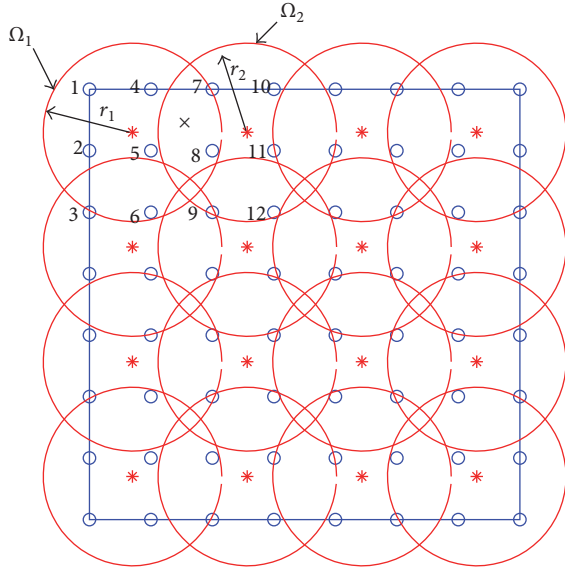


FIGURE 1: Definition of interpolation point  $x$ , central point (red \*), patch (red circle), and support radius (or patch size). The patches for interpolating point  $x$  are defined as  $\Omega_1 = \{1, 2, 4, 5, 6, 8\}$  and  $\Omega_2 = \{7, 8, 9, 10, 11, 12\}$ . The support domain of interpolation point  $x$  is defined as  $\hat{\Omega} = \Omega_1 \cup \Omega_2 = \{1, 2, 4, 5, 6, 7, 8, 9, 10, 11, 12\}$ .

**2.3. Radial Basis Function Method.** In the present method, radial basis functions with polynomial terms are used to construct the local approximation of the partition of unity method. Using radial basis functions with polynomial functions, the local approximation  $u_i(\mathbf{x})$  is given by

$$\begin{aligned} u_i(x, y) &= \sum_{i=1}^{n_i} R_i(x, y) a_i + \sum_{j=1}^m p_j(x, y) b_j \\ &= \mathbf{R}(x, y) \mathbf{a} + \mathbf{p}(x, y) \mathbf{b}, \end{aligned} \quad (9)$$

where  $\mathbf{R}(x, y)$  and  $\mathbf{p}(x, y)$  represent radial basis and polynomial functions, respectively.  $n_i$  is the total number of nodes in patch  $\Omega_i$  and  $m$  represents the number of polynomial terms.  $\mathbf{a}$  and  $\mathbf{b}$  are unknown vectors to be determined.

In the radial basis function  $R_i(x, y)$ , the variable is only related to the space distance between interpolation point  $\mathbf{x}$  and node  $\mathbf{x}_i$  and therefore the RBF method is easily implemented in high dimensional problems. Some radial basis functions such as multiquadric radial basis function (MQ-RBF), thin plate spline radial basis function (TPS-RBF), and Gaussian radial basis function (EXP-RBF) have been widely investigated in [18, 27–32]. For the present method, the MQ-RBF is adopted and given by

$$R_i(x, y) = \left(1 + \eta^2 d_i^2\right)^q, \quad (10)$$

where  $d_i = \sqrt{(x - x_i)^2 + (y - y_i)^2}$  and  $\eta$  and  $q$  are two shape parameters.

Enforcing (9) to pass through all node values in patch  $\Omega_i$ , the following equations are obtained:

$$\mathbf{u}_i = \mathbf{R}_0 \mathbf{a} + \mathbf{P}_m \mathbf{b}, \quad (11)$$

where

$$\mathbf{a}^T = [a_1, a_2, \dots, a_{n_i}],$$

$$\mathbf{b}^T = [b_1, b_2, \dots, b_m],$$

$$\mathbf{u}_i^T = [u_1, u_2, \dots, u_{n_i}],$$

$\mathbf{R}_0$

$$= \begin{bmatrix} R_1(x_1, y_1) & R_2(x_1, y_1) & \cdots & R_{n_i}(x_1, y_1) \\ R_1(x_2, y_2) & R_2(x_2, y_2) & \cdots & R_{n_i}(x_2, y_2) \\ \vdots & \vdots & \ddots & \vdots \\ R_1(x_{n_i}, y_{n_i}) & R_2(x_{n_i}, y_{n_i}) & \cdots & R_{n_i}(x_{n_i}, y_{n_i}) \end{bmatrix}, \quad (12)$$

$$\mathbf{P}_m^T = \begin{bmatrix} 1 & 1 & \cdots & 1 \\ x_1 & x_2 & \cdots & x_{n_i} \\ y_1 & y_2 & \cdots & y_{n_i} \\ \vdots & \vdots & \ddots & \vdots \\ p_m(x_1) & p_m(x_2) & \cdots & p_m(x_{n_i}) \end{bmatrix}.$$

Adding polynomial terms is an extra requirement. In order to guarantee unique approximation [48], the following conditions are usually imposed:

$$\sum_{i=1}^{n_i} p_j(x_i, y_i) a_i = 0, \quad j = 1, 2, \dots, m, \quad (13)$$

which can be rewritten in matrix form

$$\mathbf{P}_m^T \mathbf{a} = \mathbf{0}. \quad (14)$$

Vectors  $\mathbf{a}$  and  $\mathbf{b}$  can be obtained by (11) and (14), and then substitute into (9), the local approximation function  $u_i(x, y)$  is eventually expressed as

$$u_i(x, y) = \Phi_i \mathbf{u}_i, \quad (15)$$

where

$$\begin{aligned} \Phi_i &= \mathbf{R}(x, y) \mathbf{S}_a + \mathbf{P}(x, y) \mathbf{S}_b, \\ \mathbf{S}_b &= [\mathbf{P}_m^T \mathbf{R}_0 \mathbf{P}_m]^{-1} \mathbf{P}_m^T \mathbf{R}_0^{-1}, \\ \mathbf{S}_a &= \mathbf{R}_0^{-1} [\mathbf{I} - \mathbf{P}_m \mathbf{S}_b]. \end{aligned} \quad (16)$$

The existence of inverse matrix  $\mathbf{R}_0^{-1}$  for arbitrary scattered nodes has been given by Wendland [30]. Finally, the shape functions associated to all nodes in the patch  $\Omega_i$  can be expressed as

$$\Phi_i(\mathbf{x}) = [\phi_i^1(\mathbf{x}), \phi_i^2(\mathbf{x}), \dots, \phi_i^{n_i}(\mathbf{x})]. \quad (17)$$

**2.4. RBF-PUM Shape Functions and Mathematical Properties.** The radial basis functions are selected as local approximation

and the global approximation  $u^h(\mathbf{x})$  in (4) can be expressed as

$$u^h(\mathbf{x}) = \sum_{i \in I(\mathbf{x})} w_i(\mathbf{x}) \Phi_i(\mathbf{x}) \mathbf{u}_i = \tilde{\Phi}(\mathbf{x}) \tilde{\mathbf{U}}_s, \quad (18)$$

where  $\tilde{\mathbf{U}}_s$  is nodal displacement vector composed of all the nodes in the union of the patches  $\hat{\Omega} = \bigcup_{i \in I(\mathbf{x})} \Omega_i$  and  $\tilde{\Phi}(\mathbf{x})$  is the vector of the RBF-PUM shape functions given by

$$\begin{aligned} \tilde{\Phi}(\mathbf{x}) &= \sum_{i \in I(\mathbf{x})} w_i(\mathbf{x}) \Phi_i(\mathbf{x}) \\ &= [\tilde{\phi}_1(\mathbf{x}), \tilde{\phi}_2(\mathbf{x}), \dots, \tilde{\phi}_{\hat{n}}(\mathbf{x})], \end{aligned} \quad (19)$$

where  $\hat{n}$  is the total number of nodes in domain  $\hat{\Omega}$ . It is noted that the dimension of the RBF shape functions  $\Phi_i(\mathbf{x})$  may be less than  $\hat{n}$ , but they can be expanded to vector with dimension  $\hat{n}$ .

The derivative functions of the RBF-PUM shape functions can be obtained using Leibniz's rule:

$$\mathbf{D}^\alpha \tilde{\Phi}(\mathbf{x}) = \sum_{i \in I(\mathbf{x})} \sum_{|\beta| \leq |\alpha|} \binom{\alpha}{\beta} \mathbf{D}^\beta w_i(\mathbf{x}) \mathbf{D}^{\alpha-\beta} \Phi_i(\mathbf{x}), \quad (20)$$

where  $\alpha, \beta \in \mathbf{N}_0^2$  are multi-indices and  $\mathbf{D}^\alpha = \partial^{|\alpha|} / \partial x^\alpha$  is a spatial differential operator.

The RBF-PUM method inherits the advantages of the RBF meshless method and the following are the mathematical properties of the RBF-PUM shape functions:

- (1) The RBF-PUM shape functions possess the delta function property:

$$\tilde{\phi}_i(\mathbf{x}_j) = \delta_{ij}. \quad (21)$$

- (2) The RBF-PUM shape functions possess the property of partition of unity:

$$\sum_{i=1}^{\hat{n}} \tilde{\phi}_i(\mathbf{x}) = 1. \quad (22)$$

- (3) If the RBFs include at least linear polynomial terms, the RBF-PUM shape functions can ensure an exact reproduction of linear polynomials; that is,

$$\sum_{i=1}^{\hat{n}} \tilde{\phi}_i(\mathbf{x}) x_i = x. \quad (23)$$

- (4) Local compactly supported property.
- (5) Especially for  $\text{card}(I(\mathbf{x})) = 1$ , the RBF-PUM shape functions are the RBF shape functions as well as their derivative functions.

The RBF-PUM shape functions and their derivative functions are shown in Figures 2 and 3 for 1D and 2D space, respectively. In Figure 2, six regularly distributed nodes in interval  $[0, 1]$  are used for the construction of the shape functions and plotted in different colours. In Figure 3, the shape function and its derivative of point  $(0, 0)$  are plotted in interval  $[-1, 1] \times [-1, 1]$ . It can be observed that the RBF-PUM shape functions have interpolation property and local compactly supported property.

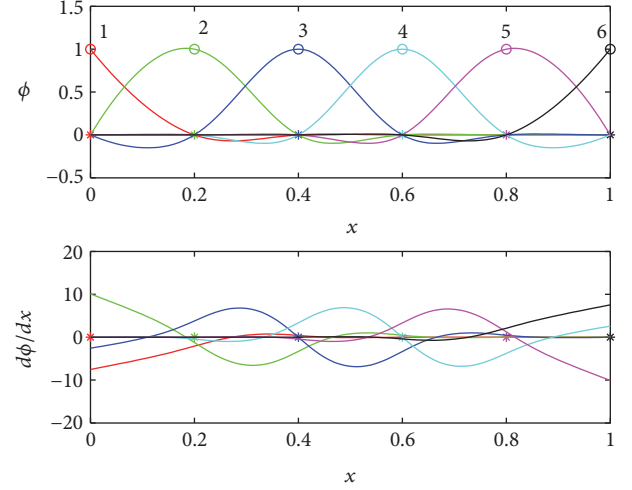


FIGURE 2: RBF-PUM shape functions and their derivatives in 1D space.

### 3. Variational Equations for Piezoelectric Structures

The variational equations for linear piezoelectricity are presented in this section. Considering a two-dimensional piezoelectric problem in domain  $\Omega$  with boundary  $\Gamma$ , the governing equations are given by

$$\begin{aligned} \nabla_s^T \boldsymbol{\sigma} + \mathbf{f} &= \mathbf{0}, \\ \nabla^T \mathbf{D} &= \mathbf{0}, \end{aligned} \quad (24)$$

where  $\boldsymbol{\sigma}, \mathbf{D}$  are stress and electric displacement vector, respectively.  $\mathbf{f}$  is body force density. The operators  $\nabla_s$  and  $\nabla$  in  $x$ - $z$  plane are given by

$$\nabla_s = \begin{bmatrix} \frac{\partial}{\partial x} & 0 & \frac{\partial}{\partial z} \\ 0 & \frac{\partial}{\partial z} & \frac{\partial}{\partial x} \end{bmatrix}^T, \quad (25)$$

$$\nabla = \begin{bmatrix} \frac{\partial}{\partial x} & \frac{\partial}{\partial z} \end{bmatrix}^T.$$

The boundary conditions are given by

$$\begin{aligned} \boldsymbol{\sigma} \mathbf{n} &= \bar{\mathbf{t}}, \quad \text{on } \Gamma_\sigma \\ \mathbf{u} &= \bar{\mathbf{u}}, \quad \text{on } \Gamma_u \\ \mathbf{D} \mathbf{n} &= -\bar{q}, \quad \text{on } \Gamma_q \\ \phi &= \bar{\phi}, \quad \text{on } \Gamma_\phi, \end{aligned} \quad (26)$$

where  $\bar{\mathbf{u}}$  and  $\bar{\phi}$  denote prescribed displacements and electric potential, respectively.  $\mathbf{n}$  is the unit outward normal vector.  $\bar{\mathbf{t}}$  and  $\bar{q}$  are the surface traction and charge, respectively.

The strain vector related to displacement is

$$\boldsymbol{\varepsilon} = \nabla_s \mathbf{u} = \nabla_s \mathbf{N}_u \hat{\mathbf{u}} = \mathbf{B}_u \hat{\mathbf{u}} \quad (27)$$

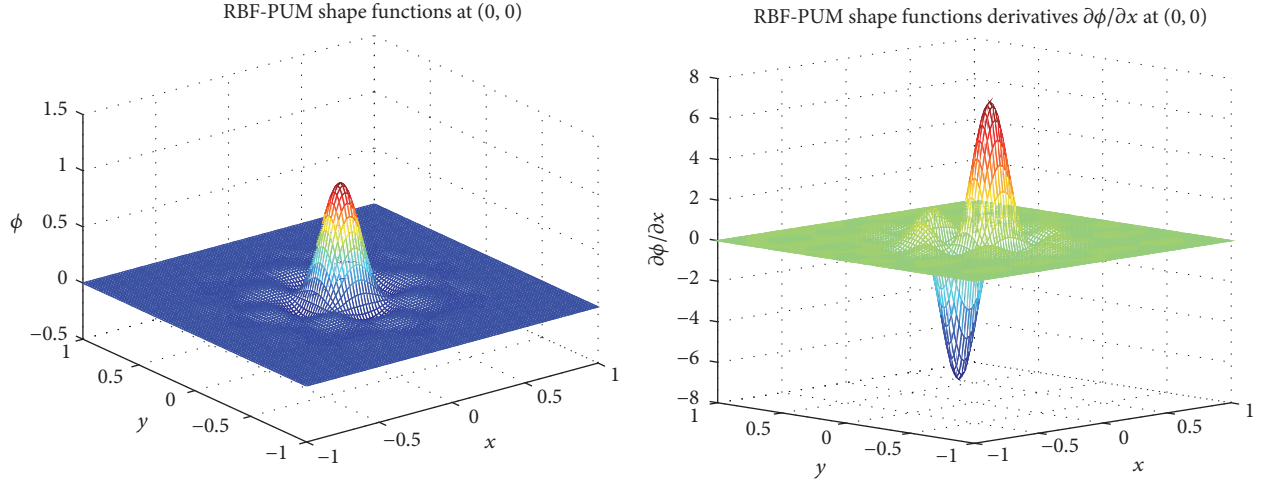


FIGURE 3: RBF-PUM shape function and its derivative of point (0,0) in 2D space.

and the electric field vector is

$$\mathbf{E} = -\nabla\phi = -\nabla(\mathbf{N}_\phi\hat{\phi}) = -\mathbf{B}_\phi\hat{\phi}, \quad (28)$$

where

$$\begin{aligned} \hat{\mathbf{u}} &= [u_1 \ w_1 \ u_2 \ w_2 \ \cdots \ u_n \ w_n]^T \\ \hat{\phi} &= [\phi_1 \ \phi_2 \ \cdots \ \phi_n]^T \\ \mathbf{N}_u &= \begin{bmatrix} \tilde{\phi}_1 & 0 & \cdots & \tilde{\phi}_n & 0 \\ 0 & \tilde{\phi}_1 & \cdots & 0 & \tilde{\phi}_n \end{bmatrix} \\ \mathbf{N}_\phi &= [\tilde{\phi}_1 \ \tilde{\phi}_2 \ \cdots \ \tilde{\phi}_n] \\ \mathbf{B}_u &= \begin{bmatrix} \tilde{\phi}_{1,x} & 0 & \cdots & \tilde{\phi}_{n,x} & 0 \\ 0 & \tilde{\phi}_{1,z} & \cdots & 0 & \tilde{\phi}_{n,z} \\ \tilde{\phi}_{1,z} & \tilde{\phi}_{1,x} & \cdots & \tilde{\phi}_{n,z} & \tilde{\phi}_{n,x} \end{bmatrix} \\ \mathbf{B}_\phi &= \begin{bmatrix} \tilde{\phi}_{1,x} & \cdots & \tilde{\phi}_{n,x} \\ \tilde{\phi}_{1,z} & \cdots & \tilde{\phi}_{n,z} \end{bmatrix}. \end{aligned} \quad (29)$$

The constitutive relations for piezoelectric structures are given by

$$\begin{aligned} \boldsymbol{\sigma} &= \mathbf{c}\boldsymbol{\varepsilon} - \mathbf{e}^T \mathbf{E} \\ \mathbf{D} &= \mathbf{e}\boldsymbol{\varepsilon} + \boldsymbol{\kappa}\mathbf{E}, \end{aligned} \quad (30)$$

where  $\mathbf{c}$ ,  $\mathbf{e}$ , and  $\boldsymbol{\kappa}$  are the elastic stiffness matrix, piezoelectric matrix, and dielectric matrix, respectively.

The constitutive relations can also be expressed explicitly in matrix form:

$$\begin{bmatrix} \sigma_x \\ \sigma_z \\ \tau_{xz} \end{bmatrix} = \begin{bmatrix} c_{11} & c_{13} & 0 \\ c_{13} & c_{33} & 0 \\ 0 & 0 & c_{55} \end{bmatrix} \begin{bmatrix} \varepsilon_x \\ \varepsilon_z \\ \gamma_{xz} \end{bmatrix} - \begin{bmatrix} 0 & e_{31} \\ 0 & e_{33} \\ e_{15} & 0 \end{bmatrix} \begin{bmatrix} E_x \\ E_z \end{bmatrix}, \quad (31)$$

$$\begin{bmatrix} D_x \\ D_z \end{bmatrix} = \begin{bmatrix} 0 & 0 & e_{15} \\ e_{31} & e_{33} & 0 \end{bmatrix} \begin{bmatrix} \varepsilon_x \\ \varepsilon_z \\ \gamma_{xz} \end{bmatrix} + \begin{bmatrix} \kappa_{11} & 0 \\ 0 & \kappa_{33} \end{bmatrix} \begin{bmatrix} E_x \\ E_z \end{bmatrix}.$$

The mechanical and electrical constitutive relations can also be given by

$$\begin{bmatrix} \varepsilon_x \\ \varepsilon_z \\ \gamma_{xz} \end{bmatrix} = \begin{bmatrix} s_{11} & s_{13} & 0 \\ s_{13} & s_{33} & 0 \\ 0 & 0 & s_{55} \end{bmatrix} \begin{bmatrix} \sigma_x \\ \sigma_z \\ \tau_{xz} \end{bmatrix} - \begin{bmatrix} 0 & d_{31} \\ 0 & d_{33} \\ d_{15} & 0 \end{bmatrix} \begin{bmatrix} E_x \\ E_z \end{bmatrix}, \quad (32)$$

$$\begin{bmatrix} D_x \\ D_z \end{bmatrix} = \begin{bmatrix} 0 & 0 & d_{15} \\ d_{31} & d_{33} & 0 \end{bmatrix} \begin{bmatrix} \sigma_x \\ \sigma_z \\ \tau_{xz} \end{bmatrix} + \begin{bmatrix} \xi_{11} & 0 \\ 0 & \xi_{33} \end{bmatrix} \begin{bmatrix} E_x \\ E_z \end{bmatrix},$$

where  $\mathbf{s}$  is the elastic compliance matrix,  $\mathbf{d}$  is the piezoelectric strain matrix, and  $\boldsymbol{\xi}$  is the dielectric matrix. The relationships between these constant matrixes can be transforming each other.

The generalized energy functional  $\Pi$  is determined by a summation of strain energy, electric energy, and energy of external work as follows:

$$\begin{aligned} \Pi &= \int_{\Omega} \left[ \frac{1}{2} \boldsymbol{\varepsilon}^T \boldsymbol{\sigma} - \frac{1}{2} \mathbf{D}^T \mathbf{E} - \mathbf{u}^T \mathbf{f} \right] d\Omega \\ &\quad - \int_{\Gamma} [\mathbf{u}^T \bar{\mathbf{t}} + \phi^T \bar{q}] d\Gamma. \end{aligned} \quad (33)$$

Using the generalized variational principle, the variational form of piezoelectric structures can be derived:

$$\begin{aligned} \delta\Pi = & \int_{\Omega} [\delta\boldsymbol{\varepsilon}^T \boldsymbol{\sigma} - \delta\mathbf{E}^T \mathbf{D} - \delta\mathbf{u}^T \mathbf{f}] d\Omega \\ & - \int_{\Gamma} [\delta\mathbf{u}^T \bar{\mathbf{t}} + \delta\phi^T \bar{q}] d\Gamma = 0. \end{aligned} \quad (34)$$

Substituting (27)–(30) into (34), the linear piezoelectric equations can be obtained:

$$\begin{bmatrix} K_{uu} & K_{u\phi} \\ K_{u\phi}^T & K_{\phi\phi} \end{bmatrix} \begin{bmatrix} \hat{\mathbf{u}} \\ \hat{\phi} \end{bmatrix} = \begin{bmatrix} \mathbf{F} \\ \mathbf{Q} \end{bmatrix}, \quad (35)$$

where

$$\begin{aligned} K_{uu} &= \int_{\Omega} \mathbf{B}_u^T \mathbf{c} \mathbf{B}_u d\Omega, \\ K_{u\phi} &= - \int_{\Omega} \mathbf{B}_u^T \mathbf{e}^T \mathbf{B}_{\phi} d\Omega, \\ K_{\phi\phi} &= \int_{\Omega} \mathbf{B}_{\phi}^T \boldsymbol{\kappa} \mathbf{B}_{\phi} d\Omega, \\ \mathbf{F} &= \int_{\Omega} \mathbf{N}_u^T \mathbf{f} d\Omega + \int_{\Gamma_r} \mathbf{N}_u^T \bar{\mathbf{t}} d\Gamma, \\ \mathbf{Q} &= - \int_{\Gamma_q} \mathbf{N}_{\phi}^T \bar{q} d\Gamma. \end{aligned} \quad (36)$$

#### 4. Numerical Examples

Numerical examples for piezoelectric structures are used to study the RBF-PUM. The choice of the shape parameters  $q$  and  $\eta$  is an open issue and has been discussed in the RBF-based methods [18, 31]. When shape parameter  $q$  is chosen as an integer, the moment matrix is ill-conditioned. Therefore, shape parameter  $q$  cannot be an integer and, generally, the optimal parameters may change with the practical problems. The effects of the shape parameters on numerical results are also discussed in this paper. In some problems, unless otherwise stated, the two shape parameters  $q = 1.95$  and  $\eta = 2.0$  investigated the performance of the present method. Gauss integration scheme is used for all numerical examples: the boundary and each background cell adopt 4 and  $4 \times 4$  Gauss integration, respectively.

In the RBF-PUM, the patch fill distance is used as a measure of the density of central points and defined as

$$H = \sup_{\mathbf{x} \in \Omega} \min_{1 \leq i \leq M} \|\mathbf{x} - X_i\|, \quad (37)$$

which indicates how well the central points  $\{X_i\}_{i=1}^N$  fill in problem domain. For regularly distributed central points, the patch fill distance is proportional to the distance of central points.

The support radius or the patch size is defined as

$$r_i = \alpha_r \times H, \quad (38)$$

where  $\alpha_r$  is a nondimensional coefficient. The patch size usually controls the number of nodes in each patch and therefore parameter  $\alpha_r$  can be adjusted according to node density and the patch fill distance.

For the purpose of error estimation and convergence studies, the relative error is defined as

$$E_r = \frac{\|\mathbf{u}^{\text{ex}} - \mathbf{u}^{\text{nu}}\|_2}{\|\mathbf{u}^{\text{ex}}\|_2}, \quad (39)$$

where “ex” and “nu” represent exact and numerical solutions, respectively.

*4.1. Shear Deformation of Piezoelectric Strip.* The shear deformation of a square piezoelectric strip polarized in  $z$ -direction is taken into consideration. The piezoelectric strip is made of material PZT-5 and its material properties are given as follows:

$$\begin{aligned} s_{11}: & 16.4 \times 10^{-6} \text{ (mm)}^2/\text{N} \\ s_{13}: & -7.22 \times 10^{-6} \text{ (mm)}^2/\text{N} \\ s_{33}: & 18.8 \times 10^{-6} \text{ (mm)}^2/\text{N} \\ s_{55}: & 47.5 \times 10^{-6} \text{ (mm)}^2/\text{N} \\ \sigma_0: & -5.0 \text{ N}/(\text{mm})^2 \\ \sigma_1: & 20.0 \text{ N}/(\text{mm})^2 \\ L: & 1.0 \text{ mm} \\ d_{31}: & -172 \times 10^{-9} \text{ mm}/\text{V} \\ d_{33}: & 374 \times 10^{-9} \text{ mm}/\text{V} \\ d_{15}: & 584 \times 10^{-9} \text{ mm}/\text{V} \\ \xi_{11}: & 1.53105 \times 10^{-8} \text{ N}/\text{V}^2 \\ \xi_{33}: & 1.505 \times 10^{-7} \text{ N}/\text{V}^2 \\ V_0: & 1000 \text{ V} \\ h: & 0.5 \text{ mm} \end{aligned}$$

The strip is subjected a uniform load  $\sigma_0$  on the top and bottom boundaries and an applied voltage  $V_0$  on the left and right boundaries as shown in Figure 4. Since the applied electric field is perpendicular to polarization direction, it induces a shear strain. The overall deformation of the piezoelectric strip is a superposition of the deformation due to the shear strain and the applied load.

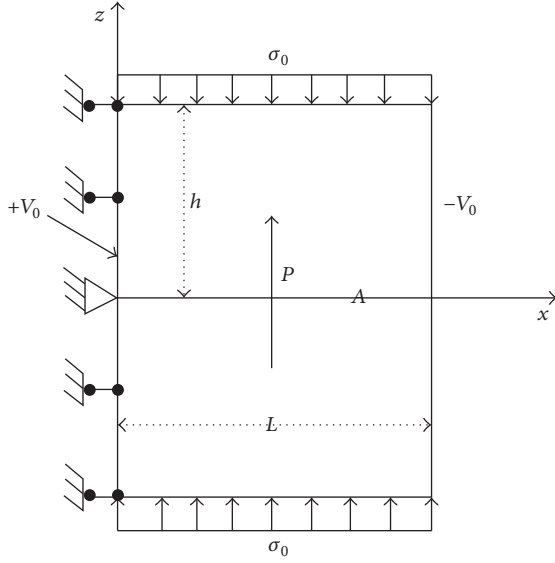


FIGURE 4: Piezoelectric strip subjected to a uniform load and an applied voltage.

The following boundary conditions of the piezoelectric strip are given by

$$\begin{aligned}
 \phi_{,z}(x, \pm h) &= 0, \\
 \sigma_z(x, \pm h) &= \sigma_0, \\
 \tau_{xz}(L, z) &= 0, \\
 \tau_{xz}(x, \pm h) &= 0, \\
 \phi(L, z) &= -V_0, \\
 \sigma_x(L, z) &= 0, \\
 \phi(0, z) &= +V_0, \\
 u(0, z) &= 0, \\
 w(0, 0) &= 0.
 \end{aligned} \tag{40}$$

The analytical solutions for this shear problem are given by [49]

$$\begin{aligned}
 u &= s_{13}\sigma_0, \\
 w &= \frac{d_{15}V_0x}{h} + s_{33}\sigma_0z, \\
 \phi &= V_0\left(1 - 2\frac{x}{L}\right).
 \end{aligned} \tag{41}$$

The problem domain is represented by both  $11 \times 11$  regular nodes and 121 irregular nodes in Figure 5. The PU cover consists of  $M = m^2(5 \times 5)$  regular circular patches and the coefficient  $\alpha_r = 1.2$  is taken here.  $10 \times 10$  square background cells are used for numerical integration.

The obtained results of the present method are plotted in Figure 6, in which symbols R and IR denote regular and irregular nodes, respectively. Figure 6(a) shows the horizontal

displacement  $u$  along  $z = 0$  and the deflection  $w$  along  $z = 0$  is plotted in Figure 6(b). The variation of the electric potential  $\phi$  is depicted in Figure 6(c). The results of the RBF method are also presented in these figures and the size of influence domain of the RBF method is taken as 4.0 times average nodal distance. The results of the RBF-PUM method and the RBF method are very accurate comparing with the analytical solutions. Moreover, the present results are slightly better than those of the RBF method.

The computed mechanical deformation results of the present method for irregular nodes are plotted in Figure 7, which seems quite reasonable for the shear deformation. The convergence curves and convergence rates of displacements  $u$  and  $w$  and electric potential  $\phi$  using the linear regression are shown in Figure 8 for regular nodes. It can be seen that the present results are very accurate even for coarse node distribution. The relative errors will decrease with the increase of nodes. It is due to the fact that the number of nodes using in the RBF-PUM shape functions increases with the node density and the numerical results become better.

In the RBF-PUM, the common requirement for all patches is that they cover the problem domain and boundary. Numerical results are usually influenced by the patch size, since the number of nodes using in the construction of the RBF-PUM shape function are influenced by the patch size. It is great of interest to study the effects of the patch size on numerical results. The results of displacements and electric potential at point A ( $x = 3L/4, z = 0$ ) are listed in Table 1. The present method gives stable and accurate results for different patch sizes and nodal patterns. The solutions will converge to the analytical solutions for a larger patch size. It is due to the fact that increasing the patch size will lead to an increase of the number of nodes in each patch and the RBF-PUM shape function for a given interpolation point contains more data information for a larger patch size. However, it should be noted that the optimal parameter  $\alpha_r$  may change with the patch fill distance and the coefficient  $\alpha_r$  can be adjusted according to the patch fill distance.

**4.2. Bending Deformation of Piezoelectric Strip.** The same material and geometry of the piezoelectric strip in bending are studied. The top and bottom surfaces are subjected to an applied voltage and the right side is applied to a linear stress as depicted in Figure 9. The analytical solutions of displacements and electric potential are given by [50]

$$\begin{aligned}
 u &= s_{11}\left(\sigma_0 - \frac{d_{31}V_0}{s_{11}h}\right)x + s_{11}\left(1 - \frac{d_{31}^2}{s_{11}\xi_{33}}\right)\sigma_1xz, \\
 w &= s_{13}\left(\sigma_0 - \frac{d_{31}V_0}{s_{11}h}\right)z + s_{13}\left(1 - \frac{d_{33}d_{31}}{s_{13}\xi_{33}}\right) \\
 &\quad - s_{11}\left(1 - \frac{d_{31}^2}{s_{11}\xi_{33}}\right)\sigma_1\frac{x^2}{2}, \\
 \phi &= V_0\frac{z}{h} - \frac{d_{31}\sigma_1}{2\xi_{33}}(h^2 - z^2),
 \end{aligned} \tag{42}$$

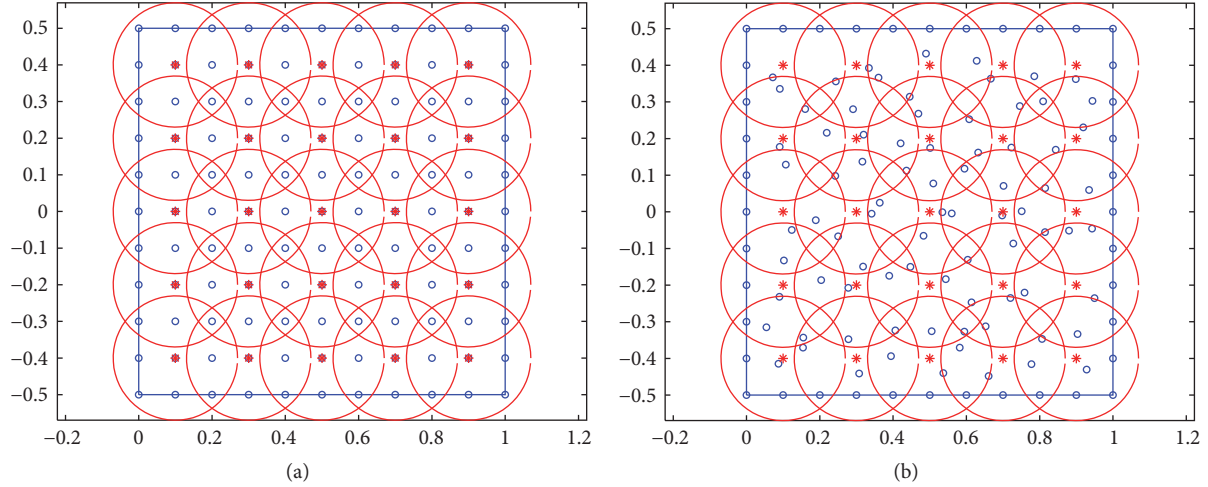


FIGURE 5: Node distribution and partition of the piezoelectric strip in shear: (a) regular nodes with regular central points; (b) irregular nodes with regular central points.

TABLE 1: Numerical results of displacements  $u_A \times 10^{-5}$  (mm) and  $w_A \times 10^{-4}$  (mm) and electric potential  $\phi_A$  (V) at point A ( $x = 3L/4, z = 0$ ) for different patch sizes.

$\alpha_r$		1.1	1.2	1.3	1.4	1.5	1.6	1.8	2.0	Exact
$u_A$	R	2.70774	2.70762	2.70747	2.70740	2.70753	2.70752	2.70752	2.70752	2.70750
	IR	2.70523	2.70372	2.70676	2.70783	2.70844	2.70735	2.70760	2.70804	
$w_A$	R	8.76021	8.76018	8.76018	8.76025	8.76045	8.76068	8.76078	8.76089	8.76000
	IR	8.76367	8.76041	8.75980	8.75963	8.76029	8.75998	8.75991	8.75998	
$\phi_A$	R	-499.92	-499.92	-499.93	-499.94	-500.01	-500.00	-500.02	-500.03	-500.00
	IR	-500.79	-500.05	-499.96	-499.94	-500.03	-499.97	-499.98	-499.98	

and the boundary conditions for this problem are given by

$$\begin{aligned}
 \phi_{,z}(x, \pm h) &= \pm V_0, \\
 \sigma_z(x, \pm h) &= 0, \\
 \tau_{xz}(x, z \pm h) &= 0, \\
 \phi_{,x}(L, z) &= 0, \\
 \sigma_x(L, z) &= \sigma_0 + \sigma_1 z, \\
 \tau_{xz}(L, z) &= 0, \\
 \phi_{,x}(0, z) &= 0, \\
 u(0, z) &= 0, \\
 w(0, 0) &= 0.
 \end{aligned} \tag{43}$$

To demonstrate the efficiency of the proposed method for irregular central points, 25 circular patches with irregular central points are used for the bending analysis of the piezoelectric strip. The central points and nodes are plotted in Figure 10, in which the patch fill distance is about  $H = 0.1938$  and the coefficient  $\alpha_r = 1.2$  is also taken here.

The solutions of the RBF-PUM, the RBF method, and the analytical method are shown in Figure 11. The displacement  $u$  and electric potential  $\phi$  along  $x = L$  are plotted in

Figures 11(a) and 11(c), respectively. The variation of the deflection  $w$  along the bottom of the piezoelectric strip is depicted in Figure 11(b). It can be observed that the present results match the analytical solutions very well even for irregular central points and the present results are more accurate than the RBF results by comparing with the analytical solutions.

**4.3. A Parallel Piezoelectric Bimorph Beam.** Consider a two-layer parallel piezoelectric bimorph beam as shown in Figure 12. The beam is made of material PVDF with the same thickness and polarization direction and the material properties are summarized as follows:

$$\begin{aligned}
 E &: 2.0 \times 10^9 \text{ Pa} \\
 \nu &: 0.29 \\
 e_{31} &: 0.046 \text{ C/m}^2 \\
 e_{32} &: 0.046 \text{ C/m}^2 \\
 \kappa_{11} &: 0.1062 \times 10^{-9} \text{ F/m} \\
 \kappa_{33} &: 0.1062 \times 10^{-9} \text{ F/m}
 \end{aligned}$$

For this problem, a unity voltage (1V) is applied across the thickness between the surfaces and the intermediate electrode. In this study, a plane stress problem is assumed. For

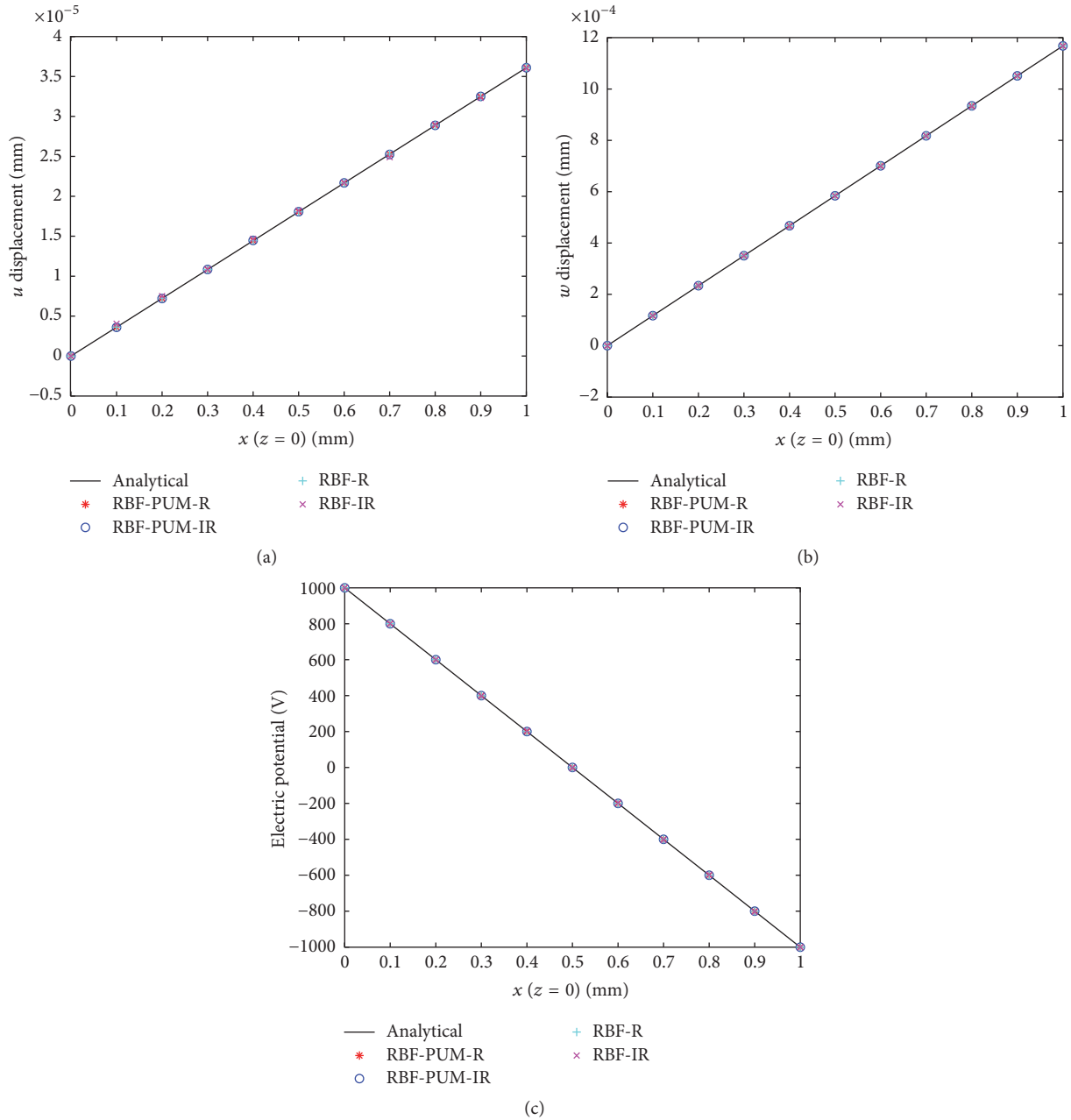


FIGURE 6: Comparisons of the present solutions, the RBF solutions, and the analytical solutions of the piezoelectric strip in shear: (a) the variation of the horizontal displacement  $u$  along  $z = 0$ ; (b) the variation of the vertical displacement  $w$  along  $z = 0$ ; (c) the variation of the electric potential  $\phi$  along  $z = 0$ .

an applied voltage  $V$ , the tip deflection  $\delta$  can be approximated as [51]

$$\delta = \frac{2L^2 V d_{31}}{H^2}, \tag{44}$$

where  $L$  is the length of the beam,  $H$  is the total thickness, and  $d_{31}$  is the piezoelectric strain constant. The size of the beam is taken as  $L = 5$  mm and  $H = 0.4$  mm and the tip deflection computed by (44) is  $\delta = 1.0206 \times 10^{-8}$  m.

Considering the thickness-length ratio of the beam, a total of  $21 \times 4$  regular patches and  $51 \times 5$  regular nodes are used to represent the problem domain. Due to its geometric symmetry, only one-half of the patches of the top beam are shown in Figure 13, where the central points are at the upper and down quarter through the thickness direction and the coefficient  $\alpha_r = 1.2$  is taken.

The tip deflections for different node densities are listed in Table 2 and the present results are very close to the results given by the ABAQUS [19]. The effect of the patch size on

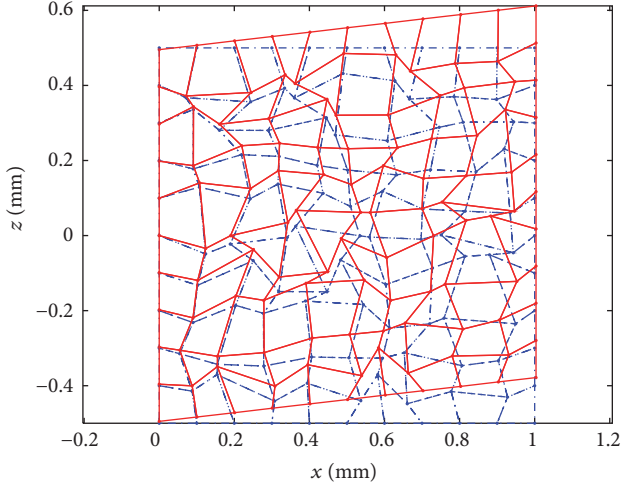


FIGURE 7: The shear deformation of the piezoelectric strip for irregular nodes. Note that the displacements plotted are magnified 100 times.

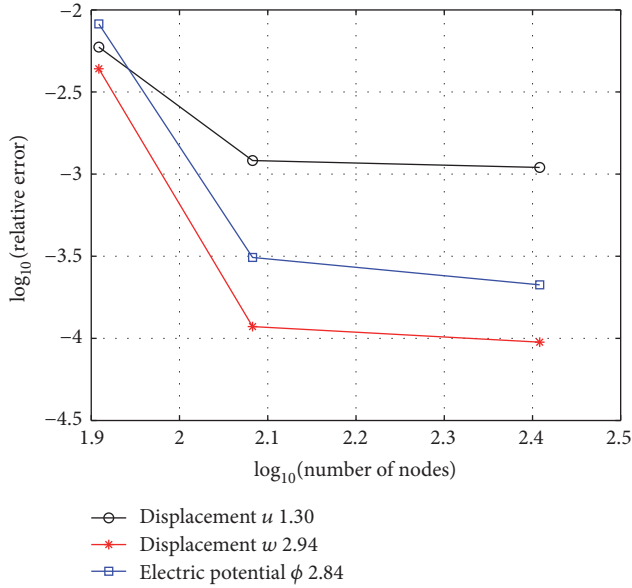


FIGURE 8: Convergence property of displacements  $u$  and  $w$  and electric potential  $\phi$  for regular nodes.

the tip deflection is investigated in Table 3. As the patch size increases, the number of nodes in each patch will increase as well as the nodes using in the construction of the RBF-PUM shape functions. The obtained solutions will converge for a larger patch size. The shape parameters  $q$  and  $\eta$  are also studied in Tables 4 and 5, respectively. It can be observed that increasing the parameter  $q$  leads to an increase of the tip deflection, but it changes very slowly and the tip deflection keeps a constant for different values of parameter  $\eta$ . All the results computed by present method are very stable and slightly larger than the analytical solution. It may be due to using the equations derived by the Euler-Bernoulli model and the numerical method results in a less stiff model [19].

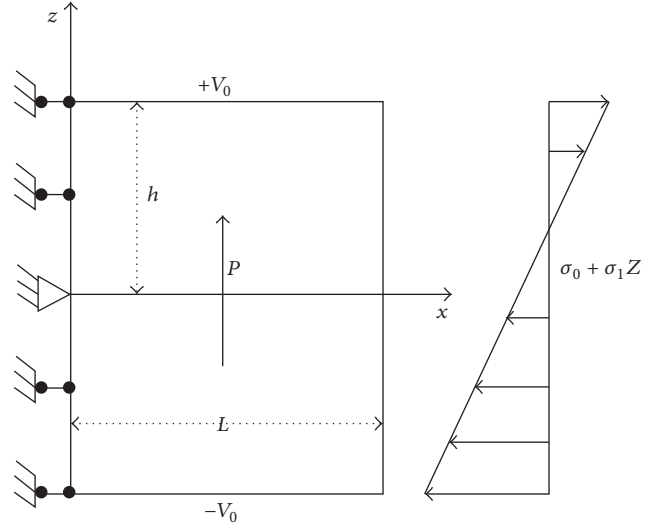


FIGURE 9: Piezoelectric strip subjected to a linear stress and an applied voltage.

**4.4. Piezoelectric Cook's Membrane.** The piezoelectric Cook's membrane problem is solved using the present method. The geometry and applied unity tip load  $F$  are shown in Figure 14. The lower surface of the membrane is prescribed by zero voltage. Cook's membrane is made of PZT-4 material provided as follows:

$$\begin{aligned}
 c_{11}: & 139 \times 10^3 \text{ N/mm}^2 \\
 c_{13}: & 74.3 \times 10^3 \text{ N/mm}^2 \\
 c_{33}: & 113 \times 10^3 \text{ N/mm}^2 \\
 c_{55}: & 25.6 \times 10^3 \text{ N/mm}^2 \\
 e_{15}: & 13.44 \times 10^6 \text{ pC/mm}^2 \\
 e_{31}: & -6.98 \times 10^6 \text{ pC/mm}^2 \\
 e_{33}: & 13.84 \times 10^6 \text{ pC/mm}^2 \\
 \kappa_{11}: & 6.00 \times 10^9 \text{ pC/GVmm} \\
 \kappa_{33}: & 5.47 \times 10^9 \text{ pC/GVmm}
 \end{aligned}$$

The analytical solutions of this problem are unavailable and the best known numerical results are given by Long et al. [42] using the finite element method with a fine mesh. The results of the displacement, the electric potential, the first principal stress, and the electric flux density at nodes  $A, B, C$  are

$$\begin{aligned}
 w_A &= 2.109 \times 10^{-4} \text{ mm}, \\
 \phi_A &= 1.732 \times 10^{-8} \text{ GV} \\
 \sigma_{1B} &= 0.21613 \text{ N/mm}^2, \\
 D_C &= 22.409 \text{ pC/mm}^2.
 \end{aligned} \tag{45}$$

The problem is represented by  $7 \times 4$  circular patches and  $25 \times 7$  regular nodes as shown in Figure 15. The patch fill distance is about  $H = 5.341$  and the coefficient is  $\alpha_r = 1.5$ . The results and relative errors percentage of the present

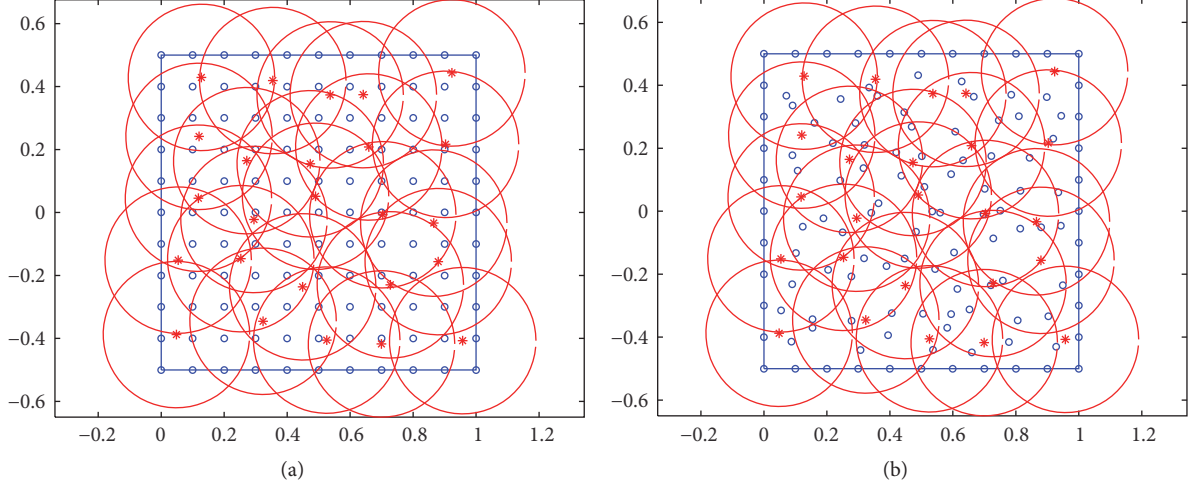


FIGURE 10: Node distribution and partition of the piezoelectric strip in bending: (a) regular nodes with irregular central points; (b) irregular nodes with irregular central points.

TABLE 2: The tip deflection of the piezoelectric beam for different nodes when  $q = 1.95$ ,  $\eta = 2.0$ ,  $\alpha_r = 1.2 (\times 10^{-8} \text{ m})$ .

Background cell	$40 \times 4$	$50 \times 4$	$60 \times 4$	$70 \times 4$	$80 \times 4$	$100 \times 4$	CPS4E [19]
Nodal density	$41 \times 5$	$51 \times 5$	$61 \times 5$	$71 \times 5$	$81 \times 5$	$101 \times 5$	
Tip deflection	1.0715	1.0719	1.0705	1.0737	1.0736	1.0719	1.073

method for different nodal densities are listed in Table 6 together with the results of the smoothed finite element method [8]. In the smoothed FEM, a fine mesh with  $24 \times 24$  elements is used for this problem. It can be seen that the present results of the displacement  $w_A$  and the first principal stress  $\sigma_{1B}$  are in very good accord with the results given by the FEM. Although the errors of the electric potential  $\phi_A$  and the electric flux density  $D_C$  are slightly larger, the present method still achieves reasonable prediction.

**4.5. A Piezoelectric Bimorph Optical Microscanner.** The purpose of this problem is to simulate the linear tilt angle of the reflected light through a mirror of an optical microscanner. The device is composed of two parallel bimorphs connected by a mirror at the tip center as depicted in Figure 16. Each bimorph has length  $L = 10 \mu\text{m}$  and height  $h = 0.5 \mu\text{m}$  and the length of the mirror is  $\lambda = 1 \mu\text{m}$ . The two-layer piezoelectric bimorph is made of PVDF material and its material properties are summarized as follows:

$$\begin{aligned}
 c_{11}: & 2.18 \times 10^{-3} \text{ N}/\mu\text{m}^2 \\
 c_{13}: & 6.33 \times 10^{-4} \text{ N}/\mu\text{m}^2 \\
 c_{33}: & 2.18 \times 10^{-3} \text{ N}/\mu\text{m}^2 \\
 c_{55}: & 7.75 \times 10^{-4} \text{ N}/\mu\text{m}^2 \\
 e_{31}: & 4.6 \times 10^{-8} \text{ N}/\text{V}\mu\text{m} \\
 e_{33}: & 4.6 \times 10^{-8} \text{ N}/\text{V}\mu\text{m} \\
 \kappa_{11}: & 1.062 \times 10^{-10} \text{ N}/\text{V}^2 \\
 \kappa_{33}: & 1.062 \times 10^{-10} \text{ N}/\text{V}^2
 \end{aligned}$$

When a voltage is applied on the surfaces, the bimorphs deflect in opposite direction so that the mirror moves up and

down, resulting in the change of the tilt angle  $\beta$ . The direction of the reflected light can be changed with applied different voltages and the tip deflection  $\delta$  can be calculated by the present method. For sufficient small rotation, the angle  $\beta$  can be approximated from the tip deflection

$$\beta = \frac{2\delta}{\lambda}. \quad (46)$$

The boundary conditions of the bottom layer are

$$\begin{aligned}
 \phi^{(1)}(x, -h) &= V_0, \\
 \sigma_z^{(1)}(x, -h) &= 0, \\
 \tau_{xz}^{(1)}(x, -h) &= 0, \\
 \phi^{(1)}(x, 0) &= 0, \\
 \sigma_z^{(1)}(x, 0) &= \sigma_z^{(2)}(x, 0), \\
 \tau_{xz}^{(1)}(x, 0) &= \tau_{xz}^{(2)}(x, 0), \\
 \phi_{,x}^{(1)}(0, z) &= 0, \\
 u^{(1)}(0, z) &= 0, \\
 w^{(1)}(0, z) &= 0, \\
 \phi_{,x}^{(1)}(L, z) &= 0, \\
 \sigma_x^{(1)}(L, z) &= 0, \\
 \tau_{xz}^{(1)}(L, z) &= 0.
 \end{aligned} \quad (47)$$

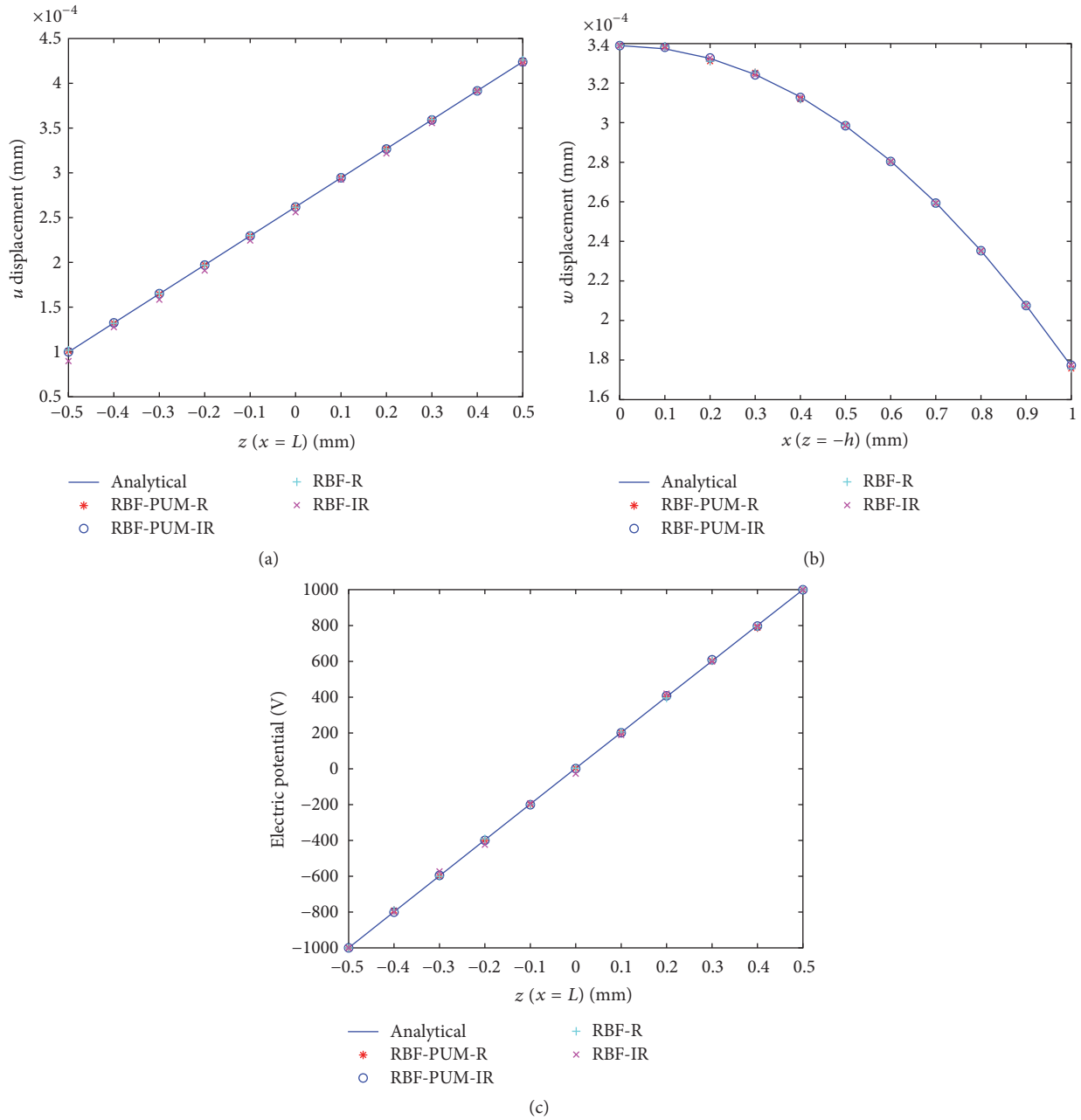


FIGURE 11: Comparisons of the present solutions, the RBF solutions, and the analytical solutions of the piezoelectric strip in bending: (a) the variation of the horizontal displacement  $u$  along  $x = L$ ; (b) the variation of the vertical displacement  $w$  along  $z = -h$ ; (c) the variation of the electric potential  $\phi$  along  $x = L$ .

TABLE 3: Effects of the patch size on the tip deflection for  $51 \times 5$  nodes when  $q = 1.95, \eta = 2.0 (\times 10^{-8} \text{ m})$ .

$\alpha_r$	1.1	1.2	1.3	1.4	1.5	1.6	1.7	1.8
Tip deflection	1.0494	1.0719	1.0721	1.0725	1.0726	1.0738	1.0738	1.0738

TABLE 4: Effects of parameter  $q$  on the tip deflection for  $51 \times 5$  nodes when  $\eta = 2.0, \alpha_r = 1.2 (\times 10^{-8} \text{ m})$ .

$q$	0.95	0.98	1.03	1.05	1.08	1.92	1.95	1.98
Tip deflection	1.0709	1.0709	1.0710	1.0710	1.0710	1.0719	1.0719	1.0719

TABLE 5: Effects of parameter  $\eta$  on the tip deflection for  $51 \times 5$  nodes when  $q = 1.95$ ,  $\alpha_r = 1.2 (\times 10^{-8} \text{ m})$ .

$\eta$	0.5	0.75	1.0	1.25	1.5	2.0	2.5	3.0
Tip deflection	1.0719	1.0719	1.0719	1.0719	1.0719	1.0719	1.0719	1.0719

TABLE 6: Numerical results of piezoelectric Cook's membrane and relative errors for different nodal densities.

Background cell	Node density	$w_A \times 10^{-4} (\text{mm})$	$\phi_A \times 10^{-8} (\text{GV})$	$\sigma_{1B} (\text{N/mm}^2)$	$D_c (\text{pC/mm}^2)$
$12 \times 6$	$13 \times 7$	2.1132	1.7104	0.21582	23.2896
		(0.199%)	(-1.247%)	(-0.143%)	(3.930%)
$24 \times 6$	$25 \times 7$	2.1099	1.6401	0.21764	23.1817
		(0.043%)	(-5.306%)	(0.699%)	(3.448%)
$36 \times 6$	$37 \times 7$	2.1234	1.6173	0.21763	23.2457
		(0.683%)	(-6.622%)	(0.694%)	(3.734%)
$48 \times 6$	$49 \times 7$	2.1342	1.6306	0.21718	22.9610
		(1.195%)	(-5.855%)	(0.486%)	(2.463%)
$12 \times 12$	$13 \times 13$	2.1431	1.7593	0.21740	24.1962
		(1.617%)	(1.576%)	(0.588%)	(7.975%)
$24 \times 12$	$25 \times 13$	2.1356	1.7779	0.21637	23.9918
		(1.261%)	(2.650%)	(0.111%)	(7.063%)
$36 \times 12$	$37 \times 13$	2.1370	1.7935	0.21600	24.0339
		(1.328%)	(3.551%)	(-0.060%)	(7.251%)
$48 \times 12$	$49 \times 13$	2.1377	1.7944	0.21612	24.0447
		(1.361%)	(3.603%)	(-0.005%)	(7.299%)
Nguyen-Van et al. [8]		2.100	1.703	0.2109	20.754
		(-0.379%)	(-1.674%)	(-2.406%)	(-7.385%)
Long et al. [42]		2.109	1.732	0.21613	22.409

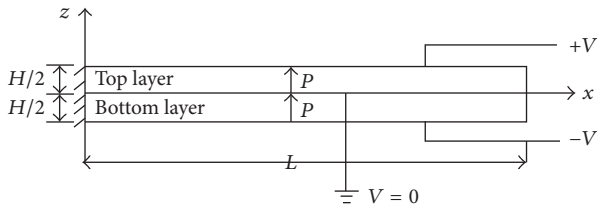


FIGURE 12: A parallel piezoelectric bimorph beam.

And the boundary conditions of the top layer are

$$\phi^{(2)}(x, 0) = \phi^{(1)}(x, 0),$$

$$u^{(2)}(x, 0) = u^{(1)}(x, 0),$$

$$w^{(2)}(x, 0) = w^{(1)}(x, 0),$$

$$\phi^{(2)}(x, h) = V_0,$$

$$\sigma_z^{(2)}(x, h) = 0,$$

$$\tau_{xz}^{(2)}(x, h) = 0,$$

$$\phi_{,x}^{(2)}(0, z) = 0,$$

$$u^{(2)}(0, z) = 0,$$

$$w^{(2)}(0, z) = 0,$$

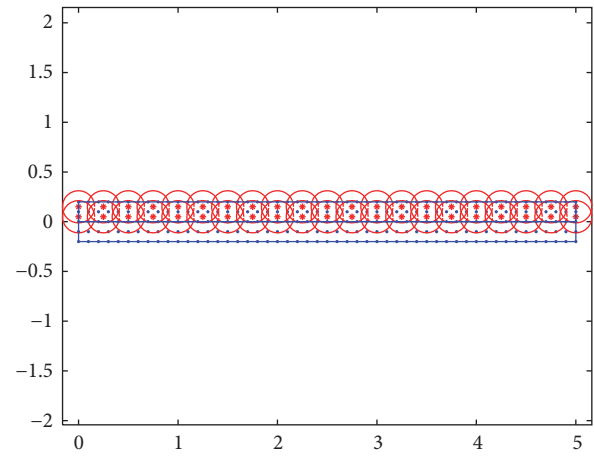


FIGURE 13: Node distribution and patches of the top beam.

$$\phi_{,x}^{(2)}(L, z) = 0,$$

$$\sigma_x^{(2)}(L, z) = 0,$$

$$\tau_{xz}^{(2)}(L, z) = 0.$$

(48)

Considering the geometry of the optical microscanner device, node arrangements and patches are very similar to the

TABLE 7: Numerical results of piezoelectric optical microscanner device for different nodal densities ( $\mu\text{m}$ ).

Applied voltage (V)	$40 \times 4$	$50 \times 4$	$60 \times 4$	$80 \times 4$	$100 \times 4$	PCM [43]
	$41 \times 5$	$51 \times 5$	$61 \times 5$	$81 \times 5$	$101 \times 5$	
1.00	$4.8742E-03$	$4.8766E-03$	$4.8631E-03$	$4.8754E-03$	$4.8716E-03$	$4.9360E-03$
2.00	$9.7484E-03$	$9.7533E-03$	$9.7262E-03$	$9.7508E-03$	$9.7431E-03$	$9.8720E-03$
5.00	$2.4371E-02$	$2.4383E-02$	$2.4316E-02$	$2.4377E-02$	$2.4358E-02$	$2.4681E-02$
10.00	$4.8742E-02$	$4.8766E-02$	$4.8631E-02$	$4.8754E-02$	$4.8716E-02$	$4.9362E-02$
15.00	$7.3113E-02$	$7.3149E-02$	$7.2947E-02$	$7.3131E-02$	$7.3074E-02$	$7.4043E-02$
20.00	$9.7484E-02$	$9.7533E-02$	$9.7262E-02$	$9.7508E-02$	$9.7431E-02$	$9.8724E-02$
25.00	$1.2186E-01$	$1.2192E-01$	$1.2158E-01$	$1.2188E-01$	$1.2179E-01$	$1.2341E-01$
50.00	$2.4371E-01$	$2.4383E-01$	$2.4316E-01$	$2.4377E-01$	$2.4358E-01$	$2.4681E-01$

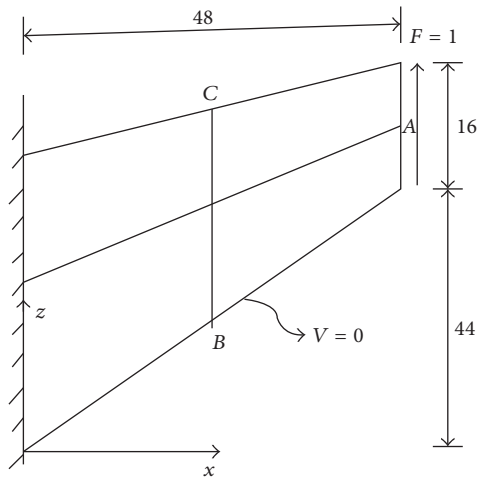


FIGURE 14: Cook's membrane.

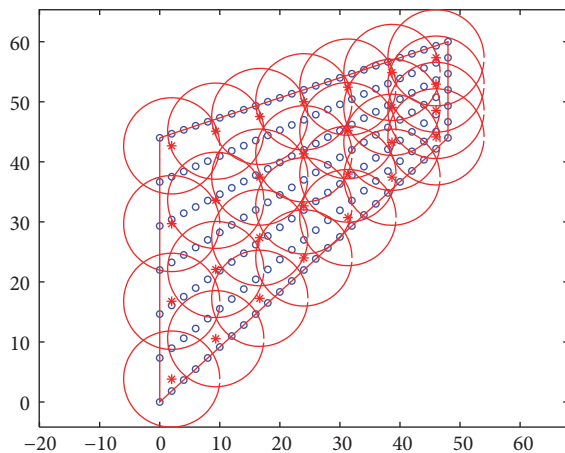


FIGURE 15: Node distribution and patches.

parallel piezoelectric bimorph beam. The central points are at the upper and down quarter through the thickness direction.  $21 \times 4$  patches and  $\alpha_r = 1.2$  are used for this problem.

The tip displacements calculated for several applied voltages with different nodal densities are listed in Table 7, in which the first two rows represent background cells and nodal densities, respectively. The numerical results obtained by the

meshless point collocation method (PCM) [43] are also given in the table. In the PCM, the reproducing kernel particle approximation is used for the displacement field and electric potential. The governing equations and boundary conditions are satisfied only at specific nodes. In the present method, the system equations are derived by the variational principle and numerical integration is required. Although the present results are very close to the PCM solutions, there are still some differences between these two different numerical methods.

From the tip deflection, the title angle of the mirror can be calculated by (46). The title angles varying with different applied voltages for  $51 \times 5$  regular nodes are shown in Figure 17. The results obtained by the node-based element (NSPE-T3, NSPE-Q4), the cell-based element (SPQ4), and the FEM-T3 [52] are also shown in Figure 17. The linear variation of the angle is in good agreement with the PCM.

## 5. Conclusions

In this paper, a meshless radial basis function based on partition of unity method is presented for studying 2D piezoelectric structures. The multiquadric radial basis functions are used for local approximation and Shepard's method is used for the construction of weight functions in the partition of unity method. The weak form equations are derived by the generalized variational principle. The mechanical displacements and electric potential are approximated using the RBF-PUM shape functions which inherit all advantages of the RBF shape functions. The RBF-PUM shape functions have been shown excellent interpolation property and therefore the boundary conditions can be imposed easily without special treatments.

Numerical examples are calculated to illustrate the efficiency of the proposed method for static problems. The effects of some parameters including the shape parameters, the patch size, and nodal density have also been studied in detail. The obtained results are compared with the solutions of the analytical method and other numerical methods such as the RBF method, the finite element method, and the smoothed finite element method. The present results are very accurate and are in excellent agreement with the analytical solutions.

## Competing Interests

The authors declare that they have no competing interests.

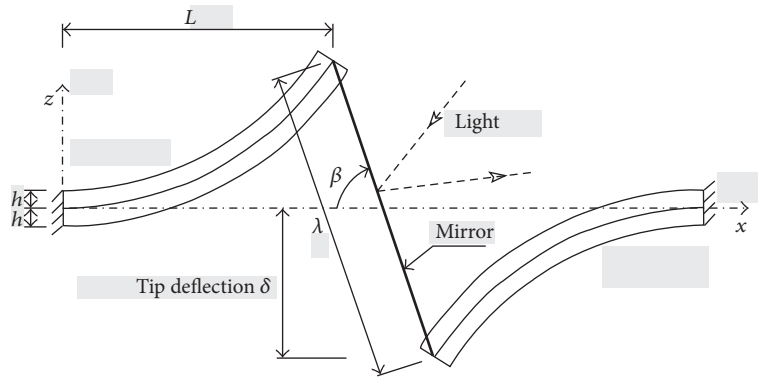


FIGURE 16: A piezoelectric bimorph optical microscanner device.

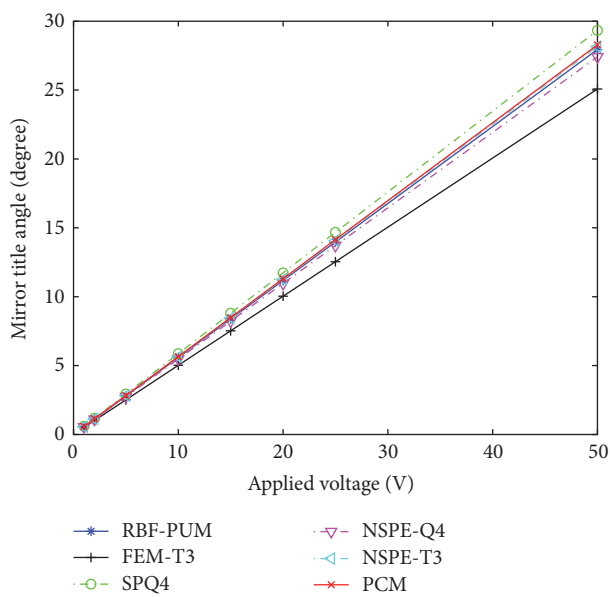


FIGURE 17: The variation of the angle under different applied voltages.

### Acknowledgments

This work is supported by the National Natural Science Foundation of China (nos. 11172192 and 11572210) and the Graduate Innovation Project of Jiangsu Province (KYLX16\_0095).

### References

[1] C. D. Mercer, B. D. Reddy, and R. A. Eve, "Finite element method for piezoelectric media," Applied Mechanics Research Unit Technical Report 92, University of Cape Town/CSIR, 1987.

[2] H. Allik and T. J. R. Hughes, "Finite element method for piezoelectric vibration," *International Journal for Numerical Methods in Engineering*, vol. 2, no. 2, pp. 151–157, 1970.

[3] K. Y. Sze, X.-M. Yang, and L.-Q. Yao, "Stabilized plane and axisymmetric piezoelectric finite element models," *Finite Elements in Analysis and Design*, vol. 40, no. 9-10, pp. 1105–1122, 2004.

[4] J. Mackerle, "Smart materials and structures—a finite element approach—an addendum: a bibliography (1997–2002)," *Modelling and Simulation in Materials Science and Engineering*, vol. 11, no. 5, pp. 707–744, 2003.

[5] F. García-Sánchez and C. Zhang, "2D transient dynamic analysis of cracked piezoelectric solid by a timedomain BEM," *Computer Methods in Applied Mechanics and Engineering*, vol. 197, pp. 3108–3121, 2008.

[6] A. Sáez, F. García-Sánchez, and J. Dominguez, "Hypersingular BEM for dynamic fracture in 2D piezoelectric solids," *Computer Methods in Applied Mechanics and Engineering*, vol. 196, pp. 235–246, 2006.

[7] Ch. Zhang, F. García-Sánchez, and A. Sáez, "Time-domain BEM analysis of cracked piezoelectric solids under impact loading," in *Computational Mechanics*, pp. 206–218, Springer, 2007.

[8] H. Nguyen-Van, N. Mai-Duy, and T. Tran-Cong, "A smoothed four-node piezoelectric element for analysis of two-dimensional smart structures," *Computer Modeling in Engineering and Sciences*, vol. 23, no. 3, pp. 209–222, 2008.

[9] L. B. Lucy, "A numerical approach to the testing of the fission hypothesis," *The Astronomical Journal*, vol. 82, pp. 1013–1024, 1977.

[10] R. A. Gingold and J. J. Monaghan, "Smoothed particle hydrodynamics: theory and application to non-spherical stars," *Monthly Notices of the Royal Astronomical Society*, vol. 181, no. 3, pp. 375–389, 1977.

[11] B. Nayroles, G. Touzot, and P. Villon, "Generalizing the finite element method: diffuse approximation and diffuse elements," *Computational Mechanics*, vol. 10, no. 5, pp. 307–318, 1992.

[12] T. Belytschko, Y. Y. Lu, and L. Gu, "Element-free Galerkin methods," *International Journal for Numerical Methods in Engineering*, vol. 37, no. 2, pp. 229–256, 1994.

[13] W. K. Liu, S. Jun, and Y. F. Zhang, "Reproducing kernel particle methods," *International Journal for Numerical Methods in Fluids*, vol. 20, no. 8-9, pp. 1081–1106, 1995.

[14] C. A. Duarte and J. T. Oden, "An  $h$ - $p$  adaptive method using clouds," *Computer Methods in Applied Mechanics and Engineering*, vol. 139, no. 1–4, pp. 237–262, 1996.

[15] G. R. Liu and Y. T. Gu, "A point interpolation method for two-dimensional solids," *International Journal for Numerical Methods in Engineering*, vol. 50, no. 4, pp. 937–951, 2001.

[16] G. R. Liu and Y. T. Gu, "Local point interpolation method for stress analysis of two-dimensional solids," *Structural Engineering and Mechanics*, vol. 11, no. 2, pp. 221–236, 2001.

- [17] G. R. Liu, K. Y. Dai, K. M. Lim, and Y. T. Gu, "A point interpolation mesh free method for static and frequency analysis of two-dimensional piezoelectric structures," *Computational Mechanics*, vol. 29, no. 6, pp. 510–519, 2002.
- [18] G. R. Liu and Y. T. Gu, *An Introduction to Meshfree Methods and Their Programming*, Springer, Amsterdam, The Netherlands, 2005.
- [19] G. R. Liu, K. Y. Dai, K. M. Lim, and Y. T. Gu, "A radial point interpolation method for simulation of two-dimensional piezoelectric structures," *Smart Materials and Structures*, vol. 12, no. 2, pp. 171–180, 2003.
- [20] T. Q. Bui, M. N. Nguyen, C. Zhang, and D. A. K. Pham, "An efficient meshfree method for analysis of two-dimensional piezoelectric structures," *Smart Materials and Structures*, vol. 20, no. 6, Article ID 065016, pp. 1–16, 2011.
- [21] S. N. Atluri and T. Zhu, "A new meshless local Petrov-Galerkin (MLPG) approach in computational mechanics," *Computational Mechanics*, vol. 22, no. 2, pp. 117–127, 1998.
- [22] J. Sladek and V. Sladek, "Meshless local Petrov-Galerkin method for plane piezoelectricity," *CMC-Computers Materials & Continua*, vol. 4, pp. 109–118, 2006.
- [23] J. Sladek, V. Sladek, and C. Zhang, "Dynamic crack analysis in functionally graded piezoelectric solids by meshless local petrov-galerkin method," *Key Engineering Materials*, vol. 348–349, pp. 149–152, 2007.
- [24] J. Sladek, V. Sladek, C. Zhang, P. Sulek, and L. Starek, "Fracture analyses in continuously nonhomogeneous piezoelectric solids by the MLPG," *Computer Modeling in Engineering and Sciences*, vol. 19, no. 3, pp. 247–262, 2007.
- [25] J. Sladek, V. Sladek, C. Zhang, and P. Sulek, "Application of the MLPG to thermo-piezoelectricity," *CMES-Computer Modeling in Engineering and Sciences*, vol. 22, no. 3, pp. 217–233, 2007.
- [26] P. Lancaster and K. Salkauskas, "Surfaces generated by moving least squares methods," *Mathematics of Computation*, vol. 37, no. 155, pp. 141–158, 1981.
- [27] E. J. Kansa, "Multiquadrics-A scattered data approximation scheme with applications to computational fluid-dynamics-I surface approximations and partial derivative estimates," *Computers and Mathematics with Applications*, vol. 19, no. 8-9, pp. 127–145, 1990.
- [28] E. J. Kansa, "Multiquadrics—a scattered data approximation scheme with applications to computational fluid-dynamics—II solutions to parabolic, hyperbolic and elliptic partial differential equations," *Computers and Mathematics with Applications*, vol. 19, no. 8-9, pp. 147–161, 1990.
- [29] G. E. Fasshauer, *Meshfree Approximation Methods with MATLAB*, World Scientific Publishing, 2007.
- [30] H. Wendland, "Error estimates for interpolation by compactly supported radial basis functions of minimal degree," *Journal of Approximation Theory*, vol. 93, no. 2, pp. 258–272, 1998.
- [31] J. G. Wang and G. R. Liu, "On the optimal shape parameters of radial basis functions used for 2-D meshless methods," *Computer Methods in Applied Mechanics and Engineering*, vol. 191, no. 23-24, pp. 2611–2630, 2002.
- [32] R. Schaback and H. Wendland, *Characterization and Construction of Radial Basis Functions*, Cambridge University Press, Cambridge, UK, 2001.
- [33] X. Zhang, K. Z. Song, M. W. Lu, and X. Liu, "Meshless methods based on collocation with radial basis functions," *Computational Mechanics*, vol. 26, no. 4, pp. 333–343, 2000.
- [34] H. Y. Hu, J. S. Chen, and W. Hu, "Weighted radial basis collocation method for boundary value problems," *International Journal for Numerical Methods in Engineering*, vol. 69, no. 13, pp. 2736–2757, 2007.
- [35] F. Chu, L. Wang, and Z. Zhong, "Finite subdomain radial basis collocation method," *Computational Mechanics*, vol. 54, no. 2, pp. 235–254, 2014.
- [36] J. M. Melenk and I. Babuska, "The partition of unity finite element method: basic theory and applications," *Computer Methods in Applied Mechanics and Engineering*, vol. 139, no. 1–4, pp. 289–314, 1996.
- [37] I. Babuska and J. M. Melenk, "The partition of unity method," *International Journal for Numerical Methods in Engineering*, vol. 40, no. 4, pp. 727–758, 1997.
- [38] S. Rajendran and B. R. Zhang, "A 'FE-meshfree' QUAD4 element based on partition of unity," *Computer Methods in Applied Mechanics and Engineering*, vol. 197, no. 1–4, pp. 128–147, 2007.
- [39] B. R. Zhang and S. Rajendran, "'FE-Meshfree' QUAD4 element for free-vibration analysis," *Computer Methods in Applied Mechanics and Engineering*, vol. 197, no. 45–48, pp. 3595–3604, 2008.
- [40] J. P. Xu and S. Rajendran, "A partition-of-unity based 'FE-Meshfree' QUAD4 element with radial-polynomial basis functions for static analyses," *Computer Methods in Applied Mechanics and Engineering*, vol. 200, no. 47-48, pp. 3309–3323, 2011.
- [41] Y. Yang, D. Xu, and H. Zheng, "A partition-of-unity based 'FE-meshfree' triangular element with radial-polynomial basis functions for static and free vibration analysis," *Engineering Analysis with Boundary Elements*, vol. 65, pp. 18–38, 2016.
- [42] C. S. Long, P. W. Loveday, and A. A. Groenwold, "Planar four node piezoelectric elements with drilling degrees of freedom," *International Journal for Numerical Methods in Engineering*, vol. 65, no. 11, pp. 1802–1830, 2006.
- [43] R. R. Ohs and N. R. Aluru, "Meshless analysis of piezoelectric devices," *Computational Mechanics*, vol. 27, no. 1, pp. 23–36, 2001.
- [44] D. Shepard, "A two-dimensional interpolation function for irregularly spaced points," in *Proceedings of the 23rd ACM National Conference (ACM '68)*, pp. 517–24, 1968.
- [45] H. Wendland, "Fast evaluation of radial basis functions: methods based on partition of unity," in *Approximation Theory X Wavelets Splines & Applications*, pp. 473–483, 2002.
- [46] A. S. Vaighani, A. Heryudono, and E. Larsson, "A radial basis function partition of unity collocation method for convection-diffusion equations arising in financial applications," *Journal of Scientific Computing*, vol. 64, no. 2, pp. 341–367, 2015.
- [47] H. Wendland, "Piecewise polynomial, positive definite and compactly supported radial functions of minimal degree," *Advances in Computational Mathematics*, vol. 4, no. 4, pp. 389–396, 1995.
- [48] M. A. Golberg, C. S. Chen, and H. Bowman, "Some recent results and proposals for the use of radial basis functions in the BEM," *Engineering Analysis with Boundary Elements*, vol. 23, no. 4, pp. 285–296, 1999.
- [49] V. Z. Paarton and G. K. Mikhailov, *Applied Mechanics: Soviet Reviews*, vol. 2 of *Electromagnetoelasticity*, Hemisphere, 1989.
- [50] P. Gaudenzi and K.-J. Bathe, "An iterative finite element procedure for the analysis of piezoelectric continua," *Journal of Intelligent Material Systems and Structures*, vol. 6, no. 2, pp. 266–273, 1995.

- [51] *Product Catalogue*, Piezo Systems Inc., Cambridge, Mass, USA, 1995.
- [52] H. Nguyen-Van, N. Mai-Duy, and T. Tran-Cong, "A node-based element for analysis of planar piezoelectric structures," *Computer Modeling in Engineering & Sciences*, vol. 36, no. 1, pp. 65-96, 2008.

## Research Article

# A Novel Multiobjective Quantum-Behaved Particle Swarm Optimization Based on the Ring Model

Di Zhou,<sup>1</sup> Yajun Li,<sup>1</sup> Bin Jiang,<sup>1</sup> and Jun Wang<sup>2,3,4</sup>

<sup>1</sup>*School of Design Art & Media, Nanjing University of Science and Technology, China*

<sup>2</sup>*School of Digital Media, Jiangnan University, China*

<sup>3</sup>*Department of Radiology and BRIC, University of North Carolina at Chapel Hill, Chapel Hill, NC, USA*

<sup>4</sup>*Fujian Provincial Key Laboratory of Information Processing and Intelligent Control, Minjiang University, Fuzhou, China*

Correspondence should be addressed to Di Zhou; [zhoudi@njust.edu.cn](mailto:zhoudi@njust.edu.cn)

Received 20 August 2016; Revised 26 September 2016; Accepted 10 October 2016

Academic Editor: Cheng-Tang Wu

Copyright © 2016 Di Zhou et al. This is an open access article distributed under the Creative Commons Attribution License, which permits unrestricted use, distribution, and reproduction in any medium, provided the original work is properly cited.

Due to its fast convergence and population-based nature, particle swarm optimization (PSO) has been widely applied to address the multiobjective optimization problems (MOPs). However, the classical PSO has been proved to be not a global search algorithm. Therefore, there may exist the problem of not being able to converge to global optima in the multiobjective PSO-based algorithms. In this paper, making full use of the global convergence property of quantum-behaved particle swarm optimization (QPSO), a novel multiobjective QPSO algorithm based on the ring model is proposed. Based on the ring model, the position-update strategy is improved to address MOPs. The employment of a novel communication mechanism between particles effectively slows down the descent speed of the swarm diversity. Moreover, the searching ability is further improved by adjusting the position of local attractor. Experiment results show that the proposed algorithm is highly competitive on both convergence and diversity in solving the MOPs. In addition, the advantage becomes even more obvious with the number of objectives increasing.

## 1. Introduction

Optimization problems with more than one objective are rather common in real-world practice, such as information system design [1], reservoir flood control operation (RFCO) problem [2], community detection [3] in social networks, and battery hybrid storage system optimization problems [4]. In such multiobjective optimization problems (MOPs), the objectives to be optimized are normally in conflict with each other, which means there is no unique solution to these problems. Instead, we are supposed to find Pareto optimal solutions that represent the best possible compromises among all the objectives.

In recent years, due to their population-based nature, a variety of evolutionary algorithms are applied to address the MOPs. Among these algorithms, particle swarm optimization (PSO) has attracted great interest for its relatively simple operation and competitive performance. Since the

first multiobjective PSO (MOPSO) proposed in 1999 [5], more than fifty variants of MOPSOs have been reported in literature, among which OMOPSO [6] proposed by Sierra and Coello is one of the most representative methods. Sierra and Coello [7] had given a survey of the existing studies on OMOPSOs before 2006, and the state-of-the-art MOPSOs are summarized by Zhou et al. [8]. Since classical PSO is designed for single-objective optimization problems and cannot be applied to multiobjective optimization problems directly, most of the existing studies have focused on how to extend PSO to its multiobjective versions, such as researches on how to select the global and local best particles [9–11], as well as how to maintain good points found so far.

However, as proved by Van Den Bergh [12], the classical PSO is not a global search algorithm, not even a local one, according to the convergence criteria provided by Solis and Wets [13]. Therefore, MOPSOs, which are derived from PSO, are unable to converge to global optima.

Quantum-behaved particle swarm optimization (QPSO) [14], first introduced by Sun et al. in 2004, is a new population-based algorithm, which is inspired by quantum mechanics and the trajectory analysis of PSO. Besides the introduction of mean best position (*mbest*), the particles in QPSO are assumed to follow a double exponential distribution in a quantum  $\delta$  potential well around its local focus when a new position is sampled, which is the most significant difference between QPSO and PSO. Therefore, QPSO needs no velocity vectors for particles at all. Since its first proposal, QPSO has shown its success in solving a wide range of single-objective optimization problems [15–17].

In contrast with PSO, the global convergence of QPSO can be guaranteed if the contraction-expansion (CE) coefficient of the algorithm is properly selected [18, 19]. Sun et al. proved that the QPSO is a form of contraction mapping on the probability metric space and its orbit is probabilistic bounded, and, in turn, the algorithm converges asymptotically to the global optimum. It is the exact reason why QPSO outperforms PSO as well as most of the other evolutionary algorithms.

Although QPSO has been successfully applied in conventional single-objective optimization problems due to its global convergence and easy control, it is rarely used in solving multiobjective optimization problems [20, 21]. Although the QPSO algorithm can be global convergent, the CE coefficient is generally selected to be relatively small in order to accelerate the convergence of the algorithm for real-world problems so that premature convergence can result when the algorithm is performed for the MOPs. To eliminate this defect, we propose a novel position-update mechanism based on the ring model and combine it with the classical QPSO. This leads to MOQPSOr, an enhanced QPSO method which can be applied to the multiobjective optimization problems. The combination of the ring model with QPSO has several merits. Firstly, it employs a novel communication mechanism between particles using the ring model. This modification enables the swarm to have much larger mutate scope compared to the original QPSO, which effectively slows down the descent speed of the swarm diversity, solving the problem of premature caused by the quick convergence when applying QPSO directly into multiobjective optimization. Secondly, in this ring model, by adjusting the position of local attractor, the global searching ability is enhanced at the beginning of iteration, while the local searching ability is enhanced in the later stage of iteration. By employing this novel position-update strategy based on the ring model, the efficiency of MOQPSOr on multiobjective optimization is further improved, since there is no need for any additional mutation operation.

The rest of the paper is organized as follows: After a brief introduction of the background of PSO and QPSO in Section 2, a novel ring model for position update is proposed in Section 3 and a new version of multiobjective quantum-behaved particle swarm optimization algorithm (MOQPSOr) is presented by integrating the new position-update strategy into it accordingly. Numerical tests and performance comparison on 12 benchmark functions are provided in Section 4. Finally, the paper is concluded in Section 5.

## 2. Related Work

Being a heuristic search technique that simulates the sociology behaviour of an organism, particle swarm optimization (PSO) [22, 23] has become one of the most popular methods in the fields of evolutionary computation. In PSO, each particle represents a candidate solution to the problem and flies through a  $D$ -dimensional search space according to the following position-update equation:

$$\begin{aligned} V_{i,j}(t+1) &= \omega \cdot V_{i,j}(t) + c_1 \cdot r_{1,j}(t) \\ &\quad \cdot [pbest_{i,j}(t) - X_{i,j}(t)] + c_2 \cdot r_{2,j}(t) \\ &\quad \cdot [gbest_j(t) - X_{i,j}(t)], \\ X_i(t+1) &= X_i(t) + V_i(t+1), \end{aligned} \quad (1)$$

where the current position and velocity of  $i$ th particle at the  $t$ th iteration are represented, respectively, as  $X_i(t) = (X_{i,1}(t), X_{i,2}(t), \dots, X_{i,D}(t))$  and  $V_i(t) = (V_{i,1}(t), V_{i,2}(t), \dots, V_{i,D}(t))$ .  $pbest_i$  is the best previous position of particle  $i$ , while  $gbest$  is the position of the best particle in the whole swarm. The parameters  $r_1$  and  $r_2$  are different random numbers distributed uniformly on  $(0,1)$ , and  $c_1$  as well as  $c_2$  denote the acceleration coefficients that typically are both set to a value of 2.0, which implies that the “social” and “cognition” parts have the same influence on the velocity update. The parameter  $\omega$  is known as the inertia weight and is usually set to a positive value chosen from a linear or nonlinear function of the iteration number.

Compared with PSO, the most significant advantage of QPSO is that its global convergence can be theoretically guaranteed [18]. In addition, QPSO is much easier to be controlled, benefiting from the fact that it only has one parameter. Trajectory analyses demonstrated the fact that convergence of the whole particle swarm may be achieved if each particle converges to its local attractor  $p_i = (p_{i1}, p_{i2}, \dots, p_{iD})$  [24]:

$$\begin{aligned} p_{i,j}(t) &= \frac{[c_1 \cdot r_{1,j}(t) \cdot pbest_{i,j}(t) + c_2 \cdot r_{2,j}(t) \cdot gbest_j(t)]}{[c_1 \cdot r_{1,j}(t) + c_2 \cdot r_{2,j}(t)]}, \end{aligned} \quad (2)$$

$$\text{or: } p_{i,j}(t) = \varphi \cdot pbest_{i,j}(t) + (1 - \varphi) \cdot gbest_j(t),$$

where  $\varphi$  is a sequence of uniformly distributed random numbers in  $(0,1)$ .

Unlike PSO, each individual particle in QPSO moves in the search space with a  $\delta$  potential on each dimension, of whose center is point  $p_{i,j}$ . When a particle  $x_i$  evolves its position in this  $\delta$  potential, the new position  $X_i(t+1)$  is subject to an exponential distribution whose probability density function is

$$\begin{aligned} F(|X_i(t+1) - p_i(t)|) &= \frac{1}{L_i(t)} \exp\left(-\frac{2|X_i(t+1) - p_i(t)|}{L_i(t)}\right), \end{aligned} \quad (3)$$

where  $L_i$  determines the distribution scope. In QPSO, the distribution scope of each particle is set elaborately to relate to its relative position in the whole swarm:

$$L_{i,j} = 2\beta \cdot |mbest_j(t) - X_{i,j}(t)|, \quad (4)$$

where  $mbest$  is the mean of the personal best positions among all particles:

$$\begin{aligned} mbest(t) &= (mbest_1(t), mbest_2(t), \dots, mbest_D(t)) \\ &= \left( \frac{1}{M} \sum_{i=1}^M pbest_{i,1}(t), \frac{1}{M} \right. \\ &\quad \left. \cdot \sum_{i=1}^M pbest_{i,2}(t), \dots, \frac{1}{M} \sum_{i=1}^M pbest_{i,D}(t) \right). \end{aligned} \quad (5)$$

In this way, particles far away from the center of the whole swarm will have a larger searching scope, while those particles close to the middle can only search in a relatively limited small space. Therefore, the position of the particle in QPSO is updated according to the following iteration equation:

$$X_{i,j}(t+1) = p_{i,j} \pm \beta \cdot |mbest_j - X_{i,j}(t)| \cdot \ln\left(\frac{1}{\mu}\right), \quad (6)$$

where  $\mu$  is a random number uniformly distributed in (0,1) and  $\beta$  is called Contraction-Expansion Coefficient, which is employed to control the convergence speed of the algorithm. As proved by Sun et al. [14],  $\beta$  must be set as  $\beta < 1.782$  to guarantee convergence of the particle.

### 3. Proposed Method

**3.1. Novel Ring Model Based Position-Update Strategy.** From the perspective of both empirical evidence and theory analysis, the global search ability as well as the convergence rate of QPSO and its variants has been fully discovered on the single-objective optimization problems. However, this advantage of QPSO leads to premature convergence when it is applied directly to the multiobjective optimizations. Without the loss of generality, a multiobjective optimization problem can be formulated as follows:

$$\min F(x) = [f_1(x), f_2(x), \dots, f_M(x)]^T, \quad (7)$$

where  $f_i$  ( $i = 1, 2, \dots, M$ ) are the objective functions, while  $x = [x_1, x_2, \dots, x_D]^T \in \Omega$  is the vector of decision variable. The optimization performance is generally measured by two aspects: closeness to the ideal Pareto front and distribution of the approximated solutions [8]. However, the quick convergence property of QPSO is apt to lead rapid decline of the swarm's diversity, which becomes a serious problem that must be addressed when it is extended into multiobjective optimization.

Each particle in QPSO is located in an exponential distributed potential, with the center  $p_i$  and distribution scope  $L_i$ , respectively. Figure 1 illustrates the relationship between the particle position and its distribution scope in

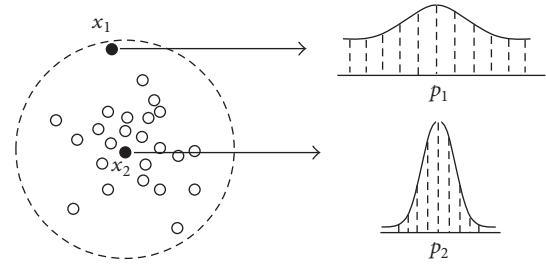


FIGURE 1: The dependence of the search scope of the particle on the distance of the particle from the mean best position.

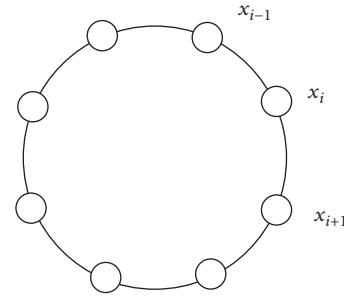


FIGURE 2: All the particles in the swarm are arranged in circle in MOQPSO.

QPSO. Here,  $x_1$  represents the particle far away from the mean best position ( $mbest$ ) of the swarm and its corresponding distribution at next iteration with the center  $p_1$  visualised on upper right;  $x_2$  denotes the particle near the mean best position of the swarm with  $p_2$  being the center of the exponential distribution of its position at next iteration. According to the iteration equation of QPSO, we can see in the figure that  $x_2$  has a much smaller variation scope than  $x_1$ . That is, the closer  $x_i$  to the mean best position, the smaller the scope of the variation. Only those particles away from the  $mbest$ , like  $x_1$ , have the large variation scope. That implies that, in original QPSO, a certain number of particles in the swarm are supposed to have small, or even very close to zero, distribution scopes.

In order to control the descent speed of the swarm diversity, we propose a novel position-update strategy based on the ring model. In this model, for a swarm with  $M$  particles, all the particles are arranged in a circle like Figure 2, numbered as  $x_1, x_2, \dots, x_{i-1}, x_i, x_{i+1}, \dots, x_M$ . Different from the way of deciding particle's variation scope according to its location in the swarm in original QPSO, in our proposed method, when the particle  $x_i$  evolves, its variation scope is decided by the distance to its next-numbered particle  $x_{i+1}$ . Accordingly, for the iteration equation of particle  $x_i$ , we replace  $mbest$  by  $pbest_{i+1}$ , which represents the personal best position of particle  $x_{i+1}$ . Since particles in the swarm are distributed randomly and independently, the position of  $x_{i+1}$  can locate everywhere in the search space theoretically. That means that particles with continuous indices are not necessarily adjacent in position. The particles around the center of the swarm could also have the opportunity to mutate

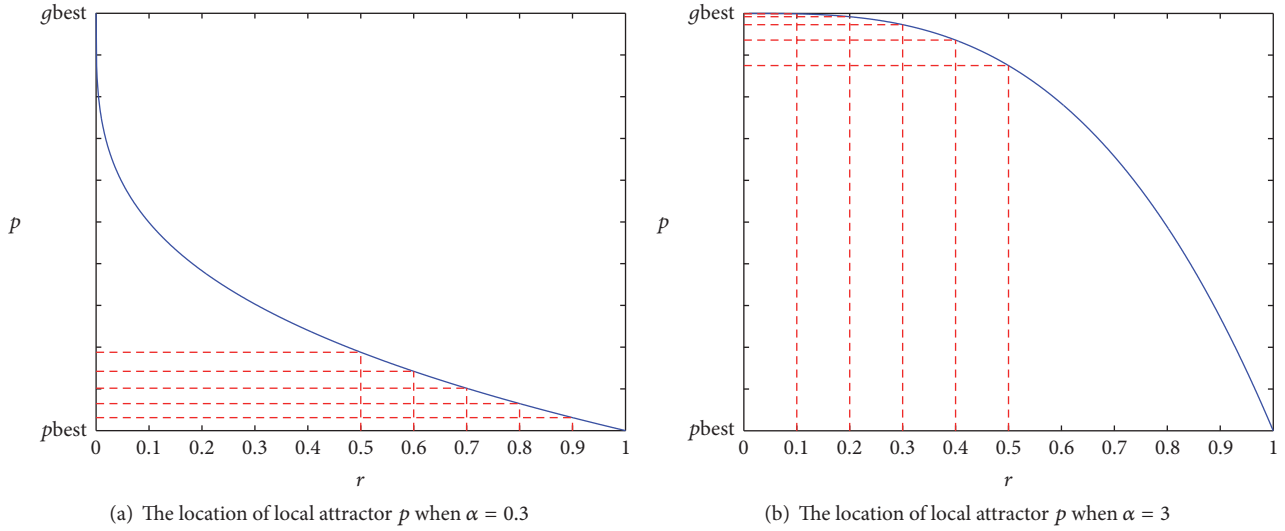


FIGURE 3: The relationship between the location of the local attractor  $p$  and the value of  $r$  for different values of  $\alpha$ .

with large scopes. Therefore, by this novel position-update strategy, the swarm of MOQPSOr can mutate more than the original QPSO, which subsequently leads to the slowdown of the descent speed of the swarm diversity.

In terms of the local attractor  $p_i$ , in QPSO, it is set to lie uniform-randomly in the hyperrectangle with  $pbest_i$  and  $gbest$  being two ends of its diagonal. Generally speaking, the local searching ability will be enhanced when  $p_i$  moves towards  $gbest$ , and when  $p_i$  moves towards  $pbest_i$ , the global searching ability will be enhanced. Therefore, in MOQPSOr,  $p_i$  is given larger probabilities locating near  $pbest_i$  in the beginning and near  $gbest$  in the later stage of iteration, respectively

Based on the above analysis, particles in MOQPSOr that move according to the position-updating strategy can be described as follows:

$$X_{i,j}(t+1) = p_{i,j} \pm \beta \cdot |pbest_{i+1,j}(t) - X_{i,j}(t)| \cdot \ln\left(\frac{1}{\mu}\right), \quad \mu \sim U(0,1), \quad (8)$$

$$\text{where: } p_{i,j} = gbest_j + (pbest_{i,j} - gbest_j) \cdot r^\alpha, \quad (9)$$

$$r \sim U(0,1),$$

where parameter  $\alpha$  is called Searching Coefficient, by adjusting which, local attractor  $p_{i,j}$  can be controlled to appear near  $pbest_{i,j}$  or  $gbest_j$ . Figure 3 plots the distribution of  $p$ 's location formulated in (9), where the horizontal axis denotes the random number  $r$  and the vertical axis denotes  $p$ 's location between  $pbest$  and  $gbest$ .  $\alpha = 0.3$  and  $\alpha = 3$  are used as examples to demonstrate situations when  $\alpha < 1$  and  $\alpha > 1$ , respectively. From the red dotted lines, it could be seen that when  $\alpha = 0.3$ ,  $p$  has half probability to locate in  $[pbest, 0.812pbest + 0.188gbest]$ , which is much closer to  $pbest$  than to  $gbest$ . In Figure 3(b), when  $\alpha = 3$ ,  $p$  has

half probability to locate in  $[0.125pbest + 0.875gbest, gbest]$ , which is closer to  $gbest$  than to  $pbest$ . That is, when  $\alpha < 1$ , the local attractor  $p$  would appear near  $pbest$  with large probability. The smaller the value of  $\alpha$  is, the closer the point  $p$  gathers towards  $pbest$ . On the contrary, when  $\alpha > 1$ ,  $p$  would appear with large probability near  $gbest$ . The bigger the value of  $\alpha$  is, the closer the point  $p$  gathers towards  $gbest$ . Therefore, the algorithm's global searching ability could be enhanced by setting  $\alpha < 1$ , while the local searching ability could be enhanced by setting  $\alpha > 1$ .

**3.2. Multiobjective QPSO with Ring Model (MOQPSOr).** In MOQPSOr, we adopt the concept of crowding distance [25] for the leader selection. Whenever a leader particle needs to be selected as the global best position from the external archive, the crowding factor of each leader is calculated, followed by the subsequent selection by means of a binary tournament based on these crowding factors. A particle with larger crowding distance has more chances to be chosen as leader.

Crowding distance of each individual is also used to decide which leaders would keep over generations when the maximum external archive size is exceeded in MOQPSOr. The particle in the archive with the smallest crowding distance will be removed first whenever needed.

Since MOQPSOr could have already slowed down the descent speed of the swarm diversity by the novel position-update strategy based on ring model, there is no need for any additional mutation operation. The procedure of the MOQPSOr algorithm could be described as follows.

*Step 1* (initialization).

*Step 1.1.* Parameter settings are as follows: the swarm size  $M$ , the external archive size  $E_{size}$ , the stopping criterion  $T_{max}$ , iteration time  $t = 0$ , Searching Coefficient  $\alpha$ , and Contraction-Expansion Coefficient  $\beta$ .

*Step 1.2.* Initialize the swarm randomly within the feasible solution space  $X = (X_1, X_2, \dots, X_M)$ , as well as the personal best positions  $pbest = (pbest_1, pbest_2, \dots, pbest_M)$ , where  $pbest_i = X_i$ ,  $i \in [1, M]$ .

*Step 1.3.* Initialize the external archive  $E$  as the nondominated solution in  $pbest$ .

*Step 2 (termination).* If termination condition is met, stop and return all the individuals in the current  $E$ . Otherwise, go to Step 3.

*Step 3 (reproduction).* For each particle  $X_i$ ,  $i \in [1, M]$ , note the following.

*Step 3.1.* Select a global best position  $gbest_i$  from external archive.

*Step 3.2.* Update position by (8) and (9).

*Step 3.3.* Update personal best position  $pbest_i$ .

*Step 4 (external archive update).*

*Step 4.1.* Consider  $E(t+1) = E(t) \cup pbest$ .

*Step 4.2.* Remove dominated solutions in  $E(t+1)$ .

*Step 4.3.* If the size of the current  $E$  is larger than  $E_{size}$ , calculate the crowding distance of each individual in  $E$ , sort them in descending order of crowding distance, and keep the first  $E_{size}$  individuals in  $E(t+1)$ .

*Step 5.* Consider  $t = t + 1$ ; go to Step 2.

## 4. Experiments and Analysis

*4.1. Test Functions.* Walking-Fish-Group (WFG) [26], a well-designed multiobjective test suite which provides a truer means of assessing the performance of optimization algorithms on a wide range of different problems, is used to validate the performance of our approach in 2-objective space. Compared with the other two commonly used suite of ZDT [27] and DTLZ [28], WFG test suite is more challenging and contains a number of problems that exhibit properties not evident in ZDT and DTLZ, including nonseparable problems, deceptive problems, a truly degenerate problem, a mixed shape Pareto front problem, problems scalable in the number of position-related parameters, and problems with dependencies related to position and distance parameters.

Besides WFGs, another three 3-objective benchmark functions, which are acknowledged for the extreme difficulty to optimize in the DTLZ test suite, are also involved in the comparison test. DTLZ2 tests the ability of global convergence by providing a spherical Pareto front. DTLZ4 assesses the maintainability of a good distribution of solutions by generating a nonuniform distribution of points along the true Pareto front. The Pareto front of DTLZ7 is the intersection of a straight line and a hyperplane. All these twelve benchmark problems are listed in Table 1.

*4.2. Performance Metrics.* To assess the performance of algorithms in this experiment, three quality indicators are considered: Additive Unary  $\varepsilon$ -indicator ( $I_{\varepsilon+}^1$ ) [29], hypervolume ( $I_{HV}$ ) [30], and the Inverted Generational Distance (IGD) [31].

*Additive Unary  $\varepsilon$ -Indicator ( $I_{\varepsilon+}^1$ ).* It measures the convergence of the resulting Pareto fronts. A lower value indicates a better approximation set. For an approximation set  $X$ , the additive Unary  $\varepsilon$ -indicator is defined as [32]

$$I_{\varepsilon+}^1(X) = \inf_{\varepsilon \in \mathbb{R}} \{ \forall z^2 \in P \exists z^1 \in X : z^1 \succeq z^2 \}, \quad (10)$$

where  $P$  is the ideal Pareto front.

*Hypervolume ( $I_{HV}$ ).* This metric measures both convergence and diversity of the solutions. The higher the  $I_{HV}$  values are, the better the algorithm performs. Generally speaking, the hypervolume measures the volume of the space dominated by the approximation set, bounded by a reference point.  $I_{HV}(X)$  of an approximation set  $X$  can be mathematically defined as

$$I_{HV}(X) = \Lambda \left( \bigcup_{(x_1, \dots, x_d) \in X} [r_1, x_1] \times \dots \times [r_d, x_d] \right), \quad (11)$$

where  $r = (r_1, r_2, \dots, r_d)$  is the reference point and  $\Lambda$  is the usual Lebesgue measure.

*Inverted Generational Distance (IGD).* Inverted Generational Distance is the average distance from every solution in the reference set to the nearest solution in the approximation set; it, therefore, reflects convergence of the solutions. The fewer the IGD values, the better the algorithm's performance. The IGD metric is calculated for the solution set  $X$  using the reference point set  $Z$  as follows:

$$IGD(Z, X) = \frac{1}{|Z|} \sum_{i=1}^{|Z|} \min_{j=1}^{|X|} d(z_i, x_j), \quad (12)$$

where  $d(z_i, x_j)$  is the distance between  $z_i$  and  $x_j$  in the objective space.

*4.3. Algorithm for Comparison and Parameter Setting.* In this experiment, five state-of-the-art multiobjective optimization algorithms are chosen for comparison, including the most efficient and widely used multiobjective particle swarm optimizer OMOPSO [6] and another two well-known PSO-based multiobjective optimization algorithms:  $\sigma$ MOPSO [33] and pdMOPSO [34], as well as two competitive evolutionary multiobjective optimizers: NSGA-II [25] and PESA-II [35].

To make a fair comparison, the population size and the leader archive in MOQPSo and all the other five comparison algorithms are fixed to 100 for all test instances. The stopping condition is set to 250 iterations, which means a total of 25000 function evaluations. For MOQPSo,  $\alpha$  increases linearly from 0.6 to 1.2, and  $\beta$  is set to 0.3. For OMOPSO,  $\sigma$ MOPSO, and pdMOPSO, the sets of  $C_1$ ,  $C_2$ , and  $\omega$ , as well as the mutation method and the mutation probability are all the

TABLE 1: Description of the test functions.

Code	Objective functions	Feature	Objectives
WFG1	$\min_{f_m} f_m = x_M + 2m \left( \prod_{i=1}^{M-m} \left( 1 - \cos \left( \frac{x_i \pi}{2} \right) \right) \right) \cdot \left( 1 - \sin \left( \frac{x_{M-m+1} \pi}{2} \right) \right)$ $\min_{f_M} f_M(x) = x_M + 2m \left( 1 - x_1 - \frac{\cos(2A\pi x_1 + \pi/2)}{2A\pi} \right)^\alpha$ $x = \{x_1, \dots, x_M\} = \{\max(t_M^p, A_1)(t_M^p - 0.5) + 0.5, \dots, \max(t_M^p, A_{M-1})(t_M^p - 0.5) + 0.5, t_M^p\}$ $t^p = \{t_1^p, \dots, t_M^p\} \leftarrow t^{p-1} \leftarrow \dots \leftarrow t^1$ $t_{i=1:k}^1 = y_i \quad t_{i=k+1:n}^1 = s\_linear(y_i, 0.35)$ $t_{i=1:k}^2 = y_i \quad t_{i=k+1:n}^2 = b\_flat(y_i, 0.8, 0.75, 0.85)$ $t_{i=1:n}^3 = b\_poly(y_i, 0.02)$ $t_{i=1:2M-1}^4 =$ $r\_sum \left( \{y_{(i-1)k/(M-1)+1}, \dots, y_{ik/(M-1)}\}, \left\{ 2 \left( \frac{(i-1)k}{(M-1)} + 1 \right), \dots, \frac{2ik}{(M-1)} \right\} \right)$ $t_{i=M}^4 = r\_sum(\{y_{k+1}, \dots, y_n\}, \{2(k+1), \dots, 2n\})$	Mixed, convex/concave, Unimodal, separable	2
WFG2	$f_{n=i:M-1}$ and $t^1$ are as those from WFG1, $\min_{f_M} f_M(x) = x_M + 1 - (x_1)^\alpha \cos^2(A(x_1)^\beta \pi), \quad \alpha = \beta = 1, \quad A = 5$ $t_{i=1:k}^2 = y_i \quad t_{i=k+1:k+1/2}^2 = r\_nonsep(\{y_{k+2(i-k)-1}, y_{k+2(i-k)}\}, 2)$ $t_{i=1:2M-1}^3 = r\_sum(\{y_{(i-1)k/(M-1)+1}, y_{ik/(M-1)}\}, \{1, \dots, 1\})$ $t_M^3 = r\_sum(\{y_{k+1}, \dots, y_{k+1/2}\}, \{1, \dots, l\})$ $t_{i=M}^4 = r\_sum(\{y_{k+1}, \dots, y_n\}, \{2(k+1), \dots, 2n\})$	Convex, disconnected, Unimodal, multimodal, nonseparable	2
WFG3	$\min_{f_1} f_1(x) = x_M + 2m \prod_{i=1}^{M-1} x_i$ $\min_{f_m} f_m = x_M + 2m \prod_{i=1}^{M-m} x_i \cdot (1 - x_{M-m+1})$ $\min_{f_M} f_M(x) = 1 - x_1$ $t^{1,3}$ are as those from WFG2	Linear, degenerate, unimodal, nonseparable	2
WFG4	$\min_{f_1} f_1(x) = x_M + 2m \left( \prod_{i=1}^{M-1} \sin \left( \frac{x_i \pi}{2} \right) \right)$ $\min_{f_m} f_m = x_M + 2m \left( \prod_{i=1}^{M-m} \sin \left( \frac{x_i \pi}{2} \right) \right) \cdot \cos \left( \frac{x_{M-m+1} \pi}{2} \right)$ $\min_{f_M} f_M(x) = x_M + 2m \cos \left( \frac{x_1 \pi}{2} \right)$ $t_{i=1:n}^1 = s\_multi(y_i, 30, 10, 0.35)$ $t_{i=1:M-1}^2 = r\_sum(\{y_{(i-1)k/(M-1)+1}, \dots, y_{ik/(M-1)}\}, \{1, \dots, 1\})$ $t_M^2 = r\_sum(\{y_{k+1}, \dots, y_n\}, \{1, \dots, 1\})$	Concave, multimodal, separable	2
WFG5	$f_{n=i:M}$ and $t^2$ are as those from WFG4, $t_{i=1:n}^1 = s\_decept(y_i, 0.35, 0.001, 0.05)$	Concave, deceptive, separable	2

TABLE I: Continued.

Code	Objective functions	Feature	Objectives
WFG6	$f_{m=1:M}$ are as those from WFG4, $t^1$ as those from WFG1, $t^2_{i=1:M-1} = r\_nonsep \left( \{y_{(-1)k/(M-1)+1}, \dots, y_{ik/(M-1)}\}, \frac{k}{(M-1)} \right)$ $t^2_M = r\_nonsep (\{y_{k+1}, \dots, y_n\}, l)$	Concave,unimodal,nonseparable	2
WFG7	$f_{m=1:M}$ are as those from WFG4, $t^2$ as $t^1$ from WFG1, $t^3$ as $t^2$ from WFG4, $t^1_{i=1:k} = b\_param \left( \{y_{i+1}, \dots, y_n\}, \{1, \dots, 1\}, \frac{0.98}{49.98}, 0.02, 50 \right)$ $t^1_{i=k+1:n} = y_i$	Concave,unimodal,separable	2
WFG8	$f_{m=1:M}$ are as those from WFG4, $t^2$ as $t^1$ from WFG1, $t^3$ as $t^2$ from WFG4, $t^1_{i=1:k} = y_i$ $t^1_{i=k+1:n} = b\_param \left( \{y_i, r\_sum (\{y_1, \dots, y_{i-1}\}, \{1, \dots, 1\}), \frac{0.98}{49.98}, 0.02, 50 \right)$	Concave,unimodal,nonseparable	2
WFG9	$f_{m=1:M}$ are as those from WFG4, $t^3$ as $t^2$ from WFG6, $t^1_{i=1:n-1} = b\_param \left( \{y_i, r\_sum (\{y_{i+1}, \dots, y_n\}, \{1, \dots, 1\}), \frac{0.98}{49.98}, 0.02, 50 \right)$ $t^1_{i=n} = y_n$ $t^2_{i=1:k} = s\_decept (y_i, 0.35, 0.001, 0.05)$ $t^2_{i=k+1:n} = s\_multi (y_i, 30, 95, 0.35)$	Concave,multimodal,deceptive,nonseparable	2
DTLZ2	$\min f_1(x) = (1 + g(x_M)) \prod_{i=1}^{M-1} \cos \left( \frac{x_i \pi}{2} \right)$ $\min f_{m=2:M-1}(x) = (1 + g(x_M)) \sin \left( \frac{x_{M-m+1} \pi}{2} \right) \prod_{i=1}^{M-m} \cos \left( \frac{x_i \pi}{2} \right)$ $\min f_M(x) = (1 + g(x_M)) \sin \left( \frac{x_1 \pi}{2} \right)$ $s.t. g(x_M) = \sum_{x_i \in X_M} (x_i - 0.5)^2$	Concave,unimodal	3
DTLZ4	$f_{1:M}$ and $g(x_M)$ are both the same with DTLZ2, besides $x_i^a$ is used to replace $x_i$ $\min f_{m=1:M-1}(x) = x_m$	Concave,nonuniform	3
DTLZ7	$\min f_M(x) = (1 + g(x_M)) \left\{ M - \sum_{i=1}^{M-1} \left[ \frac{f_i}{1 + g(x_M)} (1 + \sin(3\pi f_i)) \right] \right\}$ $s.t. g(x_M) = 1 + \frac{9}{ x_M } \sum_{x_i \in X_M} x_i$	Disconnected,unimodal,multimodal	3

TABLE 2: Comparison results in terms of  $I_{\varepsilon+}^1$  between MOQPSOr and other algorithms.

Function	MOQPSOr	OMOPSO	$\sigma$ MOPSO	pdMOPSO	NSGA-II	PESA-II
WFG1	0.6662	0.7697 (+)	0.7058 (+)	0.7247 (+)	<b>0.5662</b> (–)	0.7149 (+)
WFG2	0.005945	0.01156 (+)	0.05869 (+)	0.08135 (+)	0.006621 (+)	<b>0.004953</b> (–)
WFG3	<b>0.3327</b>	0.3341 (+)	0.3345 (+)	0.3378 (+)	0.3338 (+)	0.3348 (+)
WFG4	0.02752	0.03035 (+)	0.04921 (+)	0.03004 (+)	0.01162 (–)	<b>0.01002</b> (–)
WFG5	<b>0.03067</b>	0.03071 (+)	0.03070 (+)	0.05671 (+)	0.03210 (+)	0.03367 (+)
WFG6	<b>0.006673</b>	0.007467 (+)	0.01973 (+)	0.01244 (+)	0.03534 (+)	0.04072 (+)
WFG7	<b>0.005080</b>	0.006404 (+)	0.008138 (+)	0.01039 (+)	0.01455 (+)	0.01318 (+)
WFG8	0.05696	<b>0.05381</b> (–)	0.05714 (+)	0.05401 (–)	0.05475 (–)	0.06613 (+)
WFG9	<b>0.01266</b>	0.01331 (+)	0.01308 (+)	0.01573 (+)	0.01898 (+)	0.01667 (+)
DTLZ2	<b>0.05071</b>	0.05176 (+)	0.05150 (+)	0.06394 (+)	0.1153 (+)	0.1201 (+)
DTLZ4	<b>0.05191</b>	0.05700 (+)	0.05681 (+)	0.06437 (+)	0.1069 (+)	0.1007 (+)
DTLZ7	<b>0.05656</b>	0.06321 (+)	0.06229 (+)	0.06870 (+)	0.07233 (+)	0.1459 (+)
Better (+)		11	12	11	9	10
Worse (–)		1	0	1	3	2
Score		10	12	10	6	8

TABLE 3: Comparison results in terms of  $I_{HV}$  between MOQPSOr and other algorithms.

Function	MOQPSOr	OMOPSO	$\sigma$ MOPSO	pdMOPSO	NSGA-II	PESA-II
WFG1	0.02904	0 (+)	0 (+)	0 (+)	<b>0.2046</b> (–)	0.1447 (–)
WFG2	0.5608	0.5557 (+)	0.5502 (+)	0.5489 (+)	<b>0.5626</b> (–)	0.5619 (–)
WFG3	<b>0.44197</b>	0.4408 (+)	0.4401 (+)	0.4399 (+)	0.4399 (+)	0.4399 (+)
WFG4	0.1915	0.1888 (+)	0.1898 (+)	0.1910 (+)	0.2161 (–)	<b>0.2166</b> (–)
WFG5	<b>0.1979</b>	0.1975 (+)	0.1976 (+)	0.1954 (+)	0.1949 (+)	0.1961 (+)
WFG6	<b>0.2082</b>	0.2074 (+)	0.2062 (+)	0.2003 (+)	0.1699 (+)	0.1698 (+)
WFG7	<b>0.2107</b>	0.2089 (+)	0.2065 (+)	0.2043 (+)	0.2075 (+)	0.2088 (+)
WFG8	0.1596	0.1624 (–)	0.1595 (+)	0.1629 (–)	0.1610 (–)	<b>0.1631</b> (–)
WFG9	<b>0.2324</b>	0.2314 (+)	0.2310 (+)	0.2309 (+)	0.2308 (+)	0.2317 (+)
DTLZ2	<b>0.41174</b>	0.4111 (+)	0.4102 (+)	0.4069 (+)	0.3725 (+)	0.4019 (+)
DTLZ4	<b>0.4104</b>	0.4080 (+)	0.4061 (+)	0.3921 (+)	0.3765 (+)	0.4101 (+)
DTLZ7	0.2642	<b>0.2740</b> (–)	0.2623 (+)	0.2602 (+)	0.2638 (+)	0.2538 (+)
Better (+)		10	12	11	8	8
Worse (–)		2	0	1	4	4
Score		8	12	10	4	4

same as in Durillo et al.'s work [36]. For NSGA-II and PESA-II, the crossover rate  $sbx.rate$  and the distribution index  $sbx.distributionIndex$  for simulated binary crossover are set to 1.0 and 15.0, respectively, while the mutation rate and the distribution index for polynomial mutation are set to  $pm.rate = 1/N$  and  $pm.distributionIndex = 20.0$ , where  $N$  is the number of decision variables. For PESA-II, in addition, the number of bisections in the adaptive grid archive is set to 8.

All the experiments are implemented using MOEA framework [37], an open source Java library for developing and experimenting with multiobjective evolutionary algorithms.

Every algorithm runs on each problem over 30 independent trials; and the average results of  $I_{\varepsilon+}^1$ ,  $I_{HV}$  and IGD are recorded.

**4.4. Experimental Results.** Tables 2–4 tabulate the performance results on  $I_{\varepsilon+}^1$ ,  $I_{HV}$ , and IGD, respectively. For each test function, the best result is bolded. Markers “+” and “–” in Tables 2, 3, and 4 are used to indicate the performance comparison results. “+” means MOQPSOr outperforms its rivals, while “–” means MOQPSOr underperforms. The summaries of the comparison results on each metric are also shown in each table.

Since  $I_{\varepsilon+}^1$  and IGD both mainly focus on reflecting the ability of converging to the global Pareto front, Tables 2 and 4 will be discussed together. It is obvious whether on  $I_{\varepsilon+}^1$  or on IGD metric that MOQPSOr no doubt performs best among all the algorithms. On  $I_{\varepsilon+}^1$ , MOQPSOr achieves 8 best values out of the 12 problems, as well as 2 second best values. In comparison, OMOPSO, NSGA-II, and PESA-II all get no more than 2 best values each, while  $\sigma$ MOPSO and pdMOPSO

TABLE 4: Comparison results in terms of IGD between MOQPSOr and other algorithms.

Function	MOQPSOr	OMOPSO	$\sigma$ MOPSO	pdMOPSO	NSGA-II	PESA-II
WFG1	0.576	0.6156 (+)	0.5873 (+)	0.6003 (+)	<b>0.4060</b> (–)	0.5228 (–)
WFG2	0.007339	0.009023 (+)	0.008287 (+)	0.008894 (+)	<b>0.003544</b> (–)	0.004050 (–)
WFG3	<b>0.03331</b>	0.03363 (+)	0.03398 (+)	0.03410 (+)	0.03438 (+)	0.03428 (+)
WFG4	0.01994	0.02157 (+)	0.02431 (+)	0.02386 (+)	0.005290 (–)	<b>0.004598</b> (–)
WFG5	<b>0.02733</b>	0.02739 (+)	0.02741 (+)	0.03082 (+)	0.02766 (+)	0.02749 (+)
WFG6	<b>0.004706</b>	0.005259 (+)	0.01734 (+)	0.009347 (+)	0.03296 (+)	0.03480 (+)
WFG7	<b>0.002606</b>	0.003473 (+)	0.004735 (+)	0.004981 (+)	0.005660 (+)	0.004236 (+)
WFG8	0.03933	0.03736 (–)	0.03989 (+)	0.03756 (–)	0.03725 (–)	<b>0.03649</b> (–)
WFG9	<b>0.008916</b>	0.009299 (+)	0.009313 (+)	0.009305 (+)	0.009429 (+)	0.008953 (+)
DTLZ2	<b>0.04004</b>	0.04160 (+)	0.04231 (+)	0.04583 (+)	0.07000 (+)	0.07540 (+)
DTLZ4	<b>0.04202</b>	0.04794 (+)	0.04737 (+)	0.05177 (+)	0.06859 (+)	0.06436 (+)
DTLZ7	<b>0.04426</b>	0.04523 (+)	0.04570 (+)	0.05231 (+)	0.05180 (+)	0.07088 (+)
Better (+)		11	12	11	8	8
Worse (–)		1	0	1	4	4
Score		10	12	10	4	4

do not achieve any best result at all. In terms of IGD, similarly, MOQPSOr gets the best values in 8 out of the 12 problems, while NSGA-II and PESA-II get 2 best values each. Thus, MOQPSOr claims to be able to produce solutions closer to the global Pareto front than other comparison algorithms in our study.

$I_{HV}$  measures both the convergence and the diversity of the solutions. It could be observed clearly again from Table 3 that MOQPSOr is the best-performing algorithm, yielding the best values in 7 out of 12 problems. The next best-performing algorithms are NSGA-II and PESA-II, which achieve 2 best values each. Although MOQPSOr does not get the best  $I_{HV}$  on 3-objective DTLZ7, it is the second best performing algorithm, only a little bit inferior to OMOPSO.

Figure 4 illustrates the comparison between the final nondominated fronts obtained by MOQPSOr and those by the other algorithms on 2-objective WFG6. In order to display more clearly, each comparison pair contains an overall (Figures 4(a), 4(c), and 4(e)) figure and a sectional (Figures 4(b), 4(d), and 4(f)) figure. In each diagram in Figure 4, thin blue lines demonstrate the ideal Pareto fronts of the problems, while the red dots present the nondominated solutions obtained by MOQPSOr. The black dots in the three pairs of Figures 4(a) and 4(b), Figures 4(c) and 4(d), and Figures 4(e) and 4(f) represent the Pareto front obtained by OMOPSO, NSGA-II, and PESA-II, respectively. It could be observed from Figure 4 that, in terms of the closeness to the blue real Pareto front, NSGA-II performs the worst on 2-objective WFG6. Although the nondominated solutions obtained by OMOPSO and PESA-II are both very close to the one obtained by MOQPSOr, the latter is still a little closer to the ideal Pareto front. Besides, MOQPSOr's nondominated solution shows a much better balanced distribution than OMOPSO's and PESA-II's.

Figures 5 and 6 demonstrate the final nondominated fronts found by MOQPSOr and by other algorithms on 3-objective DTLZ2 and DTLZ7. Figures 5(a), 5(c), 5(e), 5(g),

6(a), 6(c), 6(e), and 6(g) are the overall view of the fronts; Figures 5(b), 5(d), 5(f), 6(h), 6(b), 6(d), 6(f), and 6(h) are the side views. For DTLZ2, MOQPSOr obviously achieves the best performance. It could be observed from the side views that neither NSGA-II nor PESA-II can converge to the ideal Pareto front completely, with some dots astray, the convergence of NSGA-II being even worse than PESA-II. Although the nondominated front found by OMOPSO can converge to the ideal Pareto front as MOQPSOr, its distribution is less balanced. In other words, the distribution of the nondominated front achieved by MOQPSOr is the best.

It can be seen from Figure 6 that the solutions obtained by PESA-II cannot cover the entire ideal Pareto front on every plane when it runs on DTLZ7. Similar observations can also be found when NSGA-II runs on DTLZ7. In contrast, both OMOPSO and MOQPSOr can converge to the ideal Pareto front evenly.

In a word, it could be concluded that MOQPSOr is the most effective algorithm among all the 6 algorithms discussed in our study. Whether considered on solutions' convergence or the diversity, MOQPSOr outperforms all the PSO-based algorithms here on all 12 test functions. Compared with NSGA-II and PESA-II, MOQPSOr can achieve better solution sets on 8 out of 12 problems. Moreover, MOQPSOr performs the best on all the 3-objective functions.

It is worth noting that there are 4 multimodal functions in all of the 12 test problems, which are WFG2, WFG4, WFG9, and DTLZ7. It could be seen from Tables 2–4, on all these multimodal functions, that MOQPSOr performs the best except on 2-objective WFG2 and WFG4 compared with the NSGA-II and PESA-II. However, the performances of every algorithm change when coming to more-than-2-objective optimizations. Table 5 shows the performance results for all the algorithms with different number of objectives on these four multimodal benchmarks; the 3-objective and 4-objective optimization results are in italic font. It could be noticed that although MOQPSOr is not even the third best performed

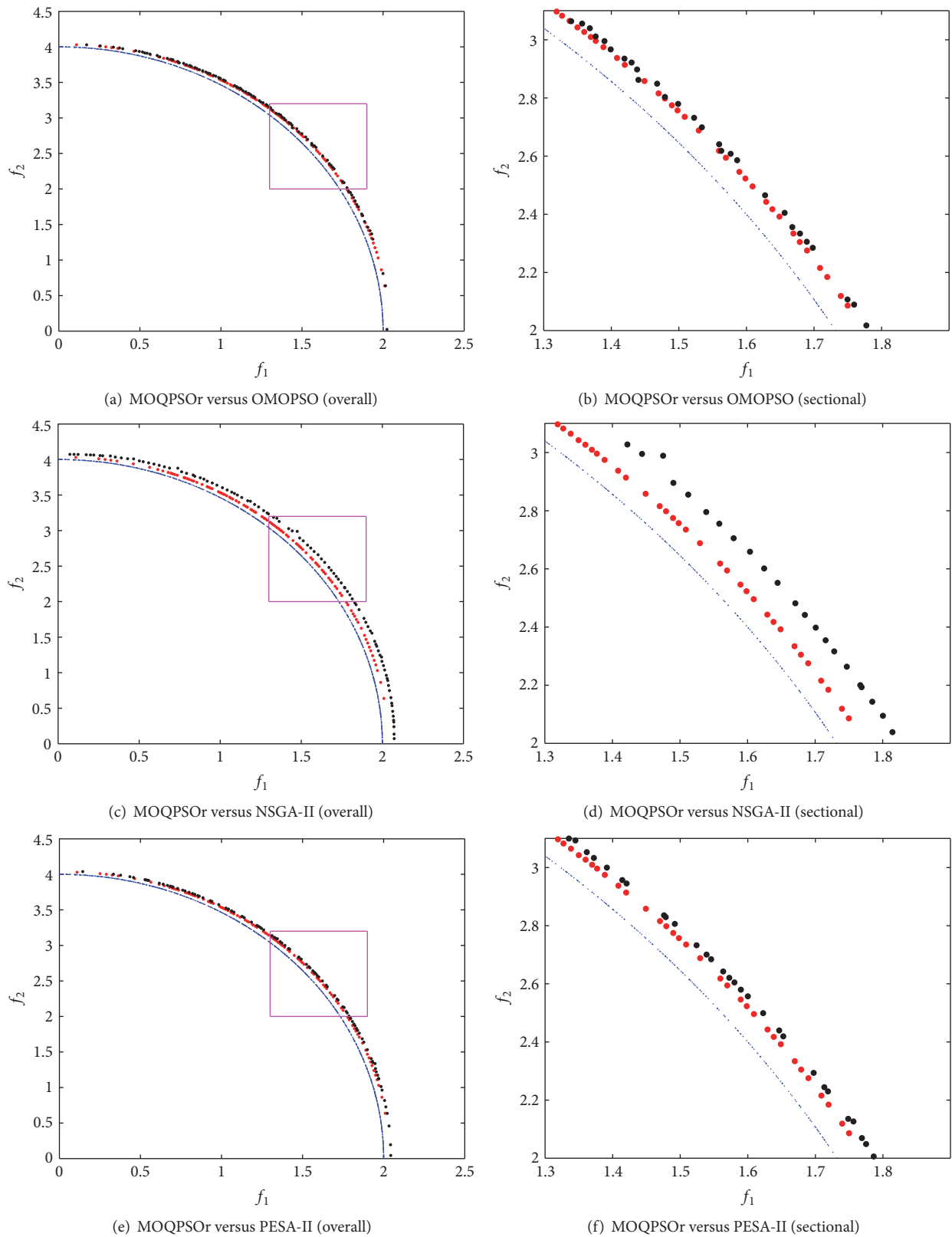


FIGURE 4: Performance comparison on 2-objective WFG6 (the blue is the true Pareto front, the red is the Pareto front obtained by MOQPSOr, and the black is the Pareto front obtained by OMOPSO, NSGA-II, and PESA-II, resp.).

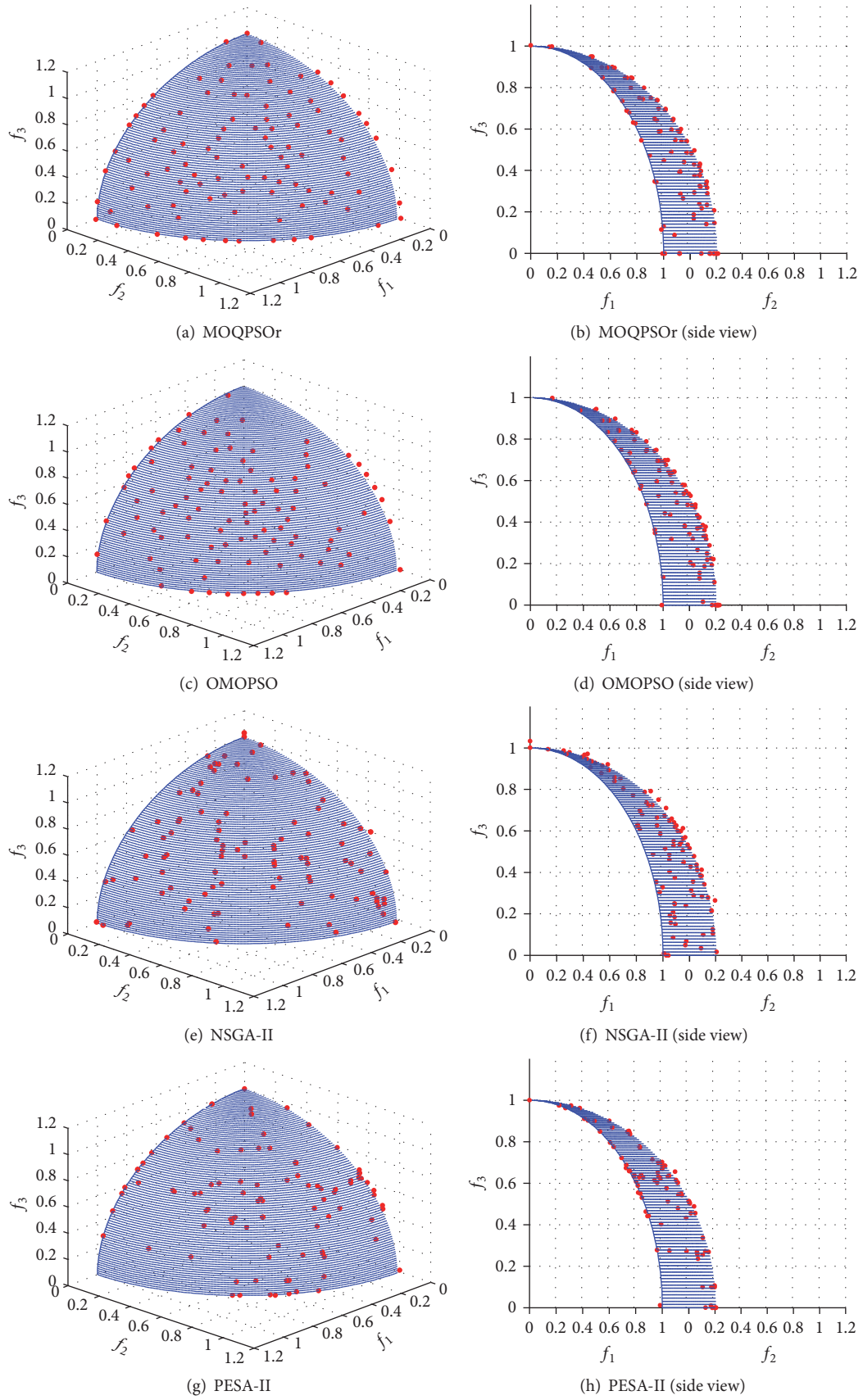


FIGURE 5: Performance on 3-objective DTLZ2 (blue is the ideal Pareto front; red is the Pareto front obtained by each algorithm).

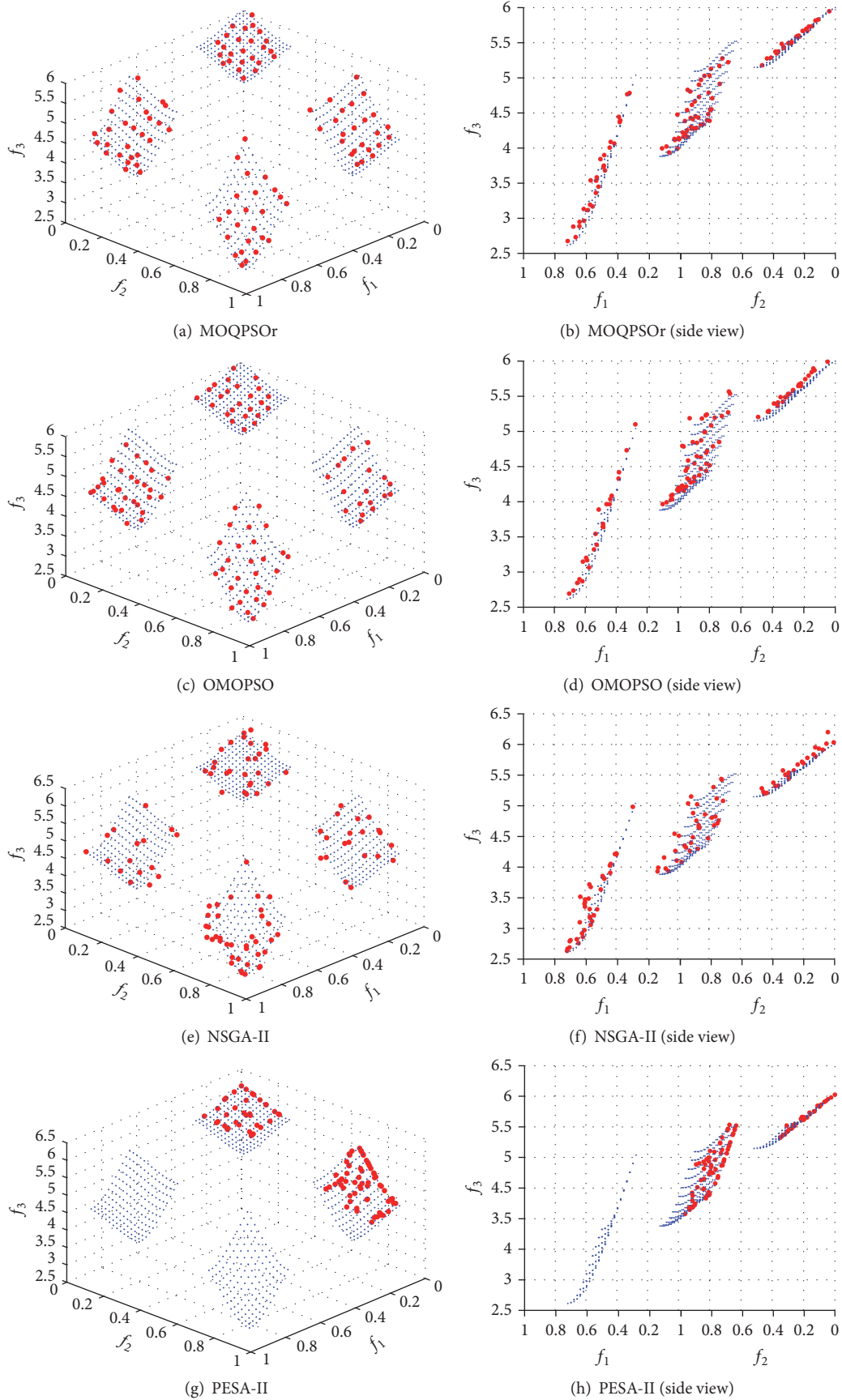


FIGURE 6: Performance on 3-objective DTLZ7 (blue is the ideal Pareto front; red is the Pareto front obtained by each algorithm).

TABLE 5: Experiment results of all the algorithms in terms of  $I_{\varepsilon+}^1$ ,  $I_{HV}$ , and IGD on multimodal functions.

Function	Objective	Metric	MOQPSOr	OMOPSO	$\sigma$ MOPSO	pdMOPSO	NSGA-II	PESA-II	
WFG2	2	$I_{\varepsilon+}^1$	0.005945	0.01156	0.05869	0.08135	0.006621	<b>0.004953</b>	
		$I_{HV}$	0.5608	0.5557	0.5502	0.5489	<b>0.5626</b>	0.5619	
		IGD	0.007339	0.009023	0.008287	0.008894	<b>0.003544</b>	0.004050	
	3	$I_{\varepsilon+}^1$	<b>0.0204</b>	0.03241	0.1060	0.1132	0.1058	0.1054	
		$I_{HV}$	<b>0.9146</b>	0.9073	0.8939	0.8903	0.8950	0.8933	
		IGD	<b>0.01768</b>	0.02480	0.02219	0.02365	0.04214	0.04180	
	4	$I_{\varepsilon+}^1$	<b>0.03501</b>	0.04775	0.1189	0.1237	0.1143	0.07031	
		$I_{HV}$	<b>0.9730</b>	0.9725	0.9401	0.9378	0.9415	0.9612	
		IGD	<b>0.01353</b>	0.01826	0.02356	0.02405	0.04531	0.03921	
	WFG4	2	$I_{\varepsilon+}^1$	0.02752	0.03035	0.04921	0.03004	0.01162	<b>0.01002</b>
			$I_{HV}$	0.1915	0.1888	0.1898	0.1910	0.2161	<b>0.2166</b>
			IGD	0.01994	0.02157	0.02431	0.02386	0.005290	<b>0.004598</b>
3		$I_{\varepsilon+}^1$	<b>0.05139</b>	0.06123	0.07329	0.06021	0.1328	0.1805	
		$I_{HV}$	<b>0.4071</b>	0.3883	0.3893	0.3935	0.3543	0.3898	
		IGD	<b>0.02830</b>	0.03492	0.04776	0.03954	0.06745	0.04754	
4		$I_{\varepsilon+}^1$	<b>0.05371</b>	0.06697	0.08031	0.06891	0.1748	0.3173	
		$I_{HV}$	<b>0.6413</b>	0.6024	0.6002	0.6176	0.4175	0.4021	
		IGD	<b>0.01308</b>	0.01865	0.02589	0.02103	0.07311	0.06605	
WFG9		2	$I_{\varepsilon+}^1$	<b>0.01266</b>	0.01331	0.01308	0.01573	0.01898	0.01667
			$I_{HV}$	<b>0.2324</b>	0.2314	0.2310	0.2309	0.2308	0.2317
			IGD	<b>0.008916</b>	0.009299	0.009313	0.009305	0.009429	0.008953
	3	$I_{\varepsilon+}^1$	<b>0.02647</b>	0.03302	0.03223	0.05873	0.138	0.1070	
		$I_{HV}$	<b>0.4230</b>	0.4206	0.4135	0.4178	0.3454	0.3793	
		IGD	<b>0.02025</b>	0.02195	0.02310	0.02241	0.06819	0.05594	
	4	$I_{\varepsilon+}^1$	<b>0.05906</b>	0.07056	0.07186	0.1092	0.2049	0.1818	
		$I_{HV}$	<b>0.6640</b>	0.6079	0.5871	0.5950	0.4314	0.5207	
		IGD	<b>0.01371</b>	0.03721	0.04133	0.04097	0.1374	0.08635	
	DTLZ7	2	$I_{\varepsilon+}^1$	0.009551	0.009263	0.009220	0.01008	<b>0.008840</b>	0.01073
			$I_{HV}$	0.3242	0.3252	0.3240	0.3227	<b>0.3292</b>	0.3285
			IGD	0.006785	0.006680	0.006733	0.006712	0.003786	<b>0.003679</b>
3		$I_{\varepsilon+}^1$	<b>0.05656</b>	0.06321	0.06229	0.06870	0.07233	0.1459	
		$I_{HV}$	0.2642	<b>0.2740</b>	0.2623	0.2602	0.2638	0.2538	
		IGD	<b>0.04426</b>	0.04523	0.04570	0.05231	0.05180	0.07088	
4		$I_{\varepsilon+}^1$	<b>0.1442</b>	0.1598	0.1560	0.1963	0.2182	0.2603	
		$I_{HV}$	0.1412	<b>0.1484</b>	0.1330	0.1289	0.1355	0.1145	
		IGD	<b>0.1156</b>	0.1285	0.1308	0.1623	0.1579	0.2725	

algorithm on 2-objective WFG2 and WFG4, with a more obvious disadvantage especially towards NSGA-II and PESA-II, it turns out to be much more effective than all of the other algorithms when dealing with the 3-objective and 4-objective optimizations. In addition, the lead swells as the number of objectives increases. In conclusion, MOQPSOr is a competitive multiobjective optimization algorithm, especially on the multimodal problems with large number of objectives.

## 5. Conclusion

Generally speaking, most multiobjective optimization algorithms are reformed from various single-objective optimizers, and the latter play vital roles in deciding the performance

of the former. Since the canonical PSO has been proved to be not a global search algorithm, even not a local one, there may exist the problem of not being able to converge to global optima in the multiobjective PSO-based algorithms. On the contrary, though QPSO's global convergence has been proved, the works on extending QPSO to multiobjective optimization are rare. Therefore, we have proposed a novel version of multiobjective QPSO algorithm based on the ring model (MOQPSOr) in this paper, whose position-update strategy is improved in comparison with QPSO, making it more suitable for multiobjective optimization problems. In MOQPSOr, all the particles are arranged in a circle. When a particle evolves, the distribution scope is decided by the distance to its next particle in numerical order,

which makes the swarm mutates more than the original QPSO. With a high degree of probability, the local attractor  $p$  is located near the personal best position during the early stage of the search but near the global best position  $gbest$  in the later stage of iteration. Unlike most MOPSOs, there is no additional mutation operation in MOQPSO. Compared with the 5 widely used evolutionary multiobjective optimization algorithms on 12 benchmark functions, the experiment results show that the proposed algorithm is highly competitive in both convergence and diversity when solving the multiobjective optimization problems. On top of that, the advantage becomes even more obvious with the number of objectives increasing.

## Competing Interests

The authors have no conflict of interests regarding the publication of this manuscript.

## Acknowledgments

This work was supported by the Natural Science Foundation of Jiangsu province (Project nos. BK20130155 and BK20130160).

## References

- [1] Y. Liu, F. Chen, M. Li, and J. Kou, "A multi-objective optimization model for information system design," in *Contemporary Research on E-Business Technology and Strategy*, pp. 486–495, Springer, 2012.
- [2] J. Luo, Y. Qi, J. Xie, and X. Zhang, "A hybrid multi-objective PSO-EDA algorithm for reservoir flood control operation," *Applied Soft Computing Journal*, vol. 34, pp. 526–538, 2015.
- [3] B. Amiri, L. Hossain, J. W. Crawford, and R. T. Wigand, "Community detection in complex networks: multi-objective enhanced firefly algorithm," *Knowledge-Based Systems*, vol. 46, pp. 1–11, 2013.
- [4] M. Fadaee and M. A. M. Radzi, "Multi-objective optimization of a stand-alone hybrid renewable energy system by using evolutionary algorithms: a review," *Renewable and Sustainable Energy Reviews*, vol. 16, no. 5, pp. 3364–3369, 2012.
- [5] J. Moore and R. Chapman, *Application of Particle Swarm to Multiobjective Optimization*, Department of Computer Science and Software Engineering, Auburn University, Auburn, Ala, USA, 1999.
- [6] M. R. Sierra and C. A. C. Coello, "Improving PSO-based multi-objective optimization using crowding, mutation and  $\epsilon$ -dominance," in *Evolutionary Multi-Criterion Optimization*, C. A. C. Coello, A. H. Aguirre, and E. Zitzler, Eds., vol. 3410 of *Lecture Notes in Computer Science*, pp. 505–519, Springer, Berlin, Germany, 2005.
- [7] M. R. Sierra and C. A. C. Coello, "Multi-objective particle swarm optimizers: a survey of the state-of-the-art," *International Journal of Computational Intelligence Research*, vol. 2, pp. 287–308, 2006.
- [8] A. Zhou, B.-Y. Qu, H. Li, S.-Z. Zhao, P. N. Suganthan, and Q. Zhang, "Multiobjective evolutionary algorithms: a survey of the state of the art," *Swarm and Evolutionary Computation*, vol. 1, no. 1, pp. 32–49, 2011.
- [9] M. A. Abido, "Multiobjective particle swarm optimization with nondominated local and global sets," *Natural Computing*, vol. 9, no. 3, pp. 747–766, 2010.
- [10] J. Branke and S. Mostaghim, "About selecting the personal best in multi-objective particle swarm optimization," in *Parallel Problem Solving from Nature—PPSN IX*, T. P. Runarsson, H.-G. Beyer, E. Burke, J. J. Merelo-Guervós, L. D. Whitley, and X. Yao, Eds., vol. 4193 of *Lecture Notes in Computer Science*, pp. 523–532, Springer, Berlin, Germany, 2006.
- [11] Y. Wang and Y. Yang, "Particle swarm optimization with preference order ranking for multi-objective optimization," *Information Sciences*, vol. 179, no. 12, pp. 1944–1959, 2009.
- [12] F. Van Den Bergh, *An Analysis of Particle Swarm Optimizers*, University of Pretoria, 2006.
- [13] F. J. Solis and R. J. B. Wets, "Minimization by random search techniques," *Mathematics of Operations Research*, vol. 6, no. 1, pp. 19–30, 1981.
- [14] J. Sun, B. Feng, and W. Xu, "Particle swarm optimization with particles having quantum behavior," in *Proceedings of the Congress on Evolutionary Computation (CEC '04)*, Portland, Ore, USA, June 2004.
- [15] L. dos Santos Coelho and P. Alotto, "Global optimization of electromagnetic devices using an exponential quantum-behaved particle swarm optimizer," *IEEE Transactions on Magnetics*, vol. 44, no. 6, pp. 1074–1077, 2008.
- [16] Y. Cai, J. Sun, J. Wang et al., "Optimizing the codon usage of synthetic gene with QPSO algorithm," *Journal of Theoretical Biology*, vol. 254, no. 1, pp. 123–127, 2008.
- [17] C. Sun and S. Lu, "Short-term combined economic emission hydrothermal scheduling using improved quantum-behaved particle swarm optimization," *Expert Systems with Applications*, vol. 37, no. 6, pp. 4232–4241, 2010.
- [18] J. Sun, X. Wu, V. Palade, W. Fang, C.-H. Lai, and W. Xu, "Convergence analysis and improvements of quantum-behaved particle swarm optimization," *Information Sciences*, vol. 193, pp. 81–103, 2012.
- [19] J. Sun, W. Fang, X. Wu, V. Palade, and W. Xu, "Quantum-behaved particle swarm optimization: analysis of individual particle behavior and parameter selection," *Evolutionary Computation*, vol. 20, no. 3, pp. 349–393, 2012.
- [20] J. D. Schaffer, "Multiple objective optimization with vector evaluated genetic algorithms," in *Proceedings of the 1st International Conference on Genetic Algorithms*, pp. 93–100, L. Erlbaum Associates, Pittsburgh, Pa, USA, July 1985.
- [21] N. Tian and Z. Ji, "Pareto-ranking based quantum-behaved particle swarm optimization for multiobjective optimization," *Mathematical Problems in Engineering*, vol. 2015, Article ID 940592, 10 pages, 2015.
- [22] J. Kennedy, "Particle swarm optimization," in *Encyclopedia of Machine Learning*, Springer, Berlin, Germany, 2011.
- [23] J. Kennedy and R. Eberhart, "Particle swarm optimization," in *Proceedings of the IEEE International Conference on Neural Networks*, pp. 1942–1948, Perth, Australia, November–December 1995.
- [24] M. Clerc and J. Kennedy, "The particle swarm-explosion, stability, and convergence in a multidimensional complex space," *IEEE Transactions on Evolutionary Computation*, vol. 6, no. 1, pp. 58–73, 2002.
- [25] K. Deb, A. Pratap, S. Agarwal, and T. Meyarivan, "A fast and elitist multiobjective genetic algorithm: NSGA-II," *IEEE Transactions on Evolutionary Computation*, vol. 6, no. 2, pp. 182–197, 2002.

- [26] S. Huband, P. Hingston, L. Barone, and L. While, "A review of multiobjective test problems and a scalable test problem toolkit," *IEEE Transactions on Evolutionary Computation*, vol. 10, no. 5, pp. 477–506, 2006.
- [27] E. Zitzler, K. Deb, and L. Thiele, "Comparison of multiobjective evolutionary algorithms: empirical results," *Evolutionary Computation*, vol. 8, no. 2, pp. 173–195, 2000.
- [28] K. Deb, L. Thiele, M. Laumanns, and E. Zitzler, *Scalable Test Problems for Evolutionary Multiobjective Optimization*, Springer, Berlin, Germany, 2005.
- [29] E. Zitzler, L. Thiele, M. Laumanns, C. M. Fonseca, and V. G. Da Fonseca, "Performance assessment of multiobjective optimizers: an analysis and review," *IEEE Transactions on Evolutionary Computation*, vol. 7, no. 2, pp. 117–132, 2003.
- [30] E. Zitzler and L. Thiele, "Multiobjective evolutionary algorithms: a comparative case study and the strength Pareto approach," *IEEE Transactions on Evolutionary Computation*, vol. 3, no. 4, pp. 257–271, 1999.
- [31] K. Deb and H. Jain, "An evolutionary many-objective optimization algorithm using reference-point-based nondominated sorting approach—part I: solving problems with box constraints," *IEEE Transactions on Evolutionary Computation*, vol. 18, no. 4, pp. 577–601, 2014.
- [32] C. M. Fonseca, J. D. Knowles, L. Thiele, and E. Zitzler, "A tutorial on the performance assessment of stochastic multiobjective optimizers," in *Proceedings of the 3rd International Conference on Evolutionary Multi-Criterion Optimization (EMO '05)*, p. 240, Guanajuato, Mexico, March 2005.
- [33] S. Mostaghim and J. Teich, "Strategies for finding good local guides in multi-objective particle swarm optimization (MOPSO)," in *Proceedings of the IEEE Swarm Intelligence Symposium (SIS '03)*, pp. 26–33, IEEE, Indianapolis, Ind, USA, April 2003.
- [34] J. E. Alvarez-Benitez, R. M. Everson, and J. E. Fieldsend, "A MOPSO algorithm based exclusively on pareto dominance concepts," in *Proceedings of the 3rd International Conference on Evolutionary Multi-Criterion Optimization (EMO '05)*, pp. 459–473, Springer, Guanajuato, Mexico, March 2005.
- [35] D. W. Corne, N. R. Jerram, J. D. Knowles, and M. J. Oates, "PESA-II: region-based selection in evolutionary multiobjective optimization," in *Proceedings of the Genetic and Evolutionary Computation Conference (GECCO '01)*, San Francisco, Calif, USA, July 2001.
- [36] J. J. Durillo, J. García-Nieto, A. J. Nebro, C. A. C. Coello, F. Luna, and E. Alba, "Multi-objective particle swarm optimizers: an experimental comparison," in *Evolutionary Multi-Criterion Optimization*, M. Ehrgott, C. M. Fonseca, X. Gandibleux, J.-K. Hao, and M. Sevaux, Eds., vol. 5467 of *Lecture Notes in Computer Science*, pp. 495–509, Springer, Berlin, Germany, 2009.
- [37] D. Hadka, *MOEA Framework User Guide. Version 2.6*, 2015.

## Research Article

# Model Test Research on the End Bearing Behavior of the Large-Diameter Cast-in-Place Concrete Pile for Jointed Rock Mass

Jingwei Cai,<sup>1</sup> Aiping Tang,<sup>1</sup> Xinsheng Yin,<sup>2</sup> Xiaxin Tao,<sup>1</sup> and Shibo Tao<sup>1</sup>

<sup>1</sup>Civil and Engineering School, Harbin Institute of Technology, Harbin 150001, China

<sup>2</sup>Civil and Engineering School, Jilin Jianzhu University, Changchun 130118, China

Correspondence should be addressed to Jingwei Cai; [cjw850607@126.com](mailto:cjw850607@126.com)

Received 13 July 2016; Revised 29 September 2016; Accepted 19 October 2016

Academic Editor: Cheng-Tang Wu

Copyright © 2016 Jingwei Cai et al. This is an open access article distributed under the Creative Commons Attribution License, which permits unrestricted use, distribution, and reproduction in any medium, provided the original work is properly cited.

For large-diameter, cast-in-place concrete piles, the end bearing capacity of a single pile is affected by discontinuous surfaces that exist in natural rock masses when the bearing layer of the pile end is located in the rock layer. In order to study the influence of the jointed dip angle on the bearing characteristics of the pile end, the discrete element models are adopted to simulate the mechanical characteristics of the jointed rock masses, and the model tests of the failure mode of the jointed rock masses were also designed. The results of the numerical calculations and modeling tests show that the joints, which have a filtering effect on the internal stress of the bedrock located at the pile end, change the load transferring paths. And the failure mode of the jointed rock foundation also changes as jointed dip angle changes. The rock located at the pile end generally presents a wedge failure mode. In addition, the Q-S curves obtained by model tests show that the ultimate end bearing capacity of a single pile is influenced by the jointed dip angle. The above results provide an important theoretical basis for how to correctly calculate end resistance for a cast-in-place concrete pile.

## 1. Introduction

To improve the end bearing capacity of large-diameter cast-in-place concrete piles, it is best to select rock strata as the bearing stratum at the pile end. Researches by Serrano and Olalla [1, 2], Yang and Yin [3], Saada et al. [4], and Imani et al. [5] focused on the rock mass according to the Hoek-Brown failure criterion, which is applied for intact rocks. However, in practical engineering, the most natural rock masses are made of rock blocks and discontinuous surfaces, and the discontinuity plays an important role in rock deformation and the failure mechanism. However, conducting a destructive test to determine the ultimate bearing capacity of a single pile in a prototype test is cost prohibitive, which limits researchers' ability to collect sufficient experimental data in order to better understand bearing behavior. This is especially true when the bedrock of the pile end is discontinuous, in which case, even with a large field test, it is very difficult to gather data necessary for a qualitative analysis of the influence of jointed

dip angles on bearing capacity. Thus, research needs to focus on how to correctly calculate the end bearing resistance of a single pile in a jointed rock foundation.

At present, some researchers conducted studies on the bearing behavior of jointed rock masses. Reik and Zacas [6] studied the strength and deformation characteristics of jointed media in true triaxial compression. Yang et al. [7] carried out uniaxial compression test of shale rock and found that there are three kinds of failure modes for the jointed rock and that a change in the dip angle caused changes in the failure modes. Yang et al. [8] conducted a uniaxial compression test using marble specimens with prefabricated joints and described the relationship between the dip angle and the failure mode of nonconsecutive jointed rock. Mas Ivars et al. [9] described a new approach they called synthetic rock mass modeling for simulating the mechanical behavior of a jointed rock mass. Zhou et al. [10] fabricated rock-like materials containing multiple fissures under uniaxial compression to further research the effects of preexisting

fissures on mechanical properties and crack coalescence of rock. Compared with previous experiments, they found five types of cracks, including wing cracks, quasi-coplanar secondary cracks, oblique secondary cracks, out-of-plane tensile cracks, and out-of-plane shear cracks and ten types of crack coalescence. Gao and Kang [11] demonstrated a numerical analysis using a discrete element method simulation for the jointed rock masses. And the numerical results indicate that fracture intensity has no significant influence on the residual strength of jointed rock masses, independent of confining conditions. Cao et al. [12] combined similar material testing and discrete element numerical method (PFC2D) to study the peak strength and failure characteristics of rock-like materials with multifissures. The failure mode can be classified into four categories: mixed failure, shear failure, stepped path failure, and intact failure. And the results show that the peak strength and failure modes in the numerically simulated and experimental results are in good agreement. Yang et al. [13] studied the relationship between the 3D morphological characteristics and the peak shear strength for jointed rock. And a new peak shear strength criterion for rock joints was proposed using two 3D morphological parameters. Furthermore, the calculated peak strengths using the proposed criterion match well with the observed values. Huang et al. [14] did a series of uniaxial compression tests to research the effects of preexisting fissures on the mechanical properties and crack coalescence process for rock-like material with two unparallel fissures. And the strength and deformability characteristics of rock with preexisting fissures are governed by cracking behavior.

Although the above research results could be applied to a jointed rock mass, the results are different from the jointed rock foundation of a pile end that supports the vertical load from the pile and thus produces different failure modes. Kulhawy and Goodman [15] put forward that the spacing of horizontal and vertical joints is the essential factors in the ultimate pile end resistance. Benmokrane et al. [16] conducted a rock-socketed pile model test and illustrated that when weak intercalated layers exist within the rock mass, the ultimate end bearing capacity is influenced by the different jointed dip angles. Maghous et al. [17] assessed the load bearing capacity of rock foundations resting on a regularly jointed rock and considered the rock matrix and the joints separately. They then compared the obtained results with those derived through considering the jointed rock mass as a homogenized medium. Sutcliffe et al. [18] analyzed the bearing capacity of rock masses containing one to three sets of closely spaced joints. Halakatevakis and Sofianos [19] used a distinct element code to analyze a series of jointed rock samples containing one to three joint sets with various spacing and dip angles and concluded that the strength of the models was independent of the joint spacing. Yu [20] proposed the extended finite element method (XFEM), a numerical method for analyzing discontinuous rock masses that is very convenient for preprocessing. In this model, discontinuities, such as joints, faults, and material interfaces, are contained in the elements, so the mesh can be generated without taking into account the existence of discontinuities. Hossein et al. [21] used distinct element method to build

a numerical model to evaluate bearing capacity of strip footing rested on anisotropic discontinuous rock mass. And the results show that the failure mechanism of rock mass depended on both geometrical parameters of joint sets and strength parameters of rock mass.

In order to study the relationship between jointed dip angles and the end bearing characteristics of a single pile, we use discrete element models to simulate the mechanical characteristics of jointed bedrock with different inclination angles. The laboratory model tests are designed to analyze the failure modes, cracking mechanism, and variations in the ultimate end bearing capacity when the jointed dip angles and jointed numbers are changed. The results obtained from the model tests are compared with the numerical analysis results to verify the correctness of the related theory of the failure mechanism of the jointed rock mass.

## 2. Numerical Analysis of the Failure Mode

*2.1. The Theoretical Basis of Discrete Element Method.* The failure modes of the jointed rock foundation are simulated with different jointed dip angles according to the discrete element method. Discrete element method (DEM) was firstly proposed by Cundall in 1971. This method is based on the discrete characteristics of material itself to establish numerical model. It shows great superiority in simulating discrete material.

The discrete element program PFC (particle flow code), which can simulate circular particle movement and interaction, is adopted to simulate the failure. The interactional force of particles is calculated according to Newton's second law and the contact law of force. Discrete element analysis considers the following interactional forces: (1) the force of gravity; (2) the contact force between particles and between particles and walls; (3) the frictional force between particles and between particles and walls. The calculated results are compared to the experimental results in order to verify the correctness of the theoretical analysis.

The basic motion equation of the discrete element is built by dynamic relaxation method as

$$m\ddot{x}(t) + c\dot{x}(t) + kx(t) = f(t), \quad (1)$$

where  $m$  is the quality of a unit;  $x(t)$  is the displacement of a unit;  $t$  is the time;  $c$  is the viscous damping coefficient;  $k$  is the stiffness coefficient;  $f(t)$  is the external load of a unit. Equation (1) can be changed into the following form as equation (2) by using the central difference method.

$$\begin{aligned} & \frac{m [x(t + \Delta t) - 2x(t) + x(t - \Delta t)]}{(\Delta t)^2} \\ & + \frac{c [x(t + \Delta t) - x(t - \Delta t)]}{(2\Delta t)^2} = f(t), \end{aligned} \quad (2)$$

where  $t$  is the calculating time step and (3) can be obtained by changing (2):

$$\begin{aligned} & x(t + \Delta t) \\ & = \frac{\{(\Delta t)^2 f(t) + (c\Delta t/2 - m)x(t - \Delta t) + [2m - k(\Delta t)^2]x(t)\}}{(m + c\Delta t/2)}. \end{aligned} \quad (3)$$

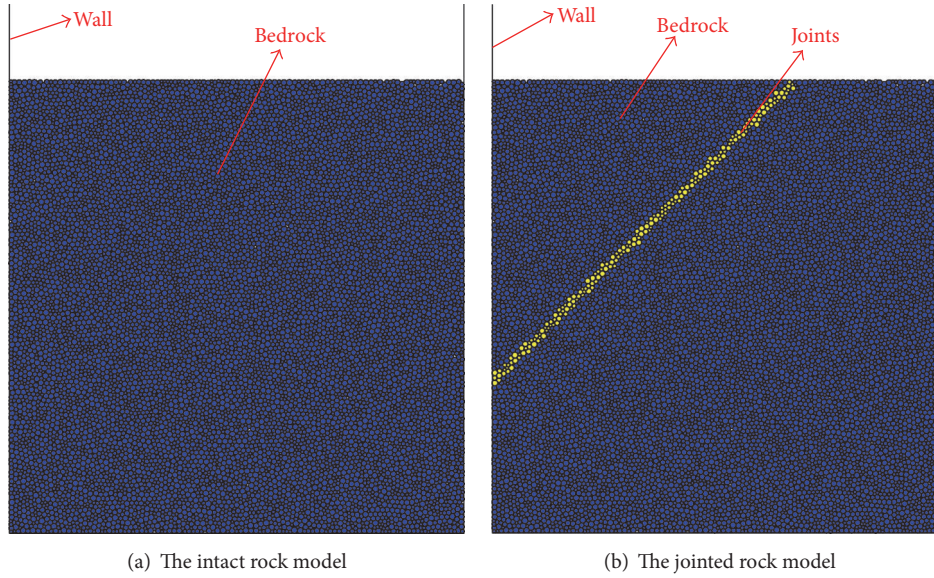


FIGURE 1: The rock model.

The velocity and acceleration of the particles in the time of  $t$  can be obtained by bringing  $x(t + \Delta t)$  into the following two equations:

$$\begin{aligned} \dot{x}(t) &= \frac{[x(t + \Delta t) - x(t - \Delta t)]}{2(\Delta t)}, \\ \ddot{x}(t) &= \frac{[\dot{x}(t + \Delta t) - 2\dot{x}(t) + \dot{x}(t - \Delta t)]}{(\Delta t)^2}. \end{aligned} \quad (4)$$

So it can be seen that the central difference method is used in discrete element method. It is an explicit solution which does not require the solution of a large matrix and saves the computing time. And this method can be used to solve some nonlinear problems.

**2.2. Setup Simulation Models and Determination of the Basic Parameters.** The model is made up of an end-closed cylindrical container filled with well-compacted round particles and a pipe-shaped model pile. The soil model with a width of  $10B$  ( $W$ ) and a height of  $10B$  is used, where  $B$  is the pile diameter and is equal to 50 mm. And the pile length is 20 mm. The roughness of the pile surface can be set up to simulate the friction coefficient.

The relative parameters of particles are shown in Table 1 obtained by general triaxial test of particle flow code. A set of parameters, which can reflect the macroscopic mechanical behavior of rock mass, are obtained by constantly adjusting the microparameters. And this set of parameters could reflect the strength and deformation characteristics of the rock materials. The rock models, which are composed of balls with the diameters uniformly varying between 2 mm and 3 mm, contained intact rock models and the jointed rock models with the dip angles of  $0^\circ$ ,  $10^\circ$ ,  $30^\circ$ ,  $45^\circ$ ,  $60^\circ$ ,  $75^\circ$  and  $90^\circ$ , respectively.

TABLE 1: The model parameters of pile particles and soil particles.

Parameters	Rock particles	Joints particles	Pile particles
Friction coefficient	0.7	0.3	0.7
Normal contact stiffness (MPa/m)	1200	100	2000
Shear contact stiffness (MPa/m)	400	100	2000
Parallel-bond normal stiffness (MPa/m)	$4e4$	$2e4$	$1e8$
Parallel-bond shear stiffness (MPa/m)	$2e4$	$1e4$	$1e8$
Density ( $\text{kg/m}^3$ )	2650	2650	2650
Normal bond stress (MPa)	500	500	1000
Shear bond stress (MPa)	500	500	1000

The following assumptions are made to simulate the process of pressing the pile: (1) the particle unit is considered elastomer; (2) the contact points between particles allow a certain amount of “overlap”; (3) compared with the particle size of itself, the “overlap” is very small; (4) the particles of rock mass are spherical unit. The boundary condition of rock mass is built through the “wall” module. The functions of the wall include the following two aspects: (1) to reach the specified initial confining pressure or axial pressure; (2) to maintain a certain confining pressure. The rock model is shown in Figure 1. And the crack distribution, the load transfer path, and the displacement field can be obtained from the results of numerical simulation.

**2.3. Crack Distribution.** It can be seen from Figure 2(a) that in intact rock the crack distribution is basically symmetrical under upper loading. As loading continues, a compaction

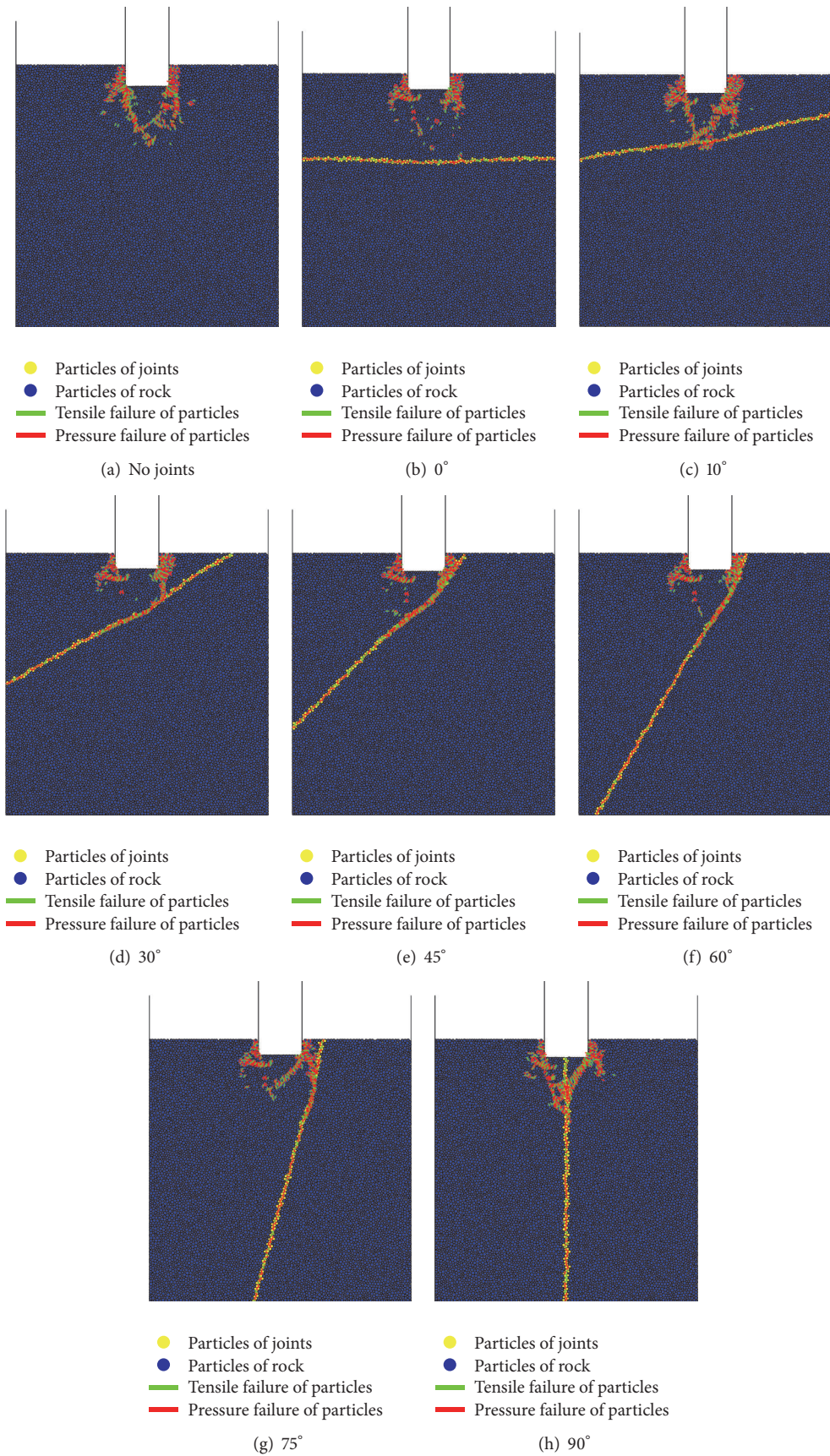


FIGURE 2: The crack distributions of single-jointed rock mass with different dip angles.

TABLE 2: Design parameters of the modeling pile and the rock.

The numbers	Material ratios (sand : cement : water)	Pile diameters (mm)	Jointed dip angles	Jointed numbers
Group A	2 : 1 : 0.6	50	0° 10° 30° 45° 60° 75° 90°	1
Group B	3 : 1 : 0.6	50	0° 10° 30° 45° 60° 75° 90°	1
Group C	2 : 1 : 0.6	50	0° 10° 30° 45° 60° 75° 90°	3

region like a cone will be generated at the pile end, and the cracks next to the compaction region are in a radial distribution. When the jointed dip angles are 0° and 10°, as shown in Figures 2(b) and 2(c), the cracks are distributed mainly above the jointed layer which reduces the end bearing capacity. When the jointed dip angle is 30°, as shown in Figure 2(d), the cracks are still distributed mainly above the jointed layer. When the value of the angle increases, as shown in Figures 2(e), 2(f), and 2(g), the phenomenon becomes more pronounced. It indicates that the cracks in the rock are distributed mainly in the rock where the loading from the pile end is applied directly and the stress of the bedrock is uneven. The rock is thus identified as anisotropic due to the existence of the joints.

**2.4. Load Transferring Path.** Figure 3 shows that the existence of the joints, which have a filtering effect on the stress in the bedrock, changes the load transfer path inside the bedrock at the pile end. In order to maintain the stability of the bedrock and avoid dislocation of the joints, the stress used to resist the upper load is reduced, which changes depending on the jointed dip angle. When the dip angle is small (0°–30°), the stress delivered from the pile end continues downward at the jointed position, and the stress distribution in the rock mass is the regional average. When the jointed dip angle increases to 45° to 75°, part of the stress is transferred to restrain the mutual movement of the jointed surfaces in order to ensure the stability of the rock mass. The load at the pile end is still mainly borne by the rock mass above the joint, but it is more obvious for the jointed dip angle of 45° to 75°. When the jointed dip angle is 90°, the stress is distributed evenly to the two parts by the joint, the distribution of the stress and displacement is symmetrical, and there is no obvious effect on the bearing capacity.

### 3. Model Testing

The spacing of joints in rock mass is usually in meters so that the volume unit becomes very large. Because large-scale mechanical testing is difficult to carry out in rock, it is not realistic to directly measure the mechanical properties of the rock. On the other hand, in situ testing of rock masses has greater ability to produce discreteness in results, so laboratory testing with similar materials could be conducted systematically in order to control the parameters and obtain reasonable mechanical properties. Thus, laboratory testing is widely used for studying the strength, deformation, and failure mechanism of jointed rock masses. In order to analyze the stress, deformation, and failure mechanism of the jointed bedrock more intuitively, a laboratory test was created for

a cast-in-place concrete pile to obtain the data regarding different jointed distributions, the ultimate bearing capacity, and the Q-S curves of a single pile.

**3.1. The Determination of Experimental Materials.** In this test, the pile body is simulated using a solid steel bar with the elastic modulus  $E$  of 2.1e5 MPa, which ensures that the pile will not be destroyed before the destruction of the bedrock. Considering the feasibility of the model test and the limitation of the site, the test uses as the model materials sand, cement, and water mixed to a specific ratio to form a mortar. Mixed ratios of similar materials are obtained by making standard test blocks and measuring the stress-strain curves to ensure that stress-strain curves similar to natural rock could be adopted. In order to determine the most suitable mixed ratios, different ratios were created. At the end, two ratios were selected as most suitable for the test because of their similarity to natural rock (sand : cement : water = 2 : 1 : 0.6 and 3 : 1 : 0.6). The uniaxial compressive strength of the prepared materials after 28 days is 6 MPa, the unconfined compressive strength ( $\sigma_c$ ) of the simulated rock material is 6 MPa, and the elastic modulus  $E_r$  is 608 MPa.

### 3.2. The Experimental Design

**3.2.1. The Loading Devices.** Taking into consideration the influence of pressing the pile into the bedrock, the size of the experimental model was determined to be 500 mm \* 500 mm \* 500 mm (length \* width \* height). So the loading box size was 520 mm \* 520 mm \* 520 mm (length \* width \* height). Four steel plates' size of 490 mm \* 490 mm was used around the testing block to constrain the horizontal displacement. The thickness of the steel plates was 20 mm, and they were fixed by the mutual pulling of long high-strength screws and solid steel squares to provide lateral confinement. The size of the bottom steel plate was 600 mm \* 600 mm with a thickness of 20 mm. In order to reduce the friction between the loading box and the testing block, a lubricant was used between the plates and the rock. The loading system is shown in Figure 4 with a maximum measuring range of 200 t as the loading device, and the loading box is shown in Figure 5. The designing parameters of the modeling pile and the rock are shown as in Table 2.

**3.2.2. The Making of the Jointed Testing Blocks.** The jointed testing blocks were created using a cutting method. The positions of the joints were marked on the testing surfaces before cutting. After cutting the joints of the blocks, rubber membranes and rubber bands were used to hold up them in order to ensure the overall stability. Then the rock model

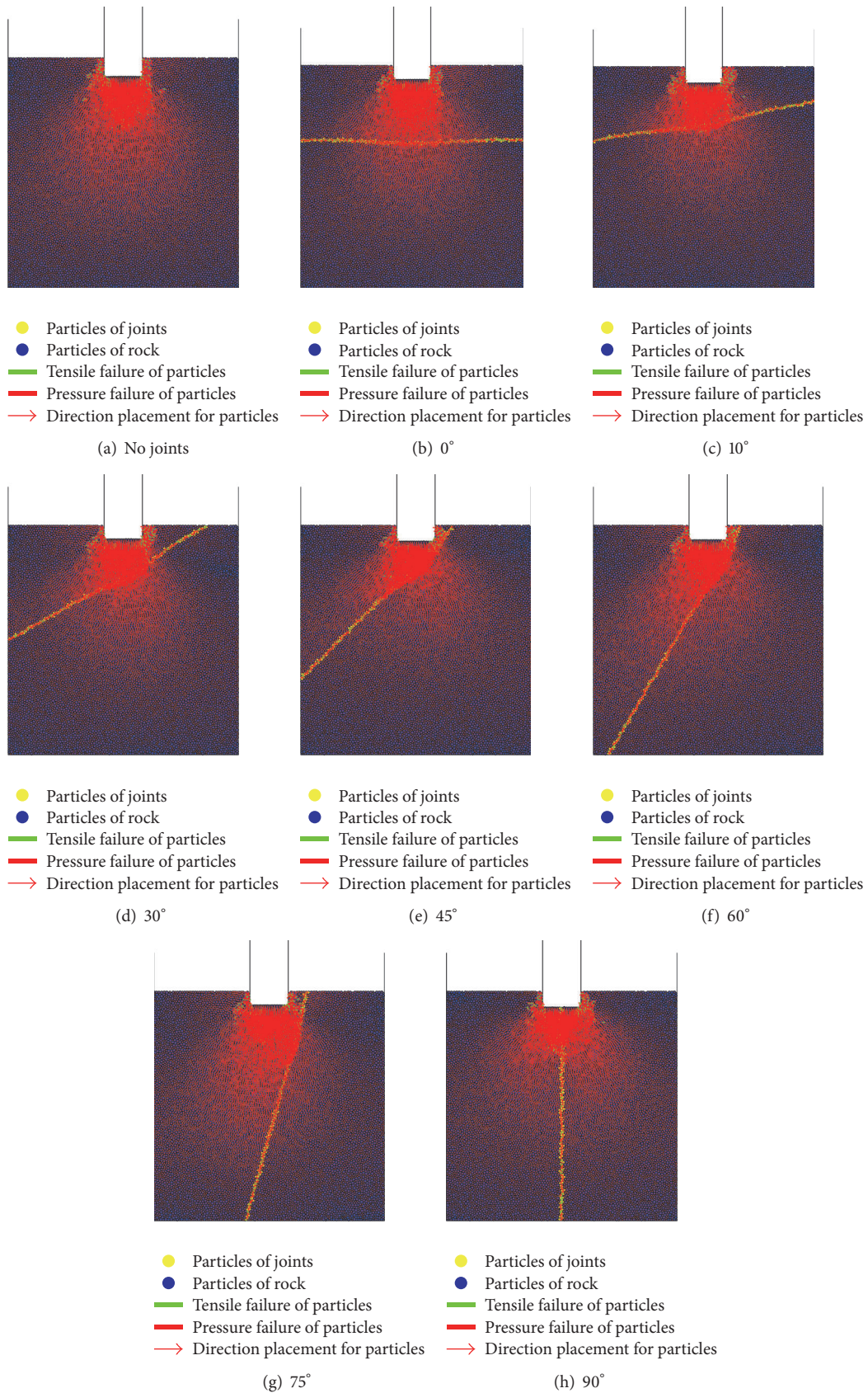


FIGURE 3: The displacement distributions of single-jointed rock mass with different dip angles.



FIGURE 4: System of electric-hydraulic servo test machine.

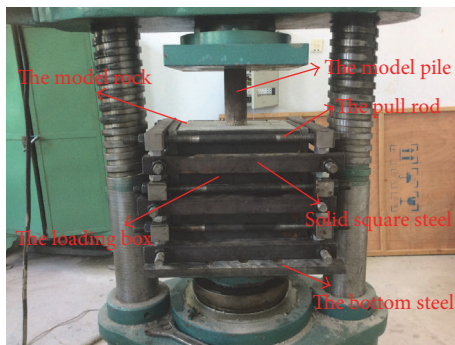


FIGURE 5: The loading box.

(the cutting blocks) was put into the loading box. It was necessary to ensure that the rock surface was horizontal and the pile body would not decline during loading. Taking into consideration the influence of the different jointed distribution angles on the failure mode of the rock, the model test used three groups of rock models with different strength. Each group of rock models contained intact rock and jointed rock with angle of  $0^\circ$ ,  $10^\circ$ ,  $30^\circ$ ,  $45^\circ$ ,  $60^\circ$ ,  $75^\circ$  and  $90^\circ$ , respectively, as shown in Figures 6(a) and 6(b).

**3.2.3. Loading Method and Data Collection.** The test adopted a rapid loading method, which means that the pile end is under sustained loading until the bedrock fails. The measurement data for displacements and settlements were recorded during the process of loading. The displacement was measured by a displacement transducer fixed on the top of the pile. Loading termination occurred when one of the following conditions was noted: (1) under a certain load level, the model appears unstable; (2) the displacement of pile body increases suddenly; or (3) the values recorded by the measuring instruments no longer change.

## 4. Comparative Analysis of the Testing Results and Numerical Calculating Results

**4.1. Crack Distribution and the Load Transferring Mode.** According to the testing results, the crack distribution and development are related to the jointed dip angles. The testing

results were recorded when the jointed dip angles were  $0^\circ$ ,  $10^\circ$ ,  $30^\circ$ ,  $45^\circ$ ,  $60^\circ$ ,  $75^\circ$ , and  $90^\circ$ , respectively. As can be seen in Figure 7, the cracks increased gradually in relation to increase in axial pressure. When the bedrock is intact, as shown in Figure 7(a), the cracks form in a radial distribution; when the bedrock has a jointed angle of  $0^\circ$  to  $10^\circ$ , as shown in Figures 7(b) and 7(c), there is no obvious influence on rock failure; when the jointed angle is  $30^\circ$  to  $45^\circ$ , as shown in Figures 7(d) and 7(e), the number of cracks is significantly reduced compared with the model with the angle of  $0^\circ$ , and the cracks are mainly concentrated near the joint surfaces. The number of cracks is also reduced when the jointed angle is  $60^\circ$  to  $75^\circ$ , as shown in Figures 7(f) and 7(g), and the rock failure is caused by the sliding of the jointed surfaces. The failing process is sharp and does not feature the propagation and accumulation process of new cracks. When the jointed angle is  $90^\circ$ , as shown in Figure 7(h), the loading direction is parallel to the joint, and the crack distribution is basically symmetrical. This means that the existence of joints does not change the failure mode of the bedrock in this condition, and the rock failure is caused by the loading of the pile end and the sliding of the jointed surface. So when the jointed dip angle is small, less than  $30^\circ$ , there is no obvious effect on the failing mode of the bedrock. When jointed angle becomes large, between  $30^\circ$  and  $75^\circ$ , the existence of joints changes the failure mode of the bedrock, and the crack distribution becomes asymmetrical. When a jointed angle is parallel to the loading direction, crack propagation results from the compression of the rock mass. The testing data show that the results of the numerical simulation are in good agreement with ones of the modeling test.

In general, the deformation of the jointed rock surface plays a controlling role in the total failure state. Comparisons of the initial state and failing state of the model rock with different jointed angles show that there is no obvious change in the jointed surface of  $0^\circ$  after failure. That is to say, when the jointed surface is perpendicular to the loading direction, the influence of the joints on the rock foundation is very small, almost negligible. However, it can be found that when the jointed dip angles are  $45^\circ$ ,  $60^\circ$ , or  $75^\circ$ , the sliding phenomenon along the jointed surface is obvious, especially at a jointed angle of  $60^\circ$ .

**4.2. The Wedge Failing Forming.** The load-carrying mechanism of the pile can be regarded as a local compression problem when the load is on the top of the pile and the weight of the overlying soil layer is relatively small. The failing process of the intact bedrock is shown in Figure 8. Firstly, the upper load is transferred to the end of the pile, and the rock mass under the pile is continuously pressed until it is crushed. Under sustained loading, the interface of the pile and the rock generates shear force. When the shear stress exceeds the shear strength, the rock will fail along a rupture angle ( $\theta$ ). At this point, a wedge failing form appears in the rock at the pile end, and the wedge splitting failure of the bedrock is produced under the local pressure load. However, the shape of the wedge differs according to the different dip angles. As shown in Figure 9, the jointed dip angles are, respectively,  $0^\circ$  and  $75^\circ$ . It is obvious that the height of the wedge becomes smaller

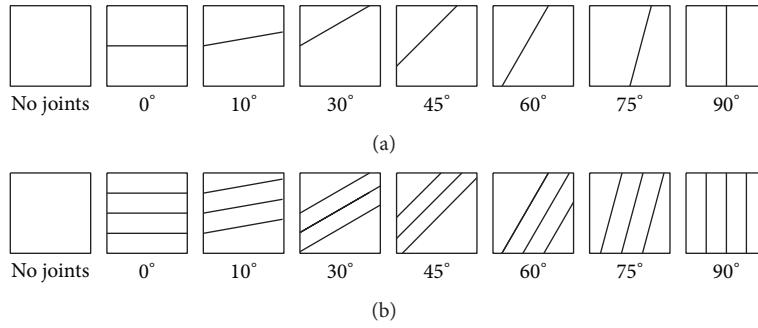


FIGURE 6: The distributions of single joints and a set of joints.



FIGURE 7: The testing crack distributions of single-jointed rock mass with different dip angles.

as the jointed inclination angle increases and the shape of the wedge is asymmetrical, which is caused by the uneven distribution of the shear stress at the end of the pile.

4.3. *Force-Displacement Curves (Q-S Curves)*. In general, the ultimate end bearing capacity is determined when the displacement of the pile top corresponds to the pile diameter

by 10%. However, the pile diameters in this model test are extremely small, and the calculated value is less than 9 mm. Given that the model pile is different from the pile in practical engineering, the final loading value of the pile top is used to represent the bearing capacity of a single pile. In the early stage of loading, the joints of the rock experienced the process of closure regardless of the size of the dip angle.

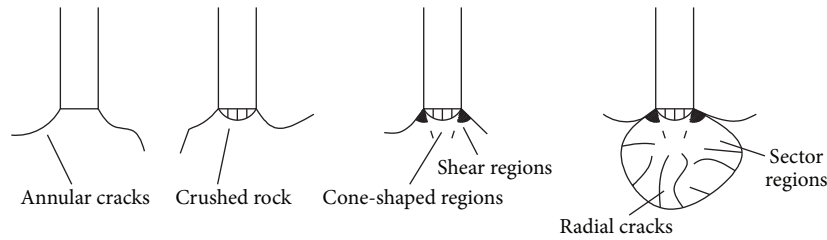


FIGURE 8: The failure process of the intact rock foundation.



FIGURE 9: The wedge failing forming.

Thus the curves of the load and displacement have shown a nearly linear relationship and gradually change to a nonlinear relationship as the rock becomes deformed, and there are obvious turning points in the Q-S curves as shown in Figures 10 and 11.

The deformation of the jointed rock mass can be divided roughly into the following four phases: (1) structural adjustment and jointed closure: the original cracks and the joints are closed, and the rock is compressed to format the early nonlinear deformation. (2) Elastic deformation and crack stable development: the curve of this phase is similar to the linear phase, and, according to the deformation mechanism, it can be subdivided into the elastic phase and the stable developing phase of micro cracking. (3) Unstable development: the strength of the joint reaches the ultimate strength, and relative sliding occurs at the jointed surfaces and microcracks continue to develop. Due to the effect of the stress concentration caused by the cracking process, cracking will continue to develop even if the external load remains constant. (4) Destruction: when the bedrock reaches the ultimate bearing capacity, its internal structure is destroyed. In this phase, cracks develop rapidly and form macroscopic cracks. At this point, rock deformation manifests mainly in the relative sliding of rock blocks along the surface of the macro cracks, and the bearing capacity decreases as deformation increases. Even so, the load value is never reduced to zero, since it is clear that the jointed rock mass still has some bearing capacity. As seen from the entire curve, for example, of Figure 10(f), the rock mass reaches the ultimate load relatively slowly, but the failing rock mass retains some residual stress because of the structural effect.

The test can also help obtain the relationship between the different jointed dip angles and the end bearing capacity of the rock. As the jointed dip angles increase from  $0^\circ$  to  $90^\circ$ , the settlement for the pile end first increases and then decreases under the same load. For example, when the load is 200 KN the settlements of the pile end for the jointed bedrock models of group A, as shown on Figure 10, are 3.6 mm, 3.8 mm, 3.9 mm, 4.3 mm, 6.5 mm, 6.3 mm, and 6.1 mm and 4.0 mm. The results indicated that the existence of the joints made the settlement of the pile end. And the phenomenon is more obvious when the jointed dip angles are  $45^\circ$ ,  $60^\circ$ , and  $75^\circ$  as seen in Figures 10(e), 10(f), and 10(g). In fact, the increments of jointed bedrock include two parts: the compression of rock and the slip of joint surface. When the jointed dip angles are  $45^\circ$ ,  $60^\circ$ , and  $75^\circ$ , the increments caused by the slip of jointed surface are increased. And the Q-S curves of Figure 11 show the same phenomenon as in Figure 10. But when the jointed dip angles are  $90^\circ$  the existence of the joints has no obvious influence on the settlement of pile end.

From Figures 10 and 11, it can be found that the settlements of three-single-joint rock are larger than that of a joint rock when the load is same. The deformation characteristics of the jointed rock mass can be obtained by comparing the Q-S curves such as a single joint of  $45^\circ$  (Figure 10(e)) and three joints of  $45^\circ$  (Figure 11(e)). The shapes of the Q-S curves before reaching the peak strength are approximately the same for the single joint bedrock and the single set of multiple joints bedrock, but the slope for the single-jointed rock is larger than that for the three-jointed rock, which shows that the deformation capacity of the single-jointed rock mass is better than that of the single set of jointed rock mass. This

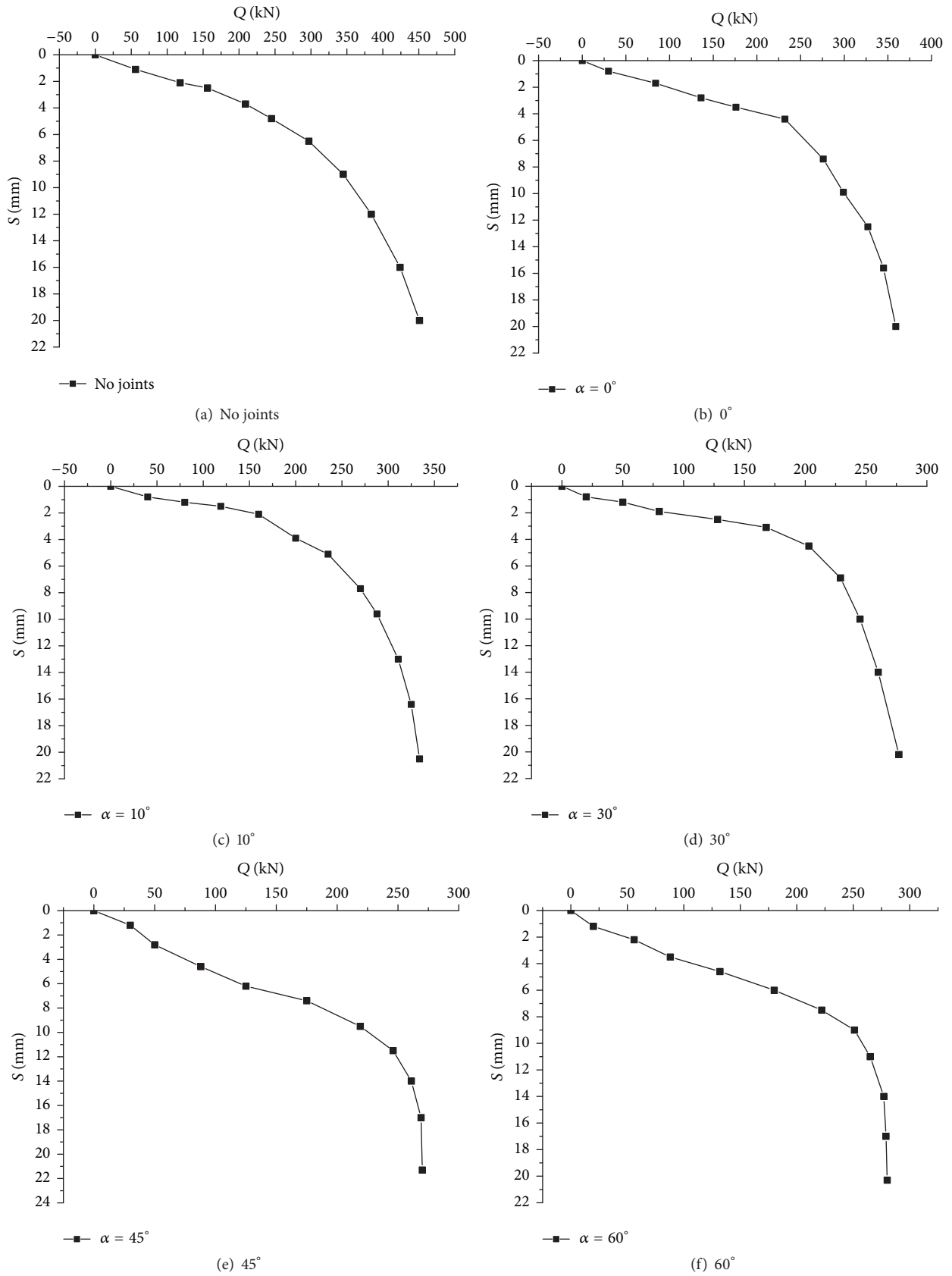


FIGURE 10: Continued.

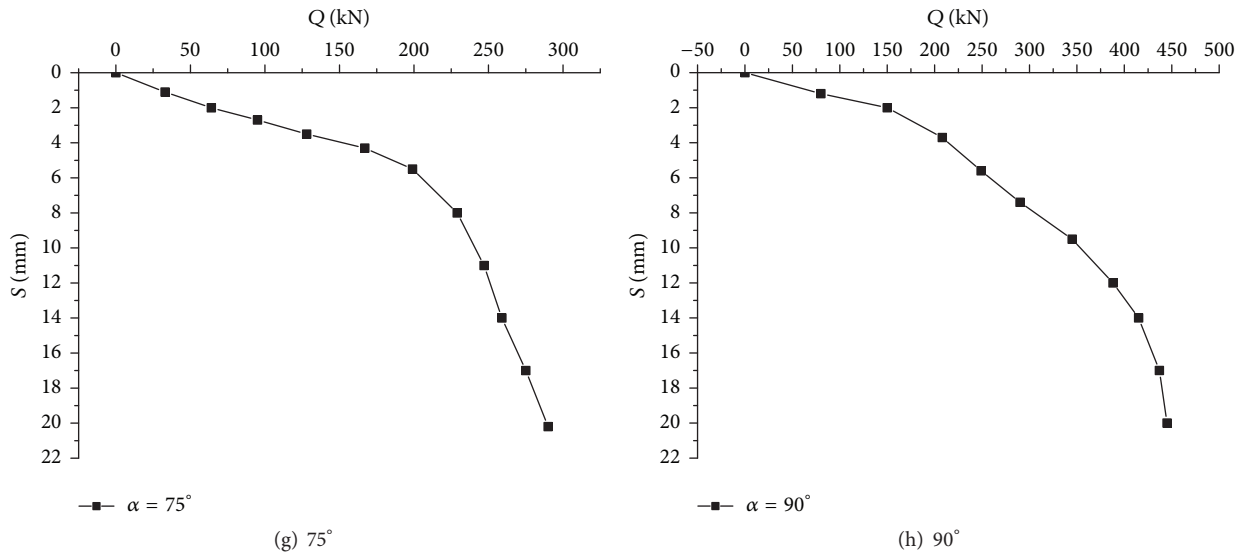


FIGURE 10: The Q-S curves of a single pile for group A.

also indicates that the ultimate bearing capacity of the single-jointed rock mass is much better than that of the three-jointed rock mass.

In addition, the Q-S curves for intact bedrock are shown as in Figure 12(a) and the Q-S curves for jointed bedrock with the dip angle of 45° are shown as in Figure 12(b). The Q-S curves show that the simulating results are in good agreement with the testing results. It also shows that the discrete element method can simulate the end bearing behavior of the jointed bedrock.

#### 4.4. Load-Bearing Characteristic

**4.4.1. The Effect of the Rock Strength on the Ultimate End Bearing Capacity.** In order to determine the relationship between the ultimate end bearing capacity of the pile and the rock strength the data obtained in the test were plotted, as shown in Figure 13, where the whole curve shows a “V” shape. And the order for end bearing capacity of the jointed rock mass of group A from being high to low is those with the dip angles of 90°, 0°, 30°, 45°, 60°, and 75°, respectively; the order for end bearing capacity of the jointed rock mass of group B from being high to low is those with dip angles of 0°, 90°, 30°, 45°, 60°, and 75°, respectively. The comparison of the bearing behavior of the pile end with the intact bedrock shows that the existence of joints reduces the end ultimate bearing capacity regardless of the arrangement of the joint dip angles. The ultimate end bearing capacity of the intact rock is 415 KN from the test result. And the ultimate end bearing capacity of jointed rock at a 45° angle is 268 KN, which is a reduction of 35.4%. These results also indicate that the existence of joints in the rock foundation leads to significant anisotropy. Moreover, the strength of the rock decreases in the presence of joints even if the jointed surface is perpendicular to the direction of maximum principal stress. However, the effect of horizontal

joints on the strength of the rock is not accidental; rather, it can be attributed to the friction and the binding effect of the jointed surface.

Comparing the different strengths of the bedrock in group A and group B, the rock strength clearly has an influence on the end bearing capacity, namely, that the ultimate end bearing capacity increases as the rock strength increases when the jointed dip angle is determined. It can be seen from Figure 13 that no matter how much the jointed dip angle is the end bearing capacity of group A is greater than that of group B. The reason is that the increasing of rock strength could increase the ability of the bedrock to resist upper load to a certain extent. But when the jointed angles of the bedrock are 45°, 60°, and 75°, the end bearing capacity does not improve significantly with the increasing of rock strength, which indicates that the jointed dip angles of bedrock are the main influence factor to the end bearing capacity.

**4.4.2. The Effect of the Jointed Number on the Ultimate End Bearing Capacity.** Figure 14 shows that the ultimate bearing capacity of the pile end differs when the rock has the same jointed dip angles, but different jointed numbers. And the order for bearing capacity of the jointed rock mass of group C from being high to low is those with dip angles of 0°, 90°, 30°, 45°, 60°, and 75°, respectively. The curves show that the same trend exists between single-jointed rock and multiple-jointed rock, which still exhibits a “V” shape. But the end bearing capacity decreases as the jointed numbers increase. The reduction in strength is obvious when the number of joints increases from 1 to 3, that is, from the rock with a single joint to the rock with multiple joints. The reason is that the increasing of the joints number of leads to the destruction of integrity of the bedrock. Furthermore, the anisotropy becomes more significant.

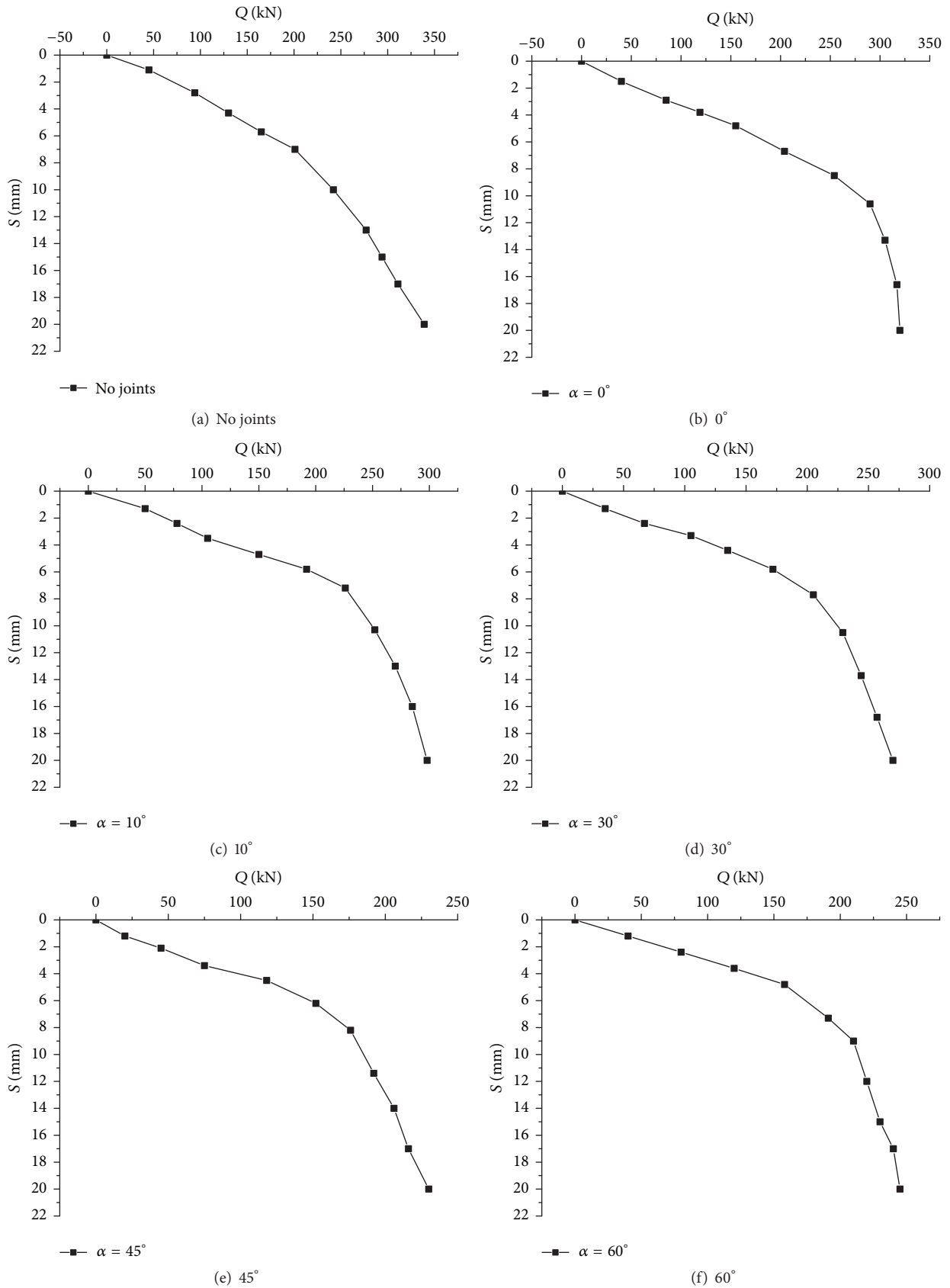


FIGURE II: Continued.

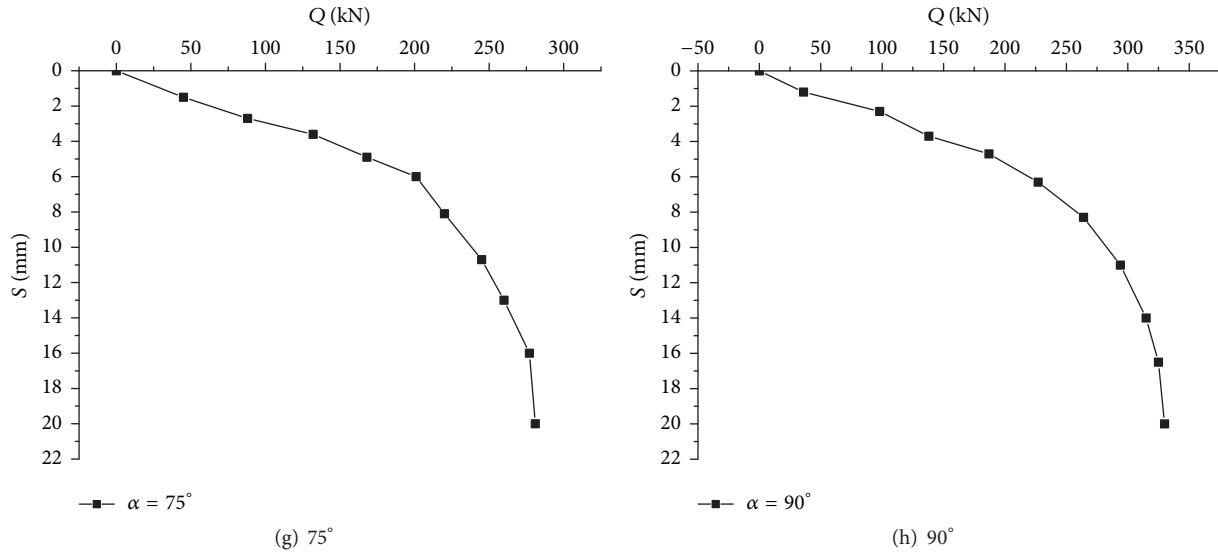


FIGURE 11: The Q-S curves of a single pile for group C.

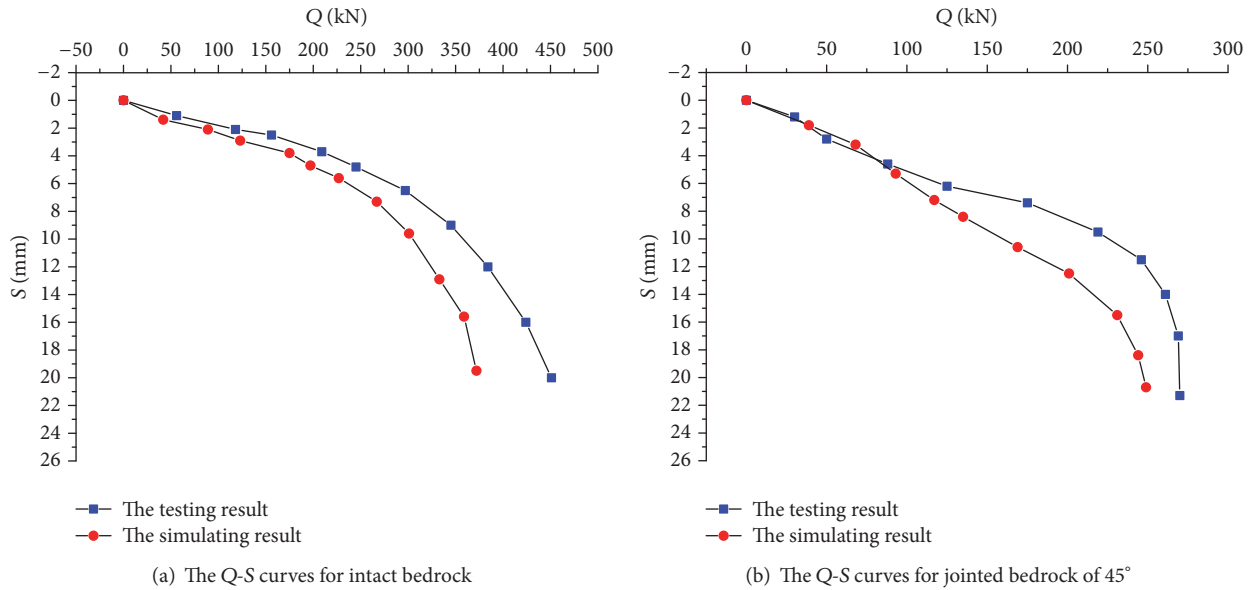


FIGURE 12: The Q-S curves of the testing results and the simulating results.

### 5. Conclusion

Based on the above analysis about the intact rock foundation and the jointed rock foundation, the following conclusions can be drawn:

- (1) The failure mode of the bedrock changes with the existence of the joints. The test results show that the jointed dip angles can change the crack distribution during the process of load transfer. When the jointed dip angle is small, less than  $30^\circ$ , the joints have no significant effect on the destruction of the bedrock; when the jointed dip angle becomes large, greater than  $30^\circ$  and less than  $75^\circ$ , the cause of cracking

includes rock compression and sliding of the jointed surfaces; and when the cracks are parallel to the direction of the dip angle, at  $90^\circ$ , the expansion of the cracks is mainly the result of rock compression.

- (2) The load transfer path of the bedrock changes because of the joints. When the jointed dip angle is small, the change of the path is not obvious, but when the angle is between  $45^\circ$  and  $75^\circ$ , the change is obvious.
- (3) The wedge failing mode of the bedrock generally occurs at the pile end, and the shape of the wedge also changes according to changes in the jointed dip angles.
- (4) The overall shape of Q-S curves for jointed rock is approximately the same. However the direction

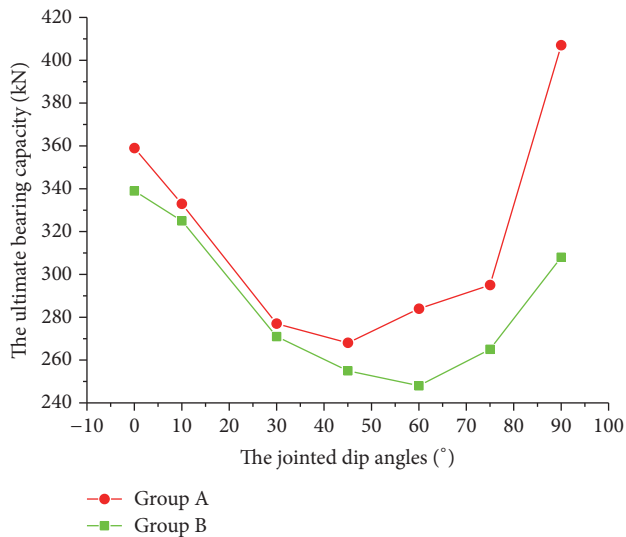


FIGURE 13: The curves for the ultimate bearing capacity of single pile under different rock strength.

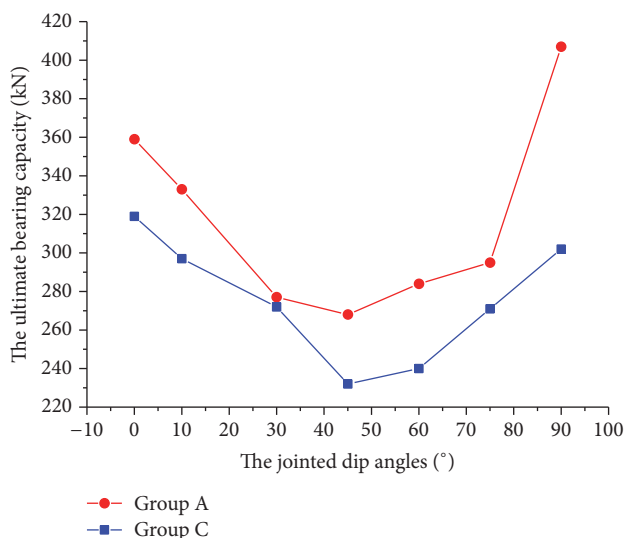


FIGURE 14: The curves for the ultimate bearing capacity of single pile under different jointed numbers.

and the turning point of the Q-S curves can change in response to changes in the jointed numbers and strength. The jointed angles affect the ultimate bearing capacity of the pile end, which increases as rock strength increases. However, when the jointed dip angle of the bedrock is  $45^\circ$  and  $60^\circ$ , the end bearing capacity does not improve significantly, indicating that the jointed dip angles of the rock foundation are controlled mainly by the load-bearing capacity.

## Competing Interests

The authors declare that they have no competing interests.

## Authors' Contributions

For the research work, Jingwei Cai and Xinsheng Yin conceived and designed the experiments; Jingwei Cai, Xiaxin Tao, and Shibo Tao performed the experiments and analyzed the data; Xinsheng Yin and Aiping Tang contributed the test materials and analysis tools; Jingwei Cai wrote the paper.

## Acknowledgments

This work was supported by a grant from National Natural Science Foundation of China (51178205).

## References

- [1] A. Serrano and C. Olalla, "Ultimate bearing capacity of an anisotropic discontinuous rock mass. Part I: basic modes of failure," *International Journal of Rock Mechanics and Mining Sciences*, vol. 35, no. 3, pp. 301–324, 1998.
- [2] A. Serrano and C. Olalla, "Ultimate bearing capacity of an anisotropic discontinuous rock mass part II: determination procedure," *International Journal of Rock Mechanics and Mining Sciences*, vol. 35, no. 3, pp. 325–348, 1998.
- [3] X.-L. Yang and J.-H. Yin, "Upper bound solution for ultimate bearing capacity with a modified Hoek-Brown failure criterion," *International Journal of Rock Mechanics and Mining Sciences*, vol. 42, no. 4, pp. 550–560, 2005.
- [4] Z. Saada, S. Maghous, and D. Garnier, "Bearing capacity of shallow foundations on rocks obeying a modified Hoek-Brown failure criterion," *Computers and Geotechnics*, vol. 35, no. 2, pp. 144–154, 2008.
- [5] M. Imani, M. Sharifzadeh, A. Fahimifar, and P. Haghparast, "A characteristic criterion to distinguish continuity of rock masses applicable to foundations," in *Proceedings of the 45th US Rock Mechanics/Geomechanics Symposium*, ARMA-11-508, San Francisco, Calif, USA, June 2011.
- [6] G. Reik and M. Zacas, "Strength and deformation characteristics of jointed media in true triaxial compression," *International Journal of Rock Mechanics and Mining Sciences & Geomechanics Abstracts*, vol. 15, no. 6, pp. 295–303, 1978.
- [7] Z. Y. Yang, J. M. Chen, and T. H. Huang, "Effect of joint sets on the strength and deformation of rock mass models," *International Journal of Rock Mechanics and Mining Sciences*, vol. 35, no. 1, pp. 75–84, 1998.
- [8] S. Q. Yang, Y. H. Dai, L. J. Han, and Z. Q. Jin, "Experimental study on mechanical behavior of brittle marble samples containing different flaws under uniaxial compression," *Engineering Fracture Mechanics*, vol. 76, no. 12, pp. 1833–1845, 2009.
- [9] D. Mas Ivars, M. E. Pierce, C. Darcel et al., "The synthetic rock mass approach for jointed rock mass modelling," *International Journal of Rock Mechanics and Mining Sciences*, vol. 48, no. 2, pp. 219–244, 2011.
- [10] X. P. Zhou, J. Bi, and Q. H. Qian, "Numerical simulation of crack growth and coalescence in rock-like materials containing multiple pre-existing flaws," *Rock Mechanics and Rock Engineering*, vol. 48, no. 3, pp. 1097–1114, 2015.
- [11] F. Q. Gao and H. P. Kang, "Effects of pre-existing discontinuities on the residual strength of rock mass—insight from a discrete element method simulation," *Journal of Structural Geology*, vol. 85, pp. 40–50, 2016.

- [12] R.-H. Cao, P. Cao, H. Lin, C.-Z. Pu, and K. Ou, "Mechanical behavior of brittle rock-like specimens with pre-existing fissures under uniaxial loading: experimental studies and particle mechanics approach," *Rock Mechanics and Rock Engineering*, vol. 49, no. 3, pp. 763–783, 2016.
- [13] J. Yang, G. Rong, D. Hou, J. Peng, and C. Zhou, "Experimental study on peak shear strength criterion for rock joints," *Rock Mechanics and Rock Engineering*, vol. 49, no. 3, pp. 821–835, 2016.
- [14] Y. H. Huang, S. Q. Yang, W.-L. Tian, W. Zeng, and L.-Y. Yu, "An experimental study on fracture mechanical behavior of rock-like materials containing two unparallel fissures under uniaxial compression," *Acta Mechanica Sinica*, vol. 32, no. 3, pp. 442–455, 2016.
- [15] F. H. Kulhawy and R. E. Goodman, "Design of foundations on discontinuous rock," in *Proceedings of the International Conference on Structural Foundations on Rock*, vol. 1, pp. 209–220, Sydney, Australia, 1980.
- [16] B. Benmokrane, K. S. Mouchaorab, and G. Ballivy, "Laboratory investigation of shaft resistance of rock-socketed piers using the constant normal stiffness direct shear test," *Canadian Geotechnical Journal*, vol. 31, no. 3, pp. 407–419, 1994.
- [17] S. Maghous, P. de Buhan, and A. Bekaert, "Failure design of jointed rock structures by means of a homogenization approach," *Mechanics of Cohesive-Frictional Materials*, vol. 3, no. 3, pp. 207–228, 1998.
- [18] D. J. Sutcliffe, H. S. Yu, and S. W. Sloan, "Lower bound solutions for bearing capacity of jointed rock," *Computers and Geotechnics*, vol. 31, no. 1, pp. 23–36, 2004.
- [19] N. Halakatevakis and A. I. Sofianos, "Strength of a blocky rock mass based on an extended plane of weakness theory," *International Journal of Rock Mechanics and Mining Sciences*, vol. 47, no. 4, pp. 568–582, 2010.
- [20] T. T. Yu, "The extended finite element method (XFEM) for discontinuous rock masses," *Engineering Computations*, vol. 28, no. 3, pp. 340–369, 2011.
- [21] S. R. Hossein, M. Mohammad, and R. D. Morteza, "Distinct element simulation of ultimate bearing capacity in jointed rock foundations," *Arabian Journal of Geosciences*, vol. 6, no. 11, pp. 4427–4434, 2013.

## Research Article

# A New Method to Solve Numeric Solution of Nonlinear Dynamic System

**Min Hu and Fengjun Li**

*School of Mathematics and Statistics, Ningxia University, Yinchuan 750021, China*

Correspondence should be addressed to Fengjun Li; [fjli@nxu.edu.cn](mailto:fjli@nxu.edu.cn)

Received 25 July 2016; Accepted 17 October 2016

Academic Editor: Lihua Wang

Copyright © 2016 M. Hu and F. Li. This is an open access article distributed under the Creative Commons Attribution License, which permits unrestricted use, distribution, and reproduction in any medium, provided the original work is properly cited.

It is well known that the cubic spline function has advantages of simple forms, good convergence, approximation, and second-order smoothness. A particular class of cubic spline function is constructed and an effective method to solve the numerical solution of nonlinear dynamic system is proposed based on the cubic spline function. Compared with existing methods, this method not only has high approximation precision, but also avoids the Runge phenomenon. The error analysis of several methods is given via two numeric examples, which turned out that the proposed method is a much more feasible tool applied to the engineering practice.

## 1. Introduction

With the advancement of science and technology, the nonlinear problems have appeared in many fields. The conventional linear approach cannot meet the requirements of solving nonlinear problems. Therefore, the nonlinear dynamic has been born, which aims at discovering complexity sciences and provides an innovative way to recognize the real and complicated systems. Bifurcation and chaos are the two typical complex dynamic behaviors of nonlinear dynamic systems. In a sense, nonlinear dynamic system is the key topic of nonlinear problems, which can study the chaotic or disordered issue and excavate the complex law of them [1, 2]. For a nonlinear dynamic system, a suitable nonlinear mathematical model should be established to reflect the inherent law of the data and then obtain the characteristics of the system. However, the nonlinear dynamic is diverse, and it changes depending on the previous state in a more complex way. Consequently, there has encountered insurmountable obstruction for applying in the practical engineering. With the existence of complicated chaotic state, it is very difficult to obtain analytic solution in general case. Naturally, people give up solving the exact solution and concentrate on studying the method with characteristics of high approximation precision and easy operation in order to describe the unknown system state.

After years of accumulation and development, there are too many methods to solve the numerical solution of nonlinear dynamic systems; the main methods are as follows: perturbation method [3], averaging method [4], Runge-Kutta method [5], Euler method [6], gradient method [7] and so on. Regretfully, these methods have certain advantages in solving certain system but obtain unappealing outcomes when solving problems of general nonlinear dynamic systems, like the lower precision, the complicity and large calculation quantity, Runge phenomenon, and so forth. So now comes the question, can we find the effective method with high approximation precision as well as avoiding the Runge phenomenon to study the nonlinear dynamic systems? It is well known that the cubic spline function has advantages of good convergence, approximation, stability, and second-order smoothness. And not only that, the cubic spline function does not exist Runge phenomenon due to the restrictions of interpolation conditions.

Given this, the purpose of this paper is to construct a new method to solve the problem mentioned above which replaces the integrand used in the existing way by the constructed cubic spline function. The paper is organized as follows. In Section 2, we recall the basic concepts from approximation theory, such as modulus of continuity. In addition, some basic knowledge of dynamic system and definition of cubic spline function are introduced. In the

following, the corresponding boundary conditions of general cubic spline function are given and a particular class of cubic spline function is constructed. In Section 4, we prove our conclusions. Two numerical results are provided in Section 5 by using the previously obtained theoretical results, and the result indicates that the numerical approach based on the cubic spline function has faster convergence and higher approximation precision than existing methods. In addition, the cubic spline function can approximate the analytic solution of nonlinear dynamic system very well. In Section 6, we briefly summarize our conclusions and foresee problems for the further study.

## 2. Preliminaries

There is a fixed rule in the dynamic system to describe how the point changes over time in the space, and a continuous dynamic system is often represented as a set of differential equations [8]:

$$\dot{x} = f(x), \quad (1)$$

where  $x : t \rightarrow x \in R^N$ , a time variable function, is used to describe the state of system  $f$ ; at least, it is a continuously differentiable function defined on Euclid space  $R^N$  or a subspace  $U \in R^N$ .

The linear combination of linearly independent solutions  $\{x^1(t), \dots, x^N(t)\}$  can be used to express the general solution of the linear dynamic system. But it is unable to work out general solution of the nonlinear dynamic system. And for all we know, the initial value problem of nonlinear dynamic system is as follows [9]:

$$\begin{aligned} \dot{x} &= f(x, t), \\ x(t_0) &= x_0, \\ x &\in R^N. \end{aligned} \quad (2)$$

There is at least one solution from  $t = 0$  on the interval of  $t \in (-c, c)$ . However, it is impossible to give a general calculation rule like the linear dynamic system. Consequently, the numerical method is commonly used for studying the solution of nonlinear dynamic system.

This so-called numerical method is actually a dispersed method. We can obtain the approximate solutions  $x_1, x_2, \dots, x_n$  of unknown function values  $x(t_1), x(t_2), \dots, x(t_n)$  on a series of discrete points  $t_1, t_2, \dots, t_n$ . The discrete points of independent variable can be fixed before and also can select different step length along with the different nodes.  $t_j, j \in 0, 1, 2, \dots, n$ , are generally equidistant nodes, namely,  $t_1 = t_0 + h, t_2 = t_0 + 2h, \dots, t_n = t_0 + nh$ , where step length  $h > 0$ ,  $x_1, x_2, \dots, x_n$ , are commonly referred to as numerical solution of initial value problem.

Considering the nonlinear dynamic system with initial value as form (2), we obtain

$$x(t_{j+1}) - x(t_j) = \int_{t_j}^{t_{j+1}} f(x(t), t) dt. \quad (3)$$

*Definition 1.* For every  $r \in N^+, \delta > 0$ , any function  $f \in [a, b]$ , the definition of  $r$ th order modulus of smoothness of  $f$  is as follows [10]:

$$w_r(f, \delta) := \sup_{a \leq x, x+rt \leq b, |t| \leq \delta} |\Delta_t^r f(x)|, \quad (4)$$

where  $\Delta_t^r f(x) := \Delta_t^1 \Delta_t^{r-1} f(x)$  and  $\Delta_t^1 f(x) := f(x+t) - f(x)$ . When  $r = 1$ , we have  $w_1(f, \delta) = w(f, \delta)$ . That is, the first-order modulus of smoothness of  $f$  is the same as modulus of continuity of  $f$ .

The smooth interpolating curves of spline function are unlikely to reveal the large oscillations feature of high-dimension polynomials. It has been widely used in cartography, pyramidal, and numerical solution methods. For example, spline function may be used for solutions of initial value problems in ordinary differential equations [11, 12].

Let  $\Delta := \{a = t_1 < t_2 < \dots < t_n = b\}$  be a partition of the interval  $[a, b]$ .

*Definition 2.* A cubic interpolation function  $S$  defined on  $\Delta$  is a real function  $S : [a, b] \rightarrow R$  with the characteristics [13]:

- $S \in C^2[a, b]$ ; namely,  $S$  is twice continuously differentiable on  $[a, b]$ .
- $S$  coincides with a polynomial of degree three on every subinterval  $[t_j, t_{j+1}]$ ,  $j = 1, 2, \dots, n$ .

## 3. Construct the Cubic Spline Function

Cubic spline interpolation function has advantages of good stability, convergence, and high approximation accuracy, which has second-order smoothness at the interpolation nodes and avoids the Runge phenomenon on account of the limitation of the interpolation condition. So we hope to replace the integrand  $f$  in (3) by the constructed cubic spline function  $S(t)$ . Meanwhile  $S(t)$  satisfies the interpolation conditions,  $y_j = f(x_j, t_j)$  ( $j = 1, 2, \dots, n$ ),  $S(t_j) = y_j$ ,  $j = 1, 2, \dots, n$ , and  $\{t_j\}$  are isometric interpolation nodes. The corresponding boundary conditions are as follows [14]:

- The first boundary condition is as follows:  $S'(t_1) = f'_1$ ,  $S'(t_n) = f'_n$ .
- The second boundary condition is as follows:  $S''(t_1) = f''_1$ ,  $S''(t_n) = f''_n$ , or more special condition  $S''(t_1) = S''(t_n) = 0$ .

The spline function  $S(t)$  is expressed by second derivative value of cubic spline function  $S''(t_j) = m_j$ ,  $j = 1, 2, \dots, n$ . The polynomial  $S''(t)$  is less than three order on the interval  $[t_j, t_{j+1}]$  and it is a linear polynomial in particular; more specifically,

$$S''(t) = m_j \frac{t_{j+1} - t}{h_j} + m_{j+1} \frac{t - t_j}{h_j}, \quad (5)$$

$$t_j \leq t \leq t_{j+1}, \quad h_j = t_{j+1} - t_j.$$

The integration constant is acquired by integrating the above equation twice and utilizing interpolation condition. And then the cubic spline function is constructed as follows:

$$\begin{aligned}
 S(t) = & m_j \frac{(t_{j+1} - t)^3}{6h_j} + m_{j+1} \frac{(t - t_j)^3}{6h_j} \\
 & + \left( y_j - \frac{m_j h_j^2}{6} \right) \frac{t_{j+1} - t}{h_j} \\
 & + \left( y_{j+1} - \frac{m_{j+1} h_j^2}{6} \right) \frac{t - t_j}{h_j},
 \end{aligned} \quad (6)$$

where  $m_j$  ( $j = 1, 2, \dots, n$ ) are unknown. Thankfully,  $m_j$  are obtained by adopting the first and second boundary condition. As the expression of  $S(t)$  is different on the interval  $[t_{j-1}, t_j]$  and  $[t_j, t_{j+1}]$ , we also ensure its smoothness at nodes  $t_j$ , namely, the smooth condition on the interpolation nodes:  $S'_j(t_j - 0) = S'_j(t_j + 0)$ . The tridiagonal equations about  $m_j$  can be obtained from the above conditions. The equations have a unique solution due to the fact that coefficient matrix of the equations is diagonally dominant matrix. We can obtain  $m_j$  based on pursuing method [15] and then put  $m_j$  into (6); the cubic spline interpolation function  $S(t)$  is acquired at last.

#### 4. Theoretical Results

**Theorem 3.** *If the integrand in (3) is replaced by the constructed cubic spline function (6), then the relationship of states at adjacent moment can be approximately represented as*

$$x_{j+1} \approx x_j + \frac{h_j^2}{12} (m_j + m_{j+1}) \left( \frac{h_j}{2} - 1 \right) + f_j. \quad (7)$$

*Proof.* Now, the integrand in (3) is approximated by  $S(t)$ ,  $t_j$  are interpolation nodes, and  $h_j = t_{j+1} - t_j$ ; then

$$\begin{aligned}
 x(t_{j+1}) - x(t_j) &= \int_{t_j}^{t_{j+1}} f(x(t), t) dt \approx \int_{t_j}^{t_{j+1}} S(t) dt \\
 &= \int_{t_j}^{t_{j+1}} \left[ m_j \frac{(t_{j+1} - t)^3}{6h_j} + m_{j+1} \frac{(t - t_j)^3}{6h_j} \right. \\
 &\quad + \left( y_j - \frac{m_j h_j^2}{6} \right) \frac{t_{j+1} - t}{h_j} \\
 &\quad \left. + \left( y_{j+1} - \frac{m_{j+1} h_j^2}{6} \right) \frac{t - t_j}{h_j} \right] dt = \int_{t_j}^{t_{j+1}} m_j \\
 &\quad \cdot \frac{(t_{j+1} - t)^3}{6h_j} dt + \int_{t_j}^{t_{j+1}} m_{j+1} \frac{(t - t_j)^3}{6h_j} dt + \int_{t_j}^{t_{j+1}} \left( y_j \right. \\
 &\quad \left. - \frac{m_j h_j^2}{6} \right) \frac{t_{j+1} - t}{h_j} dt + \int_{t_j}^{t_{j+1}} \left( y_{j+1} - \frac{m_{j+1} h_j^2}{6} \right)
 \end{aligned}$$

$$\begin{aligned}
 \cdot \frac{t - t_j}{h_j} dt &= \frac{h_j^3}{24} (m_j + m_{j+1}) + y_j - \frac{h_j^2}{12} (m_j \\
 &+ m_{j+1}) = \frac{h_j^2}{12} (m_j + m_{j+1}) \left( \frac{h_j}{2} - 1 \right) + y_j.
 \end{aligned} \quad (8)$$

According to interpolation condition  $y_j = f(x(t_j), t_j)$ , then

$$\begin{aligned}
 x(t_{j+1}) - x(t_j) &\approx \frac{h_j^2}{12} (m_j + m_{j+1}) \left( \frac{h_j}{2} - 1 \right) \\
 &+ f(x(t_j), t_j).
 \end{aligned} \quad (9)$$

In the approximate equality equation (9),  $x(t_j)$  is replaced by  $x_j$ ,  $f$  is represented by  $f_j$ , and then

$$x_{j+1} \approx x_j + \frac{h_j^2}{12} (m_j + m_{j+1}) \left( \frac{h_j}{2} - 1 \right) + f_j. \quad (10)$$

□

**Theorem 4.** *If  $S$  is a kind of cubic spline function as form (6), then the nonlinear dynamic system  $f$  can be approximated by  $S$  with the error:*

$$R(t) = S(t) - f(t) \leq \frac{1}{6} h^4 \omega(f^{(4)}, h) - \frac{h^4}{24} f^{(4)}(t), \quad (11)$$

where  $0 \leq u \leq 1$ ,  $t \in [t_j, t_{j+1}]$ ,  $j = 1, 2, \dots, n$ , and step length  $h > 0$ .

*Proof.* According to (6) and Peano theorem [16], we can know that if  $f \in C^4[0, 1]$ ,  $t \in [t_j, t_{j+1}]$ , then  $f(x, t)$  is given by

$$\begin{aligned}
 f(x, t) &= \left( f_j'' - \frac{h^2}{12} f_j^{(4)} \right) \frac{(t_{j+1} - t)^3}{6h} + \left( f_{j+1}'' - \frac{h^2}{12} \right. \\
 &\quad \cdot f_{j+1}^{(4)} \left. \right) \frac{(t - t_j)^3}{6h} + \left[ f_j - \frac{h^2}{6} \left( f_j'' - \frac{h^2}{12} f_{j+1}^{(4)} \right) \right] \\
 &\quad \cdot \frac{(t_{j+1} - t)}{h} + \left[ f_{j+1} - \frac{h^2}{6} \left( f_{j+1}'' - \frac{h^2}{12} f_{j+1}^{(4)} \right) \right] \\
 &\quad \cdot \frac{(t - t_j)}{h} \\
 &\quad - \int_0^1 [(t_{j+1} - v)^3 - h^2 (t_{j+1} - v)] \cdot f^{(4)}(v) dv \\
 &\quad \cdot \frac{(t - t_j)}{6h} \left. \right] + \frac{1}{6} \int_0^1 (t - v)^3 f^{(4)}(v) dv \\
 &\quad + \frac{h}{72} [(t - t_j)^3 - (t - t_j) h^2] (f_{j+1}^{(4)} - f_j^{(4)}) + \frac{h^2}{24} (t \\
 &\quad - t_j)^2 f_j^{(4)} - \frac{h^3}{24} (t - t_j)^2 f_j^{(4)} - \int_0^1 (t_{j+1} - v)
 \end{aligned}$$

$$\begin{aligned}
& \cdot f^{(4)}(v) dv \frac{(t-t_j)^3}{6h}, \\
R(t) = S(t) - f(t) &= \frac{h^2}{6} \bar{m}_j [(1-u)^3 - (1-u)] + \frac{h^2}{6} \\
& \cdot \bar{m}_{j+1} (u^3 - u) + \frac{h^4}{6} \int_0^1 (u-v)^3 f^{(4)}(t_j + hv) dv \\
& + \frac{h^4 u^3}{6} \int_0^1 (1-v) f^{(4)}(t_j - hv) dv + \frac{h^4}{6} u \\
& \cdot \int_0^1 [(1-v)^3 - (1-v) f^{(4)}(t_j + hv)] dv \\
& - \frac{h^4}{72} (u^3 - u) (f_{j+1}^{(4)} - f_j^{(4)}) + \frac{h^4}{24} (u - u^2) f_j^{(4)} \\
& = \frac{h^2}{6} \bar{m}_j [(1-u)^3 - (1-u)] + \frac{h^2}{6} \bar{m}_{j+1} (u^3 - u) \\
& + \frac{h^4}{6} \int_0^1 [(u-v)^3 - u^3 (1-v)] \\
& \cdot [f^{(4)}(t_j + hu) - f^{(4)}(t_j + hv)] dv + \frac{h^4}{6} \\
& \cdot u \int_0^1 (v^3 - v) [f^{(4)}(t_j - hv) - f^{(4)}(t_j)] dv \\
& + \frac{h^4}{24} u^2 [f^{(4)}(t_{j+1}) - f^{(4)}(t_j)] - \frac{h^4}{72} (u^3 - u) \\
& \cdot [f_{j+1}^{(4)}(t_{j+1}) - f_j^{(4)}(t_j)] - \frac{h^4}{24} f^{(4)}(t) (u^4 - 2u^3 \\
& + u^2) = -\frac{h^4}{24} f^{(4)}(t) (u^4 - 2u^3 + u^2) + \frac{h^4}{24} \\
& \cdot w(f^{(4)}, h) \theta_j(t) \left[ -u^4 - \frac{5}{3} u^3 - \frac{5}{3} u^2 + 4u \right]. \tag{12}
\end{aligned}$$

Due to the fact that integral form is very complicated and  $\theta_j(t)$  does not have specific expression,  $|\theta_j(x)| \leq 1$  can be estimated. When  $0 \leq u \leq 1$ ,  $0 \leq -u^4 - 5/3u^3 - 5/3u^2 + 4u \leq 4$ , and  $0 \leq u^4 - 2u^3 + u^2 \leq 1$ , hence it may be

$$\begin{aligned}
R(t) &= S(t) - f(t) \\
&= -\frac{h^4}{24} f^{(4)}(t) (u^4 - 2u^3 + u^2) \\
&+ \frac{h^4}{6} w(f^{(4)}, h) \phi_{j,0}(t), \tag{13}
\end{aligned}$$

where  $\phi_{j,0}(t) = 1/4\theta_j(t)[-u^4 - 5/3u^3 - 5/3u^2 + 4u]$  and  $|\phi_{j,0}| \leq 1$ .

And finally,  $R(t) \leq 1/6h^4 w(f^{(4)}, h) - 1/24h^4 f^{(4)}(t)$ .  $\square$

Next, the second-order smoothness property of spline function [17] is given below.

**Theorem 5.** The cubic spline function  $S(t)$  defined on interval  $[a, b]$  meets interpolation condition  $S(x_j) = y_j$ ,  $j = 1, 2, \dots, n$ . Then the function  $f(x) \in C^n[a, b]$  satisfies the above condition:  $f(x_j) = y_j$ ,  $j = 1, 2, \dots, n$ .

We have that

$$\int_a^b [S^{(n)}(x)]^2 dx \leq \int_a^b [f^{(n)}(x)]^2 dx. \tag{14}$$

Meanwhile,  $\int_a^b [S^{(n)}(x)]^2 dx = \int_a^b [f^{(n)}(x)]^2 dx$  if and only if  $f(x) \equiv S(x)$ .

*Proof.* We prove Theorem 5 by proving

$$\int_{x_1}^{x_n} [S^{(n)}(x)]^2 dx \leq \int_{x_1}^{x_n} [f^{(n)}(x)]^2 dx. \tag{15}$$

Obviously,

$$\begin{aligned}
& \int_{x_1}^{x_n} [f^{(n)}(x)]^2 dx \\
&= \int_{x_1}^{x_n} [S^{(n)}(x)]^2 dx + \int_{x_1}^{x_n} [f^{(n)}(x) - S^{(n)}(x)]^2 dx \\
&+ 2 \int_{x_1}^{x_n} S^{(n)}(x) [f^{(n)}(x) - S^{(n)}(x)]^2 dx. \tag{16}
\end{aligned}$$

We use integral subsection integration such that

$$\begin{aligned}
& 2 \int_{x_1}^{x_n} S^{(n)}(x) [f^{(n)}(x) - S^{(n)}(x)]^2 dx \\
&= 2(-1)^{n-1} \sum_{j=1}^{n-1} \int_{x_j}^{x_{j+1}} S^{(2n-1)}(x) [f'(x) - S'(x)] dx, \tag{17}
\end{aligned}$$

where  $S^{(2n-1)}(x)$  are constants on every interval  $(x_j, x_{j+1})$  and  $f(x) - S(x) = 0$  at interval endpoints  $x_j, x_{j+1}$ .

Consequently,

$$\begin{aligned}
\int_{x_1}^{x_n} [f^{(n)}(x)]^2 dx &= \int_{x_1}^{x_n} [S^{(n)}(x)]^2 dx \\
&+ \int_{x_1}^{x_n} [f^{(n)}(x) - S^{(n)}(x)]^2 dx. \tag{18}
\end{aligned}$$

Namely,  $\int_{x_1}^{x_n} [S^{(n)}(x)]^2 dx \leq \int_{x_1}^{x_n} [f^{(n)}(x)]^2 dx$ .

Let  $n = 2$  in Theorem 5; we can obtain

$$\int_a^b [S''(x)]^2 dx \leq \int_a^b [f''(x)]^2 dx. \tag{19}$$

$\square$

The next section will cover two numerical examples, and the result reflects the advantages of cubic spline function in solving the nonlinear dynamic system.

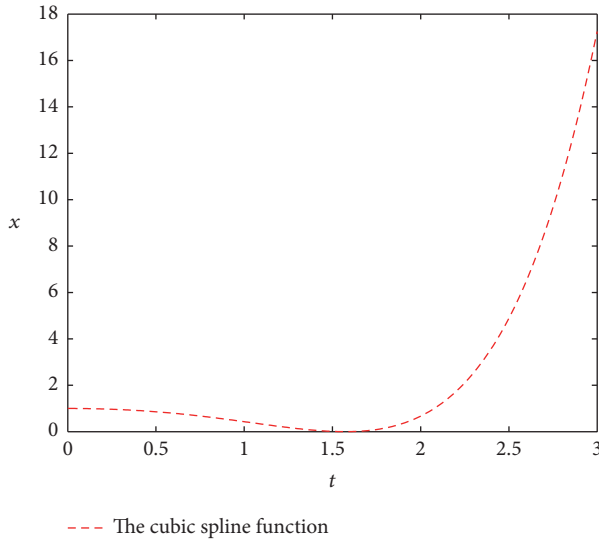


FIGURE 1: The curve of cubic spline interpolation function.

TABLE 1: Mean square errors of several numeric methods for first-order nonlinear dynamic system.

Numeric method	Mean square error
Fourth-order Runge-Kutta method	$1.2415 \times 10^{-4}$
Trapezoid method	$9.1020 \times 10^{-3}$
Euler method	$1.6205 \times 10^{-2}$
Cubic spline function	$8.0240 \times 10^{-5}$

### 5. Numerical Results

*Example 1.* Given a nonlinear dynamic system with an initial value (20), then we solve the numeric solution by using a variety of methods and compare them.

$$\begin{aligned}
 x' &= x - e^t \cos t, \\
 x(0) &= 1, \\
 0 &\leq t \leq 3.
 \end{aligned}
 \tag{20}$$

The numeric curve of cubic spline interpolation function is shown in Figure 1, and the approximate solution and exact solution of nonlinear dynamic system based on cubic spline interpolation function are given in Figure 2.

In the next moment, we solve numeric solution by adopting fourth-order Runge-Kutta method, trapezoidal algorithm, and Euler method and then comparing with cubic spline interpolation function. The mean square error and the curve of numeric method are given at last; specifically see Table 1 and Figure 3.

The curves of different approximation level by several numeric methods are shown in Figure 3.

Furthermore, in order to observe approximation accuracy of nonlinear dynamic system by different numeric methods intuitively, Figure 3(a) has been magnified in different proportions, and then we can obtain Figures 3(b), 3(c), 3(d), 3(e), and 3(f). We can find out Euler method

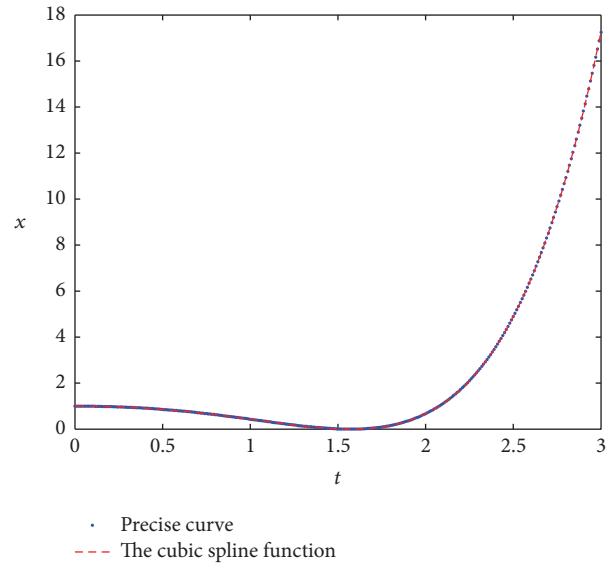


FIGURE 2: The approximate solution and precise curve.

TABLE 2: Mean square errors of several numeric methods for the second-order nonlinear dynamic system.

Numeric method	Mean square error
Fourth-order Runge-Kutta method	0.1662
Euler method	0.5479
Adams algorithm	0.3792
Cubic spline interpolation function	0.0179

has low approximate accuracy and is great in error. The precision of the fourth-order Runge-Kutta method is also high and the calculation speed is better than trapezoidal algorithm. Although we can intuitively observe that fourth-order Runge-Kutta method has good precision compared to other methods, which is inferior to the proposed method in this paper from Figure 3.

*Example 2.* A second-order nonlinear dynamic system

$$\begin{aligned}
 x'' + x &= 2e^{-x}(x - 1), \\
 x(0) &= 1, \\
 x'(0) &= 1, \\
 0 &\leq x \leq 10,
 \end{aligned}
 \tag{21}$$

is considered, and we solve the numeric solution of the system. Next, several different numeric methods will be used to solve this system; mean square errors and the curves of numeric approximation will be given at last, specifically shown in Table 2 and Figure 4.

It can be seen from Figure 4 that the approximation ratio of second-order nonlinear dynamic system based on cubic spline interpolation function is better than other numeric methods, which avoids the Runge phenomenon on account of the limitation of the interpolation condition. It can approach

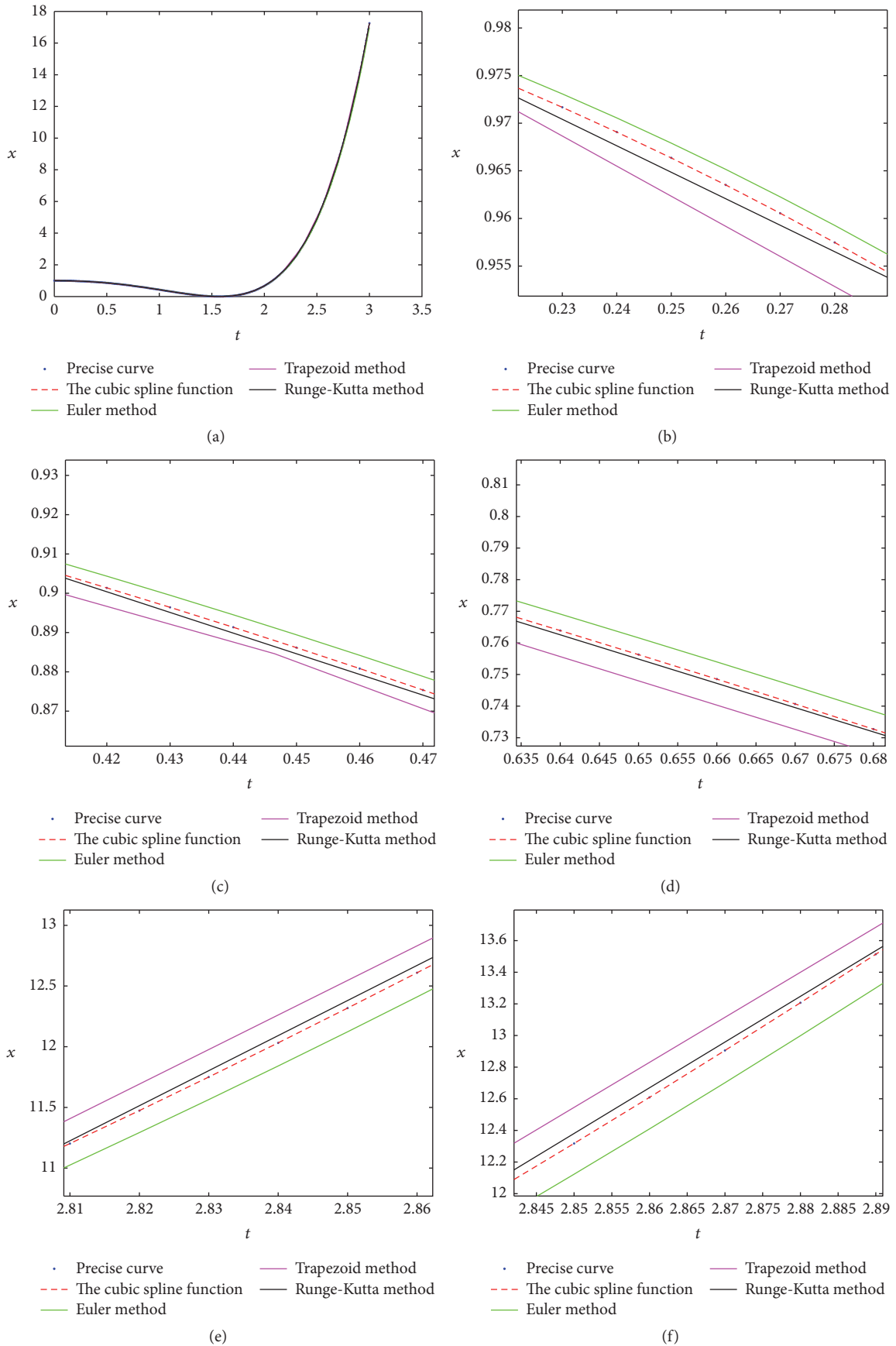


FIGURE 3: The different approximation level of several numeric methods. Note: (b), (c), (d), (e), and (f) are obtained from (a), which has been magnified in different proportions.

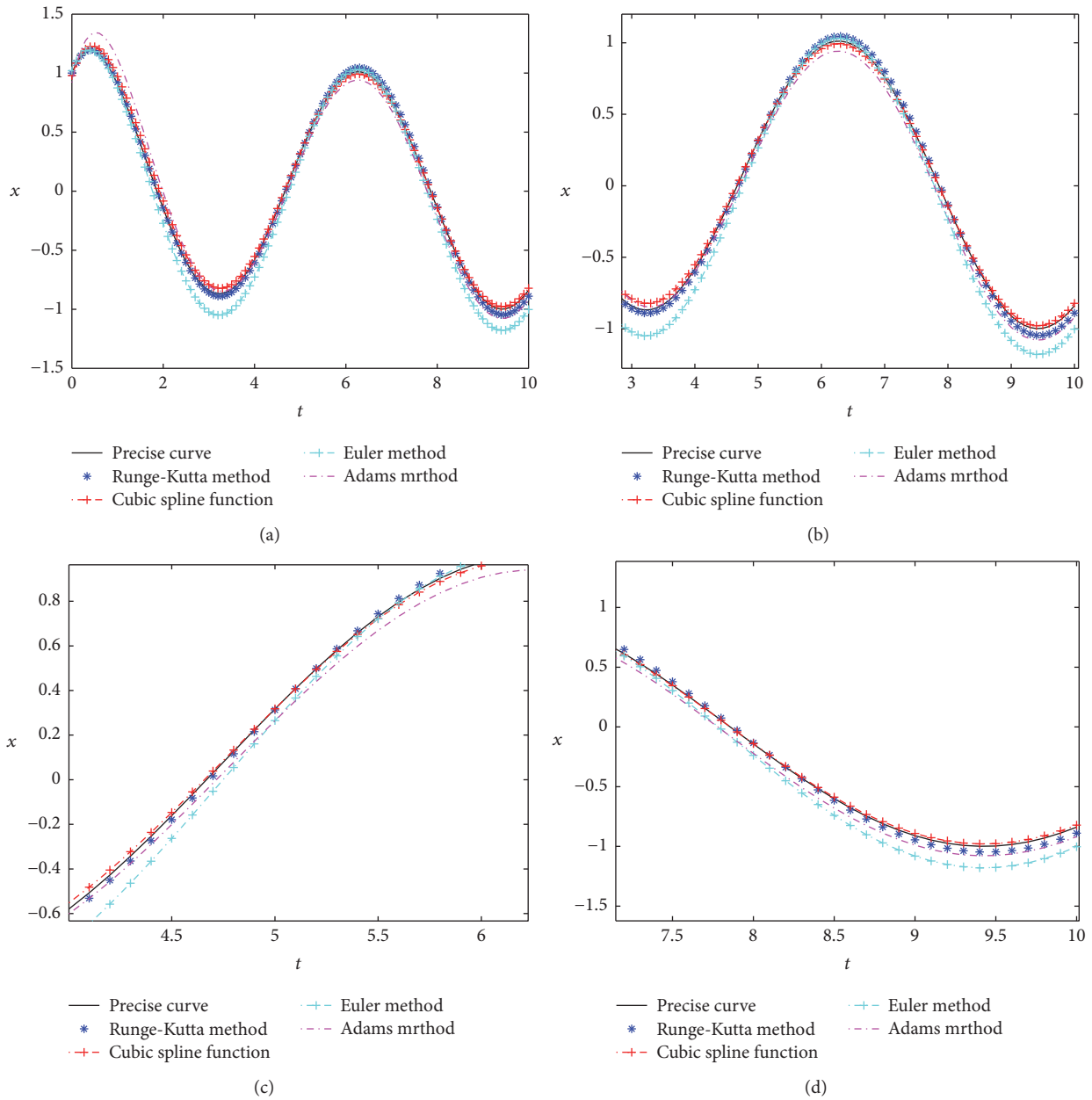


FIGURE 4: The numeric approximation curves by different methods. Note: (b), (c), and (d) are obtained from (a), which has been magnified to some extent.

the analytic solution of second-order nonlinear dynamic system with a high degree and is simple in calculation.

### 6. Conclusions and Prospects

We have discussed the numerical method based on cubic spline interpolation function to solve the numeric solution of nonlinear dynamic system in this paper. The basic theories and knowledge are introduced primarily. In the next moment, the cubic spline function is constructed according to the boundary conditions and some theory results are also given. Finally, we also demonstrate two numerical examples to reveal the effectiveness of the method proposed in this paper.

The results indicate that the proposed method based on cubic spline interpolation function is obviously advantageous compared with other methods, which has quick calculation speed and avoids the Runge phenomenon.

We finish this paper with the following prospects:

- (a) We only give the upper approximation of the constructed cubic spline function in this paper. Therefore, we hope to study the lower approximation in the further study.
- (b) The main theories only applied to first- and second-order systems, but there are many of the more complex systems in actual engineering. Consequently, it is

interesting and significant to extend the main theories in this paper to higher order nonlinear dynamic system.

## Competing Interests

The authors declare that they have no competing interests.

## Acknowledgments

This work was supported by the National Natural Science Foundation of China (Grant nos. 11261042 and 61662060).

## References

- [1] G. Chen and J. L. Moiola, "An overview of bifurcation, chaos and nonlinear dynamics in control systems," *Journal of the Franklin Institute*, vol. 331, no. 6, pp. 819–858, 1994.
- [2] A. Farshidianfar and A. Saghafi, "Global bifurcation and chaos analysis in nonlinear vibration of spur gear systems," *Nonlinear Dynamics*, vol. 75, no. 4, pp. 783–806, 2014.
- [3] L. V. Stepanova and S. A. Igonin, "Perturbation method for solving the nonlinear eigenvalue problem arising from fatigue crack growth problem in a damaged medium," *Applied Mathematical Modelling*, vol. 38, no. 14, pp. 3436–3455, 2014.
- [4] J. Giné, J. Llibre, K. Wu, and X. Zhang, "Averaging methods of arbitrary order periodic solutions and integrability," *Journal of Differential Equations*, vol. 260, no. 5, pp. 4130–4156, 2016.
- [5] H. de la Cruz, R. J. Biscay, J. C. Jimenez, and F. Carbonell, "Local linearization—Runge–Kutta methods: a class of A-stable explicit integrators for dynamical systems," *Mathematical and Computer Modelling*, vol. 57, no. 3-4, pp. 720–740, 2013.
- [6] C. M. Duque and M. P. Almeida, "The Euler-Galerkin finite element method for a non-local coupled system of reaction diffusion type," *Applied Mathematics and Computation*, vol. 296, pp. 116–126, 2016.
- [7] Y. H. Dai and Y. Yuan, "A nonlinear conjugate gradient method with a strong global convergence property," *SIAM Journal on Optimization*, vol. 10, no. 1, pp. 177–182, 1999.
- [8] D. A. Mâceş and M. A. Stadtherr, "Computing fuzzy trajectories for nonlinear dynamic systems," *Computers and Chemical Engineering*, vol. 52, pp. 10–25, 2013.
- [9] J. Guckenheimer and P. Holmes, *Nonlinear Oscillations, Dynamical Systems and Bifurcations of Vector Fields*, Springer, New York, NY, USA, 2013.
- [10] O. Blasco, "Modulus of continuity with respect to semigroups of analytic functions and applications," *Journal of Mathematical Analysis and Applications*, vol. 435, no. 1, pp. 616–626, 2016.
- [11] F. R. Loscalzo and T. D. Talbot, "Spline function approximations for solutions of ordinary differential equations," *SIAM Journal on Numerical Analysis*, vol. 4, no. 3, pp. 433–445, 1967.
- [12] A. Bellour, D. Sbibi, and A. Zidna, "Two cubic spline methods for solving Fredholm integral equations," *Applied Mathematics and Computation*, vol. 276, no. 5, pp. 1–11, 2016.
- [13] B. Sepehrian and M. K. Radpoor, "Numerical solution of nonlinear Fokker-Planck equation using finite differences method and the cubic spline functions," *Applied Mathematics and Computation*, vol. 262, pp. 187–190, 2015.
- [14] V. Baramidze, "Smooth bivariate shape-preserving cubic spline approximation," *Computer Aided Geometric Design*, vol. 44, pp. 36–55, 2016.
- [15] D. Wang, G. G. Wang, and G. F. Naterer, "Collaboration pursuing method for multidisciplinary design optimization problems," *AIAA Journal*, vol. 45, no. 5, pp. 1091–1103, 2007.
- [16] P. Hájek and M. Johaniš, "On Peano's theorem in Banach spaces," *Journal of Differential Equations*, vol. 249, no. 12, pp. 3342–3351, 2010.
- [17] Z. Chungang and W. Renhong, "Functional splines with differential degree of smoothness and their applications," *Computer Aided Design*, vol. 40, no. 5, pp. 616–624, 2008.

## Research Article

# The Application of Nonordinary, State-Based Peridynamic Theory on the Damage Process of the Rock-Like Materials

X. B. Gu<sup>1</sup> and Q. H. Wu<sup>2</sup>

<sup>1</sup>*School of Civil Engineering, Sichuan University of Science & Engineering, Sichuan, China*

<sup>2</sup>*School of Architecture and Civil Engineering, Chengdu University, Chengdu, China*

Correspondence should be addressed to X. B. Gu; 15823405952@163.com

Received 30 May 2016; Revised 3 August 2016; Accepted 16 August 2016

Academic Editor: Ninshu Ma

Copyright © 2016 X. B. Gu and Q. H. Wu. This is an open access article distributed under the Creative Commons Attribution License, which permits unrestricted use, distribution, and reproduction in any medium, provided the original work is properly cited.

Peridynamics has a great advantage over modeling the damage process of rock-like materials, which is assumed to be in a continuum interaction with each other across a finite distance. In the paper, an approach to incorporate classical elastic damage model in the nonordinary, state-based peridynamics is introduced. This method can model the dynamic damage process and stress change of rock-like materials. Then two instances about three-point bend experiment are simulated in the rock-like materials. Finally the conclusions are drawn that numerical results are close to the experimental results. So the method has a great predictable value in the geotechnical engineering.

## 1. Introduction

The rock-like material is a quasibrittle material; it is widely applied to the geotechnical engineering, for example, tunnels and lots of other underground buildings. Especially for the mountain area, the research on the damage process of rock-like materials is essential, so the prediction for the damage process of rock-like materials becomes a focus problem gradually. But it is difficult to model because the mechanical character of rock-like materials is very complex and the precise damage prediction of rock-like materials is elusive. In the geotechnical engineering, the rock-like mass includes lots of tiny cracks, even before the load is applied. The damage process of the rock-like materials is often caused by tension, compression, the change of the temperature, and so on, and the stress and displacement fields are influenced by the propagation and coalescence of the crack. Even through the damage process of rock-like materials has been investigated for many years, the damage mechanism and prediction of rock-like material are still not understood. In fact, the damage process of rock-like materials includes the initiation, propagation,

and coalescence of the crack, which will lead to a sudden collapse due to brittle damage. How to model the damage character of the rock-like materials has brought great challenge.

Over the past decades, many methods are put forward to model the damage process of rock-like materials. In the finite element-based method, singular crack-tip elements are frequently encountered [1]. Because of the crack-tip stress singularity, an external fracture criterion must be introduced to determine propagation and bifurcation of the cracks, and the nucleation question of the crack is still not solved [2]. In order to overcome the above difficulties, the extended finite element theory [3] is proposed to simulate the propagation of cracks. Although many crack questions are solved by virtue of the extended finite element theory, external and bifurcation criterion must still be introduced when displacement is discontinuous and when interaction and bifurcation of multiple cracks are involved. Besides, a series of difficulties are encountered for the problem of the three-dimensional cracks by the XFEM. In order to solve the problems of the three-dimensional cracks, such as interactions among cracks

and branching phenomenon of multiple cracks, meshless methods are developed [4]. The propagation and coalescence process of cracks can be simulated by Smooth Particle Hydrodynamics (SPH); however, the tensile instability problems are still encountered in method of SPH [5]. In order to avoid the aforementioned lacks, peridynamic theory, which is a numerical method based on the nonlocal thoughts, is introduced to model propagation and bifurcation process of cracks.

The peridynamic theory is a nonlocal meshless method; it is put forward by Silling [6], at Sandia National Laboratory. It is assumed that particles in a continuum interact with each other across a finite distance, and it formulates problems in terms of intergral equations rather than partial differential equations [7]. Therefore, the peridynamic method can be applied to model the problems of continuous or discontinuous displacements [8].

After this theory is put forward, it has been widely applied to model the damage process of different materials. Firstly, the theory is applied to model the fracture process of composite material; for example, the fracture processes in laminated composites subjected to low-velocity impact and in woven composites subject to static indentation are predicted by Askari et al. [9] and Colavito et al. [10, 11] and the fatigue crack growth analysis is done in layered heterogeneous material system using peridynamic method by Jung and Soek [12]. In addition, the notched laminated composite under biaxial loads is considered by Xu et al. [13]. Then it is applied to model the fracture process of metal material; for example, Foster et al. [14] use peridynamic viscoplastic theory to model the collapse process of metal and Wu et al. [15, 16] analyze the ductile fracture of metal materials using nonordinary state-based peridynamics. Meanwhile, Sun and Sundararaghavan [17] model the crystal material using the peridynamic plasticity theory. Immediately, it is extended to model the damage of concrete; for example, Gerstle et al. [18] model the damage process of concrete by introducing “micropolar peridynamic model.” The damage results of these materials are rather good by using the peridynamics, but for the geotechnical engineering, rock-like materials are an important material, the peridynamic theory is seldom used to model the damage process of rock-like materials, and only Ha et al. [19] use peridynamics to model the fracturing patterns of rock-like materials in compression, but the stress field description is not considered. In the paper, the application of nonordinary, state-based peridynamics in the damage process of rock-like material will be investigated. Not only the damage process of rock-like materials is described by using the method, but also the change of stress field in the damage process is depicted, so it provides a new idea to model the damage process of rock-like materials by using the peridynamics.

The paper is organized as follows. In Section 2, the state-based peridynamic theory is introduced at first, and the implementation on this method for the specific damage model is discussed. In Section 3, the state-based peridynamic numerical discretization is described. In Section 4, we represent numerical results consisting of (1) the numerical simulation about the three-point bend test of the beam

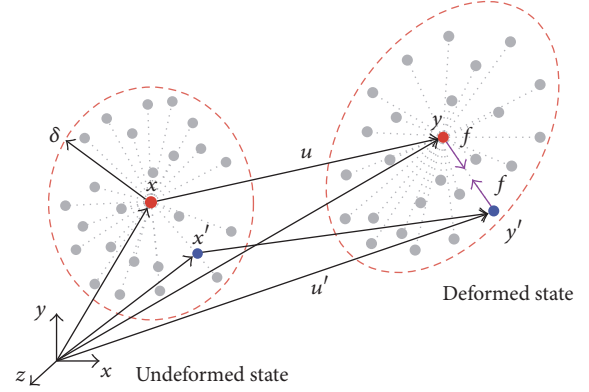


FIGURE 1: The deformation of PD material point.

and (2) the numerical simulation about the three-point bend test of Brazilian disk. In Section 5, conclusions are drawn.

## 2. Model Description

For completeness, nonordinary state-based peridynamics is reviewed briefly; it includes a summary of basic peridynamic equation, the idea of constitutive relation, and its property.

*2.1. Basic Theory.* Peridynamic theory is put forward by Silling [6] at Sandia laboratory in the United States; its basic equation of motion is shown as follows:

$$\begin{aligned} \rho(x) \ddot{u}(x, t) = & \int_H (t_{(k)(j)}(u_{(j)} - u_{(k)}, x_{(j)} - x_{(k)}, t) \\ & - t_{(j)(k)}(u_{(k)} - u_{(j)}, x_{(k)} - x_{(j)}, t)) dH \\ & + b(x, t), \end{aligned} \quad (1)$$

where  $\rho(x)$  is the density of material point  $x$ ,  $H$  is a neighborhood (Figure 1), and  $b(x, t)$  is a prescribed body force density field of material point  $x_{(k)}$  at the instance  $t$ , which represents the external force per unit reference volume square.  $t_{(k)(j)}(u_{(j)} - u_{(k)}, x_{(j)} - x_{(k)}, t)$  and  $t_{(j)(k)}(u_{(k)} - u_{(j)}, x_{(k)} - x_{(j)}, t)$  are the force density vector of material points  $x_{(k)}$  and  $x_{(j)}$ , respectively.

In the neighborhood of point  $x$ , the relative position of any point,  $x'$  and  $x$ , is  $\underline{X}\langle\xi\rangle$ , the deformation state of the bond is defined as  $\underline{Y}\langle x' - x \rangle$ , and they are expressed, respectively, as follows:

$$\begin{aligned} \underline{X}\langle\xi\rangle &= x' - x \\ \underline{Y}\langle x' - x \rangle &= (u' + x') - (u + x). \end{aligned} \quad (2)$$

The nonlocal deformation gradient  $F(x)$  of material point  $x$  is shown as the following expression:

$$F(x) = \left[ \int_H \omega(|\xi|) (\underline{Y}(\xi) \otimes \xi) dV_\xi \right] \cdot K^{-1}(x), \quad (3)$$

where  $\omega(|\xi|)$  is the influence function of the bond. It is the function of the relative origin position  $|\xi|$  between points  $x'$  and  $x$ , and  $K(x)$  is a nonlocal shape tensor defined by

$$K(x) = \left[ \int_H \omega(|\xi|) (\xi \otimes \xi) dV_\xi \right]^{-1}. \quad (4)$$

Alternatively, this integral can be defined without recourse to peridynamic states as follows:

$$F(x, t) = \left[ \int_H \omega(|x' - x|) \cdot ((u' - u) \otimes (x' - x)) dV_\xi \right] \cdot K^{-1}(x) \quad (5)$$

$$K(x) = \left[ \int_H \omega(|x' - x|) ((x' - x) \otimes (x' - x)) dV_\xi \right]^{-1}.$$

The Green-Lagrange strain sensor can be expressed as

$$C = \frac{1}{2} (F^T F - I). \quad (6)$$

The elastic strain energy  $W$  is written as

$$W = \frac{1}{2} C : \psi : C, \quad (7)$$

where  $\psi$  is the fourth-order elastic tensor and is assumed as anisotropic with cubic symmetry.

$$\psi_{ijkn} = \psi_{ijnk} = \psi_{knij} = \psi_{jikn}. \quad (8)$$

From (7), the second Piola-Kirchhoff stress is written as

$$S = \frac{\partial W}{\partial E} = \psi : C. \quad (9)$$

And Cauchy stress is found:

$$\sigma = F \left( \frac{S}{\det(F)} \right) F^T. \quad (10)$$

The first Piola-Kirchhoff stress can be written from the Cauchy stress as

$$\bar{P} = \det(F) \sigma F^{-T}. \quad (11)$$

Equation (9) is substituted into (10); the expression of the first Piola-Kirchhoff stress is rewritten as

$$\bar{P} = FS. \quad (12)$$

Peridynamic force vector state  $\underline{t}[x, t]\langle \xi \rangle$  can be expressed by the traditional stress state as

$$\underline{t}\langle x' - x \rangle = \omega(|x' - x|) \bar{P} \cdot K(x) \cdot \xi. \quad (13)$$

Substituting (12) into (13), (14) can be obtained as follows:

$$\underline{t}\langle x' - x \rangle = \omega(|x' - x|) FS \cdot K(x) \cdot \xi. \quad (14)$$

From equations (1) and (14), the basic equation in the nonordinary, state-based peridynamics can be written as

$$\begin{aligned} \rho(x_i) \ddot{u}(x_i, t) &= \int_H \omega(|x_i - x_j|) \\ &\cdot \{F_i S_i K_i^{-1}(x_j - x_i) - F_j S_j K_j^{-1}(x_i - x_j)\} dV_j \\ &+ b(x_i, t). \end{aligned} \quad (15)$$

**2.2. Damage Correspondence.** To describe the damage correspondence within the peridynamic framework, the influence function  $\omega(|x_i - x_j|)$  is introduced to represent the damage; it can be expressed as follows:

$$\omega(|x_i - x_j|) = \chi(t, \xi) \left( 1 + \frac{\delta}{|\varepsilon|} \right), \quad (16)$$

where  $\delta$  is the horizontal radius of material point  $x_i$ ,  $\varepsilon = x' - x$  is the relative displacement of any point  $x'$  and point  $x$ ,  $\chi(t, \xi)$  is a scalar function, and its expression is given:

$$\chi(t, \xi) = \begin{cases} 1 & (s(t, \xi) < s_0) \\ 0 & (s(t, \xi) > s_0), \end{cases} \quad (17)$$

where  $s$  is the stretch of the bond; it is defined as

$$s = \frac{|\varepsilon + \eta| - |\varepsilon|}{|\varepsilon|}. \quad (18)$$

$s_0$  is critical stretch; in two dimensions it is defined as [20]

$$s_0 = \sqrt{\frac{G_c}{[6\mu/\pi + 16(\kappa - 2\mu)/(9\pi^2)]\delta}}, \quad (19)$$

where  $\kappa$  is volume modulus,  $\mu$  is the shear modulus,  $G_c$  is the critical energy dissipating ratio, and it is related to the fracture toughness  $K_{IC}$ .

To model the problem of damage, the concept of local damage value is introduced; it is defined as

$$\varphi(x, t) = 1 - \frac{\int_H \chi(x, t, \varepsilon) dV}{\int_H dV_\varepsilon}, \quad (20)$$

where  $\varphi(x, t)$  is local damage value; its limitation is  $0 \leq \varphi(x, t) \leq 1$ , where 0 represents original materials and 1 represents complete disconnection of a point from all of the points with which it initially interact.

### 3. The Discretization

The region is discretized into nodes, each with a known volume in the reference configuration; taken together, the nodes

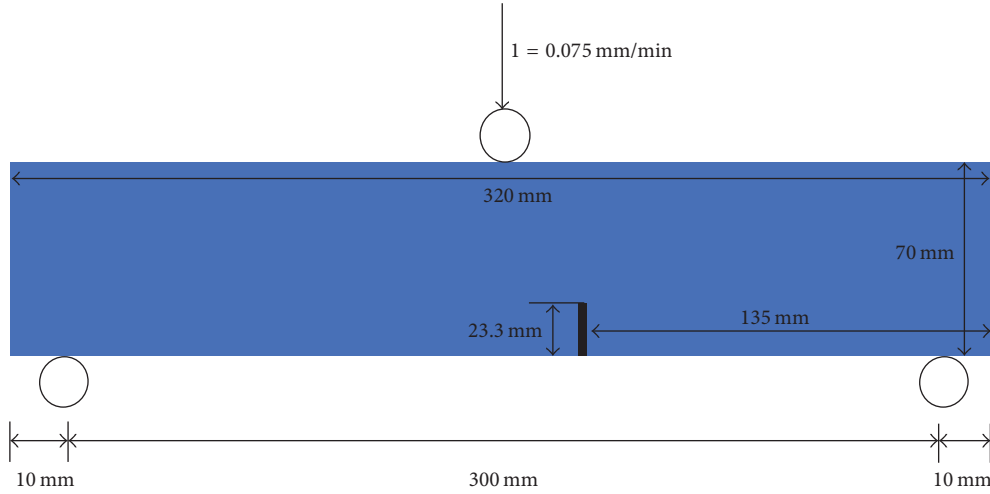


FIGURE 2: The geometric configuration.

form a grid. So the deformation gradient  $F(x)$  is discretized into the following form:

$$F_j = \sum_{i=1}^{N_j} V_i \omega(|x_i - x_j|) (y_i - y_j) \otimes (x_i - x_j) \cdot K_j^{-1}, \quad (21)$$

where a nonlocal shape sensor  $K(x)$  is discretized as

$$K_j = \sum_{i=1}^{N_j} V_i \omega(|x_i - x_j|) (x_i - x_j) \otimes (x_i - x_j), \quad (22)$$

where  $V_i$  is the volume of nodes  $x_i$ ;  $N_j$  is the magnitude of node  $x_j$  in the range of horizontal radius  $\delta$  of the node  $x_j$ .

Likewise, the discretization form of basic equation in the nonordinary, state-based peridynamics is shown as follows:

$$\rho(x_i) \ddot{u}_i^n = \sum_{j=1}^{N_i} V_j \omega(|x_j - x_i|) \cdot \{ \overline{P}_i K_i^{-1}(x_j - x_i) - \overline{P}_j K_j^{-1}(x_i - x_j) \}, \quad (23)$$

where  $\overline{P}_i$  and  $\overline{P}_j$  are the first Piola-Kirchhoff stress of nodes  $i$  and  $j$ , respectively,  $K_i$  and  $K_j$  are the shape sensor of the nodes  $i$  and  $j$ .

The acceleration  $\ddot{u}_i^n$  can be shown as

$$\ddot{u}_i^n = \frac{u_i^{n+1} - 2u_i^n + u_i^{n-1}}{\Delta t^2}, \quad (24)$$

where the superscript  $n$  represents the time step and the subscript represents the number of nodes, so  $\ddot{u}_i^n$  represents the acceleration of the node  $x_i$  at time step  $n$ .

#### 4. The Numerical Example

To evaluate the functionality of the proposed state-based peridynamic formulation, the discretized equations were implemented in a Fortran computer code for two-dimensional simulation. The following two examples are investigated, respectively.

**4.1. The Three-Point Bend Test of the Beam.** Three-point bend test [21] has been widely used for characterizing the dynamic response of materials as well as for validating numerical methods in the case of the state-based peridynamic formulation with damage. This test consists of a rectangular concrete beam with a preexisting vertical crack; its geometric configuration is shown in Figure 2. Its length is 0.32 m, the height is 0.07 m, the length of the crack in the beam is 0.0233 m, and the mechanic parameters of the concrete beam are listed as follows: the elastic modulus  $E = 32.8$  GPa, Poisson's ratio  $\nu = 0.25$ , and center point of coordinate axis is positioned in the bottom center of concrete beam.  $x$ -axis is vertical to the pressure, tension is positive, and compression is negative. The concentrated load is positioned at the upper center of the beam. the magnitude of load  $L$  is 0.075 mm/min, the concrete beam model is discretized into  $800 \times 175 = 140000$  particles, the distance between the adjacent two particles is  $\Delta x = 4 \times 10^{-4}$  m, time step  $dt = 1.3367 \times 10^{-8}$  s, the critical stretch  $s_0 = 0.002$ , the density  $\rho = 2650$  kg/m<sup>3</sup>, and  $\delta$  is adopted as  $3\Delta x$ . When it arrives at 25000 time steps, the concrete beam is fractured fully. The computed damage contour of concrete beam is shown in Figure 3, the maximum principal stress  $\sigma$  contour in the damage process of concrete beam is shown in Figure 4, the damage result in specific test is given in Figure 5, and the comparison curve between test and numerical solution is shown in Figure 6.

It can be seen from Figure 3 that, when time arrives at  $1.3367 \times 10^{-4}$  s, the crack begins to initiate along the upper tip; when time arrives at  $2.005 \times 10^{-4}$  s, the crack begins to propagate along the position where the vertical load is applied; when time arrives at  $2.6734 \times 10^{-4}$  s, the crack continues to propagate and elongate along the position where the vertical load is applied, and two support positions in the bottom of concrete beam begin to be damaged; when time arrives at  $3.34175 \times 10^{-4}$  s, the crack propagates to the position where the concentrated load is applied, and the whole concrete beam broke down fully. It can be seen from Figure 4 that, when time arrives at  $1.3367 \times 10^{-4}$  s, the stress concentration

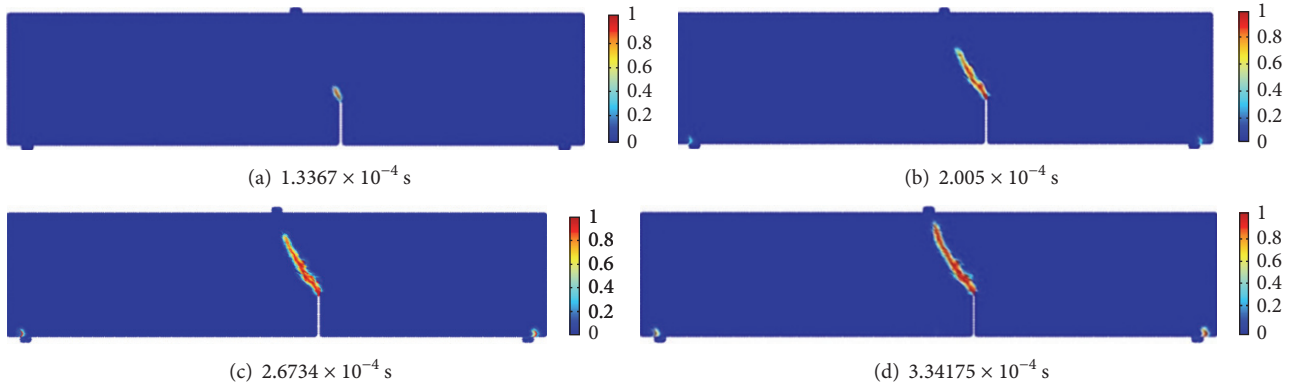


FIGURE 3: The damage contour of the beam.

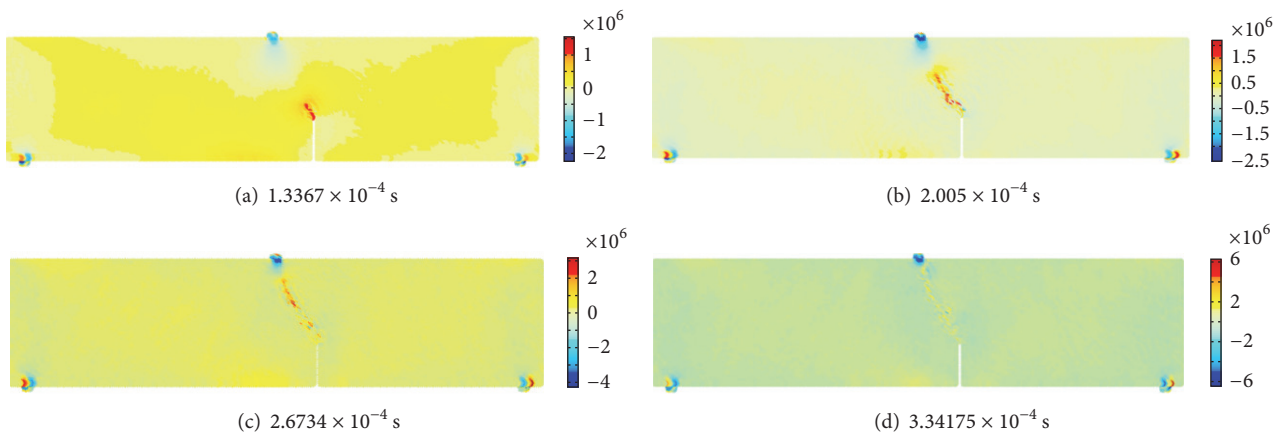


FIGURE 4: The maximum principal stress  $\sigma$  (Pa) contour of the concrete beam.



FIGURE 5: The experimental result of three-point bend in the beam [22].

begins to occur in the tip of crack, the stress concentration phenomenon is found at the position where the concentrated load is applied, and the magnitude of maximum principal stress in the tip of the crack reaches  $1.5 \times 10^6$  Pa; when time arrives at  $2.005 \times 10^{-4}$  s, the stress concentration in the tip of concrete beam continues to propagate to the position where the concentrated load is applied, and the magnitude of maximum principal stress reaches  $3.1 \times 10^6$  Pa; when time arrives at  $3.34175 \times 10^{-4}$  s, the magnitude of the stress in the tip of concrete beam reaches the maximum, whole concrete beam is destroyed fully, the magnitude of the maximum principal stress reaches  $6.02 \times 10^6$  Pa, the numerical result in Figure 3 is close to the experimental observation in Figure 5, and from Figure 6, it can be found that the numerical process in the curve of load versus displacement is consistent with the trend of experimental results. These conclusions

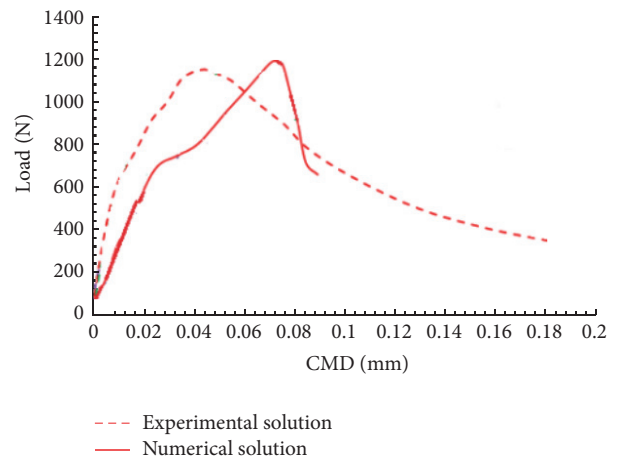


FIGURE 6: Load versus crack mouth displacement (CMD) curves obtained from the extended nonordinary, state-based peridynamic model and experiment.

demonstrate that nonordinary, state-based peridynamics can provide good prediction for the damage process of rock-like materials. In the example, the difference of the damage result between the numerical prediction and experimental

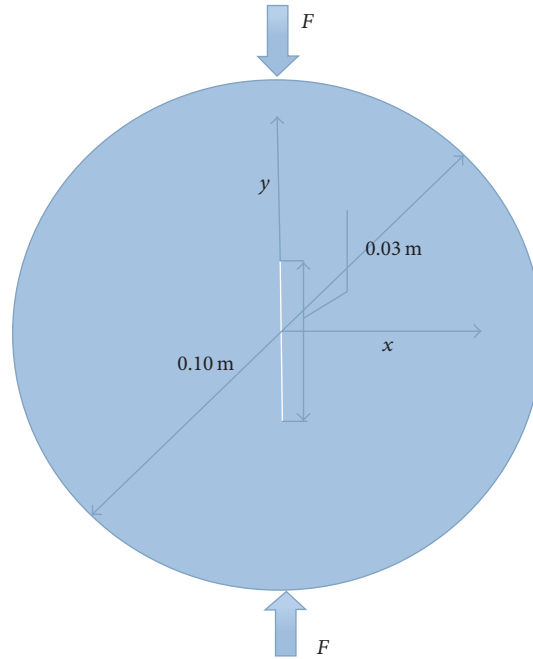


FIGURE 7: The geometric configuration of rock sample.

observation exists, and the constitutive relation of material has important influence on the difference, so the improvement for the constitutive relation of rock-like materials is necessary in my future research. It can not only improve the accuracy of numerical prediction, but also model the large deformation problem by altering the constitutive relation of materials, such as impact damage problem and blast. A critical extension is furnished to solve the problems involving severe deformation and damage by using the method.

**4.2. Failure Simulation of a Brazilian Disk under Compressive Loading.** This test consists of a circular rock sample with a preexisting vertical crack, its geometric configuration is shown in Figure 7, its diameter is 100 mm, there is a crack in the middle of sample, and its inclination angle is  $0^\circ$ . The length of crack is  $2b = 30$  mm, the mechanic parameters in this rock sample are listed as follows: the elastic modulus  $E = 21$  GPa, Poisson's ratio  $\nu = 0.22$ , and center point of coordinate axis is positioned in the center of circular disk.  $x$ -axis is vertical to the pressure, tension is positive, and compression is negative. The compressive load is located at the upper and lower tips of the circular disk and their magnitude is  $0.05$  m/s; rock sample is discretized into  $200 \times 200 = 40000$  particles, the distance between the adjacent two particles is  $\Delta x = 5 \times 10^{-4}$  m, time step  $dt = 1.3367 \times 10^{-8}$  s, the critical stretch  $s_0 = 0.002$ , the density  $\rho = 2300$  kg/m<sup>3</sup>, and  $\delta$  is adopted as  $3\Delta x$ . When it arrives at 700 time steps, the concrete beam is fractured fully. The numerical damage contour of rock sample is shown in Figure 8, the maximum horizontal principal stress  $\sigma_x$  contour is shown in Figure 9, and the damage result in specific test is given in Figure 10.

It can be seen from Figure 8 that, when time arrives at  $4.01 \times 10^{-2}$  s, the upper and lower tips of the crack begin to

initiate; when time arrives at  $6.68 \times 10^{-2}$  s, the crack along its tips continues to propagate; when time arrives at  $9.36 \times 10^{-2}$  s, the crack begins to penetrate along the direction where the concentrated load is applied. The whole rock sample fractures fully. Likewise, it can be seen from Figure 9 that, when time arrives at  $3.34 \times 10^{-2}$  s, the stress concentration in the tips of crack has taken place before the tips of crack begin to initiate, and the magnitude of the maximum principal stress in the tips of crack reaches  $4 \times 10^6$  Pa; when time arrives at  $4.01 \times 10^{-2}$  s, the crack begins to initiate, and the magnitude of the maximum principal stress reaches  $4.5 \times 10^6$  Pa; when time arrives at  $6.68 \times 10^{-2}$  s, the horizontal stress in the tips of crack continues to increase, and its magnitude reaches  $5.5 \times 10^6$  Pa; when time arrives at  $9.36 \times 10^{-2}$  s, the magnitude of the maximum horizontal stress reaches  $7.5 \times 10^6$  Pa; rock sample is fractured fully. The conclusions can be drawn from the comparison between Figures 8 and 10, the numerical results are similar to the experimental ones, and good effect can be obtained for the numerical simulation of the damage process in the rock material by using nonordinary, state-based peridynamic method, so it provides great instructional significance for the prediction of damage process in the future.

## 5. Conclusions

An extension of the state-based peridynamic constitutive correspondence framework to incorporate into elastic damage has been proposed. Then three-point bending simulation is performed with damage process. In two examples, the numerical results are compared with the experimental observation. In conclusion, the suggested method provides a

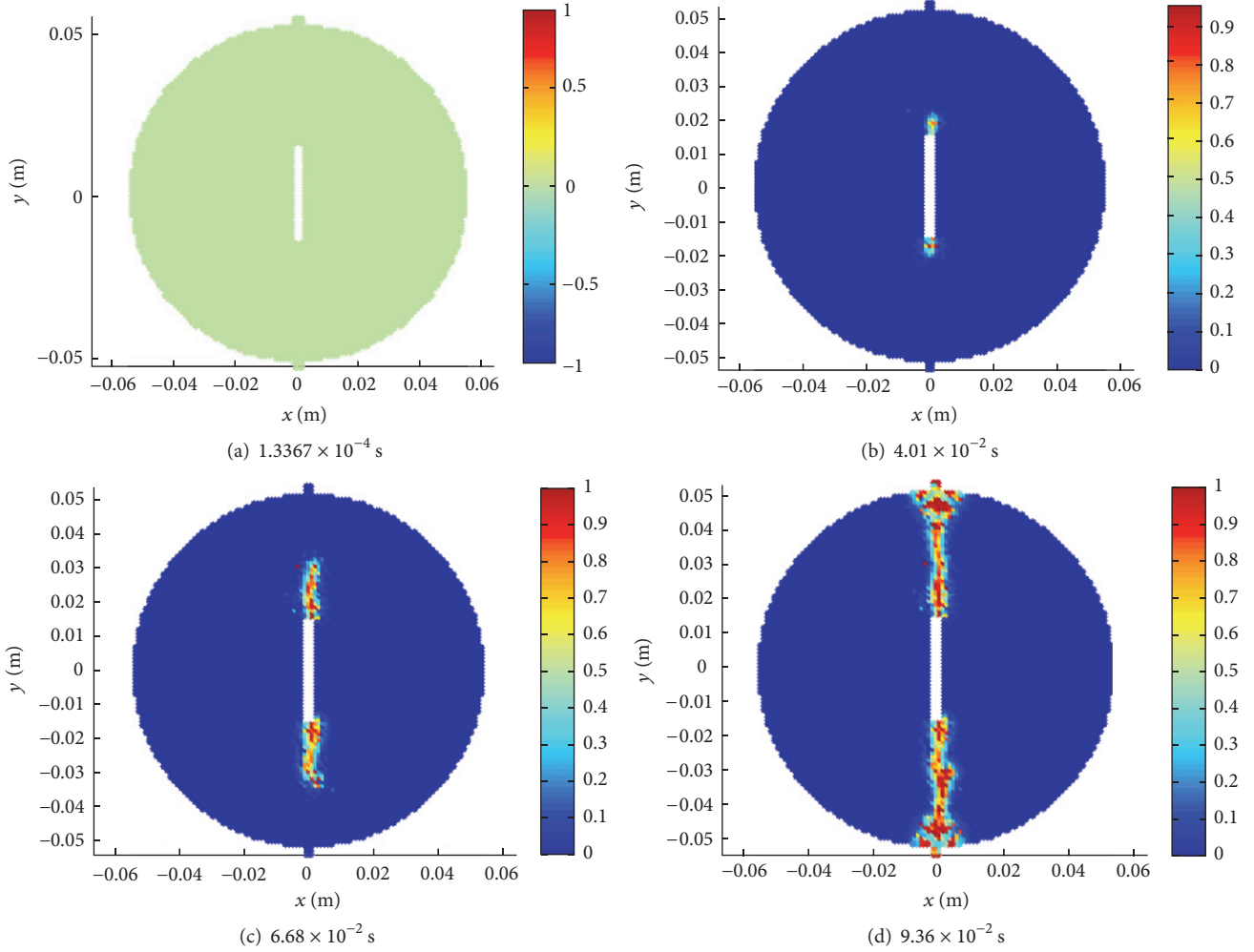


FIGURE 8: The numerical contour about the failure of rock sample.

new thought for the damage process prediction of the rock-like materials.

### Nomenclature

$\rho(x)$ : The density of material point  $x$   
 $b(x, t)$ : The applied body force density of material point  $x$  at the time  $t$   
 $u_{(j)}$ : The displacement of material point  $x_{(j)}$   
 $\xi$ : The relative origin position between material points  $x$  and  $x'$   
 $t_{(k)(j)}(u_{(j)} - u_{(k)}, x_{(j)} - x_{(k)}, t)$ : The force density vector of material point  $x_{(k)}$   
 $t_{(j)(k)}(u_{(k)} - u_{(j)}, x_{(k)} - x_{(j)}, t)$ : The force density vector of material point  $x_{(j)}$   
 $\underline{X}(\xi)$ : The relative position of points  $x'$  and  $x$   
 $\underline{Y}(x' - x)$ : The deformation state of the bond between material points  $x$  and  $x'$   
 $F(x)$ : The deformation gradient of material point  $x$

$\omega(|\xi|)$ : The influence function of the bond  
 $V$ : The volume of material point  
 $W$ : The elastic strain energy  
 $S$ : The second Piola-Kirchhoff stress  
 $\delta$ : The horizontal radius of material point  $x_i$   
 $\chi(t, \xi)$ : A scalar function of the bond between material points  $x$  and  $x'$  at time  $t$   
 $s$ : The stretch of the bond  
 $\kappa$ : The volume modulus  
 $G_c$ : The critical energy dissipating ratio  
 $\varphi(x, t)$ : The local damage value  
 $H$ : The neighborhood of material points  
 $\nu$ : Poisson's ratio  
 $C$ : The Green-Lagrange strain sensor  
 $\psi$ : The elastic tensor  
 $\bar{P}$ : The first Piola-Kirchhoff stress  
 $s_0$ : The critical stretch of the bond  
 $\mu$ : The shear modulus

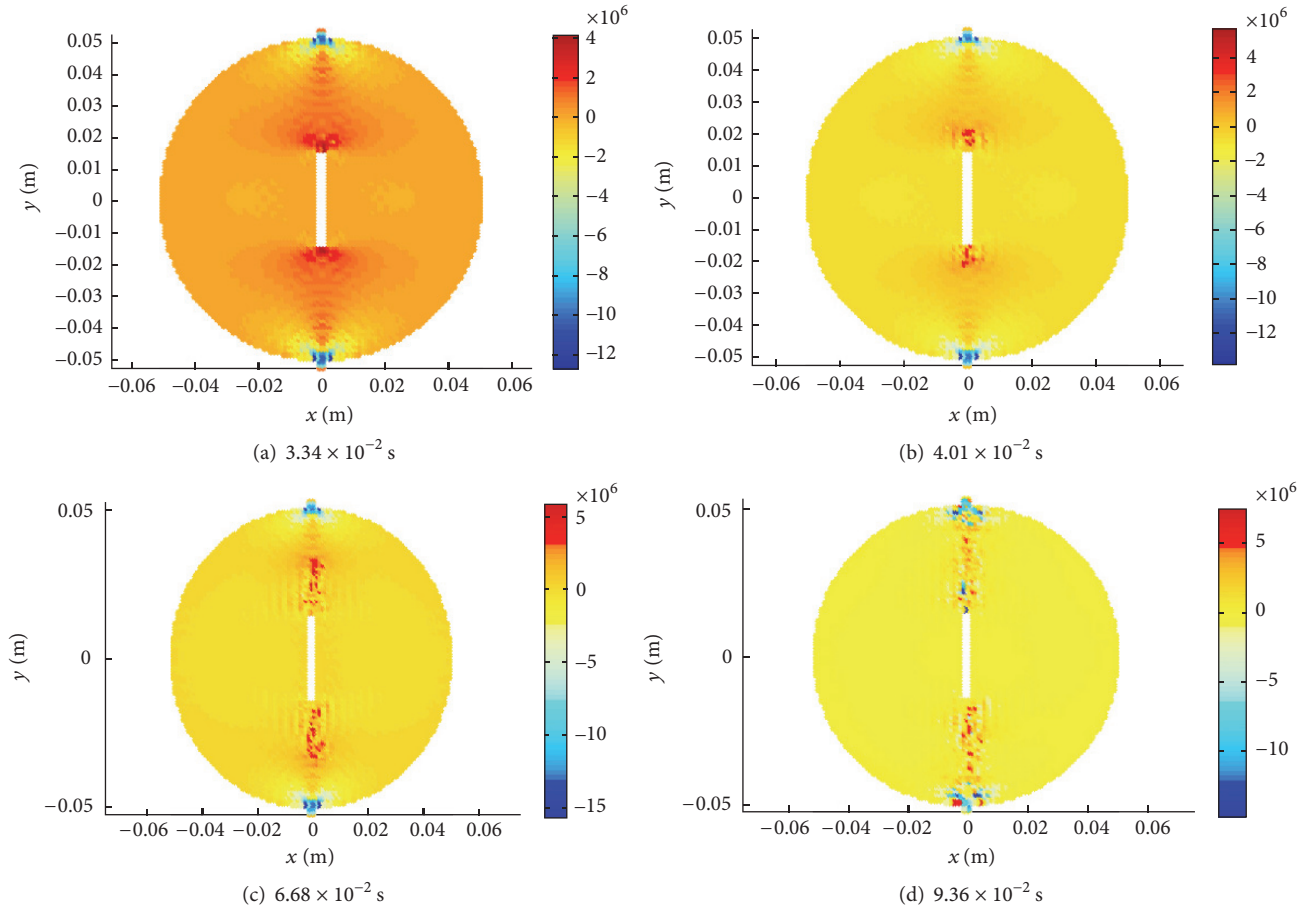


FIGURE 9: The maximum horizontal principal stress  $\sigma_x$  (Pa) contour of the rock sample.



FIGURE 10: The experimental result of the rock sample [23].

$K_{IC}$ : The fracture toughness

$\ddot{u}_i^n$ : The acceleration of the node  $x_i$  at time step  $n$ .

### Competing Interests

The authors declare that they have no competing interests.

### Acknowledgments

This work is supported by the first batch of Talent Introduction Projection in 2016 in Sichuan University of Science & Engineering (no. 2016RCL19), the projection in the Sichuan Provincial Department of Science (no. 2016GFW0137), and financial contributions from the Sichuan Province Science and Technology Plan Project (2013JY0119).

### References

- [1] N. Moës, J. Dolbow, and T. Belytschko, "A finite element method for crack growth without remeshing," *International Journal for Numerical Methods in Engineering*, vol. 46, no. 1, pp. 131–150, 1999.
- [2] T. Belytschko and T. Black, "Elastic crack growth in finite elements with minimal remeshing," *International Journal for Numerical Methods in Engineering*, vol. 45, no. 5, pp. 601–620, 1999.
- [3] G. J. Wagner, N. Moës, W. K. Liu, and T. Belytschko, "The extended finite element method for rigid particles in Stokes flow," *International Journal for Numerical Methods in Engineering*, vol. 51, no. 3, pp. 293–313, 2001.
- [4] T. Belytschko, Y. Krongauz, D. Organ et al., "Meshless methods: an overview and recent developments," *Computer Methods in*

- Applied Mechanics and Engineering*, vol. 139, no. 1–4, pp. 3–47, 1996.
- [5] L. D. Libersky and A. G. Pesehek, “Smooth particle hydrodynamics with strength of materials,” in *Advances in the Free-Lagrange Method Including Contributions on Adaptive Gridding and the Smooth Particle Hydrodynamics Method: Proceedings of the Next Free-Lagrange Conference Held at Jackson Lake Lodge, Moran, WY, USA 3–7 June 1990*, vol. 395 of *Lecture Notes in Physics*, pp. 26–248, Springer, Berlin, Germany, 1990.
- [6] S. A. Silling, “Reformulation of elasticity theory for discontinuities and long-range forces,” *Journal of the Mechanics and Physics of Solids*, vol. 48, no. 1, pp. 175–209, 2000.
- [7] S. A. Silling and F. Bobaru, “Peridynamic modeling of membranes and fibers,” *International Journal of Non-Linear Mechanics*, vol. 40, no. 2-3, pp. 395–409, 2005.
- [8] S. A. Silling, “Dynamic fracture modeling with a meshfree peridynamic code,” in *Computational Fluid and Solid Mechanics*, K. J. Bathe, Ed., pp. 641–644, Elsevier, Amsterdam, The Netherlands, 2003.
- [9] E. Askari, J. Xu, and S. Silling, “Peridynamic analysis of damage and failure in composites,” in *Proceedings of the 44th AIAA Aerospace Sciences Meeting and Exhibit (AIAA '06)*, pp. 1123–1134, Reno, Nev, USA, January 2006.
- [10] K. W. Colavito, B. Kilic, E. Celik, E. Madenci, E. Askari, and S. A. Silling, “Effect of void content on stiffness and strength of composites by a peridynamic analysis and static indentation test,” in *Proceedings of the 48th AIAA/ASME/ASCE/AHS/ASC Structures, Structural Dynamics and Materials Conference*, Paper 2007–2251, pp. 23–26, Waikiki, Hawaii, USA, April 2007.
- [11] K. W. Colavito, B. Kilic, E. Celik, E. Madenci, E. Askari, and S. Silling, “Effect of nano particles on stiffness and impact strength of composites,” in *Proceedings of the 48th AIAA/ASME/ASCE/AHS/ASC Structures, Structural Dynamics, and Materials Conference*, Paper 2007-2001, Honolulu, Hawaii, USA, April 2007.
- [12] J. Jung and J. Soek, “Fatigue crack growth analysis in layered heterogeneous material systems using peridynamic approach,” *Composite Structures*, vol. 152, pp. 403–407, 2016.
- [13] J. Xu, A. Askari, O. Weckner, H. Razi, and S. Silling, “Damage and failure analysis of composite laminates under biaxial loads,” in *Proceedings of the 48th AIAA/ASME/ASCE/AHS/ASC Structures, Structural Dynamics, and Materials Conference*, pp. 7450–7458, AIAA, Honolulu, Hawaii, USA, April 2007.
- [14] J. T. Foster, S. A. Silling, and W. W. Chen, “Viscoplasticity using peridynamics,” *International Journal for Numerical Methods in Engineering*, vol. 81, no. 10, pp. 1242–1258, 2010.
- [15] C. T. Wu and B. Ren, “A stabilized non-ordinary state-based peridynamics for the nonlocal ductile material failure analysis in metal machining process,” *Computer Methods in Applied Mechanics and Engineering*, vol. 291, pp. 197–215, 2015.
- [16] C. T. Wu, N. Ma, K. Takada, and H. Okada, “A mesh-free continuous-discontinuous approach for the ductile fracture modeling in explicit dynamics analysis,” *Computational Mechanics*, vol. 58, no. 3, pp. 391–409, 2016.
- [17] S. Sun and V. Sundararaghavan, “A peridynamic implementation of crystal plasticity,” *International Journal of Solids and Structures*, vol. 51, no. 19-20, pp. 3350–3360, 2014.
- [18] W. Gerstle, N. Sau, and S. Silling, “Peridynamic modeling of concrete structures,” *Nuclear Engineering and Design*, vol. 237, no. 12-13, pp. 1250–1258, 2007.
- [19] Y. D. Ha, J. Lee, and J.-W. Hong, “Fracturing patterns of rock-like materials in compression captured with peridynamics,” *Engineering Fracture Mechanics*, vol. 144, pp. 176–193, 2015.
- [20] O. Weckner and R. Abeyaratne, “The effect of long-range forces on the dynamics of a bar,” *Journal of the Mechanics and Physics of Solids*, vol. 53, no. 3, pp. 705–728, 2005.
- [21] X.-P. Zhou, X.-B. Gu, and Y.-T. Wang, “Numerical simulations of propagation, bifurcation and coalescence of cracks in rocks,” *International Journal of Rock Mechanics & Mining Sciences*, vol. 80, pp. 241–254, 2015.
- [22] Y. S. Jenq and S. P. Shah, “Mixed-mode fracture of concrete,” *International Journal of Fracture*, vol. 38, no. 2, pp. 123–142, 1988.
- [23] H. Haeri, K. Shahriar, M. F. Marji, and P. Moarefvand, “Experimental and numerical study of crack propagation and coalescence in pre-cracked rock-like disks,” *International Journal of Rock Mechanics and Mining Sciences*, vol. 67, pp. 20–28, 2014.

## Research Article

# An Efficient Approach for Real-Time Prediction of Rate of Penetration in Offshore Drilling

Xian Shi,<sup>1</sup> Gang Liu,<sup>1</sup> Xiaoling Gong,<sup>2</sup> Jialin Zhang,<sup>1</sup> Jian Wang,<sup>3</sup> and Hongning Zhang<sup>1</sup>

<sup>1</sup>College of Petroleum Engineering, China University of Petroleum (Huadong), Qingdao, Shandong 266580, China

<sup>2</sup>College of Information and Control Engineering, China University of Petroleum (Huadong), Qingdao, Shandong 266580, China

<sup>3</sup>College of Science, China University of Petroleum (Huadong), Qingdao, Shandong 266580, China

Correspondence should be addressed to Gang Liu; [lg196009091@sina.com](mailto:lg196009091@sina.com)

Received 11 May 2016; Accepted 28 September 2016

Academic Editor: Cheng-Tang Wu

Copyright © 2016 Xian Shi et al. This is an open access article distributed under the Creative Commons Attribution License, which permits unrestricted use, distribution, and reproduction in any medium, provided the original work is properly cited.

Predicting the rate of penetration (ROP) is critical for drilling optimization because maximization of ROP can greatly reduce expensive drilling costs. In this work, the typical extreme learning machine (ELM) and an efficient learning model, upper-layer-solution-aware (USA), have been used in ROP prediction. Because formation type, rock mechanical properties, hydraulics, bit type and properties (weight on the bit and rotary speed), and mud properties are the most important parameters that affect ROP, they have been considered to be the input parameters to predict ROP. The prediction model has been constructed using industrial reservoir data sets that are collected from an oil reservoir at the Bohai Bay, China. The prediction accuracy of the model has been evaluated and compared with the commonly used conventional artificial neural network (ANN). The results indicate that ANN, ELM, and USA models are all competent for ROP prediction, while both of the ELM and USA models have the advantage of faster learning speed and better generalization performance. The simulation results have shown a promising prospect for ELM and USA in the field of ROP prediction in new oil and gas exploration in general, as they outperform the ANN model. Meanwhile, this work provides drilling engineers with more choices for ROP prediction according to their computation and accuracy demand.

## 1. Introduction

Drilling is an expensive and necessary operation for petroleum and gas exploration. The ultimate aim in drilling operations is to increase drilling speed with less cost while maintaining safety. However, because of the geological uncertainty and many uncontrolled operational factors, the optimization of drilling is still a large challenge for oil and gas industries [1, 2]. In offshore drilling, rate of penetration (ROP) is the key parameter to optimize total rig hours. Because it can be used for formation drillability estimation, reliable and fast prediction of rate of penetration (ROP) is highly desirable.

In existing literature, some direct and indirect methods are designed to evaluate the ROP. ROP mathematical models can be used to outline changes of rock mechanical properties and drilling parameters, bit types, and design on ROP. Bourgoyne and Young (B&Y) proposed a ROP calculating model considering eight functions, whereas the relevant parameters need to be obtained by multiple regression for each data entry,

and this equation is only adequate for roller-type rock bits [3]. In addition to B&Y's equation, many authors try to find a simple link between ROP and rock properties because the majority of reservoir mechanical properties can be inferred from well logs. Howarth et al. carried out a laboratory test program for correlating the penetration rate with rock properties and reported that penetration rate correlated well with the uniaxial compressive and tensile strength of the rock [4]. Kahraman introduced a strong correlation between penetration rate and brittleness values obtained from uniaxial compressive strength and tensile strength [5]. However, the application of rock mechanical properties for ROP estimation cannot reveal the real-time downhole conditions. Therefore, it is necessary to use drilling data, but many operational parameters of the drilling equipment are found to relate to ROP. Some authors performed statistical analyses using real-time drilling data, such as weight bit on, bit rotational speed, torque, and the effect of mud properties, and some of them obtained

TABLE 1: Summary of ROP prediction models with artificial intelligence.

Reference	Model	Input number	Input layer	Output layer
Zhang et al. [22]	AHP and BPANN	9	UCS, bit size, bit type, drillability coefficient, gross hours drilled, WOB, RPM, drilling mud density, and AV (Apparent Viscosity)	ROP
Jahanbakhshi et al. [13]	ANN	20	Differential pressure, hydraulics, hole depth, pump pressure, density of the overlying rock, equivalent circulating density, hole size, formation drillability, permeability and porosity, drilling fluid type, plastic viscosity of mud, yield point of mud, initial gel strength of mud, 10 min Gel strength of mud bit type and its properties, weight on the bit and rotary speed, bit wear, and bit hydraulic power	ROP
Bahari and Seyed [11]	Fuzzy	4	UCS, rock quality designation, bit Load, and bit rotation	ROP
Amar and Ibrahim [25]	Radial-basis function and ELM	7	Depth, bit weight, rotary speed, tooth wear, Reynolds number function, ECD, and pore gradient	ROP
Bilgesu et al. [12]	ANN	9	Formation drillability, formation abrasiveness, bearing wear, tooth wear, pump rate, rotating time, rotary torque, WOB, and rotary speed	ROP
Bataee and Mohseni [2]	ANN	4	Bit diameter, WOB, RPM, and mud weight	ROP
Moran et al. [26]	ANN	6	Rock strength, rock type, abrasion, WOB, RPM, and mud weight	ROP and wear
Monazami et al. [27]	ANN	13	Drill collar outside diameter, drill collar length, kick of point, azimuth, inclination angle, weight on bit, flow rate, bit rotation speed, mud weight, solid percent, plastic viscosity, yield point, and measured depth	ROP

a certain degree of success [6–9]. As a matter of fact, there is no exact relation between ROP, rock mass properties, and different drilling variables because not only do a large number of uncertain drilling variables influence ROP but also the relationships between ROP and the affecting factors are complex and highly nonlinear. Thus, some soft computing technologies such as neural networks have been applied to ROP prediction in recent years [10]. The flexibility of this method allows engineers to analyze a wide range of information and deliver high-quality ROP prediction. Bahari and Seyed applied GA to determine constant coefficients of Bourgoyne and Young’s ROP model [11]. Table 1 shows current ROP prediction models with artificial intelligence. The results revealed that the ANN model exhibited better performance to predict penetration rate than the prediction performance of multiple regression models. In addition, neural networks can yield good correlation coefficients even if fewer data are available from filed measurements [12–15]. However, traditional ANN still has some significant shortcomings, such as a slow training process and the possibility of trapping in local extrema, which lead to dissatisfactory predictions. Therefore, it is necessary to introduce new algorithms that can potentially further improve ROP prediction accuracy.

The extreme learning machine (ELM) proposed by Huang et al. is a fast algorithm for single hidden-layer feedforward neural networks (SLFNs) [16, 17]. The way ELM trains SLFN is that it first randomly generates the weights of the hidden layer and then calculates the weights of the output layer by solving a linear system using the least square method. This learning algorithm is extremely fast and has good prediction accuracy. It has been proved in theory and in practice that this

algorithm can generate good generalization performance in most cases at speeds much faster than traditionally popular feedforward neural network learning algorithms. Until now, ELM has been widely studied and applied extensively by researchers and it has demonstrated good generalization and prediction performance in many real-life applications [18, 19]. Many algorithms such as evolutionary ELM and enhanced random search-based incremental ELM (EI-ELM) have been proposed to optimize the network structure. The above algorithms choose all or part of the hidden-layer weights randomly and select the candidate ones with the LSE (Least Squares Estimation). However, the model parameters in these algorithms are not efficient enough because only the value of the objective function is used in the search process. USA (upper-layer-solution-aware algorithm), an improved version of the ELM algorithm, gives an optimization of the number of hidden-layer nodes and the parameters modeling the problem [20]. Once the weights of the hidden layer are determined, those of the output layer can be determined as a certain function using the closed-form solution. Therefore, what we need to search for at each epoch along the gradient direction is just the weights of the hidden layer. However, the study of ELM and USA in drilling ROP prediction is rare.

This paper concentrates on ROP estimation using bit type and its properties, mud type and mud viscosity, formation parameters such as rock strength, formation drillability, and formation abrasiveness, and some critical drilling equipment operational parameters such as pump pressure, WOB, and rotary speed based on the previous drilled wells data with the ELM and USA model. The developed ELM and USA model are shown to be efficient with respect to accuracy and running

time compared to traditional ANN models. They thus provide a more reliable and faster real-time tool for predicting ROP in new wells.

## 2. Artificial Neural Networks and Extreme Learning Machines

**2.1. Methodology of Artificial Neural Networks.** Artificial neural networks (ANNs) are efficient models in approximating the unknown nonlinear functions, seeking to simulate human brain behavior by processing data on a trial-and-error basis. Because of their powerful ability in approximation and generalization, ANNs have been widely used in petroleum engineering, with applications to bit selection, reservoir characterization, EOR (enhanced oil recovery), hydraulic fracturing candidate selection, and so forth [21–24].

The network structures of ANNs are made up of a number of neurons which are distributed in layers based on their different functions. Generally, a complete neural network consists of three different types on layers, namely, an input layer, one or more hidden layers, and an output layer in which each layer includes a preset number of neurons. It has been rigorously proved that ANN can approximate any continuous function with an arbitrary precision. And ANN is thus a universal approximator. The direction of the information transmission in feedforward neural networks is from input neurons through activation of the hidden neurons to the outputs. For supervised learning, the connecting weights of the layers are updated in the training procedure by minimizing the objective function between the networks' actual outputs and the desired value. Actually, there are many different ways to fulfill the training of an ANN model: back-propagation (BP) algorithm is the most popular one. It is a typical type of supervised learning strategy in machine learning field. In general, the BP method uses the following steps: for a given specific input sample, the actual output is obtained through the information transferring on layers one by one. If the error between the produced and the desired outputs is acceptable, then stop training. If the error is not acceptable in the previous step, then the weights are changed on the interconnections that go into the output layer. Next, an error value is calculated for all of the neurons in the hidden layer that is just below the output layer. Then, the weights are adjusted for all interconnections that go into the hidden layer. The process is continued until the last layer of weights has been adjusted.

Some essential shortcomings of BP method are continually encountered in many real applications, for example, slow convergence speed and prone to being stuck in a local minimum. Thus, the standard BP algorithm sometimes shows poor performance on practical applications which mainly stems from employing the standard gradient descent method to adjust the weights. As a result, there are many different variants that have emerged in recent decades. The commonly used variants based on different optimizing strategies are with Levenberg-Marquardt (LM); the conjugate gradient method with Powell-Beale, Fletcher-Reeves, and Polak-Ribiere updates; the gradient descent method with momentum term, penalty term, and adaptive learning rate; Bayesian regulation; and scaled conjugate gradient [28].

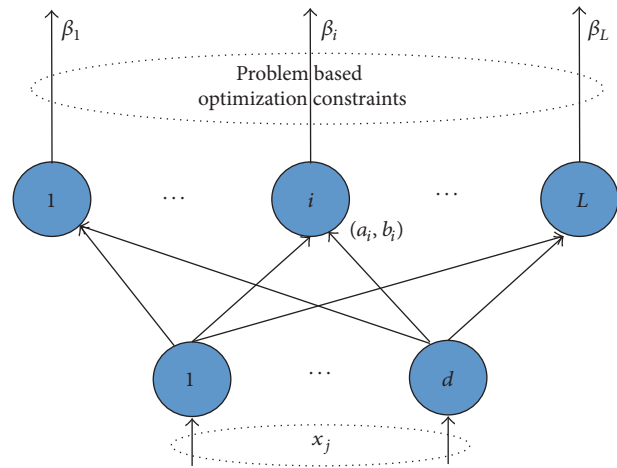


FIGURE 1: Structure and schematic diagram of the ELM method used in this paper.

### 2.2. Methodology of Extreme Learning Machines

**2.2.1. Conventional Extreme Learning Machines.** ELM was originally proposed to train a single hidden-layer feedforward neural network (SLFN) and later extended to more generalized SLFNs where the hidden layer may not be made of homogeneous neurons. Some obstacles that back-propagation neural networks faced, such as the slow training speed, the sensitivity to the selection of the parameters, and the high possibility to be trapped in local minima, can be avoided using ELM. Figure 1 illustrates the structure of the ELM method.

Neural networks are used universally for feature extraction, clustering, regression, and classification and require little human intervention in most cases. Inspired by biological learning characteristics, to overcome the challenging problems encountered by BP algorithms, ELM development sets fit hidden-layer neurons while randomly choosing the parameters at the initialization period.

The learning efficiency and effectiveness of ELM were established in 2005, while its universal approximation capability was rigorously proved later. The correspondence between specific biological neural configurations consequently appeared in the literature.

Unlike other randomness-based training methods/network models, the hidden weights can be randomly determined before the learning process, and all of the hidden neurons are independent of the training samples and one another in ELM. Once determined, both the hidden neurons and the hidden weights need not be tuned, although they are important and crucial for training. Moreover, ELM has good generalization ability, as the architecture of ELM is robust enough and has enough hidden neurons for the given problems, which is not the case for conventional learning methods highly dependent on the data.

Because the connecting weights between the input and the hidden layer do not need to be tuned, we use a simple

model with one output node as an example and give the output of the ELM as follows:

$$f_L(x) = \sum_{i=1}^L \beta_i h_i(x) = h(x) \beta, \quad (1)$$

in which  $\beta = [\beta_1, \dots, \beta_L]^T$  denotes the output weights connecting the hidden layer and the output layer, and  $h(x) = [h_1(x), \dots, h_L(x)]$  is the hidden-layer output with respect to input  $x$ .  $h(x)$  is a feature mapping. In fact, if the input is in  $d$ -dimensional space,  $h(x)$  maps it to  $L$ -dimensional hidden-layer feature space. For binary classification applications using ELM, the function of the output is

$$f_L(x) = \text{sign}[h(x) \beta]. \quad (2)$$

ELM often leads to a smaller training error with the smaller norm of weights compared with the traditional learning algorithm. According to Bartlett's theory, the smaller weights make a great contribution to a better generalization performance of neural networks with similar training errors. What makes ELM particularly noteworthy is that the values of the weights need not be adjusted during the training. The values of the input weights are randomly chosen at the beginning of the training procedure and stay fixed, while the weights of the output layer are calculated by searching for the least square solution of the following objective function.

The training error and the norm of the output weights ELM minimization are as follows:

$$\begin{aligned} \text{Minimize: } \quad & \| \mathbf{H}\beta - T \|^2 \\ & \| \beta \|^2, \end{aligned} \quad (3)$$

where  $\mathbf{H}$  is the output matrix of the hidden layer.

The main purpose of ELM is to minimize the training error as well as the norm of connecting output layer weights. According to the theory of linear systems, the weights between the hidden layer and the output layer are calculated using the following equation [17]:

$$\beta = \mathbf{H}^\dagger T, \quad (4)$$

where  $\mathbf{H}^\dagger$  is the Moore-Penrose pseudoinverse of matrix  $\mathbf{H}$  and  $T = [t_1, t_2, \dots, t_n]^T$ .

We can summarize the ELM training algorithm as follows [17]:

- (1) Set the hidden node parameters randomly, for example, input weights  $a_i$  and biases  $b_i$  with the certain hidden nodes,  $i = 1, 2, \dots, L$ .
- (2) Calculate the hidden-layer output matrix  $\mathbf{H}$  through the input and the weights as well as the biases.
- (3) Obtain the output weights matrix using (4).

The orthogonalization method, the iterative method, singular value decomposition (SVD), and so forth can be used to evaluate the Moore-Penrose pseudoinverse of a matrix [24]. By the orthogonal projection method, we can obtain

$\mathbf{H}^\dagger = (\mathbf{H}^T \mathbf{H})^{-1} \mathbf{H}^T$  when  $\mathbf{H}^T \mathbf{H}$  is nonsingular and  $\mathbf{H}^\dagger = \mathbf{H}^T (\mathbf{H} \mathbf{H}^T)^{-1}$  when  $\mathbf{H} \mathbf{H}^T$  is nonsingular. In light of ridge regression theory, we add a positive value to the diagonal of  $\mathbf{H}^T \mathbf{H}$  or  $\mathbf{H} \mathbf{H}^T$  to make the resultant solution more stable and tend to have better generalization performance.

According to ELM theory, there are many feature mapping functions that  $h(x)$  may be designed to incorporate, which gives ELM the ability to approximate any continuous target function. The actual activation functions of human brain systems seem to be more like a nonlinear piecewise continuous stimulation, though the actual functions remain unknown. In fact, the ELM model is based on two major theorems: universal approximation and classification ability.

**Theorem 1** (universal approximation theorem; see [16, 29]). *Given any bounded, nonconstant piecewise continuous function as the activation function in hidden neurons, if, by tuning parameters of the hidden neuron activation function, SLFNs can approximate any target continuous function, then, for any continuous target function  $f(x)$  and any randomly generated function sequence,  $\{h_i(x)\}_{i=1}^L$ ,  $\lim_{L \rightarrow \infty} \| \sum_{i=1}^L \beta_i h_i(x) - f(x) \| = 0$  holds with probability one given the appropriate output weights  $\beta$ .*

According to the nonlinear activation function and piecewise linear combination, ELM can approximate any continuous mapping and divide arbitrary disjoint regions of any shapes with enough randomly hidden neurons based on the nonlinear piecewise continuous activation functions and their linear combinations. In particular, the theory basis for the classification capability of ELM is as follows.

**Theorem 2** (classification capability theorem; see [17]). *Given feature mapping  $h(x)$ , if  $h(x)$  is dense in  $C(R^d)$  or in  $C(M)$ , where  $M$  is a compact set of  $R^d$ , then ELM with random hidden-layer mapping  $h(x)$  can separate arbitrary disjoint regions of any shapes in  $R^d$  or in  $M$ .*

This theorem implies that ELM with bounded nonconstant piecewise continuous functions has universal approximation capability. While it does not require updating the weights of hidden neurons in the training process, it is worth mentioning that ELM is more like the activation of the human brain with the randomly generating hidden weights without tuning.

**2.2.2. Upper-Layer-Solution-Aware (USA) Algorithm Model.**  $\mathbf{X} = [\mathbf{x}_1, \dots, \mathbf{x}_i, \dots, \mathbf{x}_N]$  is given as the set of input vectors, and each vector is denoted by  $\mathbf{x}_i = [x_{1i}, \dots, x_{ji}, \dots, x_{Di}]$  in which  $D$  is the dimension of the input vector and  $N$  is the total sum of training samples. Define  $L$  as the number of hidden units and  $C$  as the dimension of the output vector.  $\mathbf{y}_i = \mathbf{U}^T \mathbf{h}_i$  is the output of the SHLNN. Among them,  $\mathbf{h}_i = \sigma(\mathbf{W}^T \mathbf{x}_i)$  is denoted as the hidden-layer output,  $\mathbf{U}$  is denoted as weight  $L \times C$  matrix at the upper layer,  $\mathbf{W}$  is denoted as  $D \times L$  weight matrix at the lower layer, and  $\sigma(\cdot)$  is denoted as the kernel function.

Note that if  $\mathbf{x}_i$  and  $\mathbf{h}_i$  are augmented with ones, the bias terms are implicitly represented in the above formulations.

$\mathbf{T} = [\mathbf{t}_1, \dots, \mathbf{t}_i, \dots, \mathbf{t}_N]$  is given as the target vectors and each target is denoted by  $\mathbf{t}_i = [t_{1i}, \dots, t_{ji}, \dots, t_{Ci}]^T$ , and the parameters  $\mathbf{U}$  and  $\mathbf{W}$  are used to minimize the square error.

$$E = \|\mathbf{Y} - \mathbf{T}\|^2 = \text{Tr}[(\mathbf{Y} - \mathbf{T})(\mathbf{Y} - \mathbf{T})^T], \quad (5)$$

where  $\mathbf{Y} = [y_1, \dots, y_i, \dots, y_N]$ . Note that the hidden-layer values  $\mathbf{H} = [\mathbf{h}_1, \dots, \mathbf{h}_i, \dots, \mathbf{h}_N]$  are also determined uniquely if the lower-layer weights  $\mathbf{W}$  are fixed. After setting the gradient

$$\begin{aligned} \frac{\partial E}{\partial \mathbf{W}} &= \frac{\partial \text{Tr}[(\mathbf{U}^T \mathbf{H} - \mathbf{T})(\mathbf{U}^T \mathbf{H} - \mathbf{T})^T]}{\partial \mathbf{U}} \\ &= 2\mathbf{H}(\mathbf{U}^T \mathbf{H} - \mathbf{T})^T \end{aligned} \quad (6)$$

to zero, the upper-layer weights  $\mathbf{U}$  can be determined to the closed-form solution [20]:

$$\mathbf{U} = (\mathbf{H}\mathbf{H}^T)^{-1} \mathbf{H}\mathbf{T}^T. \quad (7)$$

Note that (7) defines an implicit constraint between the set of weights  $\mathbf{U}$  and the set of weights  $\mathbf{W}$ , through hidden-layer output  $\mathbf{H}$  in the SHLNN. This leads to a structure that our new algorithms will use in optimizing the SHLNN.

Regularization techniques need to be used in actual applications when hidden-layer matrix  $\mathbf{H}$  is sometimes ill-conditioned (i.e.,  $\mathbf{H}\mathbf{H}^T$  is singular) because solving (7) is relatively simple. The popular technique used in this study is based on the ridge regression theory. Even more specifically,

by adding positive value  $\mathbf{I}/\mu$  to the diagonal of  $\mathbf{H}\mathbf{H}^T$ , (7) is converted to

$$\mathbf{U} = \left( \frac{\mathbf{I}}{\mu} + \mathbf{H}\mathbf{H}^T \right)^{-1} \mathbf{H}\mathbf{T}^T, \quad (8)$$

where  $\mathbf{I}$  is the identity matrix and  $\mu$  is a positive constant (regularization coefficient) that is used to control the degree of regularization. The final solution (8) actually minimizes  $\|\mathbf{U}^T \mathbf{H} - \mathbf{T}\|^2 + \mu \|\mathbf{U}\|^2$ , in which  $\mu \|\mathbf{U}\|^2$  is  $L_2$  regularization term. Positive constant  $\mu$  is the regularization coefficient. It represents the relative importance of complexity-penalty term  $\|\mathbf{U}\|^2$  with respect to empirical risk  $\|\mathbf{U}^T \mathbf{H} - \mathbf{T}\|^2$ . When  $\mu$  approaches zero, the model tends to an unconstrained optimal problem, and then the solutions would be completely determined from the training samples. When  $\mu$  is made infinitely large, this means that the training samples are unreliable, imposing weight  $\mathbf{U}$  to be sufficiently of small values. In real applications, regularization parameter  $\mu$  is set to be a value somewhere between these two cases. The reasonable regularization parameter can efficiently affect both of the learning and prediction performance (generalization ability). Solution (8) shows better stability and better generalization performance than (7). Whenever the pseudoinverse is involved, solution (8) can be used throughout the paper.

The principle of this algorithm is very simple. Once the lower-layer weights are determined, the upper-layer weights can be determined explicitly by using the closed-form solution (8). Based on this solution, at each epoch, all we need to adjust along the gradient direction are the lower-layer weights. Gradient  $\partial E/\partial \mathbf{W}$  is obtained by considering upper-layer weights  $\mathbf{U}$  under  $\mathbf{W}$ 's effect and the training objective function is the square error. We can obtain the gradient by treating  $\mathbf{U}$  as a function of  $\mathbf{W}$  and plugging (7) into criterion (5):

$$\begin{aligned} \frac{\partial E}{\partial \mathbf{W}} &= \frac{\partial \text{Tr}[(\mathbf{U}^T \mathbf{H} - \mathbf{T})(\mathbf{U}^T \mathbf{H} - \mathbf{T})^T]}{\partial \mathbf{W}} = \frac{\partial \text{Tr} \left[ \left( [(\mathbf{H}\mathbf{H}^T)^{-1} \mathbf{H}\mathbf{T}^T]^T \mathbf{H} - \mathbf{T} \right) \left( [(\mathbf{H}\mathbf{H}^T)^{-1} \mathbf{H}\mathbf{T}^T]^T \mathbf{H} - \mathbf{T} \right)^T \right]}{\partial \mathbf{W}} \\ &= 2\mathbf{X} \left[ \mathbf{H}^T \circ (\mathbf{1} - \mathbf{H})^T \circ \left[ \mathbf{H}^\dagger (\mathbf{H}\mathbf{T}^T) (\mathbf{T}\mathbf{H}^\dagger) - \mathbf{T}^T (\mathbf{T}\mathbf{H}^\dagger) \right] \right], \end{aligned} \quad (9)$$

in which  $\mathbf{H}^\dagger = \mathbf{H}^T (\mathbf{H}\mathbf{H}^T)^{-1}$  is the pseudoinverse of  $\mathbf{H}$  and  $\circ$  is the element-wise production.

In the derivation of (9), we used the fact that  $\mathbf{H}\mathbf{H}^T$  and  $(\mathbf{H}\mathbf{H}^T)^{-1}$  are symmetric. We also used the fact that

$$\begin{aligned} &\frac{\partial \text{Tr}[(\mathbf{H}\mathbf{H}^T)^{-1} \mathbf{H}\mathbf{T}^T \mathbf{T}\mathbf{H}^T]}{\partial \mathbf{H}^T} \\ &= -2\mathbf{H}^T (\mathbf{H}\mathbf{H}^T)^{-1} \mathbf{H}\mathbf{T}^T \mathbf{T}\mathbf{H}^T (\mathbf{H}\mathbf{H}^T)^{-1} \\ &\quad + 2\mathbf{T}^T \mathbf{T}\mathbf{H}^T (\mathbf{H}\mathbf{H}^T)^{-1}. \end{aligned} \quad (10)$$

This algorithm updates  $\mathbf{W}$  by using the gradient that is defined directly in (9) as

$$\mathbf{W}_{k+1} = \mathbf{W}_k + \rho \frac{\partial E}{\partial \mathbf{W}}, \quad (11)$$

where  $\rho$  is the learning rate. The learning rate here means the updating step which is widely used in solving optimal problems. It shows how far the weights need to be moved in the direction of the given gradient  $\partial E/\partial \mathbf{W}$  and how to obtain the new weights which minimizes the objective function. One simple way is to set a positive constant value in the entire training process. In this paper, we select the suitable learning rate by means of many different simulations. This algorithm

uses the closed-form solution (8) to calculate  $U$  after updating  $W$ .

The algorithms proposed in this paper achieve significantly better classification accuracy than ELM when the same number of hidden units is used. To achieve the same classification accuracy, the algorithm requires only 1/16 of the model, and, therefore, less test time is needed.

### 3. Input Data Selection

The target research four wells were drilled at the Bohai Bay basin, which is the largest oil and gas production base offshore in China. The oilfield has experienced many production stages since 1963 and currently many projects are carried out by China National Offshore Oil Corporation (CNOOC) and ConocoPhillips China (COPC). To effectively increase production and decrease drilling cost, drilling speed control is necessary.

Due to drilling requirements and the similarity of wells located close to one another, collecting past data and utilizing the data in a useful manner have an important impact on drilling cost reduction. This means that optimum parameters are always in effect. As a matter of fact, there are various factors than can affect ROP. Previous studies show that the ROP is largely dependent on some critical parameters, which can be classified into three types: rig/bit related parameters, mud related parameters, and formation parameters. The rig/bit and mud related parameters can be manipulated, but the formation parameters have to be handled differently. Table 2 gives a brief classification of some important drilling parameters that affect ROP. To predict and optimize the ROP, both controllable and uncontrollable parameters from drilling reports were collected from daily drilling reports, lab investigations, well log, and geological information.

Because it is impossible to treat all of the relevant drilling parameters in ROP prediction, it is necessary to choose essential data based on literature surveys and statistical analysis. It was concluded that the rock properties, the drilling machine parameters, and mud properties relate to the ROP. In fact, a total of 18 drilling parameters were gathered in this study: depth, torque, rotational per speed (RPM), weight on bit, flow rates, active PVT, pump pressure, hook load, differential pressure, mud weight, mud viscosity, formation drillability, formation abrasiveness, UCS, porosity, bit size, and bit type.

- (1) The bit type/size can affect ROP in a given formation. Roller cone bits generally have three cones that rotate around their axis while teeth are milled out of the matrix or inserted. The teeth combine crushing and shearing to fracture the rock. Drag bits usually consist of a fixed cutter mechanism that can be cutting blades, diamond stones, or cutters. Today, polycrystalline diamond compact (PDC) is the most commonly used drag bit with PDC, diamond impregnated, or diamond hybrid cutters mounted on the bit blades/body. Drag bits disintegrate rock primarily through shearing. The difference in the design of roller cone and drag bits and different rock disintegration methods requires different ROP

models. Thus, the effects of the bit type are included in this model.

- (2) Operational parameters such as pump pressure and differential pressure are the most important operational hydraulic parameters affecting ROP. Pump pressure is sometimes increased to achieve a higher penetration rate for a certain depth of advance while keeping rotation constant. In addition, the mechanical factors of weight on the bit and rotary speed have linear relationships with ROP. The increase in weight on the bit can push the bit teeth or cutters further down into a formation and disintegrate more rocks, resulting in faster ROP. Bit rotation can be increased to obtain higher penetration rate, keeping the bit load constant.
- (3) Formation mechanical characteristics are uncontrollable variables for controlling ROP values. In general, decreasing the penetration rate is greatly attributed to increase of depth because by increasing the depth, rock strength increases and porosity decreases. Moreover, the larger indirect drilling resistance that results from larger UCS and hardness will also limit the depth of cut for a given set of bit design and applied operating parameters. There are two main reasons for selecting rock strength as the representative of rock properties. One is that the rock strength is calculated by a function of depth, density, and porosity; another is that this parameter can be computed by logging data or triaxial compressive experiments and scratch tests in a lab if core samples are available.
- (4) The aim of drilling mud is to remove the loose rock chips away from the bit face while the bits cool. Therefore, drilling weight, mud rheology, and solid content are confirmed as an important factor in ROP by some studies. ROP basically decreased by increasing mud viscosity, solid content, and mud weight.

In addition to the above parameters, some comprehensive parameters such as formation drillability and abrasiveness also need to be considered because these parameters can provide some important information sources about ROP prediction that cannot be described by conventional drilling data. More importantly, the model inputs should be easily acquired in real time, recorded from the respective measurement gauges on the rig. Using additional parameters as inputs can result in a large network size and consequently slow down running speed and efficiency. Thus, bit size, bit type, bit wear, UCS, formation drillability, formation abrasiveness, rotational per speed, WOB, pump pressure, mud viscosity, and mud density were selected as 11 inputs for neural network simulation. The data set used in this paper consists of more than 5000 measurements taken from this area at different wells and with different drilling rigs. Figure 2 illustrates three types of PDC bits in the drilling operation in this area.

It should be noted that data can very often be non-numeric. Because neural networks cannot be trained with nonnumeric data, it is necessary to translate nonnumeric

TABLE 2: ROP related drilling parameters classification.

Rig and bit related parameters	Formation parameters	Drilling fluid properties
Weight on bit (WOB)	Local stresses	Mud weight
Torque	Hardness	Viscosity
Rotary speed (RPM)	Mineralogy	Filtrate loss
Flow rates	Porosity and permeability	Solid content
Pump stroke speed (SPM)	Formation abrasiveness	Gel strength
Pump pressure	Drillability	Mud pH
Hook load	Depth	Yield point
Bit wear	Temperature	
Type of the bit	Unconfined compressive strength (UCS)	



FIGURE 2: Three types of PDC drilling bits.

data into numeric data. In this study, formation drillability, formation abrasiveness, bit size, and bit type are nonnumeric. Numbering classes are used in this study to perform nonnumeric translation. The formation drillability ranged between 30 and 75. The highest number represents the highest drillability and the lower drillability was for hard formations such as shales. The formation abrasiveness ranged between 1 and 8, where 8 signifies the highest abrasive formation. In addition, bit type is assigned between 1 and 12 where 12 is related to the bit type that has highest ROP average value. The bit wear values are determined between 0 and 9, where 9 indicates that a tooth is completely worn out. Table 3 shows the results for the recorded parameters and their ranges.

**4. Experimental Design**

*4.1. Model Architecture.* Determining the optimal size of the neural network model is complex. An overly complex network tends to memorize the data without learning to generalize to new situations. It concentrates too much on the data presented for learning and tends toward modeling the noise. The total number of ROP in target wells is summed up to 5500. The training subset constitutes 75% of the total data and testing subsets that include 25% of the total data. As mentioned above, inputs of neural networks include 10

TABLE 3: Summary of results for the recorded parameters.

Parameters	Ranges
Bit size/inch	5.813~8.5
Bit type	1-12
Bit wear	0-9
UCS/psi	2412~21487
Formation drillability	30-75
Formation abrasiveness	1-8
Rotational per speed/rpm	84~126
WOB/10 <sup>3</sup> lbs	24~69
Drilling mud type	1~3
Mud viscosity/cp	1~70
Pump pressure/psi	1651-3765
ROP	26.6~120.5

parameters, while the ROP is the only element in the output layer. Figure 3 is the developed neural network architecture.

*4.2. Model Performance Indicators.* The performances of neural network models are assessed by means of the correction

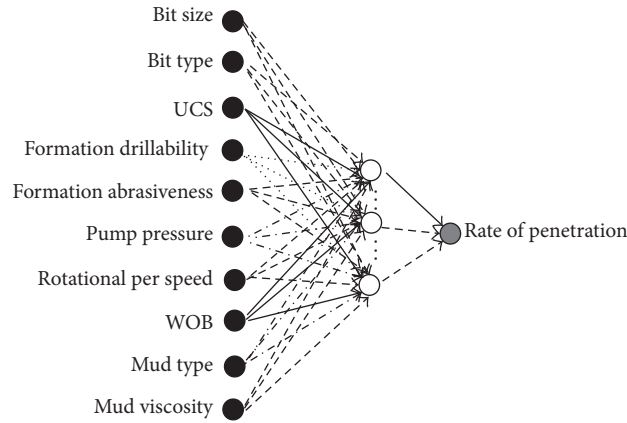


FIGURE 3: Schematic of architecture of the ELM network model. Node number of the input layer is 10, and ROP are the only node at the output layer.

coefficient ( $R^2$ ), mean absolute error (MAE), root mean square error (RMSE), and variance accounted for (VAF) performance indicators.

$R^2$  represents the proportion of the overall variance explained by the model, which can be calculated as

$$R^2 = 1 - \frac{\sum_{i=1}^n (f(x_i) - y_i)^2}{\sum_{i=1}^n f(x_i)^2 - \sum_{i=1}^n (y_i)^2 / n}. \quad (12)$$

These performance indicators can give a sense of how good the performance of a predictive model is relative to the actual value.

MSE can be described as

$$\text{MSE} = \frac{1}{n} \sum_{i=1}^n (f(x_i) - y_i)^2. \quad (13)$$

The RMSE is conventionally used as an error function for quality monitoring of the model. Model performance increases as RMSE decreases. RMSE can be calculated by the following equation:

$$\text{RMSE} = \sqrt{\frac{1}{n} \sum_{i=1}^n (f(x_i) - y_i)^2}. \quad (14)$$

VAF is often used to evaluate the correctness of a model, by comparing the measured values with the estimated output of the model. VAF is computed by the following equation:

$$\text{VAF} = \left( 1 - \frac{\text{var}[f(x_i) - y_i]}{\text{var}f(x_i)} \right) \times 100, \quad (15)$$

where, for (12)–(15),  $y_i$  is the measured data and  $f(x_i)$  denotes the predicted data,  $x_1, \dots, x_n$  are the input parameters, and  $n$  is the total data number.

**4.3. Model Parameters Selection.** As for the ANN, ELM, or USA models, the kernel function and the number of hidden nodes are critical parameters for neural network accuracy.

The accuracy with different hidden layers was compared in terms of RMSE performance indicators. When the kernel function is determined, then increase the hidden numbers incrementally until 100 is reached. Figure 4(a) illustrates the accuracy comparison with different nodes for the ANN, ELM, and USA models, respectively. As for the ELM model, the MSE between prediction results and measured values decreases as the node number of the hidden layer gradually increases with more than 65 nodes. As for the USA model, the MSE between prediction results and measured values also decreases as the node number of the hidden layer gradually increases, except for individual volatility points. As for the ANN model, the MSE between prediction results and measured values was observed in a fluctuant trend as the node number of the hidden layer gradually increases, which indicates that the choice of hidden nodes can greatly affect final accuracy.

Four types of kernels have been tested using a training data set for the ELM model, and they are the sigmoid function, radial-basis function, hardlim function, and triangular function. Figure 4(b) shows the accuracy comparison with different kernel functions for the ELM model. Among the four kernels for the ELM model, the sigmoid-based model comes to the threshold first when the node number is set to 40, while an overfitting problem appears as the node number exceeds 60. The hardlim-based, triangular-based, and radial-basis based models display a similar trend. However, it seems that the node number might exceed 60 when the minimum errors are close to the threshold for the hardlim-based model. For the triangular-based model, the RMSE reaches the lowest point at 3.11% when the node number is set as 85, while the RMSE reaches the lowest point at 3.12% when the node number is set as 95 for radial-basis based models. Figure 4(c) shows the accuracy comparison with different kernel functions for the USA model. Observe that the radial-basis based model comes to the threshold first when the node number is set as 65. As for the hardlim-based model, it seems that the node number might exceed 60 when the minimum

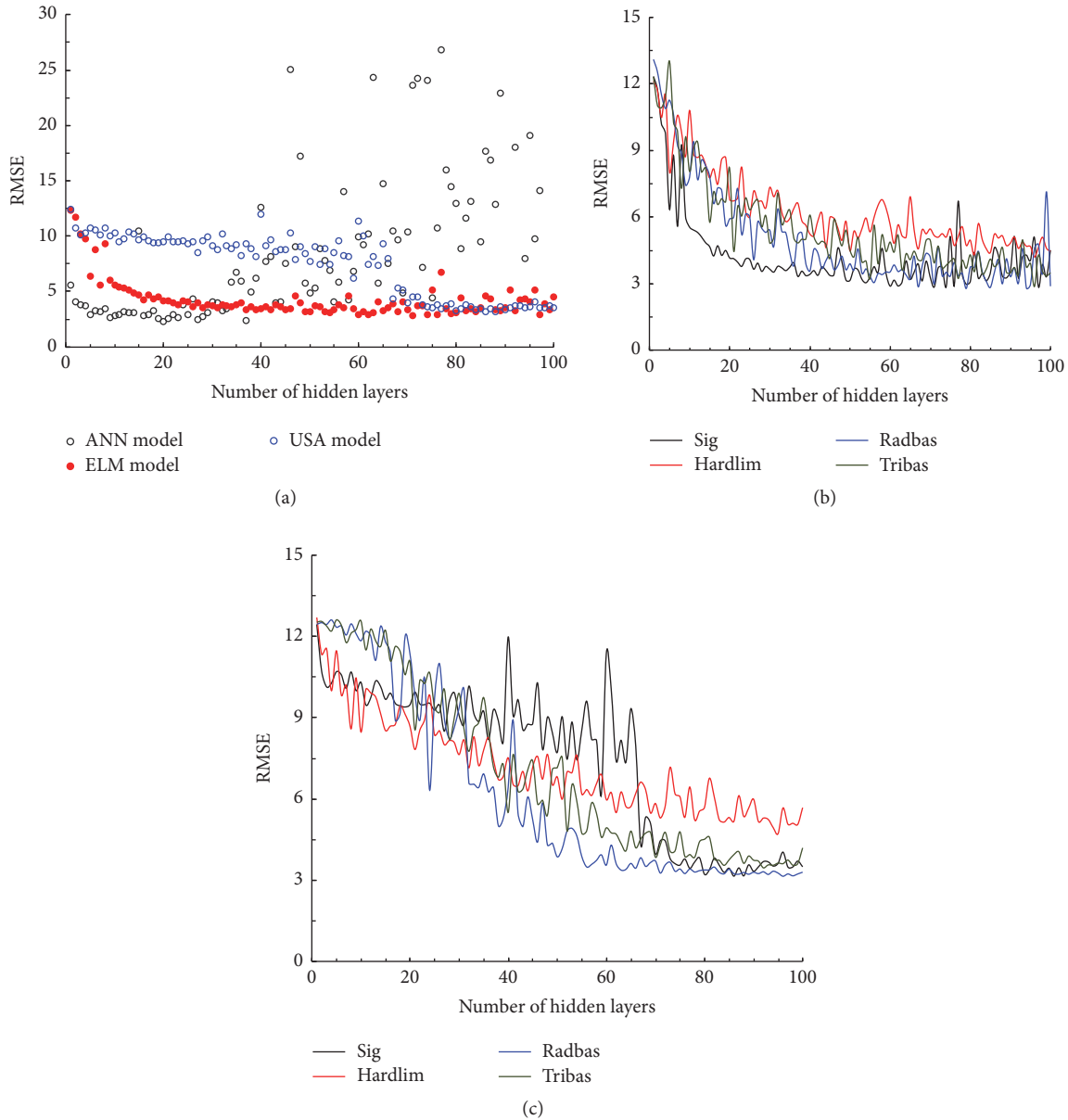


FIGURE 4: (a) The RMSE change with the increase of hidden layers; (b) comparison of RMSE with different kernel functions for the ELM network model; (c) comparison of RMSE with different kernel functions for the USA network model.

errors are close to the threshold, which is similar to the ELM model. The triangular-based and sigmoid-based models display a similar trend: the RMSE reaches the lowest point at 3.11% when the node number is set as 80 for the sigmoid model, while the RMSE reaches the lowest point at 3.48% when the node number is set as 94 for the tribasis based models.

For comparison, the classical ANN model was also used in this paper, and the sigmoid kernel is selected in the ANN model. The applied ANN architecture is a feedforward neural network, which is a network structure in which the information will propagate in one direction from input

to output. A back-propagation algorithm with Levenberg-Marquardt training function has been used for training. This algorithm can approximate any nonlinear continuous function to an arbitrary accuracy. Based on the experimental tests, and when the node number of the hidden layer is set as 36, the ANN network model can obtain the best prediction accuracy.

## 5. Results and Discussion

When the parameters for the neural network model are finally settled, the next step is to validate the model using a testing

TABLE 4: The calculated performance indicators for ANN, ELM, and USA model.

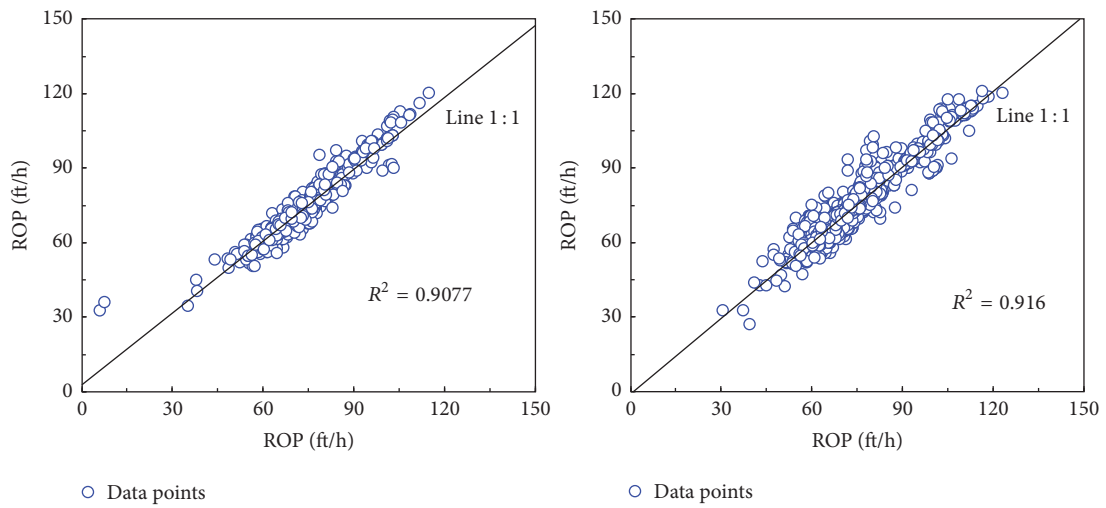
Data set	Performance indicator	ANN	ELM	USA
Training	RMSE	1.51	0.95	0.78
	MAE	7.5	4.2	2.1
	VAF	96.88	100	100
	$R^2$	0.91	0.93	0.98
Testing	RMSE	3.56	3.11	2.76
	MAE	12.7	9.7	7.65
	VAF	91.88	92.82	94.52
	$R^2$	0.90	0.92	0.94

data set. In this section, prediction performance is made between ANN, ELM, and USA models, while training time is recorded. The model accuracy can be evaluated by comparing the calculated RMSE, VAF, MAE, and  $R^2$  performance indicators for training and testing data sets presented in Table 3. Due to random subdivision processes, the performances of the models for training and validation data sets are slightly different. As seen from Table 4, the prediction performance in terms of the predefined indices is better for the testing set than for the training set. Overall,  $R^2$  values for the developed models were more than 0.95 at the training phase, while, in the case of the conventional ANN at the testing phase,  $R^2$  was found to be 0.9. The high performance of the models for the testing set can be considered to be an indication of the good generalization capabilities of the models.  $R^2$  value greater than 0.9 indicates a very satisfactory model performance, while  $R^2$  value between 0.8 and 0.9 indicates an acceptable model. Therefore, all of the developed neural networks are competent for ROP prediction.  $R^2$  of 0.99 for both the ELM and USA models in the training phase indicates higher accuracy compared to the ANN model ( $R^2$  of 0.88). Moreover, it also can be observed that the highest VAF of 94.52, the lowest RMSE of 2.76 and MAE of 7.65 belong to the USA model, indicating that the USA based model gives better prediction performance than the other models. In addition, the ELM model can also produce acceptable results, which yielded slightly fewer residual errors than the ANN models. In other words, the deviation from the observed values of penetration rate predicted by ELM is less than the deviation of the ANN model's prediction. Figure 5 shows the regression analysis of the predicted and measured ROP by different models in both training and testing phases. According to the running speed with the increase of hidden numbers in Figure 6, the obvious differences are observed, concluding that the cost time for the ELM model is less than the other two models. To visualize the quality of the prediction, predicted penetration rates and residual errors by different models are compared with the measured ones for the overall data set and shown in Figures 7 and 8, respectively. This low deviation obtained by three models also proves that ANN, ELM, and USA are competent for ROP prediction. Thus, the ELM and USA methods can both achieve high accuracy and maintain high running speeds. This study shows that ELM technology is a promising tool for ROP prediction, and this work can

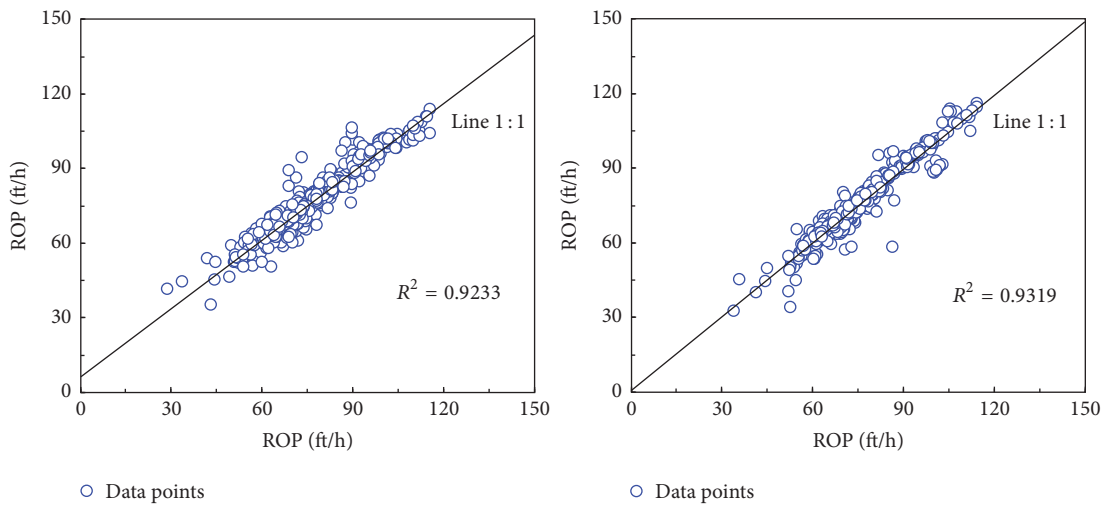
be incorporated into a software system that can be used in drilling optimization guidance.

## 6. Conclusions

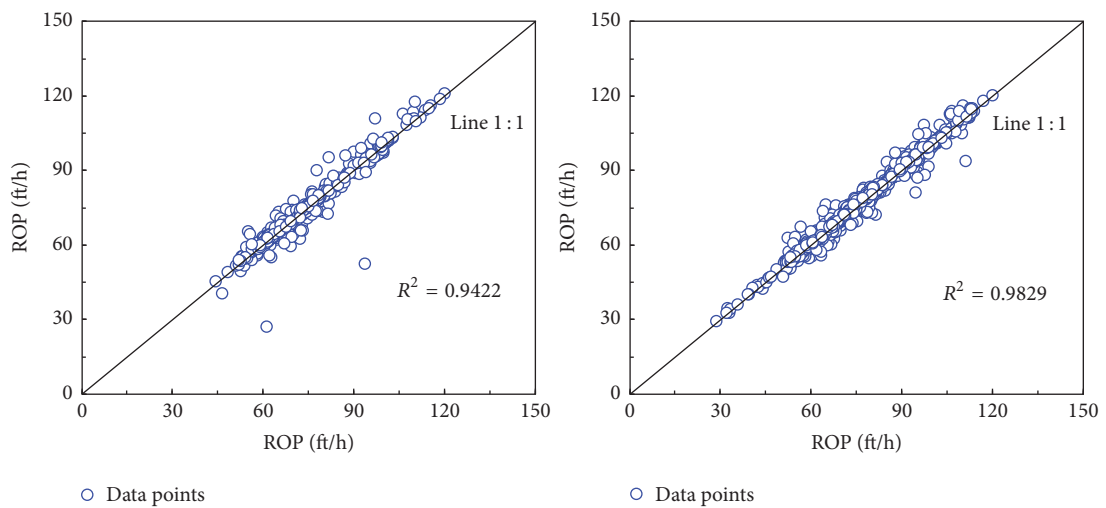
- (1) This study investigates the feasibility of ELM and its variation, the USA model, for predicting the ROP of offshore drilling operations using recorded data. This ELM and USA models can successfully predict ROP in real time, and this prediction can be used as a reference range for drilling engineers identifying drilling problems and making decisions.
- (2) Choosing the relevant parameters is typically difficult, and previous literature informed input selection. Input rock material properties are the uniaxial compressive strengths of the different rock types, formation drillability, and abrasiveness, which can be calculated from lab cores and well logging data. Moreover, the pump pressure and differential pressure are selected as important hydraulic parameters that affect ROP, while RPM and WOB are treated as the equipment operational parameters. In addition to these parameters, drilling mud properties such as mud viscosity and bit related parameters are also involved in developing neural network models. However, for systems with data values beyond the range of this study or for a new bit, it is necessary to develop new neural networks. Conversely, the wider range of input can enable the neural network models developed to have wider applications in select cases.
- (3) The results of the USA model were compared to those of the classical ANN and ELM models. Performance of the models was checked by using  $R^2$ , MAE, RMSE, and VAF performance indicators. According to the performance indicators, all of the neural networks are competent for ROP prediction, but the prediction performances of the USA model were found to be better than those of the other two models with respect to accuracy, while the ELM model had the lowest running speed. Compared to conventional ANN models, the result of this work shows the potential of some fast and flexible neural network approaches to model the ROP with high accuracy while maintaining running speed. Therefore, drilling engineers can make better



(a) ANN testing and training



(b) ELM testing and training



(c) USA testing and training

FIGURE 5: Regression analysis of the predicted and measured ROP.

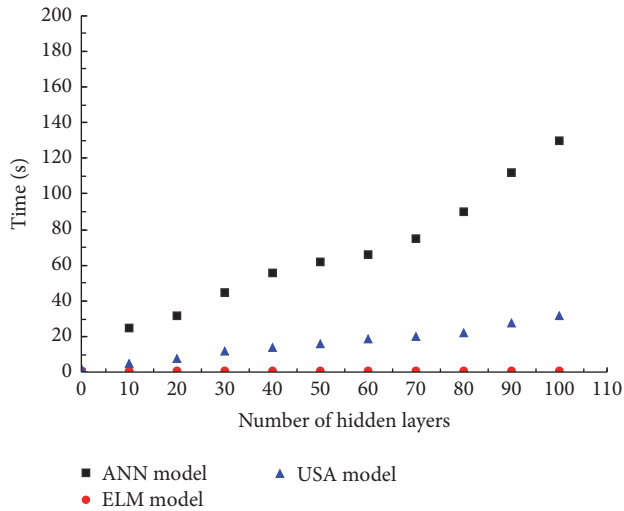


FIGURE 6: Time cost with the change of number of hidden layers.

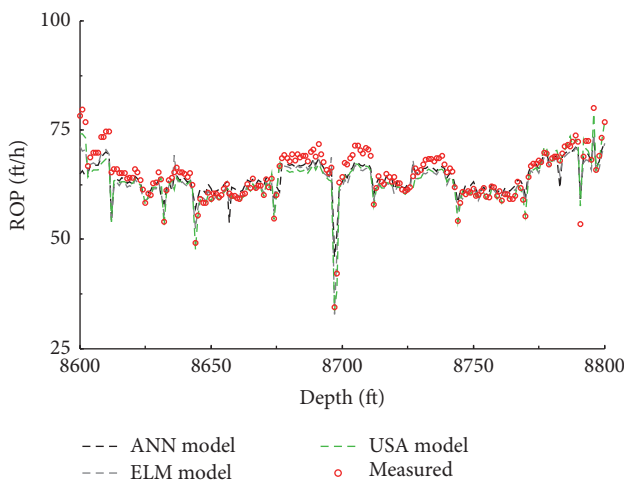


FIGURE 7: The predicted and measured ROP along the depth with developed models.

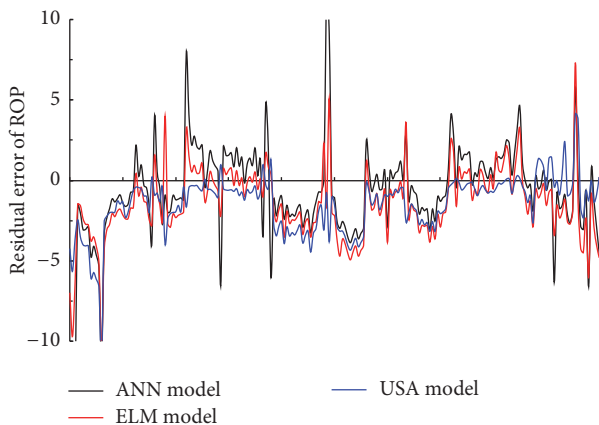


FIGURE 8: Residual errors of predicted ROP by developed models.

choices according to accuracy and computational demand in practical use.

## Competing Interests

The authors declare that there are no competing interests regarding the publication of this paper.

## Acknowledgments

This work was financially supported by the National Key Basic Research Program of China (2015CB251206), Fundamental Research Funds for the Central Universities (nos. 15CX05053A and 15CX08011A and no. 15CX02009A), Qingdao Science and Technology Project (no. 15-9-1-55-jch), National Natural Science Foundation of China (no. 61305075), the Natural Science Foundation of Shandong Province (no. ZR2013FQ004), and the Specialized Research Fund for the Doctoral Program of Higher Education of China (no. 20130133120014).

## References

- [1] V. P. Perrin, M. G. Wilmot, and W. L. Alexander, "Drilling index—a new approach to bit performance evaluation," in *Proceedings of the SPE/IADC Drilling Conference*, Paper SPE 37595, pp. 199–205, Amsterdam, The Netherlands, March 1997.
- [2] M. Bataee and S. Mohseni, "Application of artificial intelligent systems in ROP optimization: a case study in Shadegan oil field," in *Proceedings of the SPE Middle East Unconventional Gas Conference and Exhibition (UGAS '11)*, pp. 13–22, February 2011.
- [3] M. H. Bahari, A. Bahari, F. N. Moharrami, and M. B. N. Sistani, "Determining Bourgoyne and Young model coefficients using genetic algorithm to predict drilling rate," *Journal of Applied Sciences*, vol. 8, no. 17, pp. 3050–3054, 2008.
- [4] D. F. Howarth, W. R. Adamson, and J. R. Berndt, "Correlation of model tunnel boring and drilling machine performances with rock properties," *International Journal of Rock Mechanics and Mining Sciences*, vol. 23, no. 2, pp. 171–175, 1986.
- [5] S. Kahraman, "Correlation of TBM and drilling machine performances with rock brittleness," *Engineering Geology*, vol. 65, no. 4, pp. 269–283, 2002.
- [6] S. Akin and C. Karpuz, "Estimating drilling parameters for diamond bit drilling operations using artificial neural networks," *International Journal of Geomechanics*, vol. 8, no. 1, pp. 68–73, 2008.
- [7] V. Uboldi, L. Civolani, and F. Zausa, "Rock strength measurements on cuttings as input data for optimizing drill bit selection," in *Proceedings of the SPE Annual Technical Conference and Exhibition*, Paper SPE 56441, pp. 35–43, Houston, Tex, USA, October 1999.
- [8] M. J. Fear, "How to improve rate of penetration in field operations," in *Proceedings of the SPE/IADC Drilling Conference*, Paper SPE 55050, New Orleans, La, USA, 1998.
- [9] R. Rommetveit, K. S. Bjørkevoll, G. W. Halsey et al., "Drilltronics: an integrated system for real-time optimization of the drilling process," in *Proceedings of the IADC/SPE Drilling Conference*, vol. 87124, pp. 275–282, SPE, Dallas, Tex, USA, March 2004.

- [10] A. H. Paiaman, M. K. Ghassem Al-Askari, B. Salmani, B. D. Al-Anazi, and M. Masihi, "Effect of drilling fluid properties on rate of Penetration," *NAFTA*, vol. 60, no. 3, pp. 129–134, 2009.
- [11] A. Bahari and A. B. Seyed, "Trust region approach to find constants of Bourgoyne and Young penetration rate model in Khangiran Iranian gas field," in *Proceedings of the SPE Latin American and Caribbean Petroleum Engineering Conference*, Paper SPE 107520, Buenos Aires, Argentina, 2007.
- [12] H. I. Bilgesu, L. T. Tetrick, U. Altmis, Sh. Mohaghegh, and S. Ameri, "A new approach for the prediction of penetration (ROP) values," in *Proceedings of the SPE Eastern Regional Meeting*, Paper SPE 39231, Loaington, Kentucky, 1997.
- [13] R. Jahanbakhshi, R. Keshavarzi, and A. Jafarnezhad, "Real-time prediction of rate of penetration during drilling operation in oil and gas wells," in *Proceedings of the 46th US Rock Mechanics/ Geomechanics Symposium*, pp. 2390–2396, Chicago, Ill, USA, June 2012.
- [14] S. Yilmaz, C. Demircioglu, and S. Akin, "Application of artificial neural networks to optimum bit selection," *Computers and Geosciences*, vol. 28, no. 2, pp. 261–269, 2002.
- [15] H. Rahimzadeh, M. Mostofi, A. Hashemi, and K. Salahshoor, "Comparison of the penetration rate models using field data for one of the gas fields in Persian Gulf Area," in *Proceedings of the International Oil and Gas Conference and Exhibition*, Paper SPE 131253, Beijing, China, 2010.
- [16] G.-B. Huang, D. H. Wang, and Y. Lan, "Extreme learning machines: a survey," *International Journal of Machine Learning and Cybernetics*, vol. 2, no. 2, pp. 107–122, 2011.
- [17] G.-B. Huang, H. Zhou, X. Ding, and R. Zhang, "Extreme learning machine for regression and multiclass classification," *IEEE Transactions on Systems, Man, and Cybernetics, Part B: Cybernetics*, vol. 42, no. 2, pp. 513–529, 2012.
- [18] A. Mozaffari and N. L. Azad, "Optimally pruned extreme learning machine with ensemble of regularization techniques and negative correlation penalty applied to automotive engine cold-start hydrocarbon emission identification," *Neurocomputing*, vol. 131, pp. 143–156, 2014.
- [19] R. Moreno, F. Corona, A. Lendasse, M. Graña, and L. S. Galvão, "Extreme learning machines for soybean classification in remote sensing hyperspectral images," *Neurocomputing*, vol. 128, pp. 207–216, 2014.
- [20] D. Yu and D. Li, "Efficient and effective algorithms for training single-hidden-layer neural networks," *Pattern Recognition Letters*, vol. 33, no. 5, pp. 554–558, 2012.
- [21] C. Gokceoglu and K. Zorlu, "A fuzzy model to predict the uniaxial compressive strength and the modulus of elasticity of a problematic rock," *Engineering Applications of Artificial Intelligence*, vol. 17, no. 1, pp. 61–72, 2004.
- [22] J. Zhang, J. Li, Y. Hu, and J. Zhou, "The identification method of igneous rock lithology based on data mining technology," *Applied Mechanics and Materials*, vol. 466–467, pp. 65–69, 2012.
- [23] J. Cao, J. Yang, Y. Wang, D. Wang, and Y. Shi, "Extreme learning machine for reservoir parameter estimation in heterogeneous sandstone reservoir," *Mathematical Problems in Engineering*, vol. 2015, Article ID 287816, 10 pages, 2015.
- [24] E. Khamehchi, I. R. Kivi, and M. Akbari, "A novel approach to sand production prediction using artificial intelligence," *Journal of Petroleum Science and Engineering*, vol. 123, pp. 147–154, 2014.
- [25] K. Amar and A. Ibrahim, "Rate of penetration prediction and optimization using advances in artificial neural networks, a comparative study," in *Proceedings of the 4th International Joint Conference on Computational Intelligence (IJCCI '12)*, pp. 647–652, Barcelona, Spain, October 2012.
- [26] D. Moran, H. Ibrahim, A. Purwanto, and J. Osmond, "Sophisticated ROP prediction technology based on neural network delivers accurate results," in *Proceedings of the IADC/SPE Asia Pacific Drilling Technology Conference and Exhibition*, SPE 132010, pp. 100–108, Ho Chi Minh City, Vietnam, November 2010.
- [27] M. Monazami, A. Hashemi, and M. Shahbazian, "Drilling rate of penetration prediction using artificial neural network: a case study of one of Iranian southern oil fields," *Journal of Oil and Gas Business*, no. 6, pp. 21–31, 2012.
- [28] G.-B. Huang, Q.-Y. Zhu, and C.-K. Siew, "Extreme learning machine: theory and applications," *Neurocomputing*, vol. 70, no. 1–3, pp. 489–501, 2006.
- [29] X. Liu, Y. Chang, H. Lu et al., "Optimizing fracture stimulation in low-permeability oil reservoirs in the ordos basin," in *Proceedings of the SPE Asia Pacific Oil and Gas Conference and Exhibition*, Paper SPE158562, Perth, Australia, 2012.

## Research Article

# Using EVT for Geological Anomaly Design and Its Application in Identifying Anomalies in Mining Areas

Feilong Qin,<sup>1</sup> Bingli Liu,<sup>1,2</sup> and Ke Guo<sup>1</sup>

<sup>1</sup>Chengdu University of Technology, The Key Laboratory of Mathematical Geology in Sichuan, Chengdu 610059, China

<sup>2</sup>Institute of Geophysical and Geochemical Exploration, Chinese Academy of Geoscience, Langfang 065000, China

Correspondence should be addressed to Bingli Liu; liubingli-82@163.com

Received 28 April 2016; Revised 21 July 2016; Accepted 21 August 2016

Academic Editor: Cheng-Tang Wu

Copyright © 2016 Feilong Qin et al. This is an open access article distributed under the Creative Commons Attribution License, which permits unrestricted use, distribution, and reproduction in any medium, provided the original work is properly cited.

A geological anomaly is the basis of mineral deposit prediction. Through the study of the knowledge and characteristics of geological anomalies, the category of extreme value theory (EVT) to which a geological anomaly belongs can be determined. Associating the principle of the EVT and ensuring the methods of the shape parameter and scale parameter for the generalized Pareto distribution (GPD), the methods to select the threshold of the GPD can be studied. This paper designs a new algorithm called the EVT model of geological anomaly. These study data on Cu and Au originate from 26 exploration lines of the Jiguanzui Cu-Au mining area in Hubei, China. The proposed EVT model of the geological anomaly is applied to identify anomalies in the Jiguanzui Cu-Au mining area. The results show that the model can effectively identify the geological anomaly region of Cu and Au. The anomaly region of Cu and Au is consistent with the range of ore bodies of actual engineering exploration. Therefore, the EVT model of the geological anomaly can effectively identify anomalies, and it has a high indicating function with respect to ore prospecting.

## 1. Introduction

In mineral deposit prediction, searching for mineral deposits requires identification of a geological anomaly indicating that the economic value is high (“as discussed by Darehshiri et al. [1]”). A geological anomaly is a geological body or complex of bodies with obvious different compositions, structures, or orders of genesis as compared with the surrounding circumstances (“as discussed by Lu and Zhao [2]”). With the evolution of the earth, the nature, source, and intensity of force will not be the same across different times and space. In addition, the distribution of material of the earth is not uniform in time and space, which results in different events and responses, such as the tension and compression of layers, deposition and erosion of material, subsidence and uplift of the crust, simple and complex structures, and intrusion and ejection of magma; these differences form the geological anomaly (“as discussed by Pengda et al. [3]”). If a numerical value or numerical interval is used as a threshold to represent the background field, the field that is above or below the threshold constitutes a geological anomaly (“as

discussed by Cheng [4]”). The character of the geological anomaly and the size and type of mineral resources are determined by the geological environment, geological age, rock type, and structural background of the formation of the geological anomaly. With the evolution of geology, the geological anomaly has an evolution sequence in the time and space. With respect to time, evolution has the stage; with respect to space, evolution has inheritance and superposition (“as discussed by Freedman and Parsons [5]”).

Not all geological anomalies can form deposits, but the constitution of a geological anomaly is a prerequisite for the formation of deposits (“as discussed by Shen et al. [6]”). Determining which geological anomaly can result in a mineral deposit can allow effective identification of the deposit. Based on the time required for ore formation, a geological anomaly can be classified into a front ore-forming anomaly, an ore-forming anomaly, and a tail ore-forming anomaly (“as discussed by Zhao et al. [7]”). Different factors and combinations of ore-forming geologies have certain special properties related to ore formation. However, various minerals with different genetic, morphological, mineral, and

industrial types are needed to select certain geological factors and combinations. Therefore, it is necessary to find the target anomaly in all of the possible ore-forming geological anomalies; the area of the target anomaly is known as the feasible location for prospecting. According to additional information on ore formation, such as the remote sensing anomaly, geophysical anomaly, and geochemical anomaly, we can find the location of the required ore deposit; these areas are known as the favorable areas for prospecting. With more information on the geological anomaly, the area of the prospecting target will be gradually reduced, making it easy to locate the deposit. Therefore, the geological anomaly is the basis of mineral deposit prediction; it is effective in locating deposits by precisely identifying the geological anomaly. Therefore, it is important to identify more reasonable methods to locate the geological anomaly. To meet this challenge, various methods have been proposed and successfully applied with respect to the geological anomaly, such as the Three-Component Mineral Prediction theory (“as discussed by Zhao et al. [8]”), the quantitative prediction theory of geological anomaly (“as discussed by Pengda et al. [3]”), and singularity theories and methods for mineral deposit prediction (“as discussed by Cheng and Zhao [9]”). However, each method pertaining to the geological anomaly needs to meet the conditions of the algorithms when they identify the geological anomaly. In fact, not every algorithm satisfies the entire geological environment. Consequently, more algorithms related to the characteristics of the geological anomaly and those based on the environment are needed, which match the extraction criteria of the geological anomaly.

At the International Statistics Congress held in Seoul, Republic of Korea (“as discussed by Chen et al. [10]”), Pengda Zhao described the geological anomaly as an extreme value based on a mathematical foundation. For the geological background, he thought that an abnormal value was the geological anomaly, which directly infers that knowledge of the mathematical foundation of the geological anomaly is of extreme value. The extreme value analysis pertains to research on the random character in the process of quantification at a very large or small level and an estimate of the probability of an extreme event at the existing observational level, while the observation data of the geological anomaly are located in the tail end of the distribution. Therefore, the geological anomaly belongs to the EVT category. The extreme value theorem is a branch of statistics that studies the limiting distribution of the minimum and maximum value and evaluates the risk of extreme events (“as discussed by Allen et al. [11]”). In recent years, the EVT has been widely used in the fields of finance, insurance, floods, earthquakes, rainfall analysis, and so on (“as discussed by Chen and Lv [12]” and “as discussed elsewhere [12–14]”). Since the geological anomaly belongs to the EVT category, the EVT has been widely used in many fields, so we can learn from the experience of these types of applications and design the extreme value model of the geological anomaly that can effectively identify the geological anomaly. Does the EVT model of the geological anomaly really identify anomalies? This study was performed to verify the use of the model to identify anomalies in the Jiguanzui

Cu-Au mining area. The results show that the model can effectively identify the geological anomaly region.

The rest of this paper is organized as follows. Section 2 studies the EVT, the method of selecting the threshold EVT is studied, and some parameters of the EVT are also discussed. Section 3 designs the EVT model of the geological anomaly and provides a new method to increase the accuracy with which the threshold can be selected. The feasibility of using the EVT model to identify the anomaly is discussed. Section 4 will demonstrate the application of the EVT model of the geological anomaly. Some conclusions are presented in Section 5.

## 2. The Study of the EVT

*2.1. The Knowledge Related to the EVT.* In the sample data, if the parent distribution or the sample size is not fully known, the parent distribution can be obtained from the asymptotic distribution of the extreme value of the sample. While the sample data are large, the largest or smallest value from a sample has a degradation problem. However, the extremal type theorem can effectively solve this problem (“as discussed by Vanem [15]”). The extremal type theorem is presented as follows.

If  $x_1, x_2, \dots, x_n$  is a sequence of independent random variables with a common distribution, parent distribution  $F(x)$  is unknown.  $M_n$  is the largest value of the sample interval, and  $H(x)$  is a nondegenerate distribution function. If there exists a sequence of constants  $\{a_n\} > 0$  and  $\{b_n\} \in R$ ,

$$\Pr\left(\frac{M_n - b_n}{a_n} \leq x\right) \rightarrow H(x). \quad (1)$$

$H(x)$  indicates a generalized extreme value distribution. Here,  $a_n$  is a scaling constant and  $b_n$  is a location constant. Then, this limiting distribution  $H(x)$  after standardization  $(M_n - b_n)/a_n$  must be one of the three following types:

$$H(x) = \begin{cases} 0, & x \leq b \\ \exp\left\{-\left(\frac{x-b}{a}\right)^{-\alpha}\right\}, & x > b \end{cases} \quad \alpha > 0, \text{ (FRECHET)}$$

$$H(x) = \begin{cases} \exp\left\{-\left[-\left(\frac{x-b}{a}\right)^{-\alpha}\right]\right\}, & x \leq b \\ 1, & x > b \end{cases} \quad \alpha < 0, \text{ (WEIBULL)}$$

$$H(x) = \exp\left\{-\exp\left[-\left(\frac{x-b}{a}\right)\right]\right\}, \quad x \in R, \text{ (GUMBEL)}.$$

Here,  $\alpha$  is a shape parameter,  $b$  is a location parameter, and  $a$  is a scale parameter.

*2.2. The GPD Model.* In the EVT, the block maxima method (BMM) is a traditional model (“as discussed by Rivas et al.

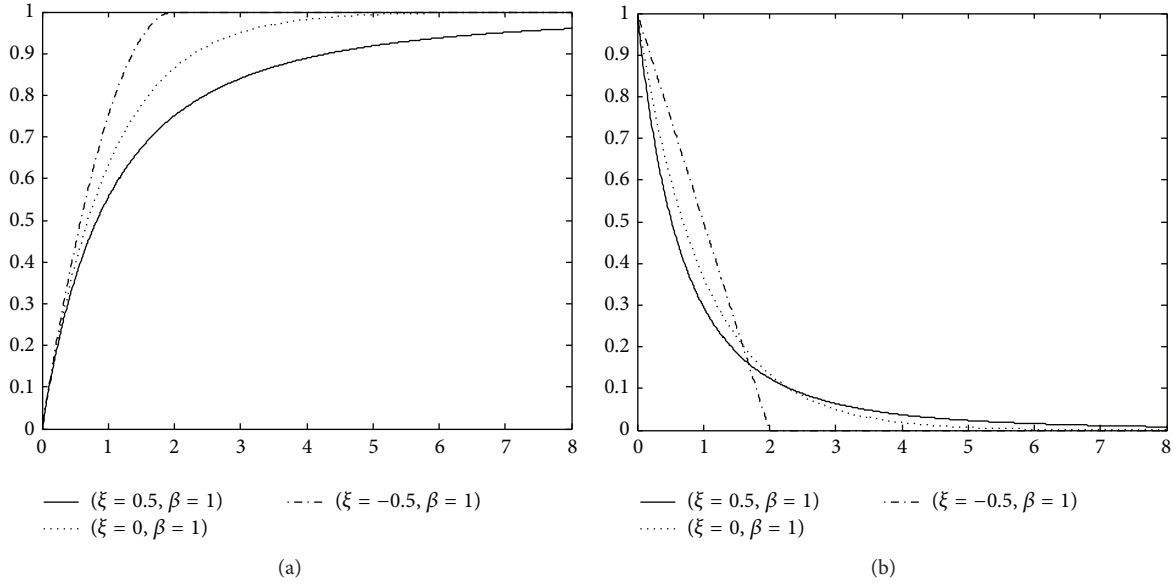


FIGURE 1: The standard GPD: (a) is the distribution function of the GPD and (b) is the density function of the GPD.

[16]). The BMM divides the sample interval into several nonoverlapping cells in accordance with the time, the length, and so on. Then, there is an extreme sequence that is formed by selecting all the maximum values of each small interval; from the extreme sequence, the parent distribution can be obtained by distribution fitting of the extremal type theorem. However, the BMM model has a problem that some maximum values of intervals are greater than those of the other intervals; thus, the validity of the BMM model is not satisfactory. The defects can be solved by generalized Pareto distribution (GPD) (“as discussed by Ashkar and El Adlouni [17]”). The GPD is a fitting of the observed data, which is greater than a certain threshold.

Here,  $x_1, x_2, \dots, x_n$  is a sequence of independent random variables with a common distribution, and  $\mu$  is a sufficiently high threshold. If there is positive number  $\beta$ , the excess distribution ( $x_i - \mu, i = 1, 2, \dots, n$ ) can be expressed as

$$G_{\xi, \beta}(x) = \begin{cases} 1 - \left(1 + \xi \frac{x - \mu}{\beta}\right)^{-1/\xi}, & \xi \neq 0 \\ 1 - e^{-(x - \mu)/\beta}, & \xi = 0, \end{cases} \quad (3)$$

where  $\xi$  is a shape parameter and  $\beta$  is a scale parameter. If  $\xi \geq 0, x \geq \mu$  and  $\xi < 0, \mu \leq x \leq -\beta/\xi + \mu$ . The sequence ( $x_i, i = 1, 2, \dots, n$ ) obeys the GPD. The general formula of the GPD is given by

$$G_{\xi, \beta}(x) = \begin{cases} 1 - \left(1 + \frac{\xi}{\beta} x\right)^{-1/\xi}, & \xi \neq 0 \\ 1 - e^{-x/\beta}, & \xi = 0. \end{cases} \quad (4)$$

Here, if  $\beta = 1$ , the expression of the GPD is referred to as the standard form. If  $\xi = -0.5, 0.5$ , and  $0$ , then the image of the standard distribution function and density distribution function of the GPD is as presented in Figure 1. From

Figure 1(a), it is seen that the tail of the GPD thickens as the shape parameter increases. Figure 1(b) shows that the density function of the GPD decreases monotonically.

The GPD requires estimates of the parameters and threshold. The shape parameter  $\xi$  and scale parameter  $\beta$  of the GPD can be estimated by the maximum likelihood function (“as discussed by Castillo and Serra [18]”). Taking the derivative of (4), we can obtain the density function of the GPD:

$$f_{\xi, \beta}(x) = \frac{1}{\beta} \left(1 + \xi \frac{x}{\beta}\right)^{-1/\xi - 1}. \quad (5)$$

Taking natural logarithms of both sides of (5), we obtain the log likelihood function:

$$L(\xi, \beta : x) = -n \ln \beta - \left(\frac{1}{\xi} + 1\right) \sum_{i=1}^n \ln \left(1 + \frac{\xi}{\beta} x_i\right). \quad (6)$$

Taking the partial derivative of  $\xi$  and  $\beta$  of (6), respectively, the likelihood equation is as follows:

$$n - (1 - \hat{\xi}) \frac{\sum_{i=1}^n x_i}{[\hat{\beta} + \hat{\xi}(x_i)]} = 0, \quad (7)$$

$$\sum_{i=1}^n \ln \left[1 + \frac{\hat{\xi}(x_i)}{\hat{\beta}}\right] - \sum_{i=1}^n \left\{ \frac{x_i}{[\hat{\beta} + \hat{\xi}(x_i)]} \right\} = 0.$$

Thus, the maximum likelihood estimate value  $\hat{\xi}$  of the shape parameter  $\xi$  and the maximum likelihood estimate value  $\hat{\beta}$  of the scale parameter  $\beta$  can be obtained from (7). In addition, the shape parameter and scale parameter of the GPD can be estimated by the moment method; the estimation results obtained by the moment method are superior to those

obtained using the likelihood function (“as discussed by Ergün and Jun [19]”). The moment method is given by

$$\hat{\xi} = \frac{[1 - (\bar{t}/\delta)^2]}{2}, \quad (8)$$

$$\hat{\beta} = \bar{t}(1 - \hat{\xi}),$$

where  $\bar{t}_i = x_i - \mu \geq 0$ ,  $\bar{t}$  is the mean value of  $t_i$ , and  $\delta$  is the standard deviation of  $t_i$ . In the GPD model, the threshold selection methods mainly concern the mean excess function (MEF) (“as discussed by Gencay and Selcuk [20]”) and Hill plotting (“as discussed by J. H. T. Kim and J. Kim [21]”). If random variable  $X$  obeys the GPD, the MEF  $E(\mu)$  is given by

$$E(\mu) = E(X - \mu | X > \mu) = \frac{(\beta + \mu\xi)}{(1 - \xi)}. \quad (9)$$

For the actual sample data,  $E(\mu)$  can be calculated by the following:

$$E(\mu) = \frac{\sum_{i=1}^n (x_i - \mu)^+}{N_n}, \quad (10)$$

where  $n$  is the total number of sample data and  $N_n$  is the total number of sample data that exceed threshold  $\mu$ . If  $x_i \geq \mu$ ,  $(x_i - \mu)^+ = x_i - \mu$  or  $x_i < \mu$ ,  $(x_i - \mu)^+ = 0$ . Then, we can plot scatter diagram  $(\mu, E(\mu))$ . In the scatter diagram, there is sufficiently high threshold  $\mu$ ; when  $x > \mu$ ,  $E(\mu)$  is an approximate linear function.

### 3. Design the EVT Model of the Geological Anomaly

For the actual observational data  $X = \{x_1, x_2, \dots, x_n\}$  of the geological anomaly, the tail distribution of the geological observational data is called the geological anomaly. Therefore, if the data are higher than sufficiently high threshold  $\mu$  in the sample data, we can model these data using the GPD. The parameters of the GPD can be estimated by the moment method or the likelihood function. Threshold  $\mu$  can also be calculated using the MEF or Hill plotting. Thus, the designed EVT model of the geological anomaly is as follows.

*Step 1* (conditional test). Before using the EVT model of the geological anomaly, the stationary and posttail of the sample data need to be tested. The common method of the conditional test is as follows: probability plot and quantile-quantile (Q-Q) plot (“as discussed by Feng et al. [22]”), augmented Dickey-Fuller (ADF) test (“as discussed by Lee and Chang [23]”), and so on.

*Step 2* (estimate the parameters of the model). For the sample data, use the moment method or likelihood function to estimate shape parameter  $\xi$  and scale parameter  $\beta$  of the GPD.

*Step 3* (determine the threshold). Select different thresholds  $\mu$  from the sample data. Then, we can calculate the MEF of the sample data through scatter diagram  $(\mu, E(\mu))$ ; there is

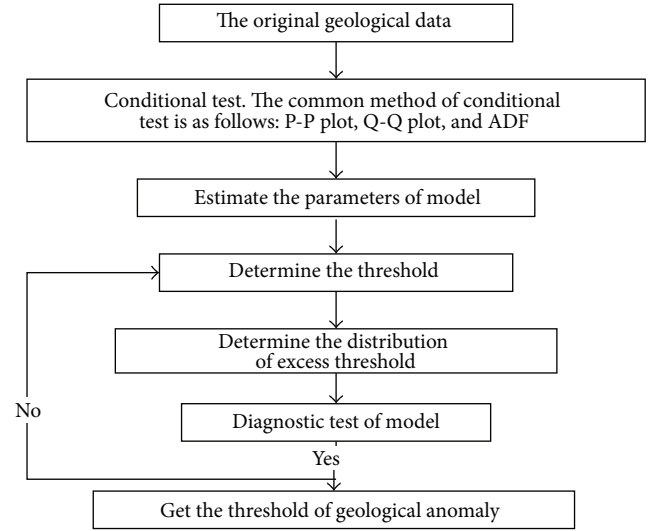


FIGURE 2: The chart of the algorithm.

sufficiently high threshold  $\mu$ , when  $x > \mu$ , and  $E(\mu)$  is an approximate linear function. Here, the value  $\mu$  is called the threshold of the geological anomaly.

*Step 4* (determine the distribution of the excess threshold). After the threshold and parameters are determined, we insert the threshold and parameters into the GPD to obtain the distribution of the excess threshold; this distribution is called the abnormal probability distribution.

*Step 5*. After the distribution of excess threshold is determined, a diagnostic test can determine whether the threshold selection is rational. The diagnostic test of the model mainly tests the consistency between the theoretical distribution and the actual distribution, especially the fitting degree of the actual data and the model distribution. The methods we usually use are the Q-Q plot and probability plot. If the test effect is not satisfactory, repeat Step 3 and determine the new reasonable threshold. The chart of the EVT model of the geological anomaly is shown in Figure 2.

In this study, the determination of threshold  $\mu$  in the EVT model is critical. If the selection of the threshold value is higher, the number of samples that exceed the threshold value is lower, and the parameters of the GPD are very sensitive to the high values of the observational data, which will cause errors in the parameter estimation. Conversely, the selection of a threshold value that is low will increase the number of observations, increasing the accuracy of the estimation of the parameters, but the excess data  $x_i - \mu$  do not obey the GPD distribution. At present, there is no clear method to select the accuracy threshold. The MEF can be used to estimate the threshold with some defects, in which the selection of the threshold is usually an interval value and not an accurate constant. Therefore, this paper provides a new method to increase the accuracy with which the threshold can be selected. In the GPD, when the initial threshold value  $\mu_0$

TABLE 1: The basic statistics of Cu and Au.

Elements	Mean	Minimum	Maximum	Std. dev	CV	Skewness	Kurtosis
Cu	641.44	53.26	17202.77	727.65	1.13	7.38	106.96
Au	70.82	7.13	1877.97	0.25	0.82	8.42	154.93

is determined, the excess data  $x_i - \mu_0$  approximately obey the GPD distribution. Regardless of any threshold  $\mu$  ( $\mu > \mu_0$ ), the shape parameter  $\xi$  and scale parameter  $\beta$  of the GPD should remain unchanged. Therefore, information can be obtained on the transformation relationship between  $\beta(\mu)$  and threshold  $\mu$  ( $\mu > \mu_0$ ) from (3).

$$\beta(\mu) = \beta(\mu_0) + \xi(\mu - \mu_0). \quad (11)$$

Let  $\beta^*(\mu) = \beta(\mu_0) + \xi(\mu - \mu_0)$ ;  $\beta^*(\mu)$  is called the modified scale, and the values of  $\beta^*(\mu)$  will not change when threshold  $\mu$  changes. Therefore, when the interval threshold value is determined by MEF, the accuracy threshold can be estimated by  $\beta^*(\mu)$ . Estimating the threshold using  $\beta^*(\mu)$  is detailed in Section 4.2.

In this paper, the EVT model of the geological anomaly takes full account of the characteristic of the geological anomaly distribution and the practical features of the EVT. Relative to the geological background value, the anomaly and extreme value can be used to describe the geological anomaly. The observations of the geological anomaly are located in the tail of the samples, which are related to the random characters in the process of quantification at the very large or small level and estimate the probability of the extreme event in the existing observation levels—these characteristics are also the contents of the EVT. The EVT is a branch of statistics that studies the limiting distribution of the minimum and maximum value and evaluates the risk of extreme events. Therefore, the mathematical foundation of the geological anomaly is described by the EVT. On the one hand, the EVT describes the characteristic of the geological anomaly distribution from the perspective of mathematics; the results from (3) show the distribution of the sample data, which is proved in (12). On the other hand, the EVT provides a quantitative and digital research method for predicting and evaluating the mineral resources, which is proved in Figure 10. Besides, this paper also discusses the methods of estimate parameters and the threshold of the EVT. Consequently, a mathematical statistical model is established for quantitative geological data and geology information where the data exceed the threshold of the sample in (12). Therefore, the ability of the EVT model to identify the geological anomaly is feasible.

#### 4. The Model Application in Identifying the Geological Anomaly of the Jiguanzui Cu-Au Mining Area

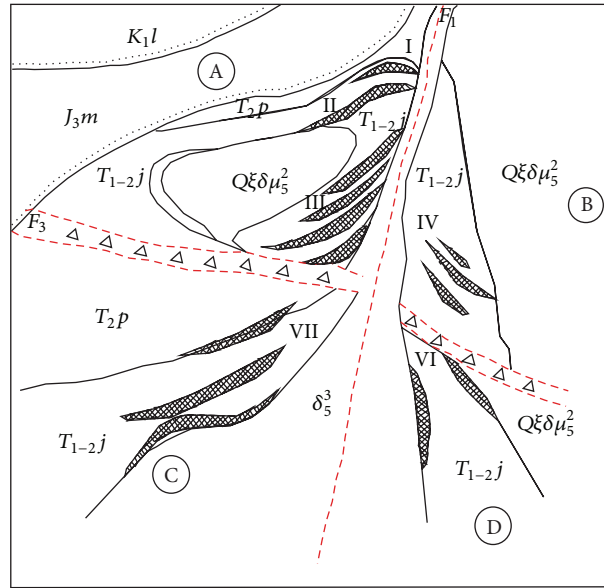
In order to show the effect of identifying the anomaly using the EVT model with geological anomaly recognition, the model was applied to identify the anomaly in an actual mining area. The study data with Cu and Au originate from 26 exploration lines of the Jiguanzui Cu-Au mining area in Hubei, China. The count of the sample data with Cu and Au

is 14309. The Jiguanzui Cu-Au mining deposit is the blind deposits at the lower part of the Quaternary overburden layer. Currently, I, II, III, and VII main ore body groups, 14 main ore bodies, and 105 small fragmentary ore bodies have been identified in the mining area. The main ore bodies of the Jiguanzui Cu-Au mining area are distributed in the 013 to 034 lines, which are 950 meters long, the width is 160–800 meters, the elevation ranges from –5 m to –1412 m deep extension, and the level projection area of the ore bodies is 0.58 square kilometers. The overall distribution of the ore bodies is northeast  $30^\circ$ , the trend of the ore bodies is northeast  $15^\circ - 72^\circ$ , and the local trend of the ore bodies is northwest. I, II, III, and VII ore bodies are arranged in the form of an echelon, in which the tendency is northwest and the local tendency is south. The main ore bodies occur in the fault basin at the edge of the northwestern rock body of the Tonglushan, near the contact zone of the dolomitic marble, the quartz monzonite diorite porphyry, and quartz diorite in the Lower Triassic Jialingjiang Formation, and near the different lithology and the echelon fracture of dolomitic marble. The pattern of the Jiguanzui Cu-Au mining deposit is shown in Figure 3.

##### 4.1. The Condition Test of the Model

**4.1.1. The Posttail Test of Sample Data.** Firstly, this paper analyses the basic statistics of the Cu and Au elements, and the results are shown in Table 1. From Table 1, we can see that the skewness of the sample data is greater than zero, and the sample data are not normally distributed, that is, distributed to the right. By observing the coefficient of variation, it is seen that the coefficient of variation of Au is smaller than that of Cu, and the stability of Au is higher than that of Cu. Besides, the kurtosis of Cu and Au is greater than that of the normal distribution (of which the kurtosis value is 3), which results in a leptokurtic distribution for Cu and Au. Therefore, the distribution of Cu and Au is shown to be skewed to the right with leptokurtic characteristics. Secondly, in order to indicate the difference between the actual distribution and normal distribution, Q-Q plot can be used for the observation test (Figure 4). The distribution of Cu and Au is also shown to be skewed to the right with posttail characteristics.

**4.1.2. The Stationary Test of the Sample Data.** The stationary test mainly inspects the self-correlation of the geological data; the common methods of the stationary test are as follows: the augmented Dickey-Fuller (ADF) and sequence correlation analysis. Through the ADF, we can obtain the test results of the sample data (Table 2). The  $t$ -statistics of Cu and Au are –33.93498 and –13.19081, respectively, which are smaller than their own 1% significant level. Therefore, the sequences of Cu and Au do not have unit roots; they are stationary sequences. The results of the sequence correlation analysis are



- $K_{1l}$  Volcaniclastic rocks of neighboring group
- $J_{3m}$  Breccia of Majiashan group
- $T_{2p}$  Pelitic siltstone of Puqi group
- $T_{1-2j}$  Dolomitic marble of Lower Triassic Jialingjiang Formation
- $Q\xi\delta\mu_5^2$  Quartz monzonite diorite porphyry
- $\delta_5^3$  Diorite
- Fracture
- Stratigraphic boundary
- Unconformity boundary
- Structural breccia
- Ore bodies and numbers
- A The first metallogenic region
- B The second metallogenic region
- C The third metallogenic region
- D The fourth metallogenic region

FIGURE 3: The pattern of the Jiguanzui Cu-Au mining deposit.

TABLE 2: The ADF test of Cu and Au.

Elements	ADT ( $t$ -statistic)	Test critical values			Probability
		1% level	5% level	10% level	
Cu	-33.93498	-2.565127	-1.940847	-1.616685	0
Au	-13.19081	-2.565127	-1.940847	-1.616685	0

shown in Figure 5, where we can see that the autocorrelation coefficients (AC) and the partial autocorrelation coefficient (PAC) are not zero, and the significance of Q-states is high, so the uncorrelated hypothesis cannot be rejected. Therefore, the sequence of the geological data is a stationary time series.

Together, the results indicate that the data follow a stationary sequence, and the distributions of Cu and Au have posttail characteristics, indicating that they are abnormally distributed. Therefore, we can use the EVT model of the geological anomaly to identify the anomaly.

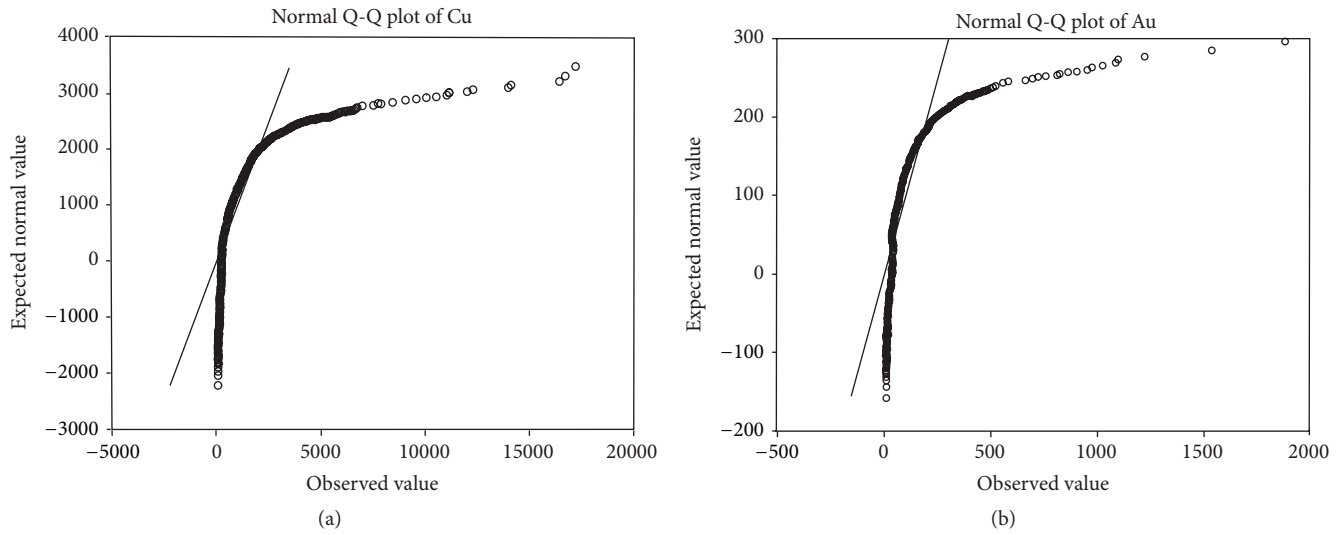


FIGURE 4: The posttail test of the sample data according to Q-Q plot. (a) is Q-Q plot test of Cu and (b) is Q-Q plot test of Au.

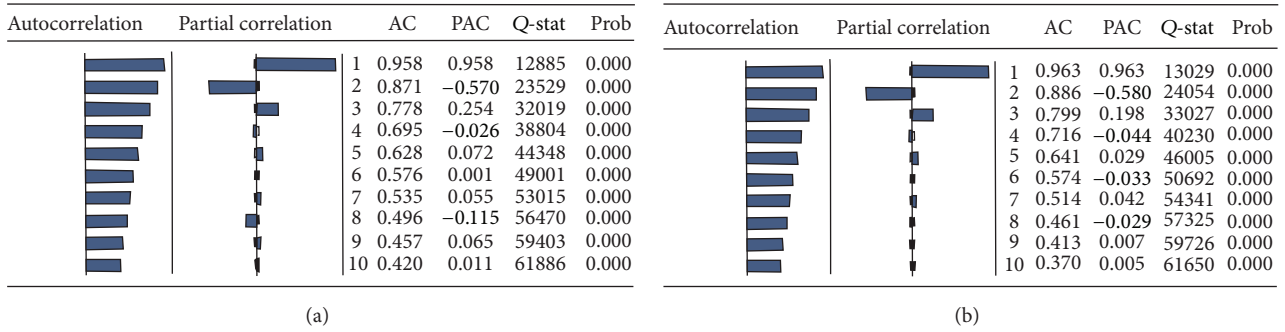


FIGURE 5: The sequence correlation analysis of the sample data. (a) is the sequence correlation analysis of Cu and (b) is the sequence correlation analysis of Au.

4.2. The Solution of the Model

4.2.1. Estimate the Parameters and Threshold. Through the EVT model of the geological anomaly, we can calculate the MEF of Cu and Au and plot the scatter diagram of the MEF (Figure 6). From Figure 6, it is seen that, in the interval [784.5406, 841.3659] with Cu and interval [72.1178, 85.1918] with Au,  $E(\mu)$  for Cu and Au follows an approximately linear distribution. These intervals are selected as the threshold for Cu and Au. As the result of the threshold selection is subjective, modified scale  $\beta^*(\mu)$  is used to estimate the accuracy threshold. Based on  $\beta^*(\mu)$ , if initial threshold value  $\mu_0$  is determined, regardless of any threshold  $\mu (\mu > \mu_0)$ , the shape parameter  $\xi$  and scale parameter  $\beta$  of GPD will not change. Uniformly selecting 50 threshold values from [784.5406, 841.3659] and [72.1178, 85.1918], respectively, we can obtain the transformation relations between  $\beta^*(\mu)$ ,  $\xi$ , and the threshold  $\mu (\mu > \mu_0)$  for Cu and Au using (3) and (11); see Figures 7 and 8. In order to ensure the accuracy of the EVT, the threshold selection is as large as possible in the permissible range of threshold estimation where the data show the stationary characteristic (“as discussed by Cao

and Zhang [24]”). From Figures 7 and 8, it is seen that the threshold of Cu is 816.4006 and that of Au is 75.4736. After the thresholds are determined, the parameters of the EVT model of the geological anomaly can be estimated using the moment method, which reveals that the shape parameter of Cu is 0.3162 and that of Au is 0.3342; the scale parameter of Cu is 440.9216 and that of Au is 31.5699. Then, inserting the thresholds and parameters into the GPD, the distribution of the excess threshold of Cu and Au can be obtained by

$$F_{Cu}(x) = 1 - \left(1 + \frac{0.3162}{440.9216}x\right)^{-1/0.3162},$$

$$F_{Au}(x) = 1 - \left(1 + \frac{0.3342}{31.5699}x\right)^{-1/0.3342}.$$

The distribution of the excess threshold is called the abnormal probability distribution. In the mineral deposit prediction, information on the geological data can be described and expressed by the distribution of the excess threshold.

4.2.2. The Diagnostic Test of the Model and Identification of the Anomaly. The diagnostic test shows whether the

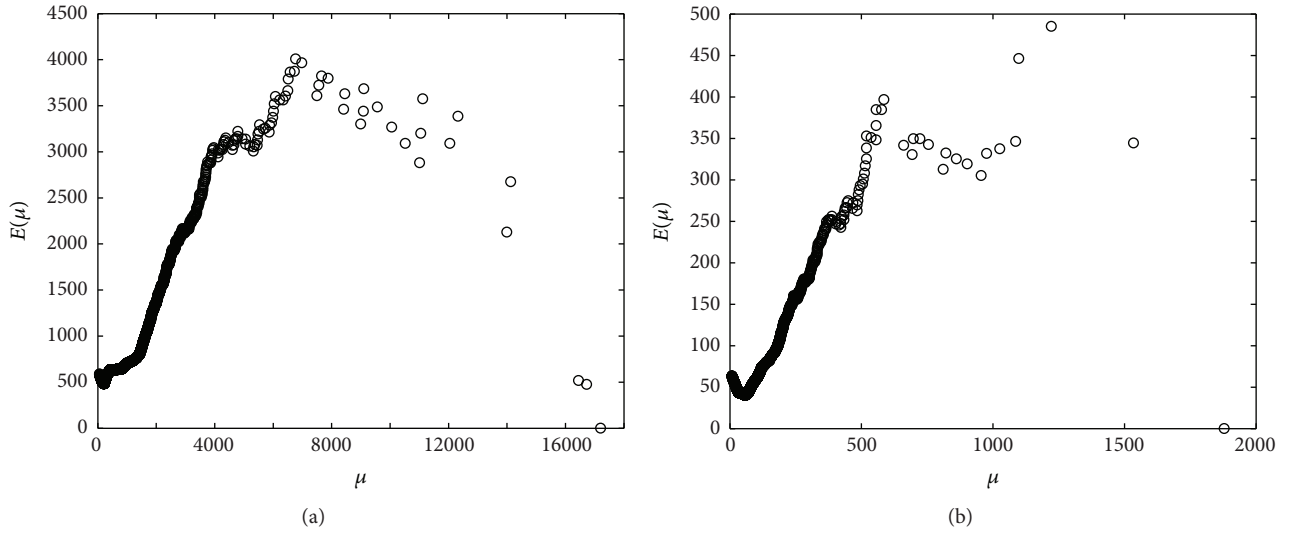


FIGURE 6: The scatter diagram of the MEF. (a) is the MEF of Cu and (b) is the MEF of Au.

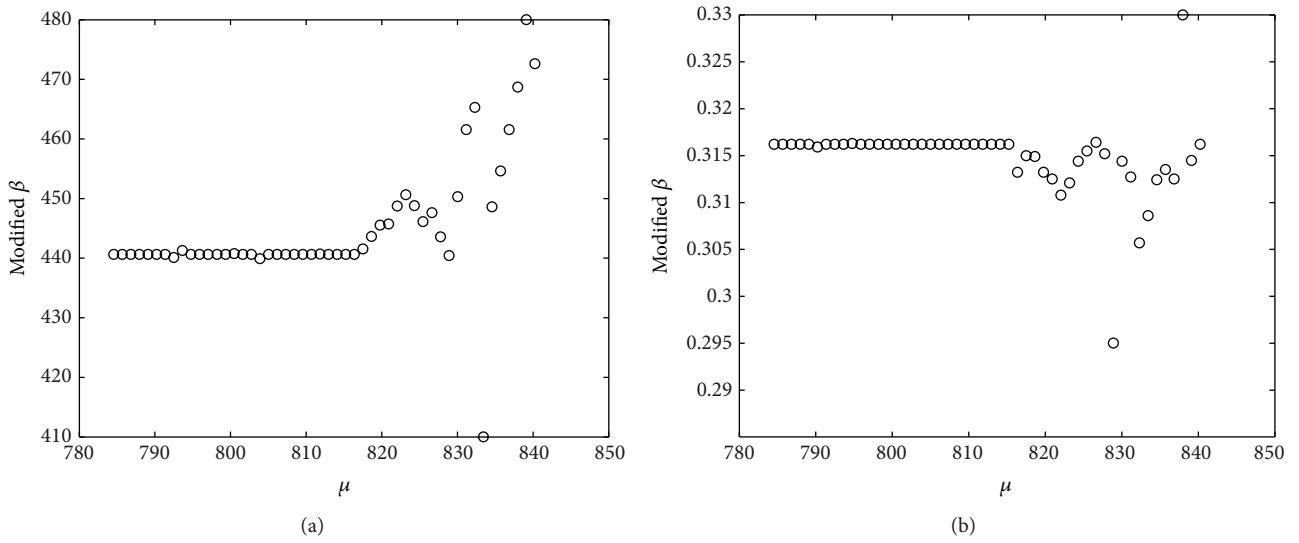


FIGURE 7: (a) and (b) show the relations between  $\beta^*(\mu)$ ,  $\xi$ , and thresholds  $\mu$  of Cu.

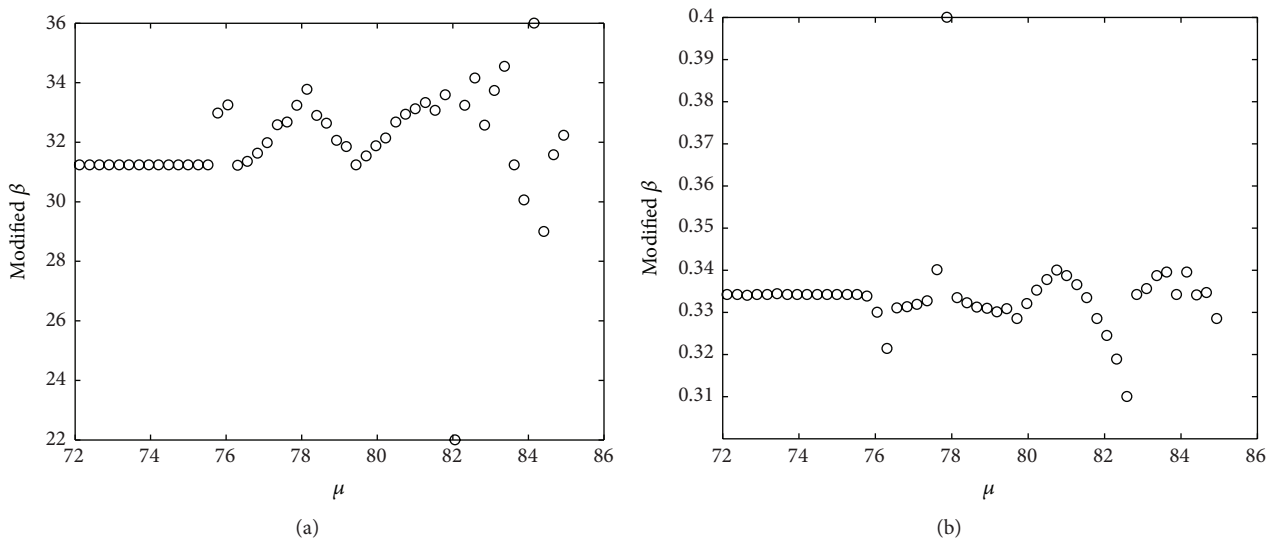


FIGURE 8: (a) and (b) show the relations between  $\beta^*(\mu)$ ,  $\xi$ , and thresholds  $\mu$  of Au.

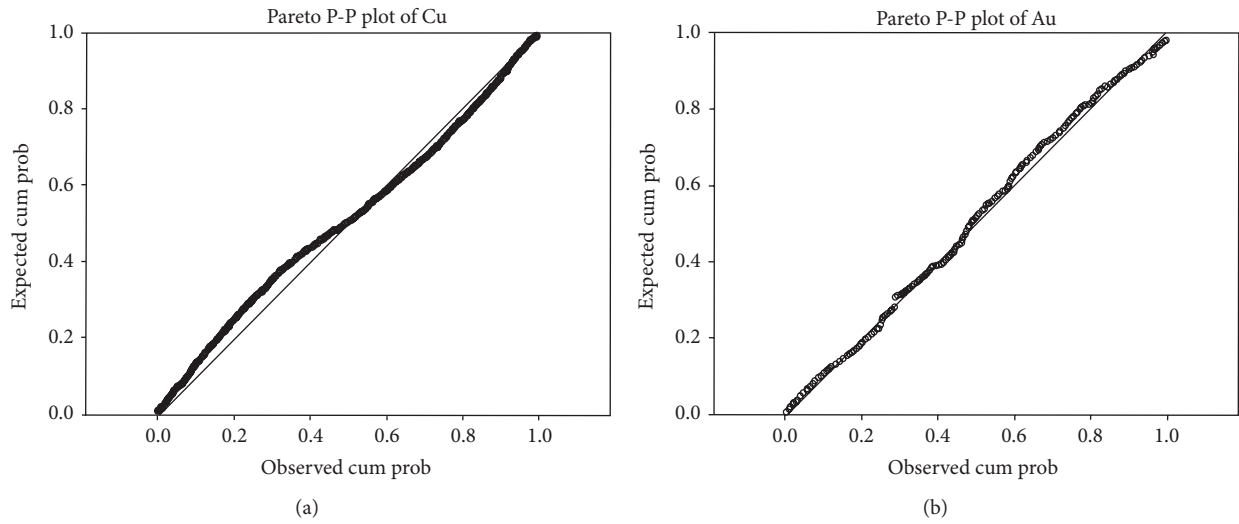


FIGURE 9: The GPD fitting of the sample data. (a) is the distribution fitting of Cu and (b) is the distribution fitting of Au.

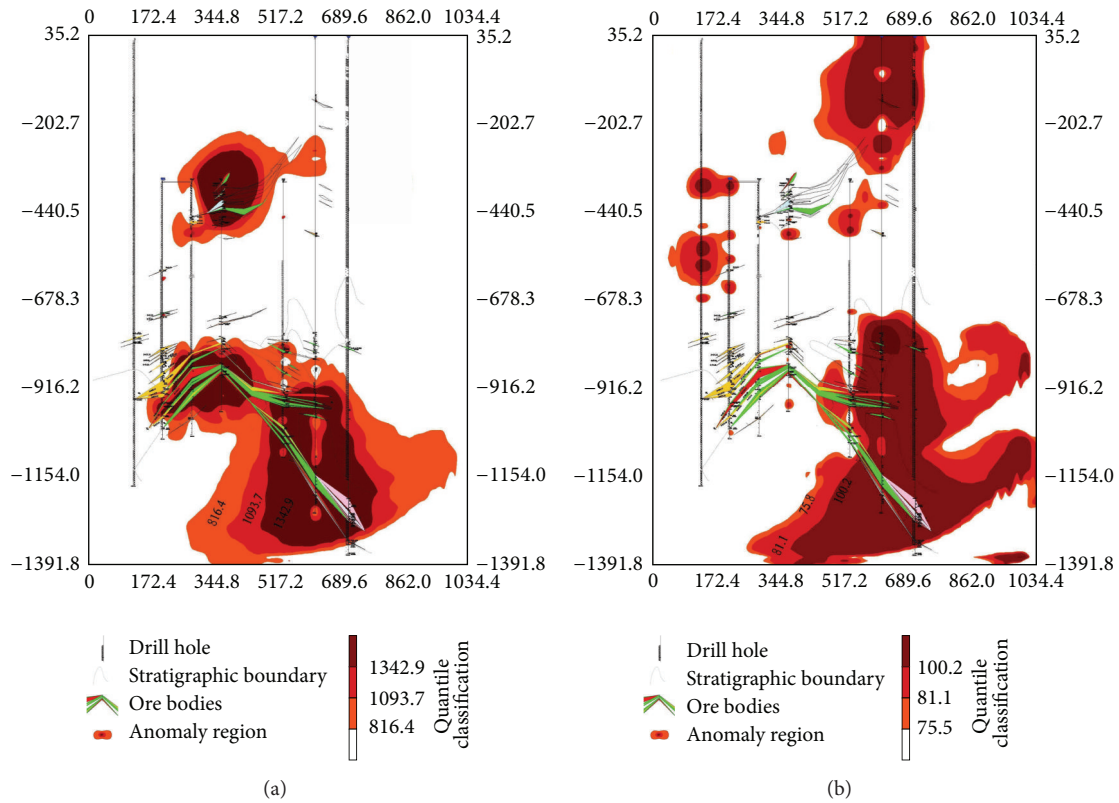


FIGURE 10: The identified anomaly region of Cu and Au. (a) is the anomaly region of Cu and (b) is the anomaly region of Au.

selection of the thresholds is reasonable. Fitting the excess threshold of the sample data using the GPD (Figure 9) indicates that the excess threshold of the sample data is in the vicinity of the line; the results show that the theoretical distribution and actual distribution of the sample data are consistent. Therefore, the threshold selection is reasonable. There are currently seven mining drill holes, that is, KZK10, KZK11, KZK23, KZK28, ZK02618, ZK02619, and ZK02620,

and the exploitation ore bodies are mostly VII main ore body in the 26 exploration lines of the Cu-Au mining area. GIS technology is used to show the geological anomaly region with the selection of the thresholds (Figure 10). From Figure 10, it is seen that the anomaly region of Cu and Au is consistent with the range of ore bodies of the actual engineering exploration, which has a high indicating function with respect to ore prospecting. The results show

that the EVT model of the geological anomaly is good at mineral deposit prediction, and it has good prospecting significance.

## 5. Conclusion

In this study, the proposed EVT model of the geological anomaly was applied to identify geochemical anomalies associated with Cu and Au mineralization. The results of this study led to the following:

- (1) The characteristics of the geological anomaly and the principle of EVT were studied; knowledge of the distribution of the EVT coincides with the distribution of the geological anomaly data. The designed EVT model of the geological anomaly takes full account of the characteristic of the geological anomaly and the practical features of the EVT. The threshold selection and parameter estimates of the model were determined.
- (2) The proposed EVT model of the geological anomaly was successfully applied to identify the geological anomaly region in the Jiguanzui Cu-Au mining area. The results show that the anomaly threshold of Cu is 816.4006 and that of Au is 75.4736; the shape parameter of Cu is 0.3162 and that of Au is 0.3342; and the scale parameter of Cu is 440.9216 and that of the Au is 31.5699. The abnormal probability distribution was also determined. Testing the results of the model by fitting the excess threshold of the sample data showed that the results of the theoretical distribution and actual distribution of the sample data were consistent.
- (3) The geological anomalies of Cu and Au predicted by the EVT model are consistent with the range of ore bodies of the actual engineering exploration. The EVT model has a high indicating function with respect to ore prospecting, and it is applicable for the exploration of mineral deposits.

## Competing Interests

The authors declare that they have no competing interests.

## Acknowledgments

This study was supported by the Geophysiochemistry Prospecting Institute of the Academy of Geological Science of China and the Program for the Core of High Spectrum of Primary Halo Geochemical Prospecting Project (no. 12120114002001), and the project of the special funds for universities was supported by the central government—the construction of discipline platform in management engineering theory and quantitative methods (no. 80000-14Z019002). The authors are grateful to the First Geological Brigade of the Hubei Geological Bureau for providing the data. They would also like to express their appreciation for the team members of the Key Laboratory of Mathematical Geology in Sichuan, China. They are grateful to Professor HongJun Liu

at Chengdu University of Technology for providing constructive advice for this study. They also thank LetPub (<http://www.letpub.com/>) for its linguistic assistance during the preparation of this manuscript.

## References

- [1] A. Darehshiri, M. Panji, and A. R. Mokhtari, "Identifying geochemical anomalies associated with Cu mineralization in stream sediment samples in Gharachaman area, northwest of Iran," *Journal of African Earth Sciences*, vol. 110, pp. 92–99, 2015.
- [2] X. Lu and P. Zhao, "Geologic anomaly analysis for space-time distribution of mineral deposits in the middle-lower Yangtze area, southeastern China," *Nonrenewable Resources*, vol. 17, no. 3, pp. 187–196, 1998.
- [3] Z. Pengda, C. Qiuming, and X. Qinglin, "Quantitative prediction for deep mineral exploration," *Journal of China University of Geosciences*, vol. 19, no. 4, pp. 309–318, 2008.
- [4] Q. Cheng, "Singularity theory and methods for mapping geochemical anomalies caused by buried sources and for predicting undiscovered mineral deposits in covered areas," *Journal of Geochemical Exploration*, vol. 122, pp. 55–70, 2012.
- [5] A. P. Freedman and B. Parsons, "Geoid anomalies over two South Atlantic fracture zones," *Earth and Planetary Science Letters*, vol. 100, no. 1–3, pp. 18–41, 1990.
- [6] P. Shen, Y. Shen, T. Liu, L. Meng, H. Dai, and Y. Yang, "Geochemical signature of porphyries in the Baogutu porphyry copper belt, western Junggar, NW China," *Gondwana Research*, vol. 16, no. 2, pp. 227–242, 2009.
- [7] J. Zhao, S. Chen, and R. Zuo, "Identifying geochemical anomalies associated with Au–Cu mineralization using multifractal and artificial neural network models in the Ningqiang district, Shaanxi, China," *Journal of Geochemical Exploration*, vol. 164, pp. 54–64, 2016.
- [8] P. Zhao, J. Chen, J. Chen, S. Zhang, and Y. Chen, "The 'three-component' digital prospecting method: a new approach for mineral resource quantitative prediction and assessment," *Natural Resources Research*, vol. 14, no. 4, pp. 295–303, 2005.
- [9] Q. Cheng and P. Zhao, "Singularity theories and methods for characterizing mineralization processes and mapping geochemical anomalies for mineral deposit prediction," *Geoscience Frontiers*, vol. 2, no. 1, pp. 67–79, 2011.
- [10] Y. Chen, P. Zhao, J. Chen, and J. Liu, "Application of the geo-anomaly unit concept in quantitative delineation and assessment of gold ore targets in western Shandong uplift terrain, eastern China," *Natural Resources Research*, vol. 10, no. 1, pp. 35–49, 2001.
- [11] D. E. Allen, A. K. Singh, and R. J. Powell, "Extreme market risk—an extreme value theory approach," *Mathematics and Computers in Simulation*, vol. 94, pp. 310–328, 2011.
- [12] Q. Chen and X. Lv, "The extreme-value dependence between the crude oil price and Chinese stock markets," *International Review of Economics and Finance*, vol. 39, pp. 121–132, 2015.
- [13] K. Whan, J. Zscheischler, R. Orth et al., "Impact of soil moisture on extreme maximum temperatures in Europe," *Weather and Climate Extremes*, vol. 9, pp. 57–67, 2015.
- [14] D. Faranda, J. M. Freitas, P. Guiraud, and S. Vaienti, "Sampling local properties of attractors via extreme value theory," *Chaos, Solitons and Fractals*, vol. 74, pp. 55–66, 2015.
- [15] E. Vanem, "Non-stationary extreme value models to account for trends and shifts in the extreme wave climate due to climate change," *Applied Ocean Research*, vol. 52, pp. 201–211, 2015.

- [16] D. Rivas, F. Caleyo, A. Valor, and J. M. Hallen, "Extreme value analysis applied to pitting corrosion experiments in low carbon steel: comparison of block maxima and peak over threshold approaches," *Corrosion Science*, vol. 50, no. 11, pp. 3193–3204, 2008.
- [17] F. Ashkar and S.-E. El Adlouni, "Adjusting for small-sample non-normality of design event estimators under a generalized Pareto distribution," *Journal of Hydrology*, vol. 530, pp. 384–391, 2015.
- [18] J. D. Castillo and I. Serra, "Likelihood inference for generalized Pareto distribution," *Computational Statistics & Data Analysis*, vol. 83, pp. 116–128, 2015.
- [19] A. T. Ergün and J. Jun, "Time-varying higher-order conditional moments and forecasting intraday VaR and Expected Shortfall," *The Quarterly Review of Economics and Finance*, vol. 50, no. 3, pp. 264–272, 2010.
- [20] R. Gencay and F. Selcuk, "Extreme value theory and value-at-risk: relative performance in emerging markets," *International Journal of Forecasting*, vol. 20, pp. 287–303, 2004.
- [21] J. H. T. Kim and J. Kim, "A parametric alternative to the Hill estimator for heavy-tailed distributions," *Journal of Banking & Finance*, vol. 54, pp. 60–71, 2015.
- [22] Z.-H. Feng, Y.-M. Wei, and K. Wang, "Estimating risk for the carbon market via extreme value theory: an empirical analysis of the EU ETS," *Applied Energy*, vol. 99, pp. 97–108, 2012.
- [23] C.-C. Lee and C.-P. Chang, "New evidence on the convergence of per capita carbon dioxide emissions from panel seemingly unrelated regressions augmented Dickey-Fuller tests," *Energy*, vol. 33, no. 9, pp. 1468–1475, 2008.
- [24] G. Cao and M. Zhang, "Extreme values in the Chinese and American stock markets based on detrended fluctuation analysis," *Physica A: Statistical Mechanics and its Applications*, vol. 436, pp. 25–35, 2015.

## Research Article

# An Improved Ant Colony Algorithm for Solving the Path Planning Problem of the Omnidirectional Mobile Vehicle

**Jiang Zhao, Dingding Cheng, and Chongqing Hao**

*School of Electrical Engineering, Hebei University of Science and Technology, Hebei, Shijiazhuang 050018, China*

Correspondence should be addressed to Dingding Cheng; [chengdingding0306@126.com](mailto:chengdingding0306@126.com)

Received 20 May 2016; Accepted 21 August 2016

Academic Editor: Cheng-Tang Wu

Copyright © 2016 Jiang Zhao et al. This is an open access article distributed under the Creative Commons Attribution License, which permits unrestricted use, distribution, and reproduction in any medium, provided the original work is properly cited.

This paper presents an improved ant colony algorithm for the path planning of the omnidirectional mobile vehicle. The purpose of the improved ant colony algorithm is to design an appropriate route to connect the starting point and ending point of the environment with obstacles. Ant colony algorithm, which is used to solve the path planning problem, is improved according to the characteristics of the omnidirectional mobile vehicle. And in the improved algorithm, the nonuniform distribution of the initial pheromone and the selection strategy with direction play a very positive role in the path search. The coverage and updating strategy of pheromone is introduced to avoid repeated search reducing the effect of the number of ants on the performance of the algorithm. In addition, the pheromone evaporation coefficient is segmented and adjusted, which can effectively balance the convergence speed and search ability. Finally, this paper provides a theoretical basis for the improved ant colony algorithm by strict mathematical derivation, and some numerical simulations are also given to illustrate the effectiveness of the theoretical results.

## 1. Introduction

Path planning, which is one of the hot topics in motion control research, requires the control object to determine the path, avoid obstacles, and achieve the goal autonomously [1]. As a special kind of mobile robot, the omnidirectional mobile robot has wide application in the field of industrial transportation. With the increase of production cost and work efficiency, the path planning problem of the omnidirectional mobile vehicle needs to be resolved as soon as possible. The path planning problem of mobile robot was proposed in the 1960s. With the research of Lozano-Perez and Wesley [2], the problem has aroused the interest of many scholars.

Simulated annealing algorithm [3], potential function theory [4], genetic algorithm [5], particle swarm algorithm [6], and ant colony algorithm [7] are representative methods of path planning, which can find the shortest path. In addition, the research on path planning has made great progress in recent years. The idea of Mo and Xu [8] solved the path planning by PSO with the position updating strategy and biogeography particle swarm optimization algorithm to increase the diversity of population and optimize the paths

in a static environment. Precup et al. [9] proposed that the adaptive charged system search algorithm was applied to the optimal path planning problem of multiple mobile robots in static environment. Several modifications and improvements of A star algorithm were introduced by Ducho et al. [10] and Guruji et al. [11] considering a static or dynamic environment. And it was the first time that MOVNS [12] was proposed to deal with the path planning problem of mobile robots about the path safety, length, and smoothness. In addition, many other findings also made contributions to the related path planning problem [13–15].

Many scholars applied ant colony algorithm [16] to solve the path planning problem because it can represent obstacles flexibly and easily by using a tabu list. On this basis, the further research was carried out. Later, according to the characteristics of the above algorithms, some methods combined ant colony algorithm and other algorithms which were proposed and had more advantages than one algorithm, such as ant colony particle swarm algorithm [2] and ant colony genetic algorithm [17]. However, the application of ant colony algorithm is much more than that. As discussed by Tiwari and Vidyarthi [18], the ant colony optimization algorithm solved



FIGURE 1: The omnidirectional mobile vehicle.

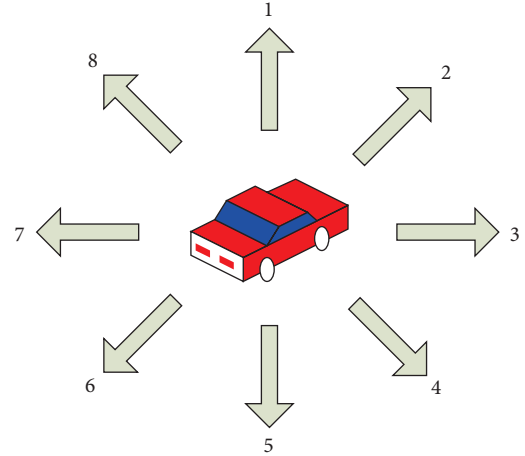


FIGURE 2: Basic motion directions.

the scheduling problem effectively through a kind of special ants that remain alive till the fitter lazy ants are generated in the successive generations. Wang et al. [19] proposed a modified ACS scheme that can identify the true attack path even without the entire network routing information. Jiang et al. [20] presented a coevolutionary improved multi-ant colony optimization algorithm to design appropriate pipe routes in the layout space under various kinds of constraints. What is more, Saidi-Mehrabad et al. [21] also made some improvements to the ant colony algorithm to solve the problem. Therefore, solving the problem in accordance with the feature of the control object, environment, and existing methods is the best way.

So, accordingly, ant colony algorithm is a key point, because it is the basis of the above methods. Therefore, based on the motion characteristics of omnidirectional mobile vehicle, this paper proposes a kind of improved ant colony algorithm. The initial pheromone distribution is nonuniform, which helps reduce the blindness of the search. In the strategy of selection, heuristic information with direction is introduced to improve the probability of finding the optimal solution. And piecewise adjusting pheromone behavior helps avoid falling into local optimal solution. Finally, the pheromone coverage and updating strategy can ensure that the algorithm can find the optimal path strictly in theory.

## 2. Problem Statement

**2.1. Control Object.** As we all know, solving the path planning problem in accordance with the feature of the control object is the best way. Different from mobile robot, the omnidirectional mobile vehicle, as shown in Figure 1, is equipped with chassis and drive which can contribute to moving in any direction. In terms of its control system, the omnidirectional mobile vehicle has 8 basic motion units, upper, upper right, right, lower right, lower, lower left, left, and upper left, as shown in Figure 2. Therefore, its form of motion, which is the output of the motion path, can be composed of a number of basic motion units.

**2.2. Problem Description.** Without considering the omnidirectional mobile vehicle height, the working environment can be considered as a two-dimensional plane. So the path planning needs to solve three problems:

- (1) In a nonchanging work environment, find a path to connect the starting point and the ending point.
- (2) Find the shortest path with avoiding all obstacles.
- (3) The algorithm should have certain simplicity, low complexity, and good stability.

## 3. Mathematical Model

**3.1. Environment Model.** In practical applications, the electronic map is often needed to represent the working environment. This paper describes the work environment using the grid method in which the grid coordinates are replaced by the position of each center point. So working environment is divided into  $M * N$  squares. And the obstacles are represented by gray grids (less than one by one count) distinguishing them from available parts. The area is numbered from top to bottom and from left to right in the literature [22], while the squares can be represented by the set of numbered  $B = \{1, 2, \dots, b, \dots, M * N\}$  which is shown in Figure 3. In order to identify obstacles, the white grid cell is represented by 0 and the gray grid unit is represented by 1. Thus, the working environment is represented by  $M * N$  binary matrix, which is denoted by  $G$ .

**3.2. Path Representation.** It can be known from the characteristics of the omnidirectional mobile vehicle and the environment representation that the resolution of the system is related to the number of grids. Finally, the path is obtained by adding the components of the solution step by step to obtain the solution. The path of the vehicle can be expressed as  $L = \{(x_1, y_1), \dots, (x_i, y_i), \dots, (x_{t-1}, y_{t-1}), (x_t, y_t)\}$ , the starting point is  $(x_1, y_1)$  denoted as  $S$ , and the ending point coordinate is  $(x_t, y_t)$  denoted as  $E$ . From the environmental model, we can know that the path can be expressed by the

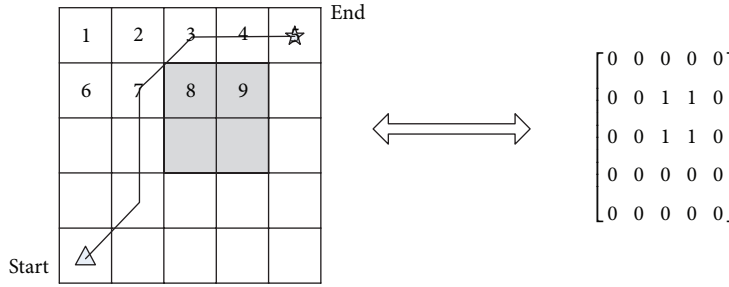


FIGURE 3: Mathematical model of working environment.

grid number  $L = \{l_1, \dots, l_i, \dots, l_{t-1}, l_t\}$  and  $(x_i, y_i)$  is replaced by  $l_i, i = 1, \dots, t - 1, t$ .

## 4. Improved Ant Colony Algorithm

### 4.1. Improvement Aspects

(1) *Nonuniform Distribution of Initial Pheromone.* In the initial phase of traditional ant colony algorithm, the pheromone distribution is described by  $M * N$  dimensional matrix, where the element  $\tau_b \in T$  represents the initial value of pheromone in  $b$  grid. As shown below,

$$\tau_b = c_0 \quad c_0 \text{ is a constant.} \quad (1)$$

To solve the problems of lack of initial pheromone and low speed of search, in literatures [10, 11] particle swarm optimization algorithm and genetic algorithm are proposed to generate an initial path which can be transformed into the initial pheromone distribution so as to reduce the blindness of the ant colony search. In order to improve the efficiency and simplicity of the algorithm, the nonuniform distribution of initial pheromone is proposed in this paper. So the pheromone distribution is described by matrix  $T$ , where element  $\tau_b \in T$ , as shown below:

$$\tau_b = \begin{cases} c_0 \times \theta_1 & b \in A \\ c_0 & \text{otherwise,} \end{cases} \quad (2)$$

where  $A$  is the collection of all numbers between number  $l_1$  and  $l_t$ ; that is to say,  $A = \{\min\{l_1, l_t\} + 1, \dots, \max\{l_1, l_t\}\}$ ;  $\theta_1$  is a constant greater than 1. Formula (2) indicates that the number of pieces of information between the starting point and the ending point is slightly higher than others. Similar to the principle of the zero point theorem, in view of the characteristics of the path, the probability of an arbitrary path set between the starting point and the ending point is 1. Therefore, the simple initial distribution strategy has advantages to reduce the blindness of ant colony search, shorten the path search time. And at the same time, it does not increase the complexity of the algorithm.

(2) *Heuristic Strategy with Direction Information.* In the traditional ant colony algorithm, the probability of the next node is selected by rotating the roulette wheel method as follows:

$$P_{l_i, l_{i+1}} = \frac{(\tau_{l_i, l_{i+1}})^\alpha (\eta_{l_i, l_{i+1}})^\beta}{\sum_{l_{i+1} \in \text{allowed}(b)} (\tau_{l_i, l_{i+1}})^\alpha (\eta_{l_i, l_{i+1}})^\beta},$$

$$\eta_{l_i, l_{i+1}} = \frac{1}{d_{l_{i+1}, l_t}}, \quad (3)$$

$$d_{l_{i+1}, l_t} = \sqrt{(x_{l_t} - x_{l_{i+1}})^2 + (y_{l_t} - y_{l_{i+1}})^2},$$

where  $P_{l_i, l_{i+1}}$  is the probability of the next node of  $l_i$ ,  $\tau_{l_i, l_{i+1}}$  is the pheromone of the path from  $l_i$  to  $l_{i+1}$ , and  $\alpha$  is the pheromone coefficient. Even  $\eta_{l_i, l_{i+1}}$  is the heuristic information of  $l_i$  to  $l_{i+1}$ , and  $\beta$  is the heuristic information parameter, where  $d_{l_{i+1}, l_t}$  is the distance between node  $l_{i+1}$  and end node  $l_t$ .  $(x_{l_{i+1}}, y_{l_{i+1}})$  and  $(x_{l_t}, y_{l_t})$  are the coordinates of  $l_{i+1}$  and  $l_t$ .

The direction information is proposed as the heuristic information of the node transfer strategy by Wang et al. [19] to solve the path planning problem without obstacle:

$$P_{l_i, l_{i+1}} = \frac{(\tau_{l_i, l_{i+1}})^\alpha (\eta_{l_i, l_{i+1}})^\beta}{\sum_{l_{i+1} \in \text{allowed}(b)} (\tau_{l_i, l_{i+1}})^\alpha (\eta_{l_i, l_{i+1}})^\beta},$$

$$\eta_{l_i, l_{i+1}} = \begin{cases} \theta_2 & \text{if state is toward the goal} \\ 1 & \text{otherwise,} \end{cases} \quad (4)$$

where  $\eta_{l_i, l_{i+1}}$  is the direction of information and  $\theta_2$  is a constant little more than 1. In order to reduce the blindness of the search, the paper puts forward the strategy of the direction information, and the probability formula is

$$P_{l_i, l_{i+1}} = \begin{cases} \frac{(\tau_{l_i, l_{i+1}})^\alpha (\eta_{l_i, l_{i+1}})^\beta \mu_{l_i, l_{i+1}}}{\sum_{l_{i+1} \in \text{allowed}(b)} (\tau_{l_i, l_{i+1}})^\alpha (\eta_{l_i, l_{i+1}})^\beta \mu_{l_i, l_{i+1}}} & l_{i+1} \in \text{the next node} \\ 0 & \text{otherwise,} \end{cases} \quad (5)$$

				☆	End
11	12	13			
16	△	18			
21	22	23			

FIGURE 4: Directional information representation.

where

$$\eta_{l_i, l_{i+1}} = \frac{1}{d_{l_{i+1}, l_i}} \quad (6)$$

$$d_{l_{i+1}, l_i} = \sqrt{(x_{l_i} - x_{l_{i+1}})^2 + (y_{l_i} - y_{l_{i+1}})^2}.$$

The direction information  $\mu_{i, i+1}$  is expressed as follows:

$$\mu_{i, i+1} = \theta_3^\gamma, \quad (7)$$

where  $\gamma$  is the number of the same directions of node  $l_i$  to next  $l_{i+1}$  and node  $l_i$  to end  $l_i$ :  $\gamma = 0, 1, 2$ . And  $\theta_3$  is a constant slightly greater than 1. As shown in Figure 4, the next node of 17 may be 11, 12, 13, 16, 18, 21, 22, and 23, where node 13 has two same directions as the end, so the direction information is  $\theta_3^2$ . And as such, the direction information of nodes 11, 12, 18, and 23 is  $\theta_3^1$ , and for 16, 21, and 22 it is  $\theta_3^0$ .

(3) *Coverage and Updating Strategy.* In the traditional ant colony algorithm, the next node position is decided by the roulette wheel method and repeated until the target point is obtained. The pheromones of all nodes are updated by the following rules after every ant  $\xi$  searching:

$$\tau_{l_i, l_{i+1}}(k, \xi + 1) = (1 - \rho) \tau_{l_i, l_{i+1}}(k, \xi) + \Delta \tau_{l_i, l_{i+1}}(k, \xi),$$

$$\tau_{l_i, l_{i+1}}(k + 1, 1) = (1 - \rho) \tau_{l_i, l_{i+1}}(k, R) + \Delta \tau_{l_i, l_{i+1}}(k, R), \quad (8)$$

$$\Delta \tau_{l_i, l_{i+1}}(k, \xi) = \begin{cases} \frac{1}{PL_{k, \xi}} & \text{through } l_i \text{ to } l_{i+1} \\ 0 & \text{otherwise,} \end{cases}$$

where  $\rho$  is the evaporation rate of pheromone, where the function is to avoid the pheromone accumulation:  $0 < \rho < 1$ .  $R$  is the number of the ants starting from the starting point in every round.  $\Delta \tau_{l_i, l_{i+1}}(k, \xi)$  is the addition of the  $k$ th round  $\xi$ th ant. And  $PL_{k, \xi}$  is the path length of the  $\xi$ th ant which can get to the end point in the  $k$ th round.

In the improved ant colony algorithm, the next node position is decided by the roulette wheel method until the

target point is obtained. And, in a cycle, the pheromone of all the nodes is updated by following the rules in each round of ants:

$$\tau'_{l_i, l_{i+1}}(k + 1) = (1 - \rho(k)) \tau_{l_i, l_{i+1}}(k) + \Delta \tau_{l_i, l_{i+1}}(k),$$

$$\tau''_{l_i, l_{i+1}}(k + 1) = \frac{\theta_4 \tau_{l_i, l_{i+1}}(0)}{\ln(k + 1)} + \Delta \tau_{l_i, l_{i+1}}(k), \quad (9)$$

$$\tau_{l_i, l_{i+1}}(k + 1) = \max \{ \tau'_{l_i, l_{i+1}}(k + 1), \tau''_{l_i, l_{i+1}}(k + 1) \}.$$

Among them,  $\Delta \tau_{l_i, l_{i+1}}(k)$  is the pheromone update part of  $l_i$  to  $l_{i+1}$  in the  $k$ th round.  $\theta_4$  is a constant, and the maximum value of the pheromone in the iterative process is the initial set value  $\tau_{\max} = \tau(0)$ .  $\rho(k)$  is the pheromone evaporation coefficient:  $0 < \rho(k) < 1$ . In the entire search space,

$$\Delta \tau_{l_i, l_{i+1}}(k) = o(\Delta \tau_{l_i, l_{i+1}}(k, 1), \dots, \Delta \tau_{l_i, l_{i+1}}(k, \xi), \dots, \Delta \tau_{l_i, l_{i+1}}(k, R - 1), \Delta \tau_{l_i, l_{i+1}}(k, R)), \quad (10)$$

where  $o(\Delta \tau_{l_i, l_{i+1}}(k, 1), \dots, \Delta \tau_{l_i, l_{i+1}}(k, R))$  is a nonzero pheromone space covering operation. For example,

$$A(1) = \begin{bmatrix} 1 & 2 & 4 \\ 0 & 0 & 1 \\ 3 & 0 & 0 \end{bmatrix},$$

$$A(2) = \begin{bmatrix} 2 & 3 & 5 \\ 1 & 0 & 0 \\ 2 & 0 & 0 \end{bmatrix}, \quad (11)$$

$$\text{so } o(A(1), A(2)) = \begin{bmatrix} 2 & 3 & 5 \\ 1 & 0 & 1 \\ 2 & 0 & 0 \end{bmatrix}.$$

In formula (10),

$$\Delta \tau_{l_i, l_{i+1}}(k, \xi) = \begin{cases} \frac{Q}{PL_{k, \xi}} \tau_{l_i, l_{i+1}}(k, \xi) & \text{through } l_i \text{ to } l_{i+1} \\ 0 & \text{otherwise.} \end{cases} \quad (12)$$

Among them,  $Q$  is a constant. It can be seen that if the ant can get to the end point, the added part of the pheromone is in inverse proportion with the length and if the ant cannot reach the ending point, it is recorded as 0. The rule can guide the search for the shortest path, improve the speed of convergence, and avoid the possibility of the pheromone accumulation caused by repeated search; meanwhile the effect on the performance of the algorithm caused by the quantity of the ants is reduced.

(4) *Evaporation Coefficient Segment.* When the problem scale is relatively large, due to the presence of pheromone evaporation, the pheromone of some nodes will be reduced greatly, even close to zero, which reduces the search ability of the algorithm. When  $\rho$  is large, the search ability is affected

by repeated selection. Meanwhile when  $\rho$  is small, the search ability of the algorithm is enhanced, but the convergence speed is decreased. Therefore, the heuristic information coefficient is adjusted as follows:

$$\rho(k+1) = \begin{cases} \theta_5 \rho(k) & \rho(k) \geq \rho_{\min} \\ \rho_{\min} & \rho(k) < \rho_{\min} \end{cases} \quad (13)$$

where  $\theta_5$  is a constant less than 1.  $k$  is the number of search rounds:  $k = 0, 1, \dots, K$ .  $\rho(0) = \rho_{\max}$ .  $\rho_{\max}$  and  $\rho_{\min}$  are the maximum and minimum of the coefficient of evaporation. The pheromone evaporation coefficient of fragmentation can enhance the search ability in the initial stage of search, increase the convergence speed later, and improve the performance of ant colony algorithm.

**4.2. Algorithm Steps.** The improved ant colony algorithm is to find the optimal path according to the following steps.

*Step 1.* The nonuniform distribution of initial pheromone is proposed and pheromone matrix  $T$  is constructed according to formula (2).

*Step 2.* Send  $K$  rounds and each round of  $R$  ants which are placed at the starting point.

*Step 3.* Send a round of ants and each ant to select the node according to the roulette wheel method, with the probability of each point calculated by formulas (5), (6), and (7).

*Step 4.* After a round of ant search, the pheromone was calculated by formulas (10) and (12), the evaporation coefficient was calculated by (13), and the pheromone was updated according to formulas (9).

*Step 5.* Send the next round of ants, and repeat above Steps 3 and 4 until the end of the iteration.

*Step 6.* Record the shortest path of each round; then draw the curve of the shortest path length of each round.

*Step 7.* Compare the shortest paths of all the ants. Finally, output the current global optimal path.

**4.3. Proof of Convergence.** The proof depends on a necessary assumption: there is a path between the starting point and the ending at least. According to formulas (10) and (12), the added part of pheromone must be greater than or equal to 0. That is,

$$\Delta \tau_{i,l_{i+1}}(k) \geq 0. \quad (14)$$

Formulas (9) show that the pheromone can be expressed as follows:

$$\tau_{i,l_{i+1}}(k) \geq \max \left( (1 - \rho(k))^k \tau(0), \frac{\theta_4 \tau(0)}{\ln(k+1)} \right). \quad (15)$$

Event  $E_k$  means that the optimal solution is obtained for the first time in the  $k$ th iteration. Therefore, event  $\bigwedge_{k=1}^K E_k$  denotes that the algorithm can find the optimal solution for the first time for  $K$  iterations. Then probability  $P(\bigwedge_{k=1}^K E_k)$  is satisfied:

$$\lim_{k \rightarrow \infty} P \left( \bigwedge_{k=1}^K E_k \right) = 1. \quad (16)$$

*Proof.*  $l_{i+1}^*$  is the choice of the  $i$ th optimal solution, and the probability of finding the optimal solution for the  $\xi$ th ant in the  $k$ th round  $p(k, \xi)$  can be obtained by formula (5) because the node selection is an independent event.

$$\begin{aligned} 1 \geq p(k, \xi) &= \prod_{i=1}^{t-1} \frac{(\tau_{i,l_{i+1}^*})^\alpha (\eta_{i,l_{i+1}^*})^\beta \mu_{i,l_{i+1}^*}}{\sum_{l_{i+1} \in \text{allowed}(b)} (\tau_{i,l_{i+1}})^\alpha (\eta_{i,l_{i+1}})^\beta \mu_{i,l_{i+1}}} \\ &= \prod_{i=1}^{t-1} \frac{(\tau_{i,l_{i+1}^*})^\alpha}{\sum_{l_{i+1} \in \text{allowed}(b)} (\tau_{i,l_{i+1}})^\alpha (\eta_{i,l_{i+1}}/\eta_{i,l_{i+1}^*})^\beta (\mu_{i,l_{i+1}}/\mu_{i,l_{i+1}^*})}. \end{aligned} \quad (17)$$

Define  $\psi(l_{i+1}) = (\eta_{i,l_{i+1}}/\eta_{i,l_{i+1}^*})^\beta (\mu_{i,l_{i+1}}/\mu_{i,l_{i+1}^*})$ , and  $\psi_{\max} = \max\{\psi(l_{i+1}), i = 1, \dots, t-1\}$ . So formula (17) can be expressed as

$$\prod_{i=1}^{t-1} \frac{(\tau_{i,l_{i+1}^*})^\alpha}{\sum_{l_{i+1} \in \text{allowed}(b)} (\tau_{i,l_{i+1}})^\alpha \psi_{\max}}. \quad (18)$$

Because of formula (12), it is known that the minimum value of pheromone in the  $k$ th iteration of the ant colony algorithm is

$$\tau_{\min}(k) \geq \frac{\theta_4 \tau(0)}{\ln(k+1)}, \quad \forall k \geq 1. \quad (19)$$

Further, the maximum value of the pheromone is the initial value by setting some parameters. So

$$\tau_{\max} = \tau(0). \quad (20)$$

And the maximum number of  $N_c(k, \xi, (l_i, l_{i+1}))$  can be expressed as

$$N_c = \max \{N_c(k, \xi, (l_i, l_{i+1}))\}, \quad i = 1, \dots, t-1, \quad (21)$$

where  $N_c(k, \xi, (l_i, l_{i+1}))$  is the number of options. By (19), (20), and (21), we can know that formula (18) meets the following relationship:

$$1 \geq P(k, \xi) > \prod_{i=1}^{t-1} \frac{(\tau_{i,l_{i+1}^*})^\alpha}{\sum_{l_{i+1} \in \text{allowed}(b)} (\tau_{i,l_{i+1}})^\alpha \psi_{\max}} \quad (22)$$

$$> \left( \frac{(\theta_4 \times \tau(0) / \ln(k+1))^\alpha}{(\tau(0))^\alpha \times N_c \times \psi_{\max}} \right)^{t-1}.$$

Record

$$\begin{aligned} d &= \left( \frac{(\theta_4 \times \tau(0))^\alpha}{(\tau(0))^\alpha \times N_c(k, \xi, (l_i, l_{i+1})) \times \psi_{\max}} \right)^{t-1} \\ &= \left( \frac{(\theta_4)^\alpha}{N_c(k, \xi, (l_i, l_{i+1})) \times \psi_{\max}} \right)^{t-1}. \end{aligned} \quad (23)$$

So, formula (22) is expressed as

$$\begin{aligned} 1 \geq P(k, \zeta) &> \prod_{i=1}^{t-1} \frac{(\theta_4 \times \tau(0) / \ln(k+1))^\alpha}{(\tau(0))^\alpha \times N_c \times \psi_{\max}} \\ &= \frac{d}{(\ln(k+1))^{(t-1)\alpha}}. \end{aligned} \quad (24)$$

From the above, we can know that

$$1 > \frac{d}{(\ln(k+1))^{(t-1)\alpha}} > 0. \quad (25)$$

The probability that the optimal solution cannot be found by any ants in the  $k$ th round is  $p(k)$ :

$$p(k) = (1 - p(k, \xi))^R. \quad (26)$$

Probability  $P(\bigvee_{k=1}^K \bar{E}_k)$  that cannot find the optimal solution for the  $K$  rounds is given as follows:

$$\begin{aligned} P\left(\bigvee_{k=1}^K \bar{E}_k\right) &= \prod_{k=1}^K p(k) = \prod_{k=1}^K (1 - p(k, \xi))^R \\ &< \prod_{k=1}^K \left(1 - \frac{d}{(\ln(k+1))^{(t-1)\alpha}}\right)^R. \end{aligned} \quad (27)$$

After the logarithm to the above formula,

$$\begin{aligned} \ln P\left(\bigvee_{k=1}^K \bar{E}_k\right) &< \sum_{k=1}^K \ln \left[1 - \left(\frac{d}{(\ln(k+1))^{(t-1)\alpha}}\right)\right]^R \\ &= R \sum_{k=1}^K \ln \left[1 - \left(\frac{d}{(\ln(k+1))^{(t-1)\alpha}}\right)\right] \\ &\leq -R \times d \sum_{k=1}^K \left(\frac{1}{(\ln(k+1))^{(t-1)\alpha}}\right) \\ &\leq -R \times d \sum_{k=1}^K \frac{1}{k+1} \end{aligned} \quad (28)$$

$$\begin{aligned} \lim_{K \rightarrow \infty} \ln P\left(\bigvee_{k=1}^K \bar{E}_k\right) &< \lim_{K \rightarrow \infty} \ln \left(-R \times d \sum_{k=1}^K \frac{1}{k+1}\right) \\ &= -\infty. \end{aligned}$$

That is,  $P(\bigvee_{k=1}^K \bar{E}_k) = 0$ . So  $\lim_{k \rightarrow \infty} P(\bigwedge_{k=1}^K E_k) = 1$ .  $\square$

## 5. Numerical Simulations

The experiments are made to demonstrate the effectiveness of the proposed algorithm. The algorithm is compiled in MATLAB software. Experiments were conducted using a comparative method to be more persuasive along with the same experimental conditions.

**5.1. Simulation Experiments.** The experiment was divided into three parts with two algorithms, the traditional ant colony algorithm and the improved ant colony algorithm. In order to compare the effects of the two algorithms, they are used in the same environment.

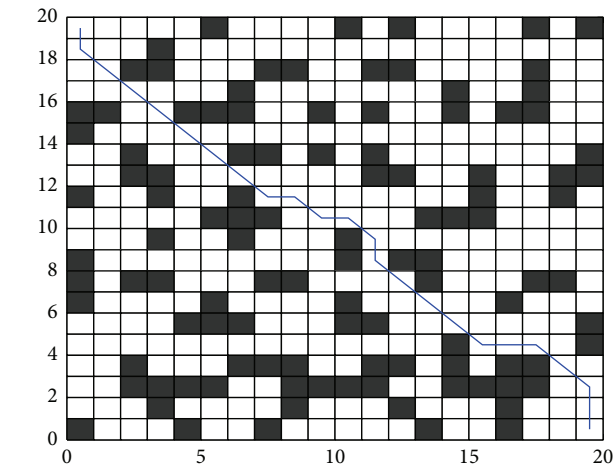
(1) *Example 1.* In this example, set the simulation environment as  $20 \times 20$  grids and the length of each unit is 1. The starting point is the upper left corner in the grid (0.5, 19.5), and the end point is the lower right corner (19.5, 0.5) (see Figure 5).

(2) *Example 2.* We set the environment as  $30 \times 30$  grids and the length of the unit is 1. The starting point is (0.5, 8.5), and the end point is (25.5, 28.5) (see Figure 6).

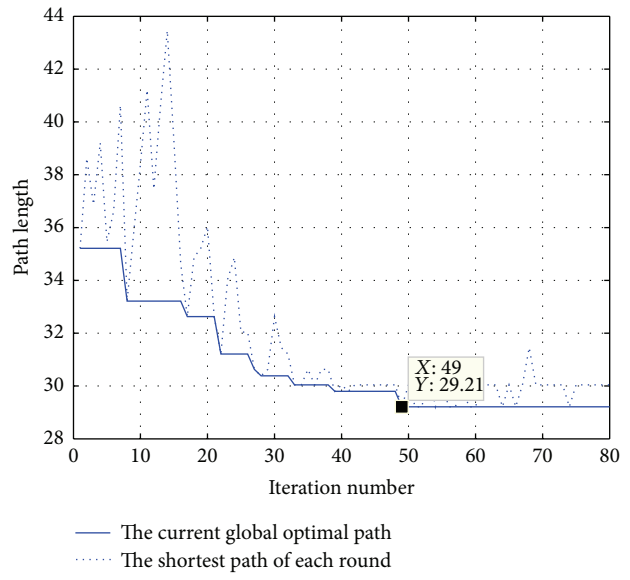
(3) *Example 3.* The experiment is made in model of  $40 \times 40$  grids and the length of each unit is 1. The starting point is set at (0.5, 39.5), and the ending point is set at (39.5, 0.5) (see Figure 7).

**5.2. Results Analysis.** As shown in Figure 5(a), it is a global optimal path in the case of Example 1. Similarly, Figures 6(a) and 7(a) are the global optimal paths in Examples 2 and 3, respectively. The obstacles in each environment are randomly selected. The three experiment results show that the ant colony algorithm and the improved ant colony algorithm both can find the global optimal paths in a variety of environments.

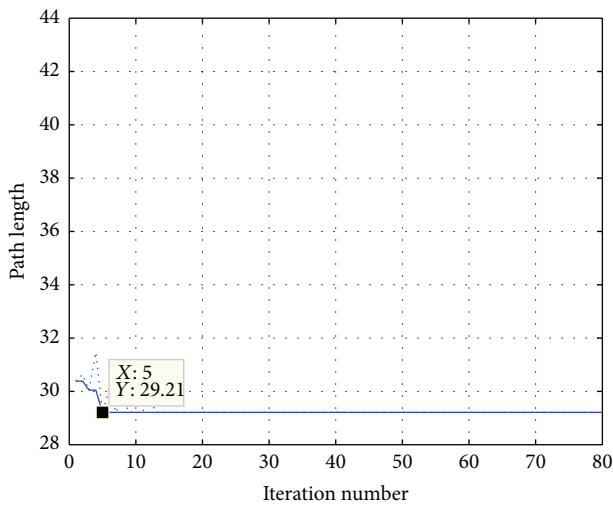
Figures 5(b) and 5(c) depict the path length iteration curves in Example 1 by traditional ant colony algorithm and the improved ant colony algorithm. And the search process about the shortest path length of each round and the current global optimal path length can be seen from the figures. By comparison, it can be seen that the shortest path length is found in the 49th iteration by traditional ant colony algorithm, while it is found in the fifth iteration by the improved algorithm. And once the optimal solution is obtained, the search will converge to the shortest path value by the improved algorithm. Similarly, Figures 6(b) and 6(c) represent the search process of the two algorithms in Example 2. The traditional ant colony algorithm finds the shortest path in the 69th iteration with value of 35.63, while the improved algorithm gets the shortest path in the ninth times. In the same way, Figures 7(b) and 7(c) show that the traditional ant colony algorithm and the improved ant colony algorithm find the shortest path in the 37th and 24th iterations, respectively. Therefore, it can be seen that the search efficiency of the improved ant colony algorithm is



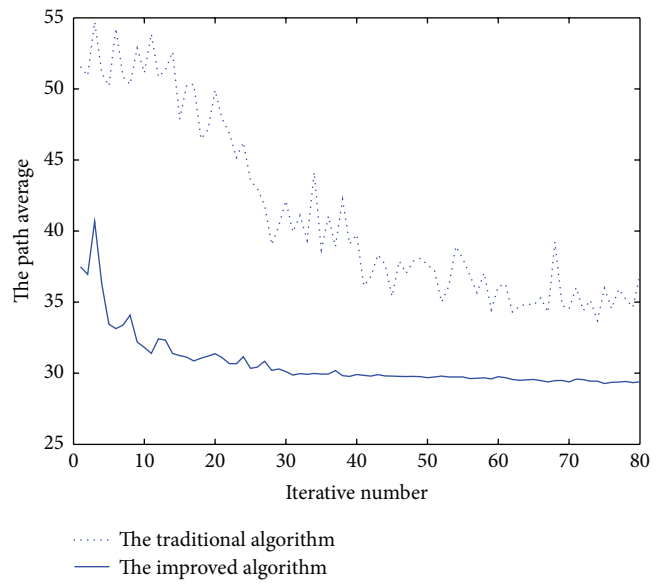
(a)



(b)



(c)



(d)

FIGURE 5: (a) Simulation results in  $20 \times 20$  grids. (b) The iterative curve by the traditional algorithm. (c) The iterative curve by the improved algorithm. (d) The path average curve length by two algorithms.

significantly higher compared to the traditional ant colony algorithm in a variety of environment.

The mean value of path iterative length often represents the convergence ability of the algorithm. Figures 5(d), 6(d), and 7(d) present the contrast of the two algorithms on the search path average value. The improved algorithm not only is faster than the ant colony algorithm but also can avoid falling into local minimum point and obtain the global optimal solution effectively either in simple environment or in a complex one.

## 6. Conclusion

In this paper, an improved ant colony algorithm is proposed for the 8 control operating units of the omnidirectional mobile vehicle. The grid method is used to establish the environment model, and the tabu list is introduced. By using the tabu list to show the obstacles and the units that have passed through, it is flexible to deal with obstacles and avoid duplicating the path. In this paper, the initial distribution of nonuniformity pheromone is presented which improves

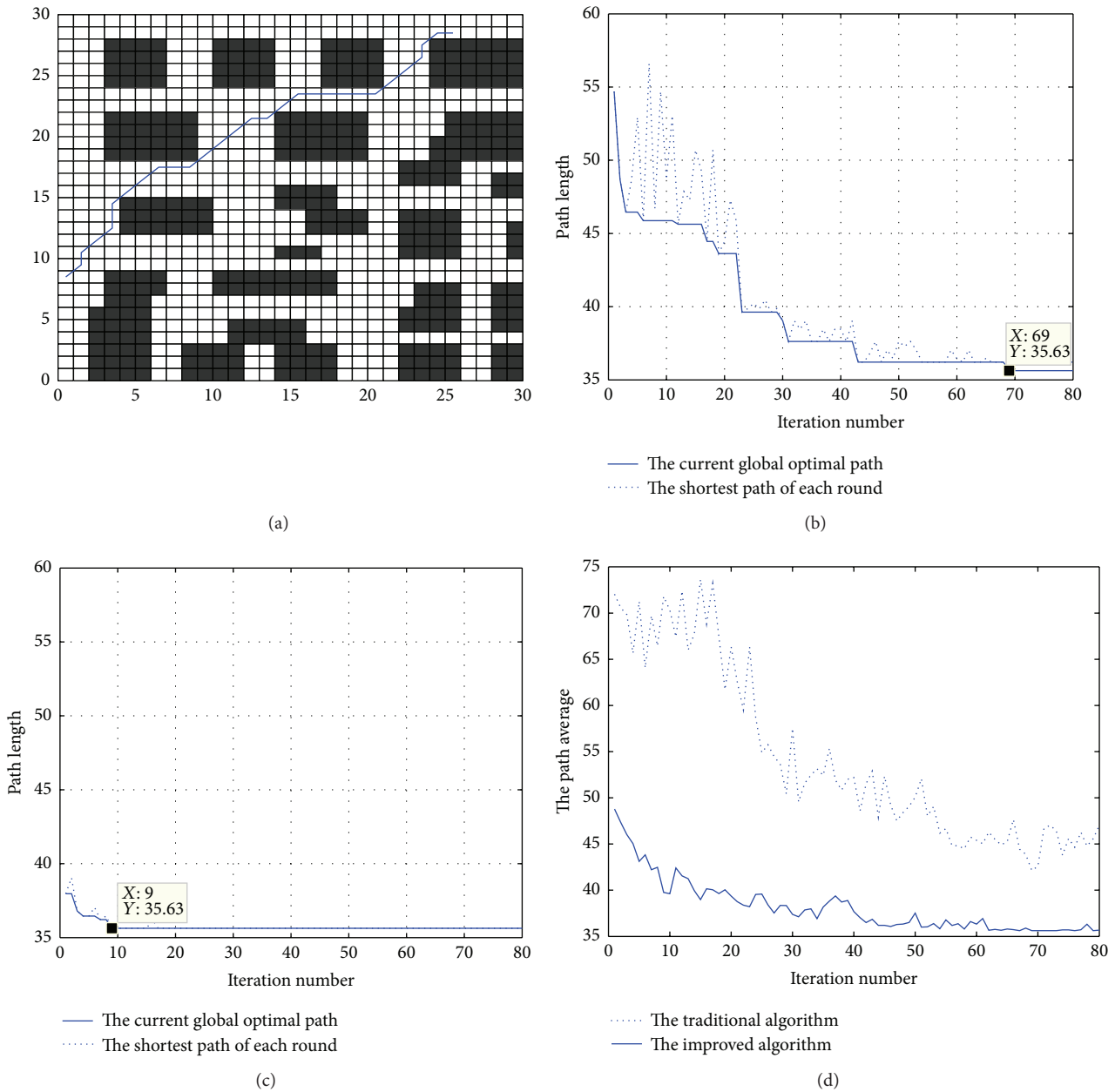


FIGURE 6: (a) Simulation results in  $30 \times 30$  grids. (b) The iterative curve by the traditional algorithm. (c) The iterative curve by the improved algorithm. (d) The path average curve length by two algorithms.

the time efficiency and the simplicity of the algorithm and reduces the search space of ant colony algorithm. Adding the direction of the selection strategy can get more effective information as the heuristic information, more actively guide the search behavior of ants, and reduce the blindness. By using the rule of coverage, the search probability is reduced, the stability of the algorithm is guaranteed, and the effect of the quantity of the ants on the performance of the algorithm is guaranteed. The pheromone evaporation coefficient is segmented and adjusted, which can effectively balance the convergence speed and search ability of the algorithm.

Finally, it is strictly proven that the probability of finding an optimal solution is limited to 1 by the improved algorithm. The improved ant colony algorithm in solving the shortest path planning problem of the omnidirectional mobile vehicle has very good performance.

### Competing Interests

The authors declare that there are no competing interests regarding the publication of this paper.

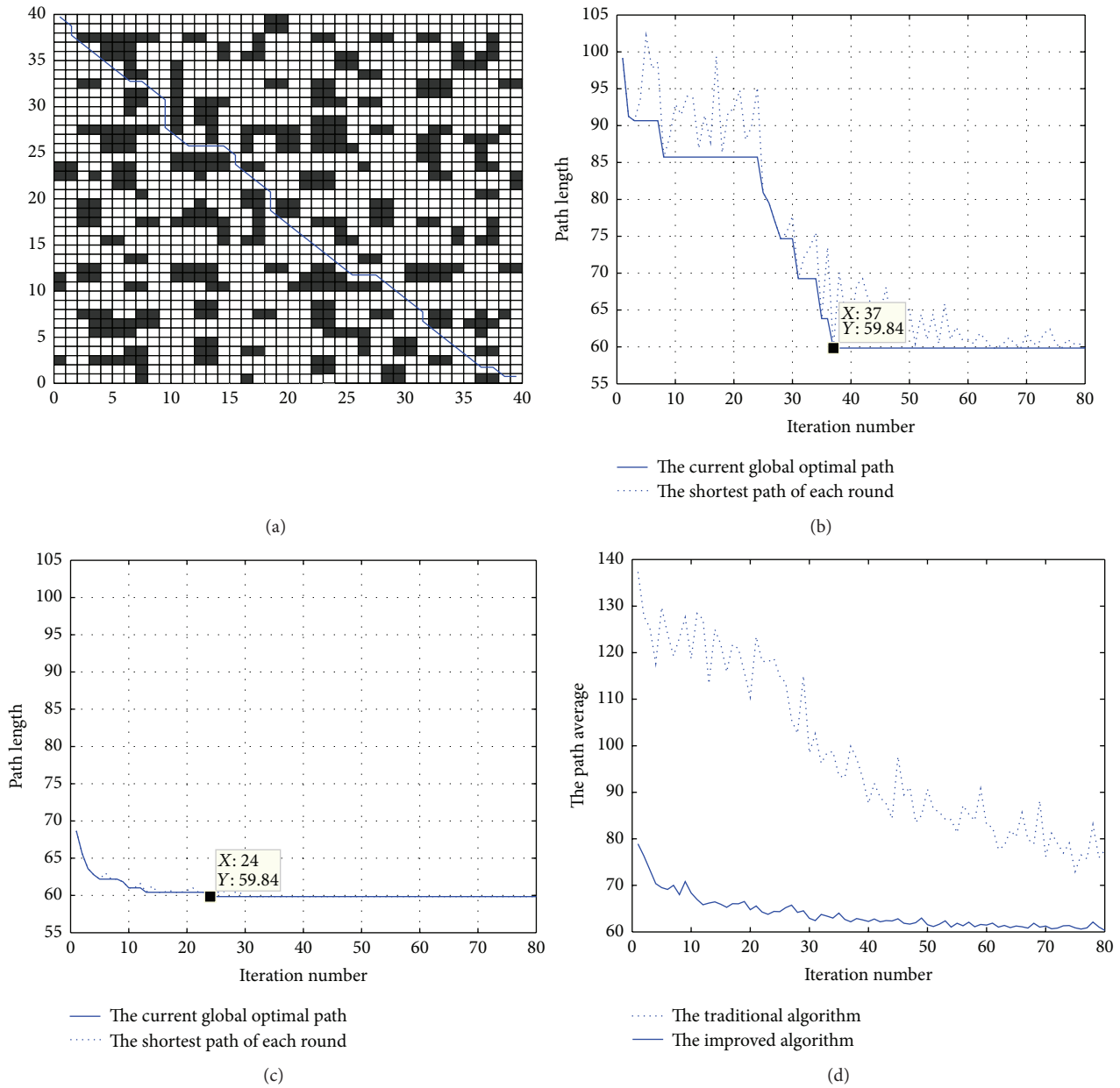


FIGURE 7: (a) Simulation results in 40 × 40 grids. (b) The iterative curve by the traditional algorithm. (c) The iterative curve by the improved algorithm. (d) The path average curve length by two algorithms.

**Acknowledgments**

This research is supported by Science and Technology Research Project of Colleges and Universities in Hebei Province (Grant no. ZD2016142), Natural Science Foundation of Hebei Province (Grant no. F2014208013), and Doctoral Scientific Research Startup Foundation of Hebei University of Science and Technology (Grant no. QD201302).

**References**

[1] Y. Y. Gao, X. G. Ruan, H. J. Song, and J. J. Yu, “Path planning method for mobile robot based on a hybrid learning approach,” *Control and Decision*, vol. 27, no. 12, pp. 1822–1827, 2012.

[2] T. Lozano-Perez and M. A. Wesley, “An algorithm for planning collision-free paths among polyedral obstacles,” *Communications of ACM*, vol. 2, pp. 959–962, 1979.

[3] E. Masehian and D. Sedighzadeh, “Classic and heuristic approaches in robot motion planning—a chronological review,” *International Journal of Mechanical, Industrial Science and Engineering*, vol. 1, no. 5, pp. 101–106, 2007.

[4] W. Lu, G. Zhang, and S. Ferrari, “An information potential approach to integrated sensor path planning and control,” *IEEE Transactions on Robotics*, vol. 30, no. 4, pp. 919–934, 2014.

[5] J. Lee, B.-Y. Kang, and D.-W. Kim, “Fast genetic algorithm for robot path planning,” *Electronics Letters*, vol. 49, no. 23, pp. 1449–1451, 2013.

- [6] Y. Fu, M. Ding, C. Zhou, and H. Hu, "Route planning for unmanned aerial vehicle (UAV) on the sea using hybrid differential evolution and quantum-behaved particle swarm optimization," *IEEE Transactions on Systems, Man, and Cybernetics: Systems*, vol. 43, no. 6, pp. 1451–1465, 2013.
- [7] M. A. P. Garcia, O. Montiel, O. Castillo, R. Sepúlveda, and P. Melin, "Path planning for autonomous mobile robot navigation with ant colony optimization and fuzzy cost function evaluation," *Applied Soft Computing*, vol. 9, no. 3, pp. 1102–1110, 2009.
- [8] H. Mo and L. Xu, "Research of biogeography particle swarm optimization for robot path planning," *Neurocomputing*, vol. 148, pp. 91–99, 2015.
- [9] R.-E. Precup, E. M. Petriu, M.-B. Radac, E.-I. Voisan, and F. Dragan, "Adaptive charged system search approach to path planning for multiple mobile robots," in *Proceedings of the 16th International Federation of Automatic Control*, pp. 294–299, Sozopol, Bulgaria, September 2015.
- [10] F. Ducho, A. Babineca, M. Kajana et al., "Path planning with modified a star algorithm for a mobile robot," *Procedia Engineering*, vol. 96, pp. 59–69, 2014.
- [11] A. K. Gururji, H. Agarwal, and D. K. Parsediya, "Time-efficient A\* algorithm for robot path planning," *Procedia Technology*, vol. 23, pp. 144–149, 2016.
- [12] A. Hidalgo-Paniagua, M. A. Vega-Rodríguez, and J. Ferruz, "Applying the MOVNS (multi-objective variable neighborhood search) algorithm to solve the path planning problem in mobile robotics," *Expert Systems with Applications*, vol. 58, pp. 20–35, 2016.
- [13] A. T. Rashid, A. A. Ali, M. Frasca, and L. Fortuna, "Path planning with obstacle avoidance based on visibility binary tree algorithm," *Robotics and Autonomous Systems*, vol. 61, no. 12, pp. 1440–1449, 2013.
- [14] M. Davoodi, F. Panahi, A. Mohades, and S. N. Hashemi, "Multi-objective path planning in discrete space," *Applied Soft Computing*, vol. 13, no. 1, pp. 709–720, 2013.
- [15] A. Hidalgo-Paniagua, M. A. Vega-Rodríguez, J. Ferruz, and N. Pavón, "MOSFLA-MRPP: multi-objective shuffled frog-leaping algorithm applied to mobile robot path planning," *Engineering Applications of Artificial Intelligence*, vol. 44, no. 2342, pp. 123–136, 2015.
- [16] G.-F. Deng, X.-P. Zhang, and Y.-P. Liu, "Ant colony optimization and particle swarm optimization for robot-path planning in obstacle environment," *Control Theory & Applications*, vol. 26, no. 8, pp. 879–883, 2009.
- [17] J. He, Z. Tu, and Y. Niu, "A method of mobile robotic path planning based on integrating of GA and ACO," *Computer Simulation*, vol. 27, no. 3, pp. 170–174, 2010.
- [18] P. K. Tiwari and D. P. Vidyarthi, "Improved auto control ant colony optimization using lazy ant approach for grid scheduling problem," *Future Generation Computer Systems*, vol. 60, pp. 78–89, 2016.
- [19] P. Wang, H.-T. Lin, and T.-S. Wang, "An improved ant colony system algorithm for solving the IP traceback problem," *Information Sciences*, vol. 326, pp. 172–187, 2016.
- [20] W.-Y. Jiang, Y. Lin, M. Chen, and Y.-Y. Yu, "A co-evolutionary improved multi-ant colony optimization for ship multiple and branch pipe route design," *Ocean Engineering*, vol. 102, pp. 63–70, 2015.
- [21] M. Saidi-Mehrabad, S. Dehnavi-Arani, F. Evazabadian, and V. Mahmoodian, "An Ant Colony Algorithm (ACA) for solving the new integrated model of job shop scheduling and conflict-free routing of AGVs," *Computers and Industrial Engineering*, vol. 86, pp. 2–13, 2015.
- [22] Z. Wang, X. Zhu, and Q. Han, "Mobile robot path planning based on parameter optimization ant colony algorithm," *Procedia Engineering*, vol. 15, pp. 2738–2741, 2011.

## Research Article

# Low Model Analysis and Synchronous Simulation of the Wave Mechanics

Wenyuan Duan, Heyuan Wang, and Meng Kan

*College of Science, Liaoning University of Technology, Jinzhou 121001, China*

Correspondence should be addressed to Wenyuan Duan; 1499206003@qq.com

Received 11 May 2016; Accepted 13 July 2016

Academic Editor: Bernard Bonello

Copyright © 2016 Wenyuan Duan et al. This is an open access article distributed under the Creative Commons Attribution License, which permits unrestricted use, distribution, and reproduction in any medium, provided the original work is properly cited.

The dynamic behavior of a chaotic system in the internal wave dynamics and the problem of the tracing and synchronization are investigated, and the numerical simulation is carried out in this paper. The globally exponentially attractive set and positive invariant set of the chaotic system are studied via constructing the positive definite and radial unbounded Lyapunov function. There are no equilibrium positions, periodic solutions, quasi-period motions, wandering recovering motions, and other chaotic attractors of the system out of the globally exponentially attractive set. Strange attractors can only locate in the globally exponentially attractive set. A feedback controller is designed for the chaotic system to realize the control of the unstable point. The second method of Lyapunov is used to discuss theoretically the rationality of the design of the controller. The driving-response synchronization method is used to realize the globally exponential synchronization. The numerical simulation is carried out by MATLAB software, and the simulation results show that the method is effective.

## 1. Introduction

Since 1960s, in the meteorological numerical research conducted by American meteorologist Lorenz, the three-dimensional truncation is carried out for the Rayleigh-Bernard heat convection problem of the infinite dimensional dynamical system to get the famous Lorenz system and the chaos phenomenon is found accidentally [1]. A lot of researches on chaos are conducted by many scholars since the discovery of chaos [1–10]. Lorenz system reveals the essential phenomenon of the nonlinear complexity as the first chaotic system [8, 9]. The chaotic attractor was formally proposed by Ruelle and Takens in 1971 and the nonperiodic flow appearing in the dissipative system was called the strange attractor by them [1]. The capture area of the strange attractor and the global stability of the chaotic system are hot spots of common concern to the people. The low mode analysis is usually used to explain and predict the chaotic phenomenon of infinite dimensional dynamical system [10]. The inertial manifold and approximate inertial manifold theories are the theoretical foundation and basis of the low mode analysis (they are considered to be a low dimensional smooth manifold with exponent attracting all tracks containing the global attractor).

The complex dynamic behavior of the infinite dimensional dynamical system usually originated from a simple origin and can be distinguished by the simple equation. The three functions of the internal gravity wave in the atmosphere are the following [11]: transmission and storage of energy and momentum, starting and organization of the convective activity, and occurrence and modulation of the turbulence. The thermal convection and turbulence caused by the internal wave are studied in essence in Lorenz's paper [10]. The chaos caused by the match of the driving factor with the dissipation factor of the turbulence appears in the internal gravity wave dynamics. The dissipation factor is too weak causing the absence of chaos when the Prandtl number  $\sigma$  is equal to 1. The concept of chaos can help explain the occurrence of atmosphere turbulence. During the day, unstable temperature stratification is the driving factor of turbulence, and the molecular viscosity and certain velocity shear are dissipation factor. At night, effective surface long wave radiation is the driving factor of turbulence. The chaos can still appear under the condition that the real atmosphere Prandtl number is equal to 0.7 after introducing the velocity shear damping. The smaller the Richardson number is, the more likely the chaos appears at night [11]. Chaos is too

sensitive to the initial value and the unpredictability of the trend of the long time of chaos exists, so the chaos system is considered to be uncontrollable and two chaos systems are considered to be synchronous impossibly by people for a long time. The OGY method was proposed since 1990 and the chaos synchronization [12–15] was used by the United States Navy laboratories to get the secure communication firstly in 1990 that changed people's original idea. The control and synchronization of chaos has become a hot spot in the field of nonlinear science in recent years.

A new chaos system is found by Liu through numerical calculation in the study of the internal wave dynamics [11]. But he did not have a comprehensive analysis of the appearance and disappearance of chaotic attractor. Based on the research of Liu, we have carried out a comprehensive and detailed discussion and numerical simulation in this system; the corresponding attractors of the system are given; at the same time, we obtain the bifurcation diagram, power spectrum, Poincare section, and return mapping of the system. The general characteristics of the behavior of the chaotic system are detected via simulation, and we discuss the global stability of the system. The globally exponentially attractive set and positive invariant set of the system are given by constructing the positive and radial unbounded Lyapunov function. According to the concept of globally exponential tracking, for any periodic solution or equilibrium, we design some simple feedback controllers to control all the trajectories of the chaotic systems tracking the special periodic solution globally. The adaptive control method is used to realize the generalized index synchronization and the effectiveness of the method is validated by the numerical simulation.

## 2. Brief Introduction of the Behavior of the Dynamics and Three-Mode System of the Internal Wave Dynamics

Three-dimensional nonlinear system is achieved by the truncated spectral method in [11] as follows:

$$\begin{aligned}\dot{x} &= -(\sigma + s)x + \sigma y, \\ \dot{y} &= rx - y - xz, \\ \dot{z} &= xy - bz,\end{aligned}\quad (1)$$

where  $\sigma$ ,  $s$ , and  $b$  are constants,  $r$  is the variational parameter, and  $x$ ,  $y$ ,  $z$  are the spectral expansion coefficient.

The linear stability analysis of system (1) is carried out by [11] and the main conclusions are as follows:

- (1) When  $0 < r < (\sigma + s)/\sigma$ , the equilibrium state  $O$  is stable.
- (2) When  $(\sigma + s)/\sigma < r < r_0 = 380.6$ , the equilibrium state  $O$  is unstable and the equilibrium states  $C_1$  and  $C_2$  are stable, where  $\lambda_1 < 0$ , the real part of the equation  $\lambda_2 = \lambda_3$  is negative, and the pitch fork bifurcation occurs when  $r = (\sigma + s)/\sigma$ .
- (3) When  $r > r_0$ , the equilibrium states  $C_1$  and  $C_2$  lose the stability, where  $\lambda_1 < 0$ . But the real part of the

equation  $\lambda_2 = \lambda_3$  is positive. The subcritical Hopf bifurcation occurs when  $r = r_0$ .

For system (1), the change rate of the volume in phase space  $(x, y, z)$  is

$$\frac{1}{V} \frac{dV}{dt} = \frac{\partial \dot{x}}{\partial x} + \frac{\partial \dot{y}}{\partial y} + \frac{\partial \dot{z}}{\partial z} = -(\sigma + s + 1 + b) < 0. \quad (2)$$

From formula (2), system (1) is the dissipative system of volume shrinkage on the whole, so movement will eventually tend to a certain attractor.

On the basis, in [11], the parameters can be selected as  $\sigma = 0.7$ ,  $s = 10$ ,  $b = 8/3$ ,  $r = 500$ , and the initial values can be selected as  $x = 10$ ,  $y = 100$ ,  $z = 400$ , step size  $h = 0.1$ . The simulation calculation and analysis on the internal wave dynamics triple modular system (1) are carried out and the projection of a part of the trajectory in the phase space in the two-dimensional plane is simulated. The space orbit of the three-dimensional space is changed into the one-dimensional map by the Poincare section method. The chaotic phenomenon exists in system (1) when  $r > r_0$  that is illustrated by analysis and calculation.

## 3. Numerical Simulation of the Dynamic Behavior of the System

More detailed numerical simulation and theoretical analysis of the dynamic behavior of system (1) are carried out in this section. The parameters can be selected as  $\sigma = 0.7$ ,  $s = 10$ ,  $b = 8/3$ ; with the increase of the  $r$ , we obtain the attractor diagram, bifurcation diagram of system (1) by simulation, and we obtain the Poincare section, power spectrum, and return mapping of system (1) by simulation, further validating the chaotic behavior of the system. The conclusions combining the simulation results with theoretical analysis are as follows:

- (1) When  $0 < r < r_1 = 15.286 \dots$ , there is only one fixed point  $O$ , and it is stable.
- (2) When  $r_1 < r < r_e = 237.9 \dots$ , point  $O$  becomes the unstable saddle-node point with one unstable direction and two stable directions. The eigenvalues of  $C_1$  and  $C_2$  all are negative real roots, so  $C_1$  and  $C_2$  are the asymptotically stable nodes.
- (3) When  $r_e < r < r_0 = 380.6 \dots$ , the equation has a negative real root and conjugate complex roots with negative real part that represents the point in one direction of  $C_1$  and  $C_2$  being asymptotically stable, while there is stable focus in the plane, which is perpendicular to this direction. Numerical calculation shows that they are global attractors, as shown in Figure 1.
- (4) When  $r > r_0$ , there is still a negative real root and others are conjugate complex roots with the positive real part that represents the point in the direction of  $C_1$  and  $C_2$  being stable and the focus in the plane vertical to the stable direction is unstable focus. Then Hopf bifurcation [16–18] appears when

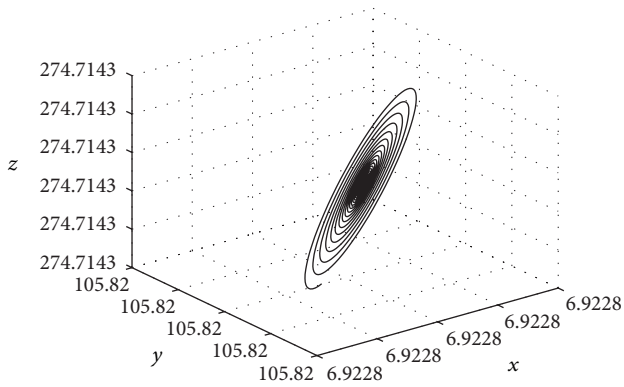


FIGURE 1:  $r_e < r < r_0 = 380.6\dots$

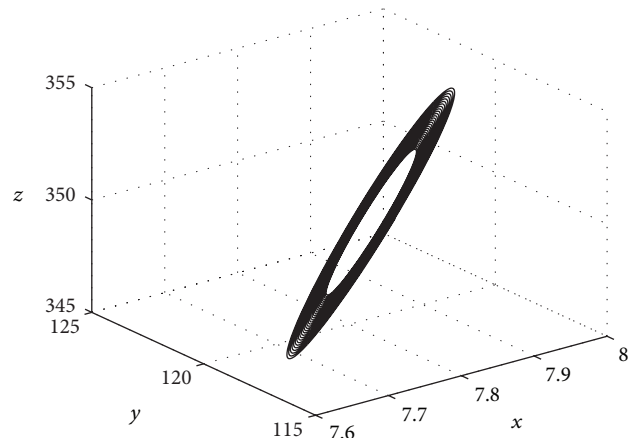


FIGURE 2:  $r > r_0$ .

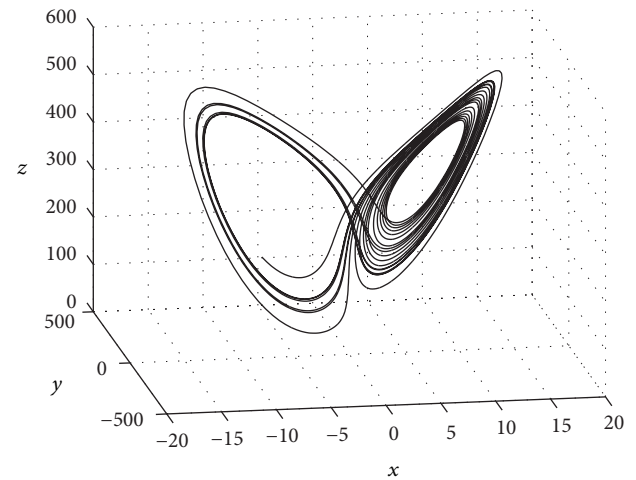


FIGURE 3:  $r > r_0$ .

$r = r_0$  and strange attractors generated to cause chaos. Eventually, the process of chaos is shown in Figures 2, 3, 4, and 5.

- (5) When  $2169.9\dots < r < 2260.7\dots$ , Figures 6 and 7 show that the attractor gradually starts to shrink into the limit cycle which is an inverted bifurcation process, and the numerical results show that the bifurcation point satisfies the Feigenbaum constant.
- (6) When  $2260.7\dots < r < 2743.1\dots$ , chaos appears firstly and then gradually disappears to shrink into the torus which is still an inverted bifurcation process; this process is shown in Figures 8, 9, and 10, and the bifurcation point satisfies the Feigenbaum constant.
- (7) The bifurcation diagram of system (1) can be seen in Figure 11. From the simulation results of the image, the whole process from the starting to the end of the chaotic phenomenon can be observed. The Poincare section, power spectrum, and return mapping in Figures 12, 13, and 14 when  $r = 800$  all show the chaotic character of the system.

#### 4. The Globally Exponentially Attractive Set and Positive Invariant Set

In the following we discuss the global stability of the chaotic system (1) in this section to get the estimation of globally exponentially attractive set and the positive invariant set of system (1).

First of all, we give some related definitions [19]. Denote by  $X = (x, y, z)$  the state vector of system (1), and  $Q \subset R^3$  as a compact set (bounded and closed set). Let  $t_0 \geq 0$  be the initial time. By  $X(t, t_0, X_0)$  we denote the solution of system (1) satisfying the initial value  $X(t_0, t_0, X_0) = X_0$ . If there is no confusion, we denote this solution by  $X(t)$ . Define the distance between the solution vector  $X(t, t_0, X_0)$  and the set  $Q$  as  $\rho(X(t, t_0, X_0), Q) = \inf_{\tilde{X} \in Q} \|X(t, t_0, X_0) - \tilde{X}\|$ . Define  $Q_\epsilon$  as any set that includes the set  $Q$ ; that is,  $Q \subset Q_\epsilon$ .

*Definition 1.* If there exists a compact set  $Q$  in the space  $R^3$  such that  $\rho(X(t), Q) \rightarrow 0$  as  $t \rightarrow \infty, \forall X_0 \in R^3/Q$ , then one calls the set  $Q$  a globally attractive set of system (1). In

other words, there exists  $T > t_0$ , such that  $X(t, t_0, X_0) \subseteq Q_\epsilon$  for  $t \geq T + t_0$ . A system with the globally attractive set is called a globally asymptotically Lagrangian stable system or a dissipative system in ultimately bounded sense. If,  $\forall X_0 \in Q, X(t, t_0, X_0) \subseteq Q$  holds for all  $t \geq t_0$ , the set  $Q$  is called a positively invariant set of system (1).

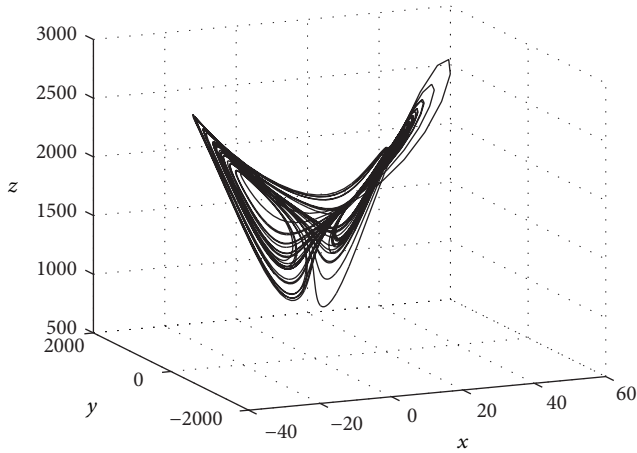
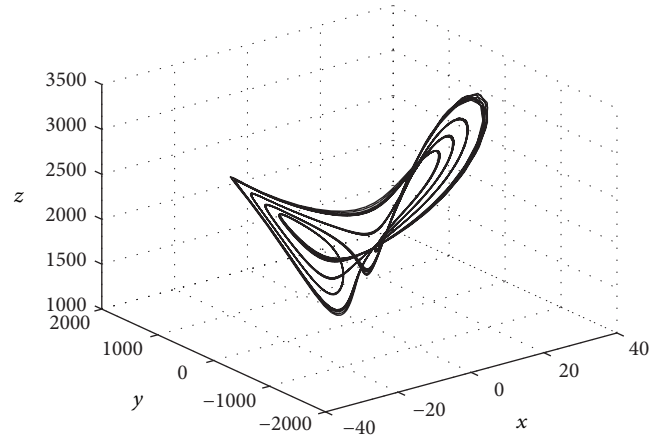
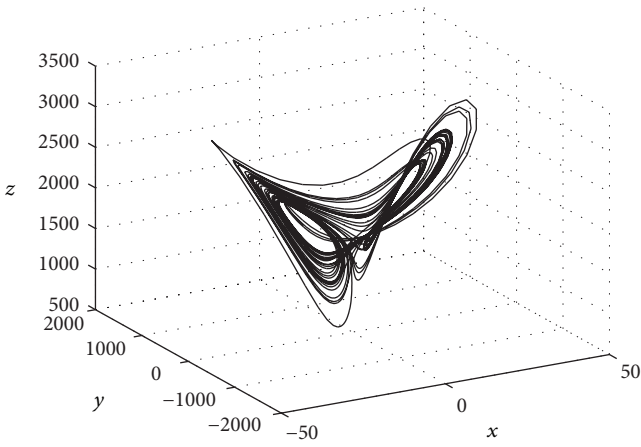
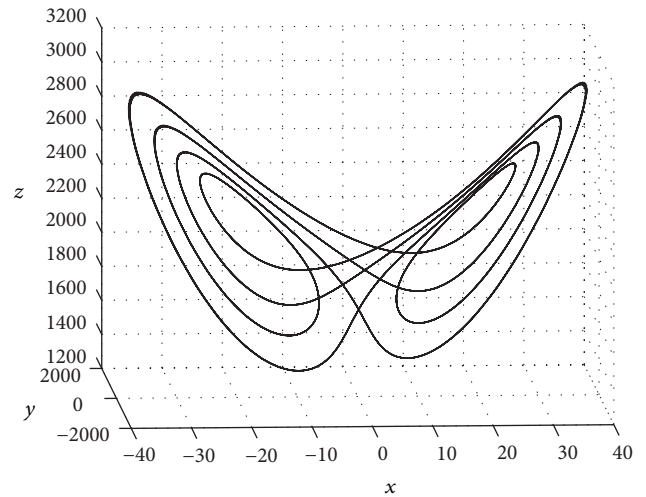
From the definition, we conclude that if  $Q$  is a globally attractive set then all  $Q_\epsilon$  are the globally attractive sets too.

**Theorem 2.** Let  $\sigma > 0, s \geq 10, b \geq 1, r \geq (\sigma + s)/\sigma$ . For any constant  $m \geq 0$ , ellipsoidal

$$\Omega_m : mx^2 + y^2 + (z - m\sigma - r)^2 \leq \frac{b^2(m\sigma + r)^2}{2b - 1} \quad (3)$$

is a globally attractive set and positively invariant set of system (1).

*Proof.* It is easy to show that if  $0 < r < (\sigma + s)/\sigma$  the unique equilibrium  $(0, 0, 0)^T$  of system (1) is globally exponentially stable. If  $r = (\sigma + s)/\sigma$ , the equilibrium  $(0, 0, 0)^T$  is stable but not asymptotically stable. Now we construct a family of

FIGURE 4:  $r > r_0$ .FIGURE 6:  $2169.9 \dots < r < 2260.7 \dots$ FIGURE 5:  $r > r_0$ .FIGURE 7:  $2169.9 \dots < r < 2260.7 \dots$ 

generalized radically infinite and positive definite Lyapunov functions as

$$V_m(X) = mx^2 + y^2 + (z - m\sigma - r)^2, \quad (4)$$

when  $m \geq 0$  is arbitrary constant. Since  $V_m(X) = 0$  holds for  $x = y = 0, z = m\sigma + r$ ,  $V_m(X)$  is not positive with respect to the state vector. The point  $(0, 0, m\sigma + r)^T$  is not the equilibrium of system (1). Therefore, the family of Lyapunov functions cannot be employed to study stability of any equilibrium of system (1). So, it is called the family of generalized positive definite Lyapunov functions.

Computing the derivative of  $V$  along the positive half-trajectory of system (1), we have

$$\begin{aligned} \dot{V} &= 2mx \cdot \dot{x} + 2y \cdot \dot{y} + 2(z - m\sigma - r) \dot{z} \\ &= 2mx \cdot (-(\sigma + s)x + \sigma y) + 2y \cdot (rx - y - xz) \\ &\quad + 2(z - m\sigma - r)(xy - bz) \\ &= -V + \left(-2m\left(\sigma + s - \frac{1}{2}\right)\right)x^2 - y^2 - (2b - 1)z^2 \end{aligned}$$

$$\begin{aligned} &+ 2(m\sigma + r)(b - 1)z + (m\sigma + r)^2 \\ &= -V + F(X), \end{aligned} \quad (5)$$

where  $X = (x, y, z)$ , and define the function

$$\begin{aligned} F(X) &= -2m\left(\sigma + s - \frac{1}{2}\right)x^2 - y^2 - (2b - 1)z^2 \\ &\quad + 2(m\sigma + r)(b - 1)z + (m\sigma + r)^2; \end{aligned} \quad (6)$$

computing the extreme value of Lagrange of function  $F(X)$  on  $(x, y, z)$ , because  $F(X)$  is the quadratic function and the local maxima are the global maximum, and letting

$$\begin{aligned} \frac{\partial F}{\partial x} &= -4m\left(\sigma + s - \frac{1}{2}\right)x = 0, \\ \frac{\partial F}{\partial y} &= -2y = 0, \end{aligned} \quad (7)$$

$$\frac{\partial F}{\partial z} = -2(2b - 1)z + 2(m\sigma + r)(b - 1) = 0,$$

we have  $x = 0, y = 0, z = (m\sigma + r)(b - 1)/(2b - 1)$ .

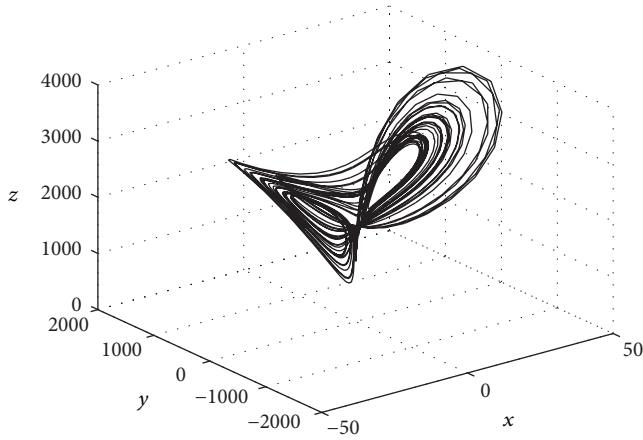


FIGURE 8:  $2260.7 \dots < r < 2743.1 \dots$

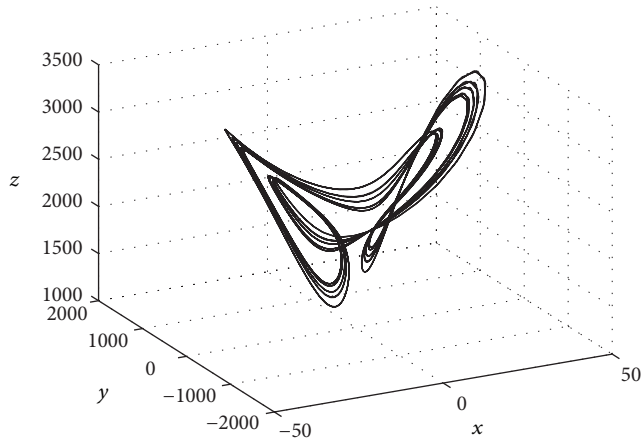


FIGURE 9:  $2260.7 \dots < r < 2743.1 \dots$

Then computing the two-order derivative of  $F(X)$ , we obtain

$$\begin{aligned} \frac{\partial^2 F}{\partial x^2} &= -4m \left( \sigma + s - \frac{1}{2} \right) < 0, \quad \left( \text{For } \sigma + s > \frac{1}{2} \right) \\ \frac{\partial^2 F}{\partial y^2} &= -2 < 0, \\ \frac{\partial^2 F}{\partial z^2} &= -2(2b - 1) < 0, \quad \left( \text{For } b > \frac{1}{2} \right) \\ \frac{\partial^2 F}{\partial x \partial y} &= \frac{\partial^2 F}{\partial y \partial z} = \frac{\partial^2 F}{\partial x \partial z} = 0, \end{aligned} \tag{8}$$

so  $\sup_{X \in \mathbb{R}^3} F(X) = F(x, y, z)|_{(x=0, y=0, z=(m\sigma+r)/(b-1)/(2b-1))} = b^2(m\sigma+r)^2/(2b-1)$ .

When  $V > b^2(m\sigma+r)^2/(2b-1)$ ,  $\dot{V} < 0$ , so we have

$$\lim_{t \rightarrow +\infty} \rho(X(t, t_0), X_0, \Omega_m) = 0; \tag{9}$$

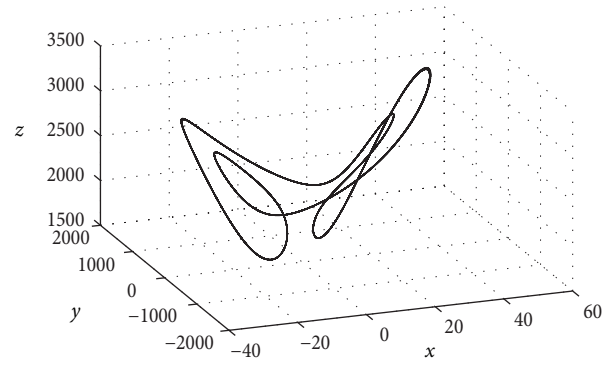


FIGURE 10:  $2260.7 \dots < r < 2743.1 \dots$

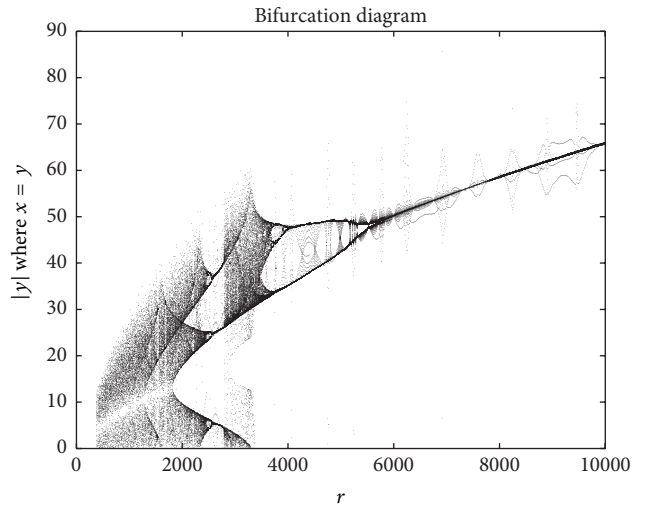


FIGURE 11: The bifurcation diagram of system (1).

now we prove (9) by contradiction. Otherwise, suppose that the trajectory of system (1) stays outside the set  $\Omega_m$ . Since  $V_m(X)$  is monotonic decreasing outside the set  $\Omega_m$ , the limit

$$\lim_{t \rightarrow +\infty} V_m(X(t)) = V_m^* > \frac{b^2(m\sigma+r)^2}{2b-1} \tag{10}$$

exists. Let

$$\begin{aligned} l = \inf_{X \in D} \left( -\frac{dV_m(X)}{dt} \right) \{ D : V_m^* \leq mx^2(t) + y^2(t) \\ + (z(t) - m\sigma - r)^2 \leq mx^2(t_0) + y^2(t_0) \\ + (z(t_0) - m\sigma - r)^2 = V_m(X(t_0)) \}, \end{aligned} \tag{11}$$

where  $l > 0$ ,  $V_m^* > 0$  are constants. So we have

$$\frac{dV_m(X)}{dt} \leq -l. \tag{12}$$

Thus, we have  $0 \leq V_m(X(t)) < V_m(X(t_0)) - l(t - t_0) \rightarrow -\infty$  for  $t \rightarrow +\infty$ . This contradiction implies that expression (9) is true.

From Definition 1, we confirm that  $\Omega_m$  is a globally attractive set and positively invariant set of system (1).  $\square$

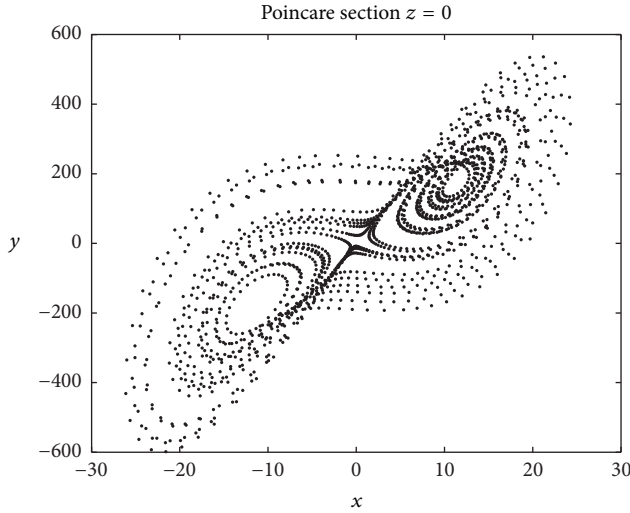


FIGURE 12: The Poincare section of system (1).

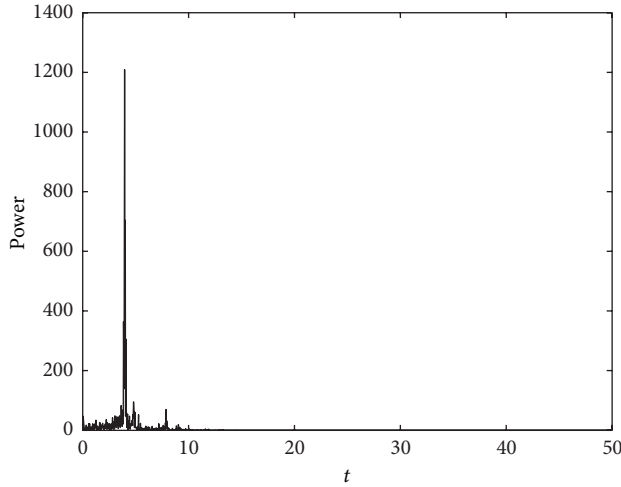


FIGURE 13: The power spectrum of system (1).

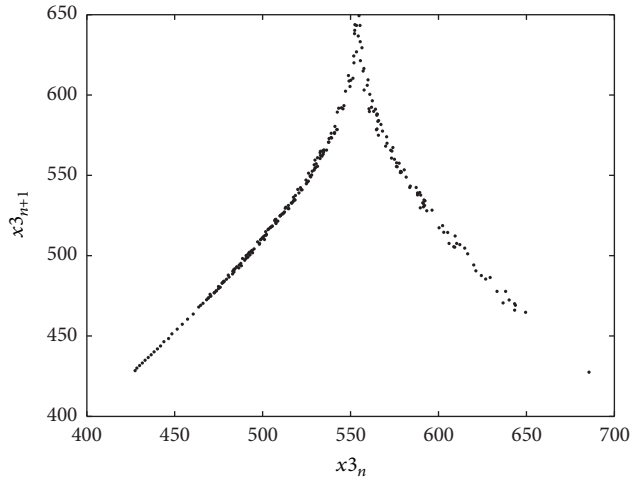


FIGURE 14: The return mapping of system (1).

*Remark 3.* (1) Taking  $m = 0$ , we get a new cylindrate formula for system (1) as

$$y^2 + (z - r)^2 \leq \frac{b^2 r^2}{2b - 1}. \quad (13)$$

(2) Taking  $m = 1$ , we get a new ellipsoidal formula for system (1) as

$$x^2 + y^2 + (z - \sigma - r)^2 \leq \frac{b^2 (\sigma + r)^2}{2b - 1}. \quad (14)$$

(3) Taking  $m = 1/\sigma$ , we get another new ellipsoidal formula for system (1) as

$$\frac{1}{\sigma} x^2 + y^2 + (z - 1 - r)^2 \leq \frac{b^2 (1 + r)^2}{2b - 1}. \quad (15)$$

(4) Taking  $m = r/\sigma$ , we get another ellipsoidal formula for system (1) as

$$\frac{r}{\sigma} x^2 + y^2 + (z - 2r)^2 \leq \frac{4b^2 r^2}{2b - 1}. \quad (16)$$

Similarly, we can get more estimation formulas by taking different value of  $m$ .

When  $0 < \sigma \leq 1$ , our estimation (14) is more accurate than estimation (15) with respect to  $y$  and  $z$ . In fact, we can observe the result from the following inequalities:

$$\begin{aligned} |y| &\leq \frac{b^2 (\sigma + r)^2}{2b - 1} \leq \frac{b^2 (1 + r)^2}{2b - 1}, \\ (1 + r) \left( 1 - \frac{b}{\sqrt{2b - 1}} \right) &\leq (\sigma + r) \left( 1 - \frac{b}{\sqrt{2b - 1}} \right) \leq z \\ &\leq (\sigma + r) \left( 1 + \frac{b}{\sqrt{2b - 1}} \right) \\ &\leq (1 + r) \left( 1 + \frac{b}{\sqrt{2b - 1}} \right). \end{aligned} \quad (17)$$

On the other hand, when  $\sigma \neq r$ , from the following inequality, we can see that our estimation (16) is better than estimation (14), with respect to  $x$ :

$$x^2 \leq \frac{4b^2 \sigma r}{2b - 1} \leq \frac{b^2 (\sigma + r)^2}{2b - 1}. \quad (18)$$

When  $\sigma = r$ , for the variable  $x$ , the estimation (16) is equal to estimation (14).

From the intersection of set theory, we construct different globally attractive sets to get effective results.

**Theorem 4.** Suppose  $\sigma > 0$ ,  $s \geq 10$ ,  $b > 0$ ,  $r \geq (\sigma + s)/\sigma$ . The cylinder given by

$$\begin{aligned} Q_1 : &\begin{cases} y^2 + (z - r)^2 \leq \tau r^2, \\ x^2 \leq \tau r^2 \left( \frac{\sigma}{\sigma + s} \right)^2, \end{cases} \quad (\text{when } 0 < b \leq 1) \\ Q_2 : &\begin{cases} y^2 + (z - r)^2 \leq \frac{b^2 r^2}{2b - 1}, \\ x^2 \leq \frac{b^2 r^2}{2b - 1} \left( \frac{\sigma}{\sigma + s} \right)^2 \end{cases} \quad (\text{when } b > 1) \end{aligned} \quad (19)$$

is a globally attractive set and positively invariant set of system (1), where  $\tau > 1$  is any constant.

*Proof.* At first, we consider the case of  $0 < b \leq 1$ . For the second and third equations of system (1), we construct a generalized positive definite and radical unbounded Lyapunov function

$$V = \frac{1}{2} (y^2 + (z - r)^2). \quad (20)$$

We compute the derivate of  $V$  along the trajectory of system (1) as

$$\begin{aligned} \dot{V} &= y \cdot \dot{y} + (z - r) \dot{z} \\ &= y \cdot (rx - y - xz) + (z - r) (xy - bz) \\ &= -y^2 - bz^2 + rbz \leq -y^2 - \frac{b}{2}z^2 + \frac{b}{2} \cdot 2 \cdot rz \\ &= -y^2 - \frac{b}{2} (z - r)^2 + \frac{b}{2}r^2 \\ &\leq -\frac{b}{2}y^2 - \frac{b}{2} (z - r)^2 + \frac{b}{2}r^2 < 0, \end{aligned} \quad (21)$$

for  $y^2 + (z - r)^2 > r^2$ . Thus the cylinder  $y^2 + (z - r)^2 \leq \tau r^2$  is a globally attractive set and positively invariant set of system (1) with respect to  $y$  and  $z$ . Then we have  $|y| \leq \sqrt{\tau}r$ .

Substituting the ultimate boundedness of  $y$  into the first equation of system (1) and employing constant variation formula, we have

$$\begin{aligned} x(t) &= x(t_0) \cdot e^{-(\sigma+s)(t-t_0)} + \int_{t_0}^t \sigma \cdot y(\omega) \\ &\quad \cdot e^{-(\sigma+s)(t-\omega)} d\omega \\ &\leq x(t_0) \cdot e^{-(\sigma+s)(t-t_0)} + \int_{t_0}^t \sigma \cdot \sqrt{\tau} \cdot r \\ &\quad \cdot e^{-(\sigma+s)(t-\omega)} d\omega \\ &= x(t_0) \cdot e^{-(\sigma+s)(t-t_0)} + \sqrt{\tau} \cdot r \\ &\quad \cdot \frac{\sigma}{\sigma+s} (1 - e^{-(\sigma+s)(t-t_0)}) \\ &= \left( x(t_0) - \sqrt{\tau} \cdot r \cdot \frac{\sigma}{\sigma+s} \right) \cdot e^{-(\sigma+s)(t-t_0)} + \sqrt{\tau} \cdot r \\ &\quad \cdot \frac{\sigma}{\sigma+s}. \end{aligned} \quad (22)$$

Therefore,

$$\begin{aligned} &\left( x(t) - \sqrt{\tau} \cdot r \cdot \frac{\sigma}{\sigma+s} \right) \\ &\leq \left( x(t_0) - \sqrt{\tau} \cdot r \cdot \frac{\sigma}{\sigma+s} \right) \cdot e^{-(\sigma+s)(t-t_0)} \rightarrow 0, \end{aligned} \quad (23)$$

for  $x(t_0) > \sqrt{\tau} \cdot r \cdot (\sigma/(\sigma+s))$ ,  $t \rightarrow +\infty$ ; that is,  $x(t)$  is greater than  $\sqrt{\tau} \cdot r \cdot (\sigma/(\sigma+s))$  and tends to  $\sqrt{\tau} \cdot r \cdot (\sigma/(\sigma+s))$  exponentially.

At the same time, we have

$$\begin{aligned} x(t) &= x(t_0) \cdot e^{-(\sigma+s)(t-t_0)} \\ &\quad + \int_{t_0}^t \sigma \cdot y(\omega) \cdot e^{-(\sigma+s)(t-\omega)} d\omega \\ &\geq x(t_0) \cdot e^{-(\sigma+s)(t-t_0)} - \sigma \cdot \sqrt{\tau} \cdot r \cdot e^{-(\sigma+s)t} \\ &\quad \cdot \int_{t_0}^t e^{(\sigma+s)\omega} d\omega \\ &= x(t_0) \cdot e^{-(\sigma+s)(t-t_0)} - \sqrt{\tau} \cdot r \\ &\quad \cdot \frac{\sigma}{\sigma+s} (1 - e^{-(\sigma+s)(t-t_0)}) \\ &= \left( x(t_0) + \sqrt{\tau} \cdot r \cdot \frac{\sigma}{\sigma+s} \right) \cdot e^{-(\sigma+s)(t-t_0)} - \sqrt{\tau} \cdot r \\ &\quad \cdot \frac{\sigma}{\sigma+s}. \end{aligned} \quad (24)$$

Thus, one can see that  $-x(t) - \sqrt{\tau} \cdot r \cdot (\sigma/(\sigma+s)) \leq -(x(t_0) + \sqrt{\tau} \cdot r \cdot (\sigma/(\sigma+s))) \cdot e^{-(\sigma+s)(t-t_0)} \rightarrow 0$ , for  $x(t_0) < -\sqrt{\tau} \cdot r \cdot (\sigma/(\sigma+s))$ . That is,  $x(t)$  is less than  $-\sqrt{\tau} \cdot r \cdot (\sigma/(\sigma+s))$  and tends to  $-\sqrt{\tau} \cdot r \cdot (\sigma/(\sigma+s))$  exponentially. Consequently, the set  $|x| \leq \sqrt{\tau} \cdot r \cdot (\sigma/(\sigma+s))$  is the globally attractive set and positively invariant set of system (1).

Consider the case of  $b > 1$ . Employing Lyapunov function (20) again, we compute the derivate of  $V$  along the trajectory of system (1) as

$$\begin{aligned} \dot{V} &= -y^2 - bz^2 + rbz \\ &= -V - \frac{1}{2}y^2 - \left( b - \frac{1}{2} \right) z^2 + r(b-1)z + \frac{1}{2}r^2 \\ &= -V + G(X), \end{aligned} \quad (25)$$

where  $X = (y, z)$ , and define the function

$$G(X) = -\frac{1}{2}y^2 - \left( b - \frac{1}{2} \right) z^2 + r(b-1)z + \frac{1}{2}r^2. \quad (26)$$

Computing the extreme value of Lagrange of function  $G(X)$  on  $(y, z)$ , because  $G(X)$  is the quadratic function and the local maxima are the global maximum, and letting

$$\frac{\partial G}{\partial y} = -y = 0, \quad (27)$$

$$\frac{\partial G}{\partial z} = -2 \left( b - \frac{1}{2} \right) z + r(b-1) = 0,$$

we have  $y = 0, z = r(b-1)/(2b-1)$ .

Computing the second partial derivative of  $G(X)$ ,

$$\frac{\partial^2 G}{\partial y^2} = -1 < 0,$$

$$\frac{\partial^2 G}{\partial x^2} = -2 \left( b - \frac{1}{2} \right) < 0, \quad \left( \text{For } b > \frac{1}{2} \right) \quad (28)$$

$$\frac{\partial^2 G}{\partial y \partial z} = 0;$$

therefore,

$$\sup_{X \in \mathbb{R}^2} G(X) = G(y, z)|_{(y=0, z=r(b-1)/(2b-1))} = \frac{b^2 r^2}{2(2b-1)}. \quad (29)$$

When  $V > b^2 r^2 / (2(2b-1))$ ,  $\dot{V} < 0$ . Now we prove by contradiction similar to Theorem 2 that  $\lim_{t \rightarrow +\infty} \rho(X(t), t_0, X_0, Q_2) = 0$ , so the set  $y^2 + (z-r)^2 \leq b^2 r^2 / (2b-1)$  is the globally attractive set and positively invariant set of system (1).

From

$$y^2 + (z-r)^2 \leq \frac{b^2 r^2}{2b-1}, \quad (30)$$

we have  $|y| \leq br/\sqrt{2b-1}$ . Similar to (23) and (24), we can get  $|x(t)| \leq (br/\sqrt{2b-1}) \cdot (\sigma/(\sigma+s))$ , so the set  $|x(t)| \leq (br/\sqrt{2b-1}) \cdot (\sigma/(\sigma+s))$  is the globally attractive set with respect to  $x$  that shows that  $Q_2$  is globally attractive set and positively invariant set of system (1).  $\square$

## 5. Applications to Global and Exponential Tracking (or Stabilizing) of Any $\omega$ -Period Solution

There are two aims of the chaotic control. One is to stabilize an unstable (or stable but not asymptotically stable) equilibrium so that it can become a globally asymptotically stable or even a globally exponentially stable one. The other is to track a special unstable  $\omega$ -period solution, that is, to control all the solutions and let them converge to this  $\omega$ -period solution. Due to existence of the globally attractive set, all the solutions will enter this globally attractive compact set. In the compact set, the right side of system (1) must satisfy Lipschitz condition. This fact ensures the existence of some linear feedback controllers so that the controlled system can track some  $\omega$ -period solution or can be stabilized.

Suppose that  $X^*(t) = (x^*(t), y^*(t), z^*(t))^T$  is any periodic solution or any equilibrium of system (1). Let  $\bar{X}(t) = X(t) - X^*(t)$ . Then  $\bar{X}(t)$  satisfies

$$\begin{aligned} \dot{\bar{x}} &= -(\sigma+s)\bar{x} + \sigma\bar{y}, \\ \dot{\bar{y}} &= r\bar{x} - \bar{y} - xz + x^*z^*, \\ \dot{\bar{z}} &= xy - x^*y^* - b\bar{z}. \end{aligned} \quad (31)$$

System (31) with controllers can be written as

$$\begin{aligned} \dot{\bar{x}} &= -(\sigma+s)\bar{x} + \sigma\bar{y} - k_1\bar{x}, \\ \dot{\bar{y}} &= r\bar{x} - \bar{y} - xz + x^*z^* - k_2\bar{y}, \\ \dot{\bar{z}} &= xy - x^*y^* - b\bar{z} - k_3\bar{z}. \end{aligned} \quad (32)$$

Now we design some simplest linear feedback controllers so that the zero solution of the controlled system (32) is globally exponentially stable. When  $X^*(t)$  is a periodic solution, we will confirm that all the solutions of system (1) track  $X^*(t)$  globally and exponentially, and when  $X^*(t)$  is an equilibrium  $X^*$ , we will prove that  $X^*$  can be globally exponentially stabilized.

**Theorem 5.** *The control parameters always can be selected as  $k_2 = k_3 = 0$  and  $k_1 > 0$  suitably large so that the zero solution of system (32) is globally exponentially stable. In other words, all the solutions of system (1) track the periodic solution  $X^*(t)$  globally and exponentially, or the equilibrium  $X^*$  can be globally and exponentially stabilized.*

*Proof.* (1) Suppose that  $X^*(t)$  is a known periodic solution. Select the parameters as

$$k_1 > \frac{y^{*2}}{4b} + \frac{1}{4}(\sigma+r-z^*)^2 - (\sigma+s). \quad (33)$$

It implies that the following matrix of periodic functions is negative definite [20–23]:

$$G_1(t) = \begin{pmatrix} -2(\sigma+s+k_1) & \sigma+r-z^* & y^* \\ \sigma+r-z^* & -2 & 0 \\ y^* & 0 & -2b \end{pmatrix}. \quad (34)$$

Denote by  $\bar{\lambda}_1(t)(G_1)$  the maximal eigenvalues of  $G_1(t)$ . Then, we have  $-\beta = \max_{t \in (0, \omega)} \bar{\lambda}_1(t)(G_1)$  ( $\beta > 0$ ).

Construct a positive definite and radical unbounded Lyapunov function for system (32) as

$$V(\bar{X}) = \bar{x}^2 + \bar{y}^2 + \bar{z}^2. \quad (35)$$

We compute the derivative of it and have

$$\begin{aligned} \frac{dV}{dt} &= 2\bar{x} \cdot \dot{\bar{x}} + 2\bar{y} \cdot \dot{\bar{y}} + 2\bar{z} \cdot \dot{\bar{z}} = 2\bar{x} \\ &\cdot (-(\sigma+s)\bar{x} + \sigma\bar{y} - k_1\bar{x}) + 2\bar{y} \\ &\cdot (r\bar{x} - \bar{y} - xz + x^*z^*) + 2\bar{z}(xy - x^*y^* - b\bar{z}) \\ &= -2(\sigma+s)\bar{x}^2 + 2\sigma\bar{x}\bar{y} - 2k_1\bar{x}^2 + 2r\bar{x}\bar{y} - 2\bar{y}^2 \\ &- 2z^*\bar{x}\bar{y} + 2y^*\bar{x}\bar{z} - 2b\bar{z}^2 = \begin{pmatrix} \bar{x} \\ \bar{y} \\ \bar{z} \end{pmatrix}^T \\ &\cdot \begin{pmatrix} -2(\sigma+s+k_1) & \sigma+r-z^* & y^* \\ \sigma+r-z^* & -2 & 0 \\ y^* & 0 & -2b \end{pmatrix} \begin{pmatrix} \bar{x} \\ \bar{y} \\ \bar{z} \end{pmatrix} \\ &\leq \bar{\lambda}_1(t)(G_1)(\bar{x}^2(t) + \bar{y}^2(t) + \bar{z}^2(t)). \end{aligned} \quad (36)$$

According to Gronwall inequation, formula (36) is transformed as

$$\begin{aligned} &(\bar{x}^2(t) + \bar{y}^2(t) + \bar{z}^2(t)) \\ &\leq (\bar{x}^2(t_0) + \bar{y}^2(t_0) + \bar{z}^2(t_0)) e^{\int_{t_0}^t \bar{\lambda}_1(s) ds}, \quad t \geq t_0. \end{aligned} \quad (37)$$

Formula (37) implies the conclusion.

(2) Suppose that the expression of  $X^*(t)$  is unknown and the amplitude of it is known or can be estimated.

Suppose  $x_g = \max_{t \in (0, \omega)} |x(t)|$ ,  $y_g = \max_{t \in (0, \omega)} |y(t)|$ ,  $z_g = \max_{t \in (0, \omega)} |z(t)|$  are amplitudes of the 3 components of the periodic solution. The parameters can be selected as

$$k_1 > \frac{y_g^2}{4b} + \frac{1}{4} (\sigma + r + z_g)^2 - (\sigma + s). \quad (38)$$

It implies that the following constant matrix is negative definite:

$$G_2 = \begin{pmatrix} -2(\sigma + s + k_1) & \sigma + r + z_g & y_g \\ \sigma + r + z_g & -2 & 0 \\ y_g & 0 & -2b \end{pmatrix}. \quad (39)$$

By  $\bar{\lambda}_2(G_2)$ , we denote the maximal eigenvalues of matrix  $G_2$ ; then  $-\gamma = \max_{t \in (0, \omega)} \bar{\lambda}_2(G_2)$ . Employing the Lyapunov function (35), we have

$$\begin{aligned} \frac{dV}{dt} &= -2(\sigma + s + k_1) \bar{x}^2 - 2\bar{y}^2 - 2b\bar{z}^2 \\ &+ 2(\sigma + r - z^*) \bar{x}\bar{y} + 2y^* \bar{x}\bar{z} \leq -2(\sigma + s + k_1) |\bar{x}|^2 \\ &- 2|\bar{y}|^2 - 2b|\bar{z}|^2 + 2(\sigma + r + z_g) |\bar{x}| |\bar{y}| + 2y_g |\bar{x}| \\ &\cdot |\bar{z}| = \begin{pmatrix} |\bar{x}| \\ |\bar{y}| \\ |\bar{z}| \end{pmatrix}^T \\ &\cdot \begin{pmatrix} -2(\sigma + s + k_1) & \sigma + r + z_g & y_g \\ \sigma + r + z_g & -2 & 0 \\ y_g & 0 & -2b \end{pmatrix} \begin{pmatrix} |\bar{x}| \\ |\bar{y}| \\ |\bar{z}| \end{pmatrix} \\ &\leq \bar{\lambda}_2(G_2) (x^2 + y^2 + z^2). \end{aligned} \quad (40)$$

Hence, we have

$$\begin{aligned} &(\bar{x}^2(t) + \bar{y}^2(t) + \bar{z}^2(t)) \\ &\leq (\bar{x}^2(t_0) + \bar{y}^2(t_0) + \bar{z}^2(t_0)) e^{-\gamma(t-t_0)}, \quad t \geq t_0. \end{aligned} \quad (41)$$

This inequality implies the conclusion.

(3) Suppose the amplitude of  $X^*(t)$  is unknown. The periodic solution is assumed to be in the globally attractive set. We can use the boundedness of globally attractive set as the boundedness of  $X^*(t)$ .

If  $b > 1$ , we select  $k_2 = k_3 = 0$  and

$$k_1 > \frac{br^2}{4(2b-1)} + \frac{1}{4} \left( \sigma + \frac{br}{\sqrt{2b-1}} \right)^2 - (\sigma + s). \quad (42)$$

This guarantees that the following constant matrix is negative definite:

$$G_3 = \begin{pmatrix} -2(\sigma + s + k_1) & \sigma + \frac{br}{\sqrt{2b-1}} & \frac{br}{\sqrt{2b-1}} \\ \sigma + \frac{br}{\sqrt{2b-1}} & -2 & 0 \\ \frac{br}{\sqrt{2b-1}} & 0 & -2b \end{pmatrix}. \quad (43)$$

Denote by  $\bar{\lambda}_3(G_3)$  the maximal eigenvalues of matrix  $G_3$ . Employing the Lyapunov function (35), we have

$$\begin{aligned} \frac{dV}{dt} &= \begin{pmatrix} \bar{x} \\ \bar{y} \\ \bar{z} \end{pmatrix}^T \begin{pmatrix} -2(\sigma + s + k_1) & \sigma + r - z^* & y^* \\ \sigma + r - z^* & -2 & 0 \\ y^* & 0 & -2b \end{pmatrix} \begin{pmatrix} \bar{x} \\ \bar{y} \\ \bar{z} \end{pmatrix} \\ &\leq \begin{pmatrix} |\bar{x}| \\ |\bar{y}| \\ |\bar{z}| \end{pmatrix}^T \\ &\cdot \begin{pmatrix} -2(\sigma + s + k_1) & \sigma + \frac{br}{\sqrt{2b-1}} & \frac{br}{\sqrt{2b-1}} \\ \sigma + \frac{br}{\sqrt{2b-1}} & -2 & 0 \\ \frac{br}{\sqrt{2b-1}} & 0 & -2b \end{pmatrix} \begin{pmatrix} |\bar{x}| \\ |\bar{y}| \\ |\bar{z}| \end{pmatrix} \\ &\leq \bar{\lambda}_3(G_3) (\bar{x}^2 + \bar{y}^2 + \bar{z}^2). \end{aligned} \quad (44)$$

Hence, we obtain

$$\bar{x}^2 + \bar{y}^2 + \bar{z}^2 \leq V(X(t_0)) e^{\bar{\lambda}_3(G_3)(t-t_0)}, \quad t \geq t_0. \quad (45)$$

This ensures the conclusion.

When  $0 < b \leq 1$ , we take

$$\begin{aligned} k_2 &= k_3 = 0, \\ k_1 &> \frac{\tau r^2}{4b} + \frac{1}{4} (\sigma + \sqrt{\tau r})^2 - (\sigma + s). \end{aligned} \quad (46)$$

It ensures that the following constant matrix is negative definite:

$$G_4 = \begin{pmatrix} -2(\sigma + s + k_1) & \sigma + \sqrt{\tau r} & \sqrt{\tau r} \\ \sigma + \sqrt{\tau r} & -2 & 0 \\ \sqrt{\tau r} & 0 & -2b \end{pmatrix}. \quad (47)$$

Denote by  $\bar{\lambda}_4(G_4)$  the matrix eigenvalues of matrix  $G_4$ . Employing the Lyapunov function (35), we have

$$\begin{aligned} \frac{dV}{dt} &= \begin{pmatrix} \bar{x} \\ \bar{y} \\ \bar{z} \end{pmatrix}^T \\ &\cdot \begin{pmatrix} -2(\sigma + s + k_1) & \sigma + r - z^* & y^* \\ \sigma + r - z^* & -2 & 0 \\ y^* & 0 & -2b \end{pmatrix} \begin{pmatrix} \bar{x} \\ \bar{y} \\ \bar{z} \end{pmatrix} \\ &\leq \begin{pmatrix} |\bar{x}| \\ |\bar{y}| \\ |\bar{z}| \end{pmatrix}^T \\ &\cdot \begin{pmatrix} -2(\sigma + s + k_1) & \sigma + \sqrt{\tau}r & \sqrt{\tau}r \\ \sigma + \sqrt{\tau}r & -2 & 0 \\ \sqrt{\tau}r & 0 & -2b \end{pmatrix} \begin{pmatrix} |\bar{x}| \\ |\bar{y}| \\ |\bar{z}| \end{pmatrix} \\ &\leq \bar{\lambda}_4(G_4)(\bar{x}^2 + \bar{y}^2 + \bar{z}^2). \end{aligned} \quad (48)$$

Hence, we obtain

$$\bar{x}^2 + \bar{y}^2 + \bar{z}^2 \leq V(X(t_0))e^{\bar{\lambda}_4(G_4)(t-t_0)}, \quad t \geq t_0. \quad (49)$$

This ensures the conclusion. The proof of Theorem 5 is complete.  $\square$

## 6. Globally Exponential Synchronization of Two Chaotic Systems

*Definition 6.* Two nonlinear dynamic systems [24] are given as follows:

$$\dot{X} = F(t, X), \quad (50)$$

$$\dot{Y} = F(t, Y) + \mu(X, Y), \quad (51)$$

where  $X, Y \in R^n$  and the function  $F$  is an  $n$ -dimensional nonlinear function. Function  $\mu$  is an  $n$ -dimensional control input function. We call system (50) the drive system and system (51) the response system. If  $\lim_{t \rightarrow \infty} \|Y(t) - X(t)\| = 0$ , then system (50) and system (51) are exponentially synchronized.

Consider two similar systems of system (1); the variables of the drive system are marked with the subscript 1 and the variables of the response system are marked with the subscript 2.

Suppose that the drive system is

$$\begin{aligned} \dot{x}_1 &= -(\sigma + s)x_1 + \sigma y_1, \\ \dot{y}_1 &= rx_1 - y_1 - x_1 z_1, \\ \dot{z}_1 &= x_1 y_1 - bz_1. \end{aligned} \quad (52)$$

The response system is

$$\begin{aligned} \dot{x}_2 &= -(\sigma + s)x_2 + \sigma y_2 + \mu_1(e_x, e_y, e_z), \\ \dot{y}_2 &= rx_2 - y_2 - x_2 z_2 + \mu_2(e_x, e_y, e_z), \\ \dot{z}_2 &= x_2 y_2 - bz_2 + \mu_3(e_x, e_y, e_z), \end{aligned} \quad (53)$$

where  $\mu_1, \mu_2$ , and  $\mu_3$  are the controllers designed satisfying  $\mu_i(0, 0, 0) = 0, i = 1, 2, 3$ .

Let  $e^T = (e_x, e_y, e_z)$ ,  $e_x = x_2 - x_1, e_y = y_2 - y_1, e_z = z_2 - z_1$ ; then we have the error dynamic system as follows:

$$\begin{aligned} \dot{e}_x &= -(\sigma + s)e_x + \sigma e_y + \mu_1, \\ \dot{e}_y &= re_x - e_y - z_2 e_x - x_2 e_z + e_x e_z + \mu_2, \\ \dot{e}_z &= y_2 e_x + x_2 e_y - e_x e_y - be_z + \mu_3. \end{aligned} \quad (54)$$

The aim is to design the effective controllers  $\mu_1, \mu_2$ , and  $\mu_3$  to ensure that the zero solution of the error dynamic system (54) is globally exponentially stable. It means that the drive system (52) and the response system (53) are globally exponentially synchronized. That is to say that  $\lim_{t \rightarrow \infty} \|e(t)\| = 0$ .

We suppose that  $|x| \leq M_x, |y| \leq M_y, |z| \leq M_z$  because the chaotic system is bounded.

*Definition 7.* If there exists constant  $\alpha > 0$  satisfying  $V(t) \leq V(t_0)e^{-\alpha(t-t_0)}$  for arbitrary  $t > t_0$ , then the origin of the system is said to be exponentially stable.

**Theorem 8.** For the error dynamic system (54), the controller is designed as follows:

$$\begin{aligned} \mu_1 &= -\sigma e_y - ke_x, \\ \mu_2 &= z_2 e_x - re_x, \\ \mu_3 &= -y_2 e_x. \end{aligned} \quad (55)$$

We can select the parameter  $k > 0$  to make the matrix

$$P = \begin{pmatrix} \sigma + s + k & 0 & 0 \\ 0 & 1 & 0 \\ 0 & 0 & b \end{pmatrix} \quad (56)$$

positive definite. Then the zero solution of the error dynamic system (54) is globally exponentially synchronized. It means that the drive system (52) and the response system (53) are globally exponentially synchronized.

*Proof.* We construct a positive definite and radical unbounded Lyapunov function as

$$V = \frac{1}{2}(e_x^2 + e_y^2 + e_z^2). \quad (57)$$

Computing the time derivative of  $V$  along the positive half-trajectory of system (1), we have

$$\begin{aligned}
 \frac{dV}{dt} &= e_x \dot{e}_x + e_y \dot{e}_y + e_z \dot{e}_z \\
 &= e_x \left( -(\sigma + s) e_x + \sigma e_y + \mu_1 \right) \\
 &\quad + e_y \left( r e_x - e_y - z_2 e_x - x_2 e_z + e_x e_z + \mu_2 \right) \\
 &\quad + e_z \left( y_2 e_x + x_2 e_y - e_x e_y - b e_z + \mu_3 \right) \\
 &= -((\sigma + s) + k) e_x^2 - e_y^2 - b e_z^2 \\
 &= \begin{pmatrix} e_x \\ e_y \\ e_z \end{pmatrix}^T \begin{pmatrix} -(\sigma + s + k) & 0 & 0 \\ 0 & -1 & 0 \\ 0 & 0 & -b \end{pmatrix} \begin{pmatrix} e_x \\ e_y \\ e_z \end{pmatrix} \\
 &= - \begin{pmatrix} e_x \\ e_y \\ e_z \end{pmatrix}^T \begin{pmatrix} \sigma + s + k & 0 & 0 \\ 0 & 1 & 0 \\ 0 & 0 & b \end{pmatrix} \begin{pmatrix} e_x \\ e_y \\ e_z \end{pmatrix} \\
 &= -e^T P e,
 \end{aligned} \tag{58}$$

where

$$P = \begin{pmatrix} \sigma + s + k & 0 & 0 \\ 0 & 1 & 0 \\ 0 & 0 & b \end{pmatrix}. \tag{59}$$

Obviously, the zero solution of the error dynamic system (54) is globally exponentially stable when the matrix  $P$  is positive definite under the condition that the following inequalities are established:

$$\begin{aligned}
 \sigma + s + k &> 0, \\
 b(\sigma + s + k) &> 0;
 \end{aligned} \tag{60}$$

we can have  $k > -(\sigma + s)$ .

Thus, when  $k > 0$ , the matrix  $P$  is positive definite and  $\dot{V}$  is negative definite. It can be observed from formula (58) and the knowledge of advanced algebra that

$$\frac{dV}{dt} \leq -\lambda_{\min}(P) (e_x^2 + e_y^2 + e_z^2) \leq -\lambda_{\min}(P) V. \tag{61}$$

Therefore,

$$V(X(t)) \leq V(X(t_0)) e^{-\lambda_{\min}(P)(t-t_0)}, \quad t \geq t_0. \tag{62}$$

When  $t \rightarrow +\infty$ ,  $V(X(t)) \rightarrow 0$ . It ensures that the zero solution of the error dynamic system (54) is globally exponentially stable. It means that the drive system (52) and the response system (53) are globally exponentially synchronized.  $\square$

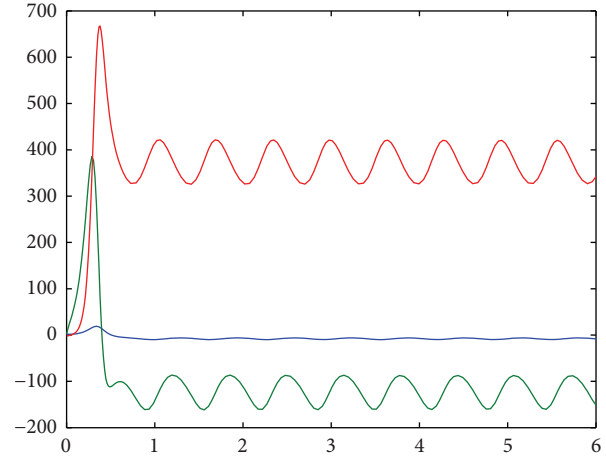


FIGURE 15: State of variants  $x, y, z$  of system (1) without control law.

## 7. Numerical Simulation

In this section, we will do some numerical simulations to verify the effectiveness of the proposed methods by using the Runge-Kutta method. In the numerical simulations, the time step size is 0.001, and the parameters are chosen as  $\sigma = 0.7$ ,  $s = 10$ ,  $b = 8/3$  to ensure the existence of system (1).

For the numerical simulation, we consider the systems given as (52) and (53). The initial values of the drive system and response system are taken as  $(x_1(0), y_1(0), z_1(0)) = (0.5, 0.9, 1.2)$ ,  $(x_2(0), y_2(0), z_2(0)) = (-0.8, -0.4, -1)$ . Hence, the initial error is  $(e_x(0), e_y(0), e_z(0)) = (-1.3, -1.3, -2.2)$ .

Considering controller in Theorem 8, we select the feedback gain  $k = 1$  as the controller law of system (53) for the linear feedback synchronization. The simulation results are illustrated in Figures 15–17. In Figure 15, we can notice that the state variants  $x, y, z$  of system (1) are unstable; this is when there is no controller. Figure 16 displays the time evolution of the drive system and the response system when we add the controller law. From Figure 16, we can see that the two systems starting from different conditions are synchronized with each other. The dynamics of synchronization error is defined as  $e(t) = \sqrt{e_x^2(t) + e_y^2(t) + e_z^2(t)}$ , whose time evolution is shown in Figure 17. It is clear that the error signals converge to zero finally.

## 8. Conclusions

In this paper, a low mode system in the internal wave dynamics is studied. Dynamical behaviors of the system are analyzed including some basic dynamical properties, such as the attractor diagram, bifurcation diagram, Poincare section, power spectrum, and return mapping, and we obtain the estimation of the globally exponentially attractive set and the positive invariant set of the system via selecting appropriate positive definite and radical unbounded Lyapunov function. On this basis, for any periodic solution, we design some feedback controllers to control all the trajectories of the chaotic system tracking the special periodic solution globally.

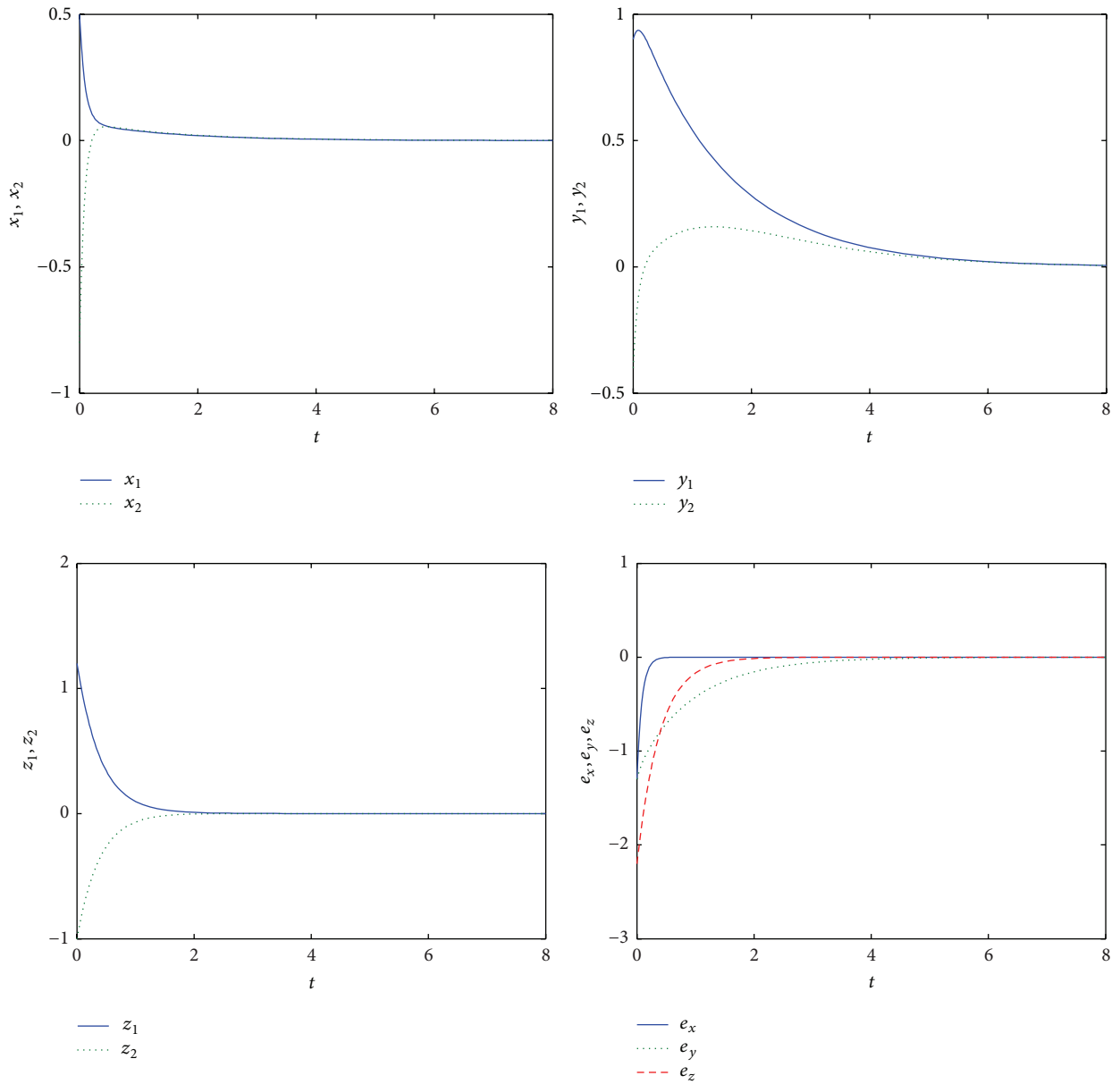


FIGURE 16: Linear feedback synchronization  $k = 1$ .

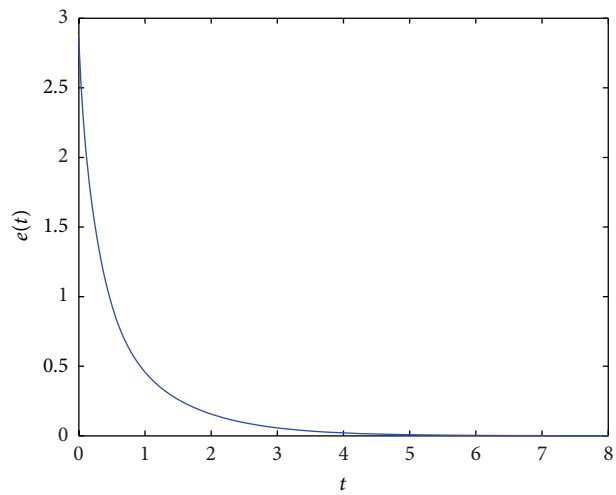


FIGURE 17: Error  $e(t)$  with the change of time  $t$ .

The globally exponential synchronization of the chaotic system is realized by the method of drive-response synchronization, and the synchronization conditions are given. The effectiveness of the method is shown by theoretical analysis and numerical simulation.

### Competing Interests

The authors declare that there are no competing interests regarding the publication of this paper.

### Acknowledgments

This research was supported by the National Natural Science Foundation of China under Project nos. 11572146 and 11526105, the Research Fund of Liaoning Provincial Education Department under Project no. L2013248, and the Jinzhou Science and Technology Special Fund under Project no. 13A1D32.

### References

- [1] E. N. Lorenz, "Deterministic non-periodic flows," *Atoms Science*, vol. 20, pp. 130–141, 1963.
- [2] Y. Shu, Y. Zhang, and H. Xu, "Control and synchronization of general Lorenz chaotic system," *Journal of Chongqing Institute of Technology (Natural Sciences)*, vol. 22, no. 8, pp. 54–61, 2008.
- [3] D. G. Thomas, B. Khomami, and R. Sureshkumar, "Nonlinear dynamics of viscoelastic Taylor-Couette flow: effect of elasticity on pattern selection, molecular conformation and drag," *Journal of Fluid Mechanics*, vol. 620, pp. 353–382, 2009.
- [4] W.-S. Kim, "Application of Taylor vortex to crystallization," *Journal of Chemical Engineering of Japan*, vol. 47, no. 2, pp. 115–123, 2014.
- [5] H. L. Swinney and J. P. Gollub, *Hydrodynamic Instabilities and the Transition to Turbulence*, Springer, Berlin, Germany, 1981.
- [6] G. I. Taylor, "Stability of a viscous liquid contained between two rotating cylinders," *Philosophical Transactions of the Royal Society of London A*, vol. 223, pp. 289–343, 1923.
- [7] H. Liu and B. Jiang, "Chaos control of gear system with elastomeric web based on multi-parameter multistep method," *Journal of Harbin Institute of Technology*, vol. 19, no. 5, pp. 23–30, 2012.
- [8] G. R. Chen and X. Dong, *From Chaos to Order: Methodologies, Perspectives and Applications*, World Scientific, Singapore, 1998.
- [9] H. L. Swinney and J. P. Gollub, *Hydrodynamic, Instabilities and the Transition to Turbulence*, Springer, Berlin, Germany, 1981.
- [10] H. Y. Wang, "The Chaos behavior and simulation of three-model systems of Couette-Taylor flow," *Acta Mathematica Scientia. Series A*, vol. 35, no. 4, pp. 769–779, 2015.
- [11] S. Liu, "The wave mechanics in chaos and atmospheric turbulence," *Science in China (Series B)*, vol. 5, 1986.
- [12] L. M. Pecora and T. L. Carroll, "Synchronization in chaotic systems," *Physical Review Letters*, vol. 64, no. 8, pp. 821–824, 1990.
- [13] L. M. Pecora and T. L. Carroll, "Driving systems with chaotic signals," *Physical Review A*, vol. 44, no. 4, pp. 2374–2383, 1991.
- [14] D.-Y. Chen, C. Wu, C.-F. Liu, X.-Y. Ma, Y.-J. You, and R.-F. Zhang, "Synchronization and circuit simulation of a new double-wing chaos," *Nonlinear Dynamics*, vol. 67, no. 2, pp. 1481–1504, 2012.
- [15] D. Chen, W. Zhao, X. Liu, and X. Ma, "Synchronization and anti-synchronization of a class of chaotic systems with nonidentical orders and uncertain parameters," *Journal of Computational and Nonlinear Dynamics*, vol. 10, no. 1, Article ID 011003, 2015.
- [16] J. Guckenheimer, *Nonlinear Oscillation, Dynamical Systems, and Bifurcation of Vector Fields*, Springer, Berlin, Germany, 1983.
- [17] J. H. Ge and J. Xu, "Hopf bifurcation and chaos in an inertial neuron system with coupled delay," *Science China Technological Sciences*, vol. 56, no. 9, pp. 2299–2309, 2013.
- [18] H. A. El-Saka, E. Ahmed, M. I. Shehata, and A. M. A. El-Sayed, "On stability, persistence, and Hopf bifurcation in fractional order dynamical systems," *Nonlinear Dynamics*, vol. 56, no. 1-2, pp. 121–126, 2009.
- [19] X. Liao, "On the new results of global attractive set and positive invariant set of the Lorenz chaotic system and the applications to chaos control and synchronization," *Science in China, Series E: Information Sciences*, vol. 34, no. 12, pp. 1404–1419, 2004.
- [20] L. Huang, *Theory and Application of the Stability and Robustness*, National Defense Industry Press, Beijing, China, 2000.
- [21] A. A. Martynyuk, "Elements of the theory of stability of hybrid systems (review)," *International Applied Mechanics*, vol. 51, no. 3, pp. 243–302, 2015.
- [22] X. Liao, *The Stability Theory and Application of Dynamical System*, National Defense Industry Press, Beijing, China, 2000.
- [23] V. I. Vorotnikov and Yu. G. Martynshenko, "On partial stability theory of nonlinear dynamic systems," *Journal of Computer and Systems Sciences International*, vol. 49, no. 5, pp. 702–709, 2010.
- [24] J. Fang, "Chaos control method, synchronization principle and its application prospect in nonlinear system (two)," *Progress in Physics*, vol. 16, no. 2, pp. 137–159, 1996.

## Research Article

# A Numerical Method Based on Daubechies Wavelet Basis and B-Spline Patches for Elasticity Problems

Yanan Liu and Keqin Din

*China Special Equipment Inspection and Research Institute, Beijing 100029, China*

Correspondence should be addressed to Yanan Liu; liuyanan@csei.org.cn

Received 11 May 2016; Revised 6 July 2016; Accepted 25 July 2016

Academic Editor: Lihua Wang

Copyright © 2016 Y. Liu and K. Din. This is an open access article distributed under the Creative Commons Attribution License, which permits unrestricted use, distribution, and reproduction in any medium, provided the original work is properly cited.

The Daubechies (DB) wavelets are used for solving 2D plane elasticity problems. In order to improve the accuracy and stability in computation, the DB wavelet scaling functions in  $[0, +\infty)$  comprising boundary scaling functions are chosen as basis functions for approximation. The B-spline patches used in isogeometry analysis method are constructed to describe the problem domain. Through the isoparametric analysis approach, the function approximation and relevant computation based on DB wavelet functions are implemented on B-spline patches. This work makes an attempt to break the limitation that problems only can be discretized on uniform grids in the traditional wavelet numerical method. Numerical examples of 2D elasticity problems illustrate that this kind of analysis method is effective and stable.

## 1. Introduction

Wavelet is a powerful mathematical tool in solving many problems in science and engineering. In recent years, there has been an increasing interest in wavelet-based methods due to their successes in some applications, such as mathematical analysis and signal processing. The wavelet-based numerical methods have been developed by many researchers. At present, there are mainly three kinds of wavelet-based numerical methods: wavelet finite element method, wavelet collocation method, and wavelet-Galerkin method. The wavelet finite element method [1–4] is based on traditional FEM. In this method, the scaling functions and wavelet functions in wavelet analysis are used as basis functions to construct the so-called shape functions on elements. In wavelet collocation method [5], the scaling functions and wavelet functions are directly used as basis functions to approximate the unknown functions instead of constructing shape functions as done in the finite element method, and the collocation approach is used for discretization. Based on Daubechies wavelet, some numerical examples for 1- and 2-dimensional model problems show that the wavelet collocation methods are stable and effective for PDE.

The wavelet-Galerkin method [6–13] is the most popular wavelet-based numerical method. Unlike the wavelet

collocation method, the Galerkin approach is used for discretization. Although the computational efficiency of Galerkin method is lower than that of collocation method, the accuracy and stability are improved remarkably. The desirable advantage of wavelet is the multiresolution property. Based on the property, the wavelet-based multiscale analysis is easy to be realized [13–19].

Although wavelets have demonstrated potential in numerical simulation, there are still some works to do for engineering application. The traditional wavelets, such as some orthogonality or biorthogonality wavelets, can describe details of problems and perform well in resolving high gradients. However, such wavelets are best suitable for problems that are discretized on uniform grids, a constraint that can be rather restrictive when it comes to modeling problems with complex geometry. By contrast, the finite elements method is very well suited for complex meshes. Some works have been made to use this kind of wavelets to solve problems with general domains [12, 13] and the wavelet-based multiscale analysis method can be used to conduct local analysis [13]. But the computational efficiency of this kind of methods still needs to be improved. The second generation wavelets can be constructed on nonuniform grids for numerical simulation [20, 21]. However, these kinds of wavelets are

either complex in construction or too simple to simulate complicated deformation.

The isogeometry analysis method [22, 23] developed in recent years presented some new ideas in numerical simulation. In this method, the B-spline functions or nonuniform rational B-spline functions are used to describe the problem geometry and the total solution domain can be divided into many B-spline patches which are similar to the elements in finite element method. Function approximation and relative computation can be implemented on B-spline patches through isoparametric analysis approach. It can be found that the traditional wavelet basis functions are similar to B-spline basis functions in framework that they must be constructed on structure grids. So it is reasonable to introduce the B-spline patches into the problems in which the traditional wavelet basis functions are used. This is an attempt to break the limitation that the traditional wavelet-based numerical methods are only restricted on uniform grids.

In this paper, the Daubechies (DB) wavelet which has orthogonality and compact support is chosen for analysis because of its good performance in numerical simulation. In order to improve the accuracy and stability in computation, the DB wavelet scaling functions in  $[0, +\infty)$  which comprise boundary scaling functions are used as basis functions for approximation. The B-spline patches constructed by the B-spline basis functions are used to describe the problem geometry. The function approximation based on DB wavelet basis functions and relevant computations are implemented on B-spline patches through the isoparametric analysis approach. Numerical examples for 2D elasticity problems are given to illustrate the effectiveness of the present method.

## 2. The Function Approximation by DB Wavelet Scaling Function

*2.1. The Basic Properties of DB Wavelet.* According to the theory of DB wavelet, the so-called scaling function  $h(x)$  and wavelet function  $g(x)$  of DB wavelet both satisfy two-scaling relation:

$$h^n(x) = \sum_{j=0}^{2n-2} p_j h^n(2x-j), \quad (1)$$

$$g^n(x) = \sum_{j=3-2n}^1 (-1)^j p_{1-j} h^n(2x-j).$$

Here, the index  $n$  denotes the ordinal number of DB wavelet series (DB wavelet with ordinal number  $n$  is abbreviated as "DB <sub>$n$</sub> " in the following), and  $j$  denotes the place.  $p_j$  ( $j = 0, 1, \dots, n-1$ ) are called filter coefficients. The supports of scaling function and wavelet function of DB wavelet are, respectively,

$$\text{supp } h^n(x) = [0, 2n-1], \quad (2)$$

$$\text{supp } g^n(x+n-1) = [0, 2n-1]. \quad (3)$$

DB wavelet function  $g^n(x)$  has  $n$  consecutive moments equal to zero. That is vanishing moment  $n$ :

$$\int_{-\infty}^{+\infty} x^k g^n(x) dx = 0, \quad k = 0, \dots, n-1. \quad (4)$$

The ordinal number of DB wavelet series is equal to the number of its vanishing moments. Furthermore, the smoothness of DB wavelet scaling functions and wavelet functions will be improved with the increase of number of vanishing moments.

From translation and dilation of a basic scaling function  $h(x)$ , we have

$$h_{i,j}(x) = h(2^{-i}x-j). \quad (5)$$

In the above equation,  $i$  and  $j$  denote, respectively, the scale and the place in wavelet space. It is obvious that the support of the function  $h_{i,j}^n(x)$  is

$$\text{supp } h_{i,j}^n = [2^{-i}j, 2^{-i}(j+2n-1)]. \quad (6)$$

According to the principle of multiresolution, the scaling function  $h_{i,j}$  can be used to build the wavelet space  $V_i$ :

$$\begin{aligned} V_i &= \text{span} \{h_{i,j}, j \in Z\}, \\ \dots &\subset V_i \subset V_{i+1} \subset V_{i+2} \subset \dots \\ \bigcap_{i \in Z} V_i &= 0, \\ \bigcup_{i \in Z} V_i &= L^2(R). \end{aligned} \quad (7)$$

In addition, the scaling function  $h(x)$  can be used to exactly represent polynomial to some degrees. For  $\alpha = 0, 1, \dots, n-1$ , we can write

$$\frac{x^\alpha}{\alpha!} = \sum_{k=-\infty}^{+\infty} P_\alpha(k) h^n(x-k). \quad (8)$$

$P_\alpha(k)$  are defined by

$$P_\alpha(X) = \sum_{n=0}^{\alpha} \frac{C_{\alpha-n}}{n!} X^n, \quad (9)$$

where

$$C_m = \int_{-\infty}^{+\infty} \frac{x^m}{m!} h^n(x) dx. \quad (10)$$

*2.2. The DB Wavelet Basis Functions on  $[0, +\infty)$ .* For  $\alpha = 0, 1, \dots, n-1$ , the boundary scaling functions are defined by

$$\tilde{h}_\alpha(x) = \sum_{k=-2n+2}^{-1} P_\alpha(k) h^n(x-k) \chi_{[0,+\infty)}(x). \quad (11)$$

From the boundary scaling functions  $\tilde{h}_\alpha(x)$ , we have the formula for all  $x$  in  $[0, +\infty)$ :

$$\frac{x^\alpha}{\alpha!} = \tilde{h}_\alpha(x) + P_\alpha(0) h^n(x) + P_\alpha(1) h^n(x-1) + \dots. \quad (12)$$

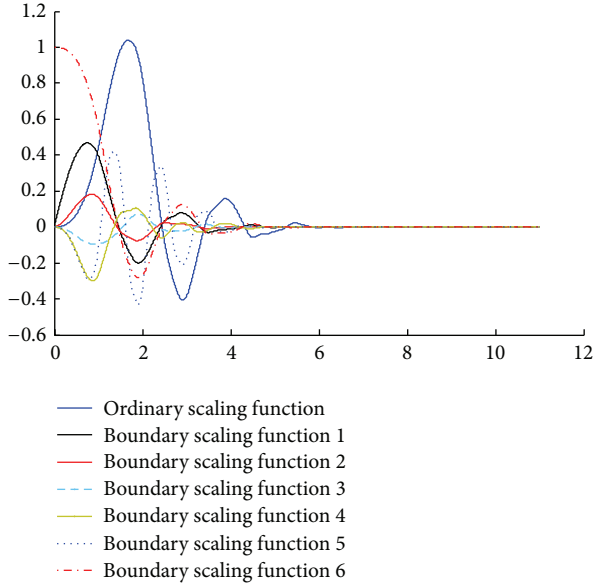


FIGURE 1: Ordinary and boundary scaling functions.

The boundary scaling functions  $\tilde{h}_\alpha(x)$ ,  $\alpha = 0, 1, \dots, n-1$ , are linearly independent and are orthogonal to the functions  $h(x-j)$  for  $j \geq 0$  (called the ordinary scaling functions on  $[0, +\infty)$ ). Figure 1 shows the boundary scaling functions and one of the ordinary scaling functions of DB6 wavelet.

For scale  $i$ , the function  $\tilde{h}_{\alpha,i}(x)$  is defined as

$$\tilde{h}_{\alpha,i}(x) = \tilde{h}_\alpha(2^i x). \quad (13)$$

Then we can define

$$V_i^{[0,+\infty)} = \text{Span} \left\{ (\tilde{h}_{\alpha,i}(\cdot))_{\alpha=0,\dots,n-1}, (h_{i,j}(\cdot))_{j \geq 0} \right\}. \quad (14)$$

It is obvious that polynomials up to degree  $n-1$  are in  $V_i^{[0,+\infty)}$ .

**2.3. The Function Approximation.** The function  $f(x)$  defined in  $[0, +\infty)$  can be approximated in  $V_i^{[0,+\infty)}$  as

$$f_i(x) = \sum_{\alpha=0}^n a_{1,\alpha} \tilde{h}_{\alpha,i}(x) + \sum_{j=0}^{+\infty} a_{2,j} h_{i,j}(x), \quad (15)$$

$$x \in [0, +\infty), \quad i, j \geq 0.$$

In the same way, the function  $f(x)$  defined in  $[0, 1]$  can be approximated in a scale as

$$f_i(x) = \sum_{\alpha=0}^n a_{1,\alpha} \tilde{h}_{\alpha,i}(x) + \sum_{j=0}^{2^i-1} a_{2,j} h_{i,j}(x), \quad (16)$$

$$x \in [0, 1], \quad i, j \geq 0.$$

It is obvious that the number of basis functions used for approximation in limited interval is finite. For 2D case, the 2D tensor product basis functions based on 1D basis functions

can be used for approximation. For example, the function  $f(x, y)$  defined in  $[0, 1] \times [0, 1]$  can be approximated as

$$\begin{aligned} f(x, y) &\approx f_{i,k}(x, y) \\ &= \sum_{\alpha_1=0}^{n-1} \sum_{\alpha_2=0}^{n-1} a_{1,\alpha_1,\alpha_2} \phi_{1,i,\alpha_1,k,\alpha_2}^n(x, y) \\ &\quad + \sum_{\alpha=0}^n \sum_{l=0}^{2^k-1} a_{2,\alpha,l} \phi_{2,i,\alpha,k,l}^n(x, y) \\ &\quad + \sum_{j=0}^{2^i-1} \sum_{\alpha=0}^{n-1} a_{3,j,\alpha} \phi_{3,i,j,k,\alpha}^n(x, y) \\ &\quad + \sum_{j=0}^{2^i-1} \sum_{l=0}^{2^k-1} a_{4,j,l} \phi_{4,i,j,k,l}^n(x, y), \end{aligned} \quad (17)$$

where

$$\begin{aligned} \phi_{1,i,\alpha_1,k,\alpha_2}^n(x, y) &= \tilde{h}_{\alpha_1,i}^n(x) \tilde{h}_{\alpha_2,k}^n(y), \\ \phi_{2,i,\alpha,k,l}^n(x, y) &= \tilde{h}_{\alpha,i}^n(x) h_{k,l}^n(y), \\ \phi_{3,i,j,k,\alpha}^n(x, y) &= h_{i,j}^n(x) \tilde{h}_{\alpha,k}^n(y), \\ \phi_{4,i,j,k,l}^n(x, y) &= h_{i,j}^n(x) h_{k,l}^n(y). \end{aligned} \quad (18)$$

The 2D domain occupied by an elastic body is usually irregular. Function approximations in nonrectangular regions are relatively difficult. In this case, those basis functions which influence the given region,  $\Omega$ , are needed:

$$\text{supp } \phi \cap \Omega \neq \emptyset. \quad (19)$$

### 3. Numerical Implementation

**3.1. Format of Approximation.** Considering the approximation formula (17), it can be found that the form of approximation by DB wavelet basis functions is the same as that in conventional meshless methods. Scaling functions are similar to shape functions, and  $a_j$  are similar to variables related to nodes. However, it should be noted that DB wavelet-based method is different from conventional meshless methods in that there is no need to use information of nodes to construct shape functions. We only need to choose proper scaling functions, wavelet functions, and the number of terms. For practical computations, formula (17) can be rewritten as

$$f_m^n(x, y) = \sum_i a_i \phi_i(x, y), \quad (20)$$

where

$$\phi_i(x, y) = h_{m,j}(x) h_{m,k}(y). \quad (21)$$

It can be found that the two place indexes  $[j, k]$  of  $\phi_i$  correspond to a serial number  $i$ .

3.2. *B-Spline Basis Functions for Describing Geometry.* B-spline functions are defined recursively starting with piecewise constants ( $p = 0$ ):

$$N_{i,0}(\xi) = \begin{cases} 1 & \text{if } \xi_i \leq \xi < \xi_{i+1} \\ 0 & \text{otherwise.} \end{cases} \quad (22)$$

For  $p = 1, 2, 3, \dots$ , they are defined by

$$N_{i,p}(\xi) = \frac{\xi - \xi_i}{\xi_{i+p} - \xi_i} N_{i,p-1}(\xi) + \frac{\xi_{i+p+1} - \xi}{\xi_{i+p+1} - \xi_{i+1}} N_{i+1,p-1}(\xi). \quad (23)$$

Important properties of B-spline basis functions are as follows:

- (1) They constitute a partition of unity; that is,  $\forall \xi$ ,

$$\sum_{i=1}^n N_{i,p}(\xi) = 1. \quad (24)$$

- (2) The support of each  $N_{i,p}$  is compact and contained in the interval  $[\xi_i, \xi_{i+p+1}]$ .

- (3) Each basis function is nonnegative; that is,  $N_{i,p}(\xi) \geq 0, \forall \xi$ .

B-spline curves in  $R^d$  are constructed by taking a linear combination of B-spline basis functions. The coefficients of the basis functions are referred to as control points. These are somewhat analogous to nodal coordinates in finite element analysis. Piecewise linear interpolation of the control points gives the so-called control polygon. In general, control points are not interpolated by B-spline curves. Given  $n$  basis functions,  $N_{i,p}$   $i = 1, 2, 3, \dots, n$ , and corresponding control points,  $B_i \in R^d$   $i = 1, 2, 3, \dots, n$ , a piecewise-polynomial B-spline curve is given by

$$C(\xi) = \sum_{i=1}^n N_{i,p}(\xi) B_i. \quad (25)$$

In 2D space, the physical coordinate of the curve can be expressed as

$$\begin{aligned} x(\xi) &= \sum_{i=1}^n N_{i,p}(\xi) x_i, \\ y(\xi) &= \sum_{i=1}^n N_{i,p}(\xi) y_i, \end{aligned} \quad (26)$$

where  $(x_i, y_i)$  is the coordinate of control points  $B_i$ .

Given a control net  $B_{i,j} \in R^d$ ,  $i = 1, 2, 3, \dots, n$ ,  $j = 1, 2, 3, \dots, m$ , a tensor product B-spline surface is defined by

$$S(\xi, \eta) = \sum_{i=1}^n \sum_{j=1}^m N_{i,p}(\xi) M_{j,q}(\eta) B_{i,j}, \quad (27)$$

where  $N_{i,p} M_{j,q}$  is 2D B-spline basis function.

3.3. *The Isoparametric Analysis Approach Based on B-Spline Patches and DB Wavelet Basis Functions.* The DB wavelets scaling functions are good basis functions for approximation. However, the method of approximation introduced in Section 2 is only suited for problems that are discretized on uniform grids. The isogeometry analysis method introduced the B-spline functions to describe problem geometry. The domain can be subdivided into B-Spline patches which are similar to elements in finite element method. The important character of B-spline patches is that they must not be regular in physical space. So they can describe complex geometry more flexibly than uniform grids. Considering the similarity between wavelet basis functions and B-spline functions in framework, this paper introduces the B-spline patches to problems using wavelet numerical method. Through isoparametric analysis approach, the function approximation and relative computations based on wavelet basis functions can be implemented on B-spline patches.

It should be noted that in the classic isogeometry analysis method [1, 7] the NURBS (nonuniform rational B-splines) are employed because they can be used to exactly construct many geometric shapes, such as circles and ellipses. In this paper, only ordinary B-splines are used because they can also describe the complex geometry with enough accuracy.

For 1D case, the approximation in parametric space by wavelet basis functions is as follows:

$$f(\xi) = \sum_{\alpha=0}^n a_{1,\alpha} \tilde{h}_\alpha(\xi) + \sum_{j=0}^{m-1} a_{2,j} h(\xi - j), \quad \xi \in (0, m). \quad (28)$$

The relationship of physical coordinate and parametric index can be expressed by B-spline basis functions:

$$x(\xi) = \sum_{i=1}^m N_{i,p}(\xi) x_i, \quad (29)$$

where  $x_i$  is the coordinate parameter related to  $N_{i,p}$ .

For 2D case, the approximation can be expressed as

$$\begin{aligned} f(\xi, \eta) &= \sum_{\alpha_1=0}^{n-1} \sum_{\alpha_2=0}^{n-1} a_{1,\alpha_1,\alpha_2} \phi_{1,\alpha_1,\alpha_2}^n(\xi, \eta) \\ &+ \sum_{\alpha=0}^{n-1} \sum_{l=0}^{m_2-1} a_{2,\alpha,l} \phi_{2,\alpha,l}^n(\xi, \eta) \\ &+ \sum_{j=0}^{m_1-1} \sum_{\alpha=0}^{n-1} a_{3,j,\alpha} \phi_{3,j,\alpha}^n(\xi, \eta) \\ &+ \sum_{j=0}^{m_1-1} \sum_{l=0}^{m_2-1} a_{4,j,l} \phi_{4,j,l}^n(\xi, \eta) \end{aligned} \quad (30)$$

$$\xi \in (0, m_1), \quad \eta \in (0, m_2),$$

$$\phi_{1,\alpha_1,\alpha_2}^n(\xi, \eta) = \tilde{h}_{\alpha_1}^n(\xi) \tilde{h}_{\alpha_2}^n(\eta), \quad (31)$$

$$\phi_{2,\alpha,l}^n(\xi, \eta) = \tilde{h}_\alpha^n(\xi) h^n(\eta - l), \quad (32)$$

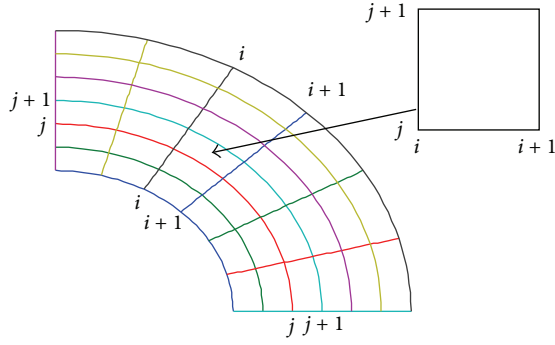


FIGURE 2: Element as parameter span for isoparametric analysis.

$$\phi_{3,j,\alpha}^n(\xi, \eta) = h^n(\xi - j)\bar{h}_\alpha^n(\eta), \quad (33)$$

$$\phi_{4,j,l}^n(\xi, \eta) = h^n(\xi - j)h^n(\eta - l). \quad (34)$$

The relationship of physical space and parametric space can be expressed by 2D tensor product B-spline basis functions:

$$\begin{aligned} x(\xi, \eta) &= \sum_{i=1}^{m_1} \sum_{j=1}^{m_2} N_{i,p}(\xi) M_{j,q}(\eta) x_{ij}, \\ y(\xi, \eta) &= \sum_{i=1}^{m_1} \sum_{j=1}^{m_2} N_{i,p}(\xi) M_{j,q}(\eta) y_{ij}, \end{aligned} \quad (35)$$

where  $x_{ij}$  and  $y_{ij}$  are, respectively, the coordinate components related to the 2D B-spline basis functions  $N_{i,p}M_{j,q}$ . The relevant first-order derivative can be expressed as

$$\begin{pmatrix} \frac{df}{dx} \\ \frac{df}{dy} \end{pmatrix} = \begin{pmatrix} \frac{dx}{d\xi} & \frac{dy}{d\xi} \\ \frac{dx}{d\eta} & \frac{dy}{d\eta} \end{pmatrix}^{-1} \begin{pmatrix} \frac{df}{d\xi} \\ \frac{df}{d\eta} \end{pmatrix}. \quad (36)$$

Based on the above approximation method, the relative numerical computation can be implemented on “elements” which are taken to be the parameter spans, namely,  $[i, i + 1] \times [j, j + 1]$ . Figure 2 illustrates a standard biunit parent element and its image in physical space.

**3.4. The Method of Discretization.** The equations for the 2D elasticity problem are expressed as follows:

$$\begin{aligned} \sigma_{ij,j} + b_i &= 0 & \text{in } \Omega \\ \sigma_{ij}n_j &= \bar{t}_i & \text{on } \Gamma_t \\ u_i &= \bar{u}_i & \text{on } \Gamma_u \end{aligned} \quad (37)$$

$i, j \in (1, 2),$

where  $\sigma_{ij}$  is the stress tensor,  $b_i$  is the body force,  $\bar{t}_i$  and  $\bar{u}_i$  are, respectively, the prescribed tension and displacement, and  $n_j$  is the unit outward normal to boundary. In general, collocation methods and Galerkin methods are dominant

in discretization. In this paper, the Galerkin approach is adopted. Consider the virtual displacement principle

$$\int_{\Omega} (\sigma_{ij,j} + b_i) \delta u_i d\Omega + \int_{\Gamma_t} (\sigma_{ij}n_j - \bar{t}_i) \delta u_i d\Gamma = 0. \quad (38)$$

$\delta u_i$  is the variation of real displacement. From formula (38), the weak form can be written as

$$\int_{\Omega} \delta e_{ij} \sigma_{ij} d\Omega = - \int_{\Gamma_t} \delta u_i \bar{t}_i d\Gamma + \int_{\Omega} \delta u_i b_i d\Omega, \quad (39)$$

where  $\delta u_i$  vanishes and  $u_i = \bar{u}_i$  on  $\Gamma_u$ .

In 2D problems, formula (30) can be used for the approximation of the two displacement field functions:  $u$  and  $v$ . For simplification, the approximation formula can be written as

$$\begin{aligned} u(\xi, \eta) &= \sum_i a_{ui} \phi_{ui}(\xi, \eta), \\ v(\xi, \eta) &= \sum_j a_{vj} \phi_{vj}(\xi, \eta), \end{aligned} \quad (40)$$

where  $a_{ui}$  and  $a_{vj}$  are unknown variables. Then we can obtain the discrete equations by introducing the approximation formula (40) into formula (39). Eventually, a group of linear algebraic equations can be obtained:

$$\mathbf{K}\mathbf{a} = \mathbf{f}, \quad (41)$$

where

$$\begin{aligned} \mathbf{a} &= [a_{u1}, a_{u2}, \dots, a_{v1}, a_{v2}, \dots]^T, \\ \mathbf{K} &= \int_{\Omega} \mathbf{B}^T \mathbf{D} \mathbf{B} d\Omega, \\ \mathbf{f}^T &= \int_{\Omega} \boldsymbol{\varphi}^T \mathbf{b} d\Omega + \int_{\Gamma_t} \boldsymbol{\varphi}^T \bar{\mathbf{t}} d\Gamma. \end{aligned} \quad (42)$$

$\mathbf{D}$  is the 2D elasticity matrix:

$$\mathbf{D} = \frac{E_0}{(1 - \nu_0^2)} \begin{bmatrix} 1 & \nu & 0 \\ \nu & 1 & 0 \\ 0 & 0 & \frac{1 - \nu}{2} \end{bmatrix}. \quad (43)$$

Plane stress is as follows:

$$\begin{aligned} E_0 &= E, \\ \nu_0 &= \nu. \end{aligned} \quad (44)$$

Plane strain is as follows:

$$E_0 = \frac{E}{1 - \nu^2}, \quad (45)$$

$$\nu_0 = \frac{\nu}{1 - \nu},$$

$$\mathbf{B} = \mathbf{L}\boldsymbol{\varphi}, \quad (46)$$

$$\mathbf{L} = \begin{bmatrix} \frac{\partial}{\partial x} & 0 \\ 0 & \frac{\partial}{\partial y} \\ \frac{\partial}{\partial y} & \frac{\partial}{\partial x} \end{bmatrix}, \quad (47)$$

$$\boldsymbol{\varphi} = \begin{bmatrix} \phi_{u1} & \phi_{u2} & \cdots & 0 & 0 & \cdots \\ 0 & 0 & \cdots & \phi_{v1} & \phi_{v2} & \cdots \end{bmatrix}. \quad (48)$$

Here,  $\mathbf{K}$  and  $\mathbf{f}$  are stiffness matrix and load vector, respectively. In addition, the derivative in formula (47) should be evaluated using formula (36). All relevant computation should be performed on parametric space.

#### 4. Numerical Examples

In this part, numerical examples for some 2D plain elasticity problems are presented using the analysis method introduced above. The results are compared with those calculated by finite element method or analytical results to show the validity of the proposed method. For simplification, the units are omitted in this paper. In addition, the DB6 wavelet is used in all examples because it performs better in accuracy and efficiency than other DB wavelets.

**4.1. Solid Circular Cylinder Subjected to Internal Pressure Loading.** Solid circular cylinder subjected to constant internal pressure loading is considered in this example. Plane strain conditions are assumed to hold in the axial direction. The problem specification is shown in Figure 3. The exact solution for the case with constant pressure is as follows:

$$\begin{aligned} u_r &= \frac{1}{E} \frac{PR_i^2}{R_o^2 - R_i^2} \left( (1 - \nu)r + \frac{R_o^2(1 + \nu)}{r} \right), \\ \sigma_r &= \frac{PR_i^2}{R_o^2 - R_i^2} \left( 1 - \frac{R_o^2}{r^2} \right), \\ \sigma_\theta &= \frac{PR_i^2}{R_o^2 - R_i^2} \left( 1 + \frac{R_o^2}{r^2} \right). \end{aligned} \quad (49)$$

The three meshes used in the analysis are shown in Figure 4. They are constructed by the cubic B-spline functions. The displacement and stress results are presented in Table 1. The pressure is set to  $p = 1$  and material constants are given by  $E = 1$  and  $\nu = 0.3$ . It can be found that the numerical results are close to the analytical results even with the first (coarsest) mesh. It is also obvious that the computational accuracy is improved with finer meshes.

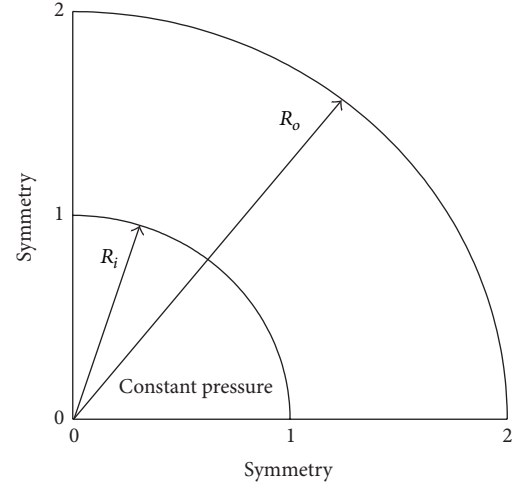


FIGURE 3: Quarter of a thick cylinder under constant internal pressure.

TABLE 1: The comparison of numerical and analytical results.

Scale	$u_r$		$\sigma_\theta$	
	Outer	Internal	Outer	Internal
Mesh 1	1.325	1.961	0.6687	1.7091
Mesh 2	1.330	1.964	0.6672	1.6761
Mesh 3	1.331	1.965	0.6684	1.6733
Analytical	1.3333	1.9667	0.6667	1.6667

**4.2. Infinite Plate with a Circle Hole.** An infinite plate with a central circular hole as shown in Figure 5 is considered. The plate is subjected to uniform unit traction along the  $x$ -axis at infinity. Symmetry of the problem is exploited to model only a quadrant of the analysis domain. The radius of the hole is set to be 0.25 and the length and width of the plate are set to be 1. The exact solutions for this problem are

$$\begin{aligned} \sigma_x &= 1 - \frac{a^2}{r^2} \left( \frac{3}{2} \cos 2\theta + \cos 4\theta \right) + \frac{3a^4}{2r^4} \cos 4\theta, \\ \sigma_{xy} &= -\frac{a^2}{r^2} \left( \frac{1}{2} \sin 2\theta + \sin 4\theta \right) + \frac{3a^4}{2r^4} \sin 4\theta, \\ \sigma_y &= -\frac{a^2}{r^2} \left( \frac{1}{2} \cos 2\theta - \cos 4\theta \right) - \frac{3a^4}{2r^4} \cos 4\theta. \end{aligned} \quad (50)$$

The exact solutions are used to compute the tractions on the traction boundaries (right and top boundaries) and symmetry boundary conditions are applied on the bottom and left edges while the inner edges are traction-free. The three meshes used in this analysis are shown in Figure 6. They are also constructed by the cubic B-spline functions.

Figure 7 shows the stress value ( $\sigma_x$ ) along the left edge obtained using different meshes. It can be found that the numerical results agree well with the analytical results even using the coarsest mesh. Table 2 shows the comparison of convergent results of stress ( $\sigma_x$ ) computed by present method and analytical results at different points in the stress

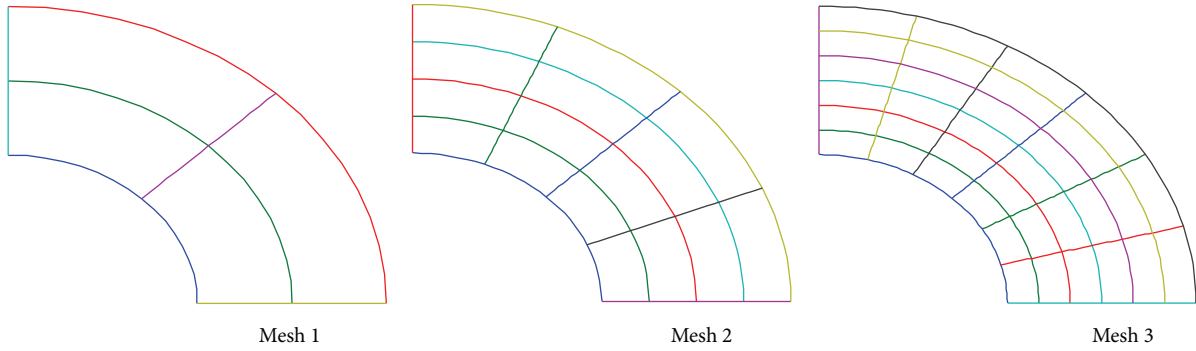


FIGURE 4: Cylinder under internal pressure. Meshes for computation.

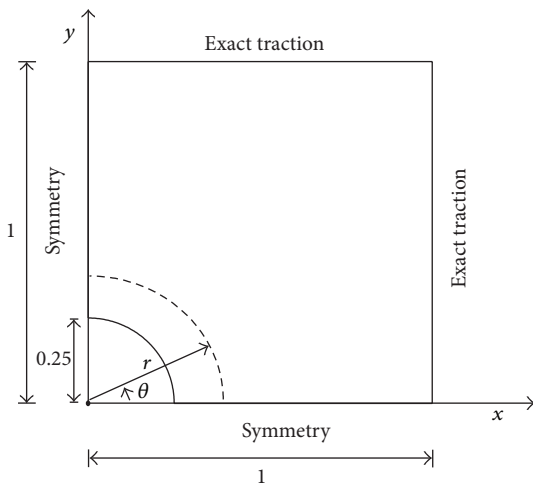


FIGURE 5: Quarter of a panel with a circle hole at its center.

TABLE 2: The comparison of convergent results of stress ( $\sigma_x$ ) in stress concentration zone.

Coordinate (x, y)	$\sigma_x$	
	Wavelet method (convergent results)	Analytical solution
(0.0, 0.25)	3.0107	3.0
(0.0, 0.277)	2.4115	2.4025
(0.0488, 0.2452)	2.7391	2.7389
(0.0579, 0.2725)	2.2156	2.2169

concentration zone. The error at every point is very small. Table 3 displays the comparison of the stress concentration factor computed using different meshes.

The plot for strain energy error is shown in Figure 8. The  $x$ -axis represents the number of degrees of freedom. The convergence of this method is evident. The above numerical results demonstrate that the present method is stable and effective for problems with general domains.

4.3. *Plate with a Square Hole.* Figure 9 depicts quarter of a panel with a square hole of  $a = 0.25$  at its center. The uniform

TABLE 3: The comparison of the stress concentration factors computed in different scales.

Scale	Stress concentration factor
Mesh 1	3.0794
Mesh 2	3.0251
Mesh 3	3.0168
Convergence	3.0107

TABLE 4: The comparison of stress values ( $\sigma_x$ ) at singular point.

Scale	Stress ( $\sigma_x$ )
Mesh 1	4.1106
Mesh 2	5.6188
Mesh 3	8.4542
FE method	12.386

tension  $p = 1$  in the horizontal direction is applied on the left and right edges of the panel.

Three meshes used in this analysis are shown in Figure 10. The stress results ( $\sigma_x$ ) along  $y = 0.25$  are shown in Figure 11. Table 4 displays the stress values ( $\sigma_x$ ) at singular point, where the results of FEM are computed using more than 22000 elements of plain eight nodes. It can be found that the present method can catch the singular character with relatively less elements. The plot for strain energy error is shown in Figure 12. The  $x$ -axis represents the number of degrees of freedom. The strain energy obtained by FEM is used for computing error. It can be observed that the present method exhibits good convergence rates and for a given number of degrees of freedom, the errors are much smaller compared with the traditional wavelet-Galerkin methods. These numerical results demonstrate that the present method can also effectively deal with problems with singularity.

4.4. *Semi-Infinite Plate under a Normal Concentration Force.* A semi-infinite plate under a normal concentration force  $P$  at its boundary is considered. The computation model of this

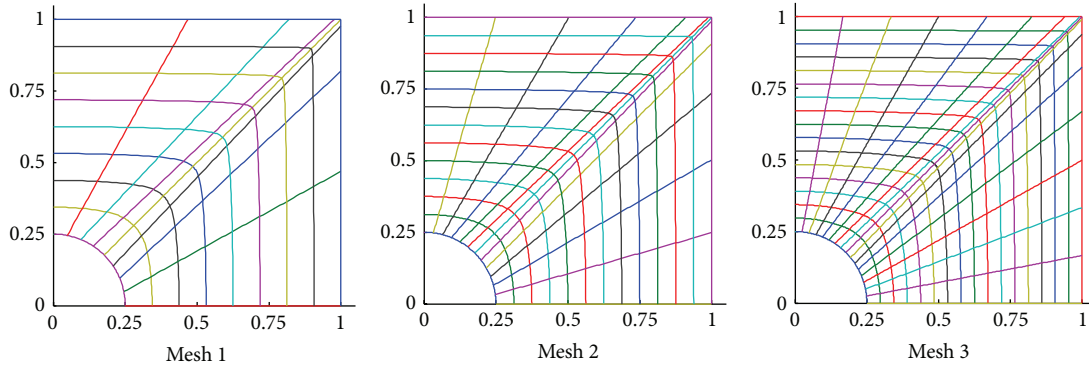


FIGURE 6: Panel with circle hole. Meshes for computation.

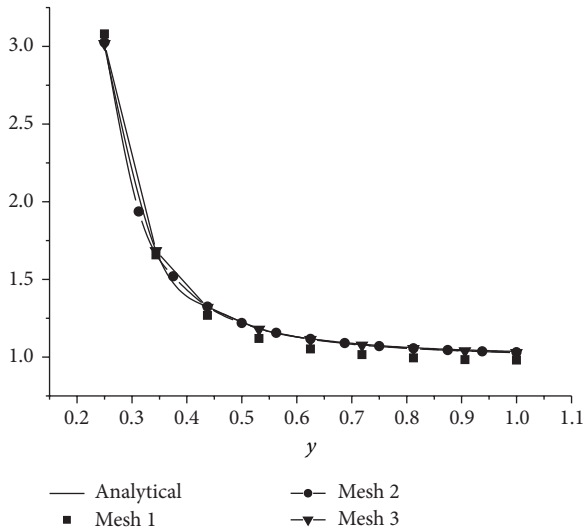


FIGURE 7: Stress ( $\sigma_x$ ) along  $y$ -axis.

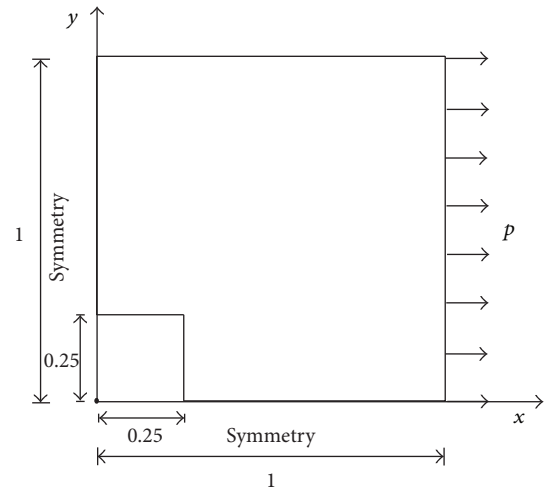


FIGURE 9: Quarter of a panel with a square hole at its center.

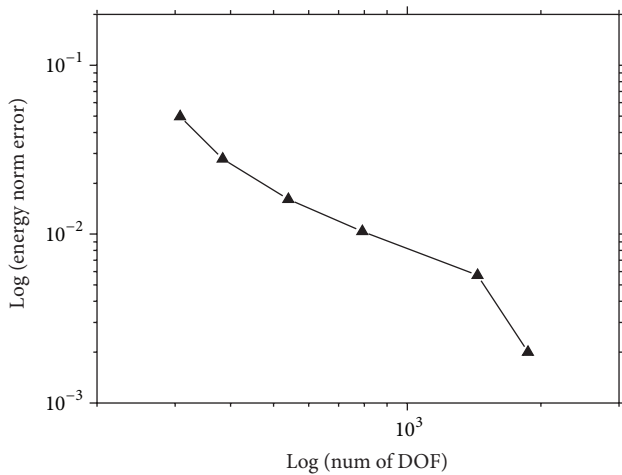


FIGURE 8: Plot of error in strain energy with respect to the number of degrees of freedom.

problem is shown in Figure 13. The radius of the semicircle in the model is  $r = 1$ . The exact solutions for this problem are

$$\begin{aligned} \sigma_x &= -\frac{2P}{\pi} \frac{x^2 y}{(x^2 + y^2)^2}, \\ \sigma_y &= -\frac{2P}{\pi} \frac{y^3}{(x^2 + y^2)^2}, \\ \sigma_{xy} &= -\frac{2P}{\pi} \frac{xy^2}{(x^2 + y^2)^2}. \end{aligned} \tag{51}$$

The exact solutions are used to compute the tractions on the traction boundaries (semicircle boundaries) while the other edges are traction-free.

Two meshes used in this analysis are shown in Figure 14. The stress results ( $\sigma_y$ ) along  $x = 0$  are shown in Figure 15. It can be found that the accuracy of stress results with two kinds of meshes is good. Furthermore, the stress results obtained using mesh 2 are close to analytical results even near the

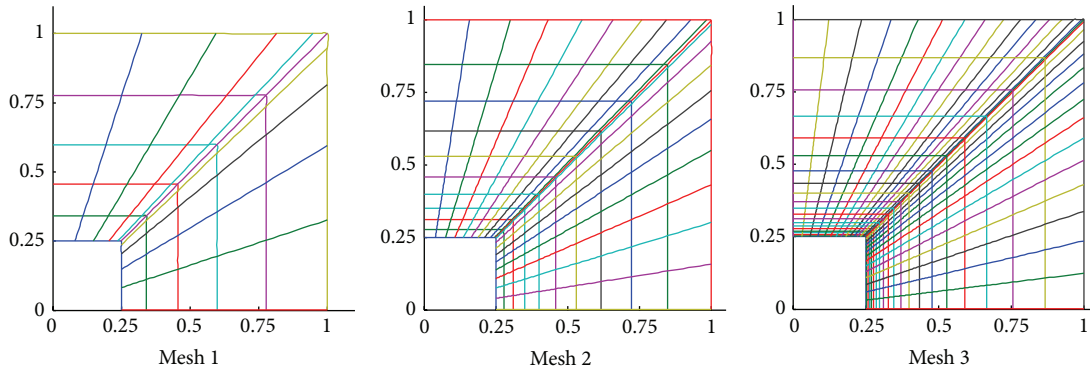


FIGURE 10: Panel with square hole. Meshes for computation.

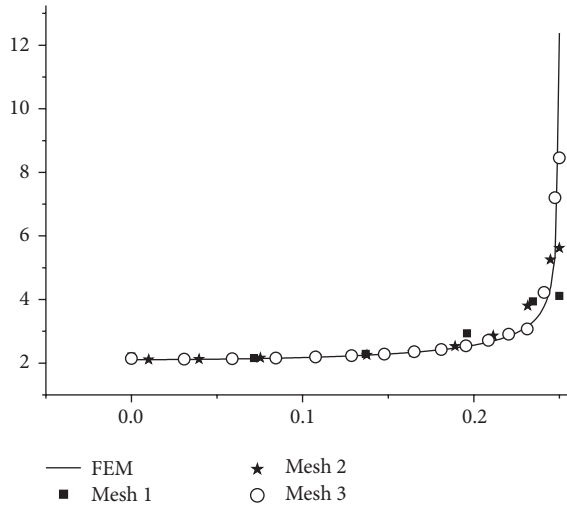


FIGURE 11: Stress ( $\sigma_x$ ) along  $y = 0.25$ .

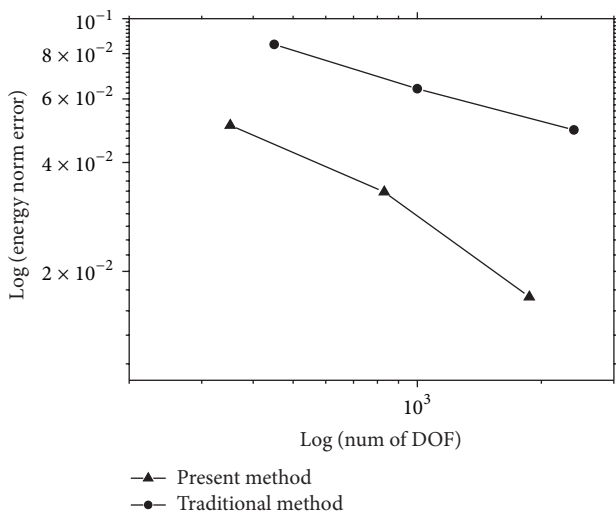


FIGURE 12: Plot of error in strain energy for problem of a plate with a square hole.

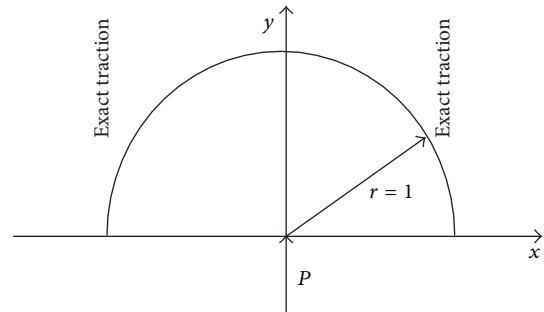


FIGURE 13: The computation model for semi-infinite plate under a normal concentration force.

singular point. The results in this example further prove that the present method can effectively analyze the problems with singularity.

### 5. Conclusion

In this paper, the DB wavelet scaling functions in  $[0, +\infty)$  which comprise edge scaling functions are chosen as basis functions for approximation. The B-spline patches are constructed to describe the problem domain. Through the iso-parametric analysis approach, the function approximation and relevant computation based on DB wavelet basis functions are implemented on B-spline patches. Compared with the traditional wavelet numerical methods which rely on uniform grids, this present method is flexible and easy to work with for numerical analysis. Numerical examples of 2D elasticity problems illustrate that this kind of analysis method is effective and stable. Furthermore, this method gives a thought to perform the traditional wavelet-based numerical analysis on nonuniform grids.

### Competing Interests

The authors declare that they have no competing interests.

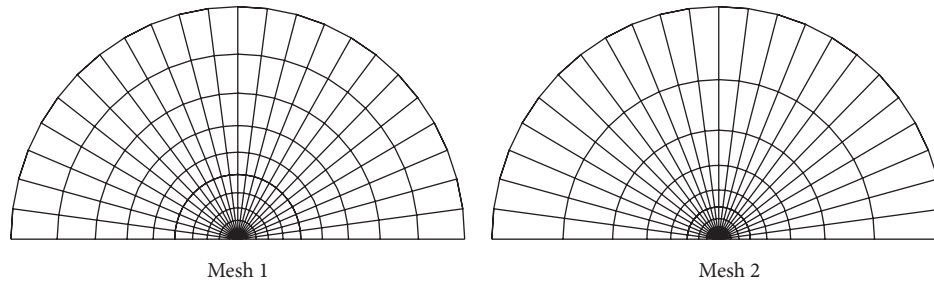


FIGURE 14: The meshes used for computation.

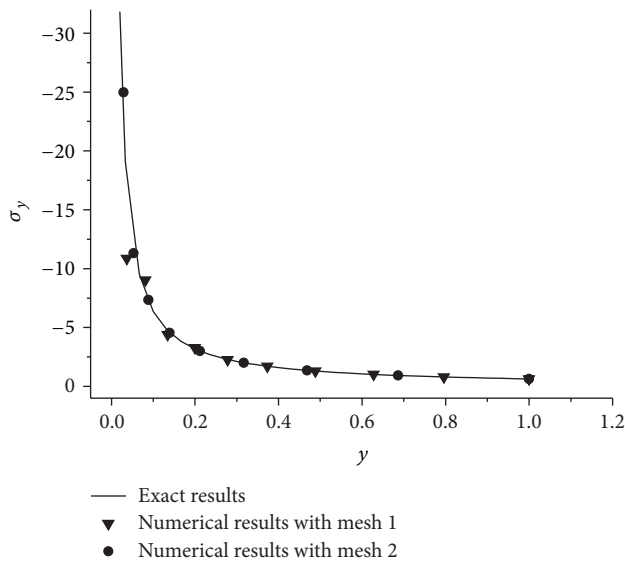


FIGURE 15: Stress ( $\sigma_y$ ) along  $x = 0$ .

## Acknowledgments

This paper was supported by the National Natural Science Foundation of China (11272358).

## References

- [1] J. Ko, A. J. Kurdila, and M. S. Pilant, "A class of finite element methods based on orthonormal, compactly supported wavelets," *Computational Mechanics*, vol. 16, no. 4, pp. 235–244, 1995.
- [2] X. Chen, S. Yang, J. Ma, and Z. He, "The construction of wavelet finite element and its application," *Finite Elements in Analysis and Design*, vol. 40, no. 5-6, pp. 541–554, 2004.
- [3] A. J. Kurdila, T. Sun, P. Grama, and J. Ko, "Affine fractal interpolation functions and wavelet-based finite elements," *Computational Mechanics*, vol. 17, no. 3, pp. 169–185, 1995.
- [4] J.-G. Han, W.-X. Ren, and Y. Huang, "A spline wavelet finite-element method in structural mechanics," *International Journal for Numerical Methods in Engineering*, vol. 66, no. 1, pp. 166–190, 2006.
- [5] S. Bertoluzza and G. Naldi, "A wavelet collocation method for the numerical solution of partial differential equations," *Applied and Computational Harmonic Analysis*, vol. 3, no. 1, pp. 1–9, 1996.
- [6] K. Amaratunga, J. R. Williams, S. Qian, and J. Weiss, "Wavelet-Galerkin solutions for one-dimensional partial differential equations," *International Journal for Numerical Methods in Engineering*, vol. 37, no. 16, pp. 2703–2716, 1994.
- [7] K. Amaratunga and J. R. Williams, "Wavelet-Galerkin solution of boundary value problems," *Archives of Computational Methods in Engineering*, vol. 4, no. 3, pp. 243–285, 1997.
- [8] A. R. Díaz, "A wavelet-Galerkin scheme for analysis of large-scale problems on simple domains," *International Journal for Numerical Methods in Engineering*, vol. 44, no. 11, pp. 1599–1616, 1999.
- [9] J. M. Restrepo and G. K. Leaf, "Wavelet-Galerkin discretization of hyperbolic equations," *Journal of Computational Physics*, vol. 122, no. 1, pp. 118–128, 1995.
- [10] S. M. Gomes and E. Cortina, "Convergence estimates for the wavelet Galerkin method," *SIAM Journal on Numerical Analysis*, vol. 33, no. 1, pp. 149–161, 1996.
- [11] Y. Liu, F. Qin, Y. Liu, and Z. Cen, "A Daubechies wavelet-based method for elastic problems," *Engineering Analysis with Boundary Elements*, vol. 34, no. 2, pp. 114–121, 2010.
- [12] Y. Liu, F. Qin, Y. H. Liu, and Z. Cen, "The 2D large deformation analysis using Daubechies wavelet," *Computational Mechanics*, vol. 45, no. 2-3, pp. 179–187, 2010.
- [13] Y. Liu, Y. H. Liu, and Z. Cen, "Multi-scale Daubechies wavelet-based method for 2-D elastic problems," *Finite Elements in Analysis and Design*, vol. 47, no. 4, pp. 334–341, 2011.
- [14] O. V. Vasilyev, S. Paolucci, and M. Sen, "A multilevel wavelet collocation method for solving partial differential equations in a finite domain," *Journal of Computational Physics*, vol. 120, no. 1, pp. 33–47, 1995.
- [15] O. V. Vasilyev and S. Paolucci, "A dynamically adaptive multilevel wavelet collocation method for solving partial differential equations in a finite domain," *Journal of Computational Physics*, vol. 125, no. 2, pp. 498–512, 1996.
- [16] O. V. Vasilyev and N. K. Kevlahan, "An adaptive multilevel wavelet collocation method for elliptic problems," *Journal of Computational Physics*, vol. 206, no. 2, pp. 412–431, 2005.
- [17] Y. Y. Kim and G.-W. Jang, "Hat interpolation wavelet-based multi-scale Galerkin method for thin-walled box beam analysis," *International Journal for Numerical Methods in Engineering*, vol. 53, no. 7, pp. 1575–1592, 2002.
- [18] J. E. Kim, G.-W. Jang, and Y. Y. Kim, "Adaptive multiscale wavelet-Galerkin analysis for plane elasticity problems and its applications to multiscale topology design optimization,"

*International Journal of Solids and Structures*, vol. 40, no. 23, pp. 6473–6496, 2003.

- [19] G.-W. Jang, J. E. Kim, and Y. Y. Kim, “Multiscale Galerkin method using interpolation wavelets for two-dimensional elliptic problems in general domains,” *International Journal for Numerical Methods in Engineering*, vol. 59, no. 2, pp. 225–253, 2004.
- [20] K. Amaratunga and J. E. Castrillon-Candas, “Surface wavelets: a multiresolution signal processing tool for 3D computational modelling,” *International Journal for Numerical Methods in Engineering*, vol. 52, no. 3, pp. 239–271, 2001.
- [21] K. Amaratunga and R. Sudarshan, “Multiresolution modeling with operator-customized wavelets derived from finite elements,” *Computer Methods in Applied Mechanics and Engineering*, vol. 195, no. 19-22, pp. 2509–2532, 2006.
- [22] T. J. Hughes, J. A. Cottrell, and Y. Bazilevs, “Isogeometric analysis: CAD, finite elements, NURBS, exact geometry and mesh refinement,” *Computer Methods in Applied Mechanics and Engineering*, vol. 194, no. 39-41, pp. 4135–4195, 2005.
- [23] J. A. Cottrell, T. J. R. Hughes, and A. Reali, “Studies of refinement and continuity in isogeometric structural analysis,” *Computer Methods in Applied Mechanics and Engineering*, vol. 196, no. 41-44, pp. 4160–4183, 2007.

## Research Article

# Flow Simulation of Suspension Bridge Cable Based on Lattice-Boltzmann Method

Liang Huang,<sup>1</sup> Yuhan Deng,<sup>1</sup> and Bo Wang<sup>2</sup>

<sup>1</sup>School of Civil Engineering, Zhengzhou University, Zhengzhou, Henan 450001, China

<sup>2</sup>School of Water Conservancy and Environment Engineering, Zhengzhou University, Zhengzhou, Henan 450001, China

Correspondence should be addressed to Yuhan Deng; dyh9511@163.com

Received 18 April 2016; Revised 21 June 2016; Accepted 10 July 2016

Academic Editor: Cheng-Tang Wu

Copyright © 2016 Liang Huang et al. This is an open access article distributed under the Creative Commons Attribution License, which permits unrestricted use, distribution, and reproduction in any medium, provided the original work is properly cited.

Suspension bridge is a kind of bridge which uses cables as the main bearing structure. Suspension bridge has the characteristics of saving materials and weak stiffness. With the increase of the span of suspension bridge, wind induced vibration has resulted in injury of several suspension bridges, which leads to a significant loss. Thus, it is imperative to study the wind vibration mechanism of cables. As for this problem, this paper based on motion theory of mesoscopic particles performs flow simulation of cables by LBM which is different from traditional computing method of fluid mechanics. By calculating the distribution function of the distribution on the grid of uniform flow field, the macroscopic motion law of the flow field around cables can be obtained, which can provide reference for wind resistant design of suspension.

## 1. Introduction

Suspension bridges use cables as the main bearing structure of the superstructure and the cable support tower is anchored on both banks and ends of the bridge. The suspension bridge which was developed from the rope bridge initially appeared in the early nineteenth century. Compared with other kinds of bridge structures, the suspension bridge can be used to span a relatively long distance with fewer materials. Therefore, the suspension bridge is especially suitable for large span highway bridges. Allowing for this consideration, many large span bridges were built based on this structure at present. The suspension bridge is composed of cable, tower, anchorage, and bridge deck system and the cables are used as the main bearing component. Suspension bridge [1] has its own unique nature: it can be built relatively high, allowing boats to pass and therefore it can be built where the water is deep or the current is swift. Suspension is a cable associating the main cable with beam carrying loads. Each point in the suspension can only withstand tension and the tension is along the tangential direction of the suspension. Suspension is relatively soft and the stiffness is small. Thus, it is easy to generate fierce deflection and vibration under wind load [2].

The performance analysis of the suspension cable under wind load is necessary.

Presently, with the development of the theory of aerodynamics and computing technology, however, numerical simulation has become an important tool for wind resistance of bridges. But apparently the blunt body dynamic method is somehow imprecise and imperfect. For complicated blunt body dynamic flow problems in structural wind engineering, it is still difficult to solve Navier-Stokes equations. Even the simplified model, such as eddy viscosity model, cannot effectively reveal the intrinsic physical mechanism of the flow around the blunt body [3]. What is more, the CFD method based on the Navier-Stokes equation has a low computational efficiency and the progress of the efficiency is limited in spite of the rapid development of computer technology. Therefore, numerical simulation is carried out in this paper by LBM based on the mesoscopic particle velocity distribution function. This method can obtain smaller vortexing behavior under the same discrete rate. In addition, the evolution of the distribution function is completed on the local grid, which is suitable for large scale parallel computing and therefore LBM has higher computational efficiency, accuracy, and stability [4].

## 2. The Lattice Boltzmann Method

The Lattice Boltzmann method [5] (LBM) is one of the most important achievements in recent 20 years of computational fluid mechanics and different from the traditional numerical methods [6] for fluid calculation and modeling method describing the movement of the molecule. LBM regards the fluid as discrete system composed of a large number of mesoscopic particles. According to the movement characteristics of the particle, a simplified LB equation is established to calculate the evolution of particle distribution function.

The Lattice Boltzmann equation [7] (LBE) is linear, but actually its nonlinearity is embedded in the left side of the LBE. In LBM, the nonlinear convection term in the macroscopic method is replaced by the linear transfer process, which is similar to the method of solving the compressible flow characteristics. LBM can be easily implemented on a parallel processing computer as a result of the fact that the collision and streaming processes are local. LBE is an integropartial differential equation, so one of the difficulties in solving LBE is the complexity of the collision integral. In order to simplify the solving process, a collision function model with a simple operator instead of collision was proposed. LBE is a special discrete form of Boltzmann-BGK equation including discrete velocity, discrete time, and space discretization. Discrete time and space can be linked by discrete velocity of particles, which makes LBM have effective parallel computing ability and effective ability to deal with complex boundaries.

The Lattice Boltzmann evolution equation of the single relaxation time is

$$\begin{aligned} f_i(x + c_i \Delta t, t + \Delta t) - f_i(x, t) \\ = -\frac{1}{\tau} [f_i(x, t) - f_i^{\text{eq}}(x, t)]. \end{aligned} \quad (1)$$

In the formula,  $\tau$ ,  $c_i$ ,  $f_i$ , and  $f_i^{\text{eq}}$  are the relaxation factor, discrete velocity, particle distribution function, and equilibrium distribution function, respectively.

In 1992, researchers including Yuehong Qian proposed the model  $DnQb$  [8].  $n$  and  $b$  refer to space dimension and discrete velocity, respectively, and the equilibrium distribution function is

$$f_i^{\text{eq}} = \omega_i \rho \left[ 1 + \frac{(c_i \cdot u^{\text{eq}})}{c_s^2} + \frac{(c_i \cdot u^{\text{eq}})^2}{2c_s^4} - \frac{(u^{\text{eq}} \cdot u^{\text{eq}})}{2c_s^2} \right]. \quad (2)$$

In the formula,  $u^{\text{eq}}$  is the macroscopic velocity. And  $c_s$  is sound velocity of the grid and  $\omega_i$  is weight coefficient. The two parameters decide that the model of lattices depends on the selecting of  $c_i$  in discrete velocity model.

In this paper, we adopted D2Q9 model (shown as Figure 1):

$$c_i = \begin{cases} (0, 0) c, & i = 0 \\ \left[ \cos \frac{(i-1)\pi}{2}, \sin \frac{(i-1)\pi}{2} \right] c, & i = 1, 2, 3, 4 \\ \sqrt{2} \left[ \cos \frac{(2i-9)\pi}{4}, \sin \frac{(2i-9)\pi}{4} \right] c, & i = 5, 6, 7, 8. \end{cases} \quad (3)$$

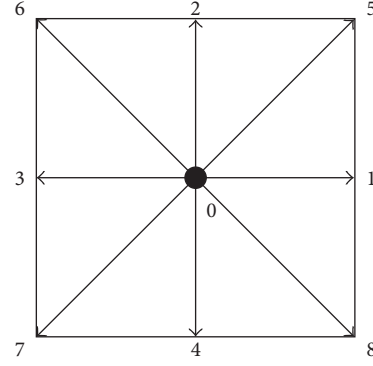


FIGURE 1: D2Q9 model.

Weight coefficient and sound velocity of lattices are as follows:

$$\omega_i = \begin{cases} \frac{4}{9}, & i = 0 \\ \frac{1}{9}, & i = 1, 2, 3, 4 \\ \frac{1}{36}, & i = 5, 6, 7, 8, \end{cases} \quad (4)$$

$$c_s^2 = \frac{1}{3} c^2.$$

In the formula,  $c = \Delta x / \Delta t$  is velocity of grid.  $\Delta x$  and  $\Delta t$  are grid length and time step, respectively.

The macroscopic velocity and momentum of fluid are

$$\begin{aligned} \rho &= \sum_i f_i, \\ \rho u &= \sum_i c_i f_i. \end{aligned} \quad (5)$$

The relationship between the fluid viscosity coefficient and the relaxation factor of the model is

$$\nu = \left( \tau - \frac{1}{2} \right) c_s^2 \Delta t. \quad (6)$$

Generally, the calculation process of LBE is as follows:

(1) Initialize the distribution function:

$$f_i(x, 0) \quad (i = 1, 2, \dots, b). \quad (7)$$

(2) Perform collision at  $t$ :

$$f_i'(x, t) = f_i(x, t) + \frac{1}{\tau} (x, t), \quad i = 1, 2, \dots, b. \quad (8)$$

(3) Perform migration:

$$f_i(x + c_i \Delta t, t + \Delta t) = f_i'(x, t), \quad i = 1, 2, \dots, b. \quad (9)$$

(4) Calculate macroscopic thermodynamic quantities:

$$\begin{aligned}\rho(x, t + \Delta t) &= \sum_i f_i(x, t + \Delta t), \\ \rho u(x, t + \Delta t) &= \sum_i c_i f_i(x, t + \Delta t).\end{aligned}\quad (10)$$

(5) Repeat steps (2)–(4) until the terminal conditions are met.

In LBM, the accurate simulation of boundary conditions [9–11] is an important and crucial problem, because the boundary conditions are not easy to determine, which needs to confirm the distribution function of the boundary. At present, the types of boundary of LBM can be divided into heuristic schemes, dynamic schemes, and interpolation/extrapolation schemes. According to the type of boundary condition, it also can be divided into the velocity boundary and the pressure boundary. Additionally, there are some special artificial boundaries, such as the entrance, exit, infinity, and symmetry.

The rebound format is usually used for simulating the boundary condition of stationary solid or obstacle flow. It is mainly refers to the fact that the projectile of solid boundary will rebound to fluid field. We can easily know that  $f_5 = f_7$ ,  $f_2 = f_4$ ,  $f_6 = f_8$ , and  $f_7$ ,  $f_4$ , and  $f_8$  can be obtained from the streaming process.

In practical application, the velocity component is usually known. Thus, a method is proposed by Zou and He to calculate the 3 unknown equilibrium distribution functions under equilibrium conditions:

$$\begin{aligned}\rho &= \frac{1}{1-u} [f_0 + f_2 + f_4 + 2(f_3 + f_6 + f_7)], \\ f_1 &= f_3 + \frac{2}{3}\rho u, \\ f_5 &= f_7 - \frac{1}{2}(f_2 - f_4) + \frac{1}{6}\rho u + \frac{1}{2}\rho u, \\ f_8 &= f_6 + \frac{1}{2}(f_2 - f_4) + \frac{1}{6}\rho u - \frac{1}{2}\rho u.\end{aligned}\quad (11)$$

Sometimes, the velocity of the exit is unknown. In these situations, we need to use extrapolation method to get the unknown distribution functions. For example,

$$\begin{aligned}f_{3,n} &= 2 \cdot f_{3,n-1} - f_{3,n-2}, \\ f_{6,n} &= 2 \cdot f_{6,n-1} - f_{6,n-2}, \\ f_{7,n} &= 2 \cdot f_{7,n-1} - f_{7,n-2}.\end{aligned}\quad (12)$$

Through the research done before, we can know that, in traditional CFD, the convection term is nonlinear. What is more, for incompressible flow problems, the pressure term is implicit. In LBM, the integral differential equation, however, is transformed into a linear differential equation. Additionally, the distribution function is used to describe the motion of the fluid, which makes us not have to construct Poisson equation. But this BGK model is only valid for small Reynolds number. We have to further research the model for high Reynolds number.

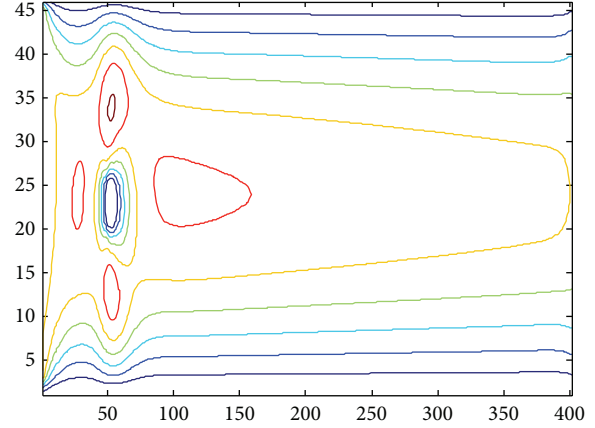


FIGURE 2: Streamline, Re = 20.

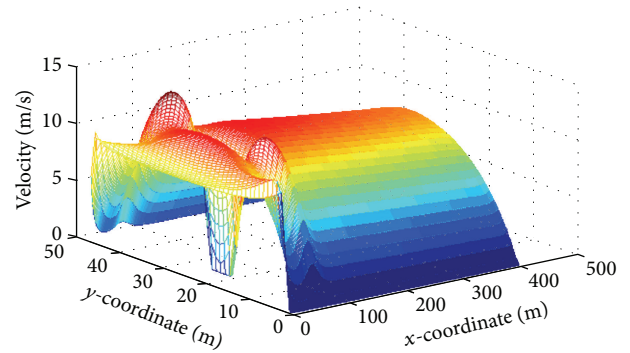


FIGURE 3: 3D graph, Re = 20.

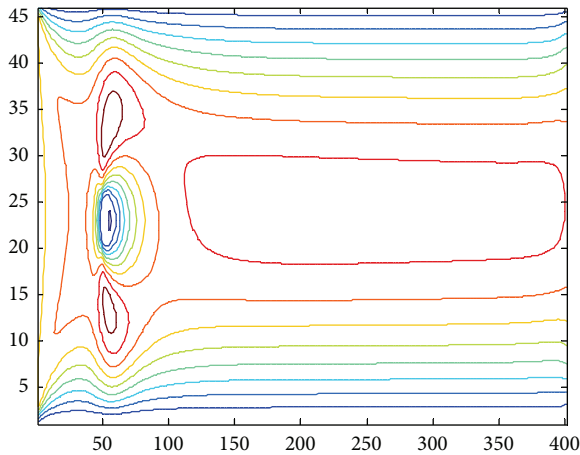
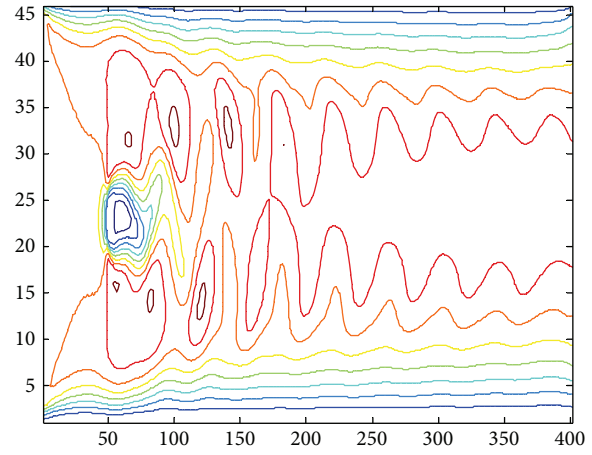
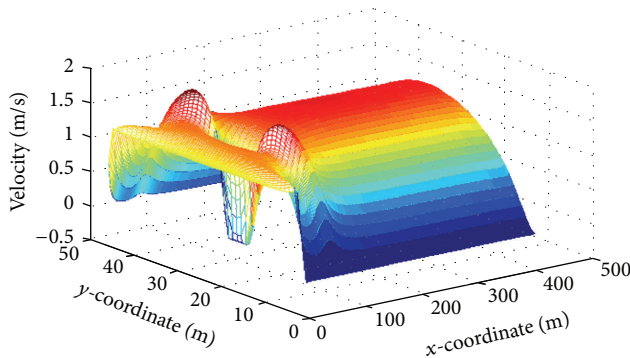
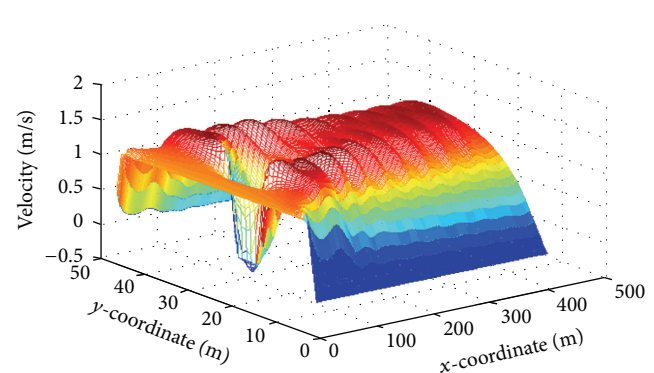
### 3. Flow Simulation of Cables

Because cables of suspension bridges have a large dynamic response under wind load [12] and the theory of LBM suitable for blunt body flow [13], this paper simulates flow around cables by LBM in order to verify the feasibility and accuracy of LBM. We choose a rectangle with 400 meters' length and 45 meters' width as the computational domain. We suppose the wind velocity is 5 m/s. We chose the standard rebounded scheme as the surface free slip boundary and dealt with the flow inlet velocity boundary and the exit constant pressure boundary by the nonequilibrium rebounded scheme. As follows, we selected cables with different quantity to simulate the flow.

#### 3.1. Single Flow Simulation

**3.1.1. Re = 20.** The barrier is a rectangular cylinder [14] of 5 m \* 5 m placed 50 meters away from the entrance. When the Reynolds number is 20, we obtain the streamline and three-dimensional graph by use of the MATLAB after 40000 steps of the calculation, as shown in Figures 2 and 3.

**3.1.2. Re = 100.** The barrier is a rectangular cylinder of 5 m \* 5 m placed 50 meters away from the entrance. When the Reynolds number is 100, we obtain the streamline and

FIGURE 4: Streamline,  $Re = 100$ .FIGURE 6: Streamline,  $Re = 1000$ .FIGURE 5: 3D graph,  $Re = 100$ .FIGURE 7: 3D graph,  $Re = 1000$ .

three-dimensional graph by use of the MATLAB after 40000 steps of the calculation, as shown in Figures 4 and 5.

**3.1.3.  $Re = 1000$ .** The barrier is a rectangular cylinder of  $5\text{ m} \times 5\text{ m}$  placed 50 meters away from the entrance. When the Reynolds number is 1000, we obtain the streamline and three-dimensional graph by use of the MATLAB after 40000 steps of the calculation, as shown in Figures 6 and 7.

We can see from the flow around the wake that the variation of the flow field is obvious, and it will gradually tend to be stable. When the Reynolds number is 20, the flow field in front of the square cylinder surface has the maximum vorticity, while the vorticity of other regions is small. When the Reynolds number increases to 100, the flow field around the square cylinder becomes unstable, which is no longer a laminar flow. When the Reynolds number increases to 1000, the flow field after a long distance around the column is still in a state of volatility. By the comparison of Figures 2–7, we can see that, with the increase of Reynolds number [15, 16], steady flow changes to unsteady flow gradually.

### 3.2. Flow Simulation of Two Circular Cylinders in Tandem

**3.2.1.  $Re = 20$ .** The barriers are two rectangular cylinders of  $5\text{ m} \times 5\text{ m}$  placed 50 meters away from the entrance. When the

Reynolds number is 20, we obtain the streamline and three-dimensional graph by use of the MATLAB after 40000 steps of the calculation, as shown in Figures 8 and 9.

**3.2.2.  $Re = 100$ .** The barriers are two rectangular cylinders of  $5\text{ m} \times 5\text{ m}$  placed 50 meters away from the entrance. When the Reynolds number is 100, we obtain the streamline and three-dimensional graph by use of the MATLAB after 40000 steps of the calculation, as shown in Figures 10 and 11.

We can see from the flow around the wake that the variation of the flow field is obvious, and it will gradually tend to be stable. When the Reynolds number is 20, the streamline has been closed at 400 m, while when the Reynolds number is 100, the streamline may be closed in a long distance. By comparison of Figures 8–11, we can see that, with the increase of Reynolds number, steady flow changes to unsteady flow gradually.

After single and double flow simulation, we can conclude that when the Reynolds number is small, flow field will become stable quickly. With the increase of Reynolds number, steady flow changes to unsteady flow gradually, which proves that LBM is not fit for numerical simulation with high Reynolds number. Therefore, we should carry out numerical simulation with small Reynolds number.

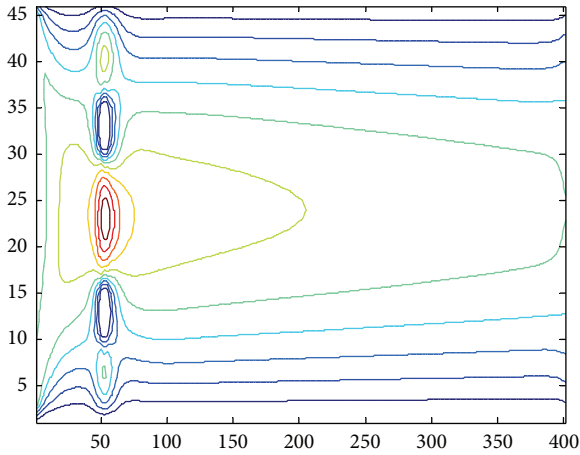


FIGURE 8: Streamline, Re = 20.

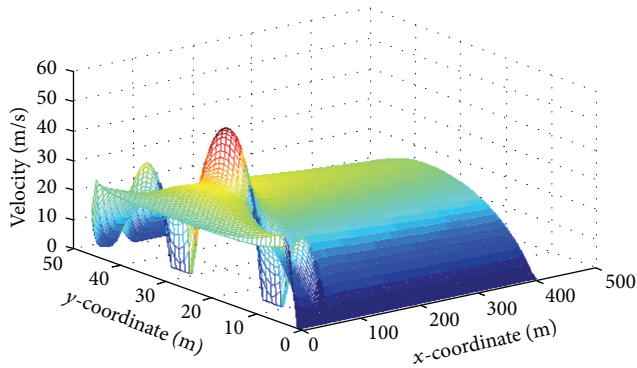


FIGURE 9: 3D graph, Re = 20.

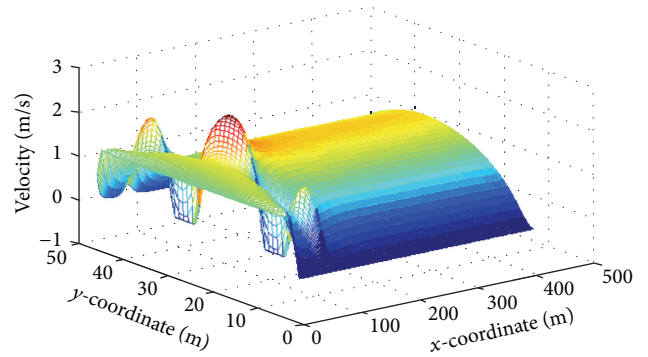


FIGURE 11: 3D graph, Re = 100.

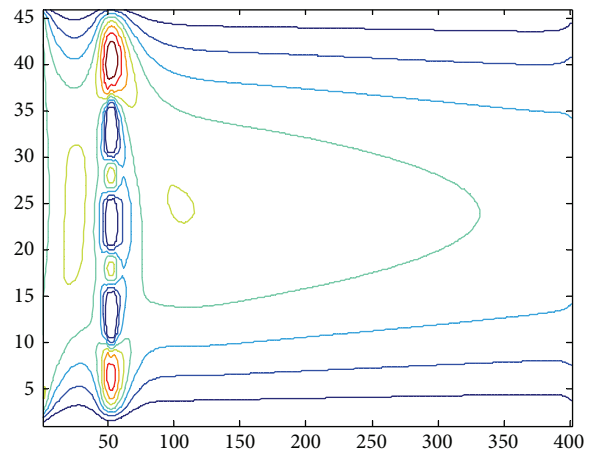


FIGURE 12: Streamline, Re = 20.

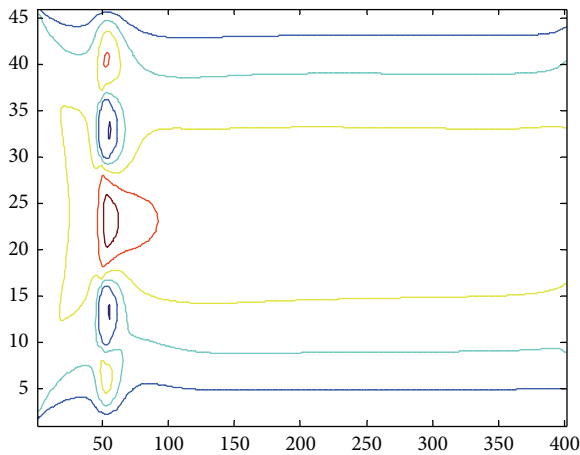


FIGURE 10: Streamline, Re = 100.

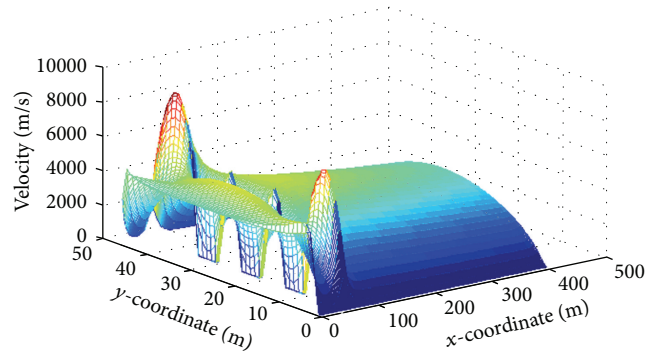


FIGURE 13: 3D graph, Re = 20.

3.3. *Flow around Three Cylinders in Tandem.* The barriers are three rectangular cylinders of 5 m \* 5 m placed 50 meters away from the entrance. When the Reynolds number is 20, we obtain the streamline and three-dimensional graph by use of the MATLAB after 40000 steps of the calculation, as shown in Figures 12 and 13.

We can see from the flow around the wake that the variation of the flow field is obvious, and it will gradually tend to be stable. The flow field at both sides of the side column varies greatly, but the flow field between the two columns varies little. By comparison of Figures 2 and 3, Figures 8 and 9, and Figures 12 and 13, we can see that the less the obstacles, the easier for flow field tending to be stable.

3.4. *Flow Simulation of Double Column Parallel.* The barriers are two rectangular cylinders of 5 m \* 5 m placed 50 meters

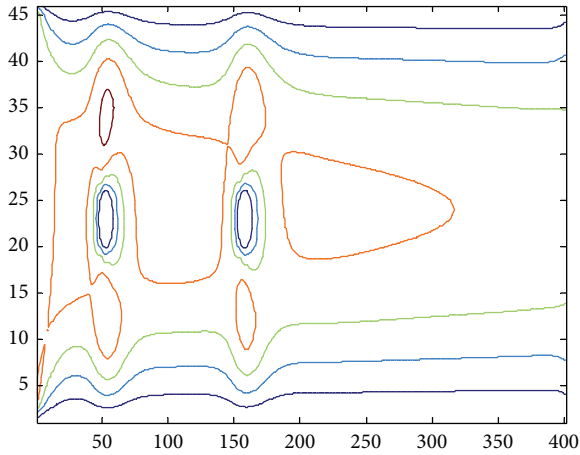


FIGURE 14: Streamline, Re = 20.

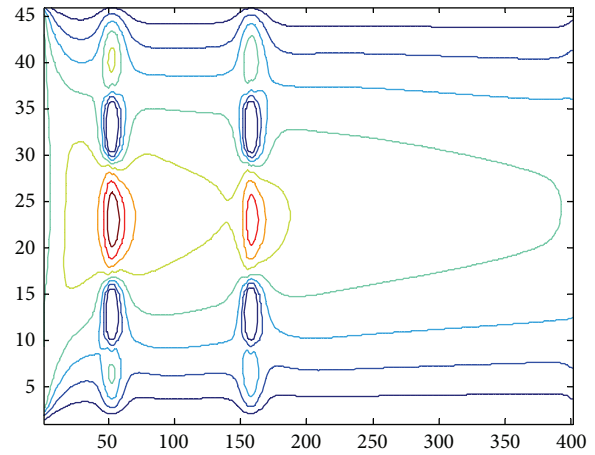


FIGURE 16: Streamline, Re = 20.

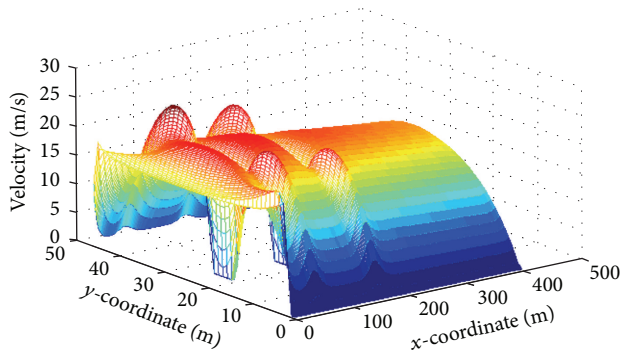


FIGURE 15: 3D graph, Re = 20.

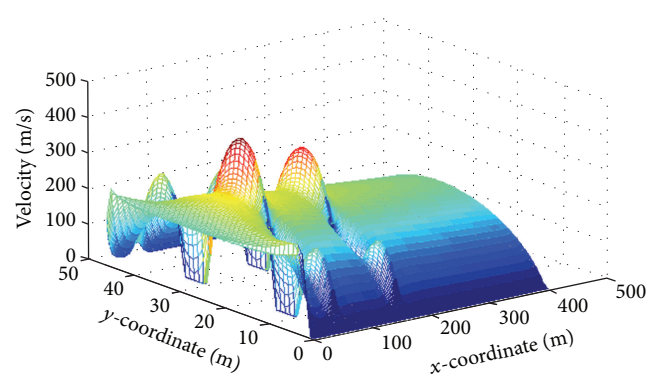


FIGURE 17: 3D graph, Re = 20.

and 155 meters away from the entrance, respectively. When the Reynolds number is 20, we obtain the streamline and three-dimensional graph by use of the MATLAB after 40000 steps of the calculation, as shown in Figures 14 and 15.

We can see from the flow around the wake that the variation of the flow field is obvious, and it will gradually tend to be stable. The flow field at both sides of the side column varies greatly, but the flow field between the two columns varies little. By comparison of Figures 8 and 9 and Figures 14 and 15, we can see that the less the obstacles, the easier for flow field tending to be stable.

**3.5. Flow Simulation of Four Column Parallel.** The barriers are four rectangular cylinders of 5 m \* 5 m placed 50 meters and 155 meters away from the entrance, respectively. When the Reynolds number is 20, we obtain the streamline and three-dimensional graph by use of the MATLAB after 40000 steps of the calculation, as shown in Figures 16 and 17.

We can see from the flow around the wake that the variation of the flow field is obvious, and it will gradually tend to be stable. By comparison of Figures 14 and 15 and Figures 16 and 17, we can see that the less the obstacles, the easier for flow field tending to be stable.

## 4. Conclusion

Because the accuracy of existing numerical simulation method is low, this paper puts forward a numerical simulation with high accuracy and good stability based on LBE. We compile the calculation program by use of MATLAB to simulate stationary flow of single, double, or multiple columns, and we obtain the streamlines and three-dimension graph which can be used to study the characteristics of cables around the flow. Through the calculation, we draw the conclusions: when the Reynolds number is high, steady flow changes to unsteady flow resulting in the fact that LBM is not suitable for numerical simulation with high Reynolds number, while when the Reynolds number is low, the flow is steady flow, and the variation of the flow field around cables is obvious. The flow field tends to be stable after a while, which is in accordance with practical theory. Thus, LBM is suitable for flow simulation around cables with small Reynolds number.

## Competing Interests

The authors declare that they have no competing interests.

## Acknowledgments

This paper is supported by the National Natural Science Foundation of China (11472248).

## References

- [1] X. Zhao, K. Gouder, J. M. Graham, and D. J. Limebeer, "Buffet loading, dynamic response and aerodynamic control of a suspension bridge in a turbulent wind," *Journal of Fluids and Structures*, vol. 62, pp. 384–412, 2016.
- [2] A. Larsen and G. L. Larose, "Dynamic wind effects on suspension and cable-stayed bridges," *Journal of Sound and Vibration*, vol. 334, no. 1, pp. 2–28, 2015.
- [3] Z. Shang, "Numerical investigations of supercavitation around blunt bodies of submarine shape," *Applied Mathematical Modelling*, vol. 37, no. 20–21, pp. 8836–8845, 2013.
- [4] C. Demuth, S. Mishra, M. A. A. Mendes, S. Ray, and D. Trimis, "Application and accuracy issues of TRT lattice Boltzmann method for solving elliptic PDEs commonly encountered in heat transfer and fluid flow problems," *International Journal of Thermal Sciences*, vol. 100, pp. 185–201, 2016.
- [5] X. Shan, "The mathematical structure of the lattices of the lattice Boltzmann method," *Journal of Computational Science*, 2016.
- [6] M. Wang, Y. T. Feng, and C. Y. Wang, "Numerical investigation of initiation and propagation of hydraulic fracture using the coupled bonded particle–lattice Boltzmann method," *Computers & Structures*, 2016.
- [7] P. Otte and M. Frank, "Derivation and analysis of Lattice Boltzmann schemes for the linearized Euler equations," *Computers & Mathematics with Applications*, vol. 72, no. 2, pp. 311–327, 2016.
- [8] Y. Feng, P. Sagaut, and W.-Q. Tao, "A compressible lattice Boltzmann finite volume model for high subsonic and transonic flows on regular lattices," *Computers & Fluids*, vol. 131, pp. 45–55, 2016.
- [9] Y. Wang, C. Shu, C. J. Teo, and L. M. Yang, "An efficient immersed boundary-lattice Boltzmann flux solver for simulation of 3D incompressible flows with complex geometry," *Computers & Fluids*, vol. 124, pp. 54–66, 2016.
- [10] Z. Li, J. Favier, U. D'Ortona, and S. Poncet, "An immersed boundary-lattice Boltzmann method for single- and multi-component fluid flows," *Journal of Computational Physics*, vol. 304, pp. 424–440, 2016.
- [11] A. Amiri Delouei, M. Nazari, M. H. Kayhani, and G. Ahmadi, "A non-Newtonian direct numerical study for stationary and moving objects with various shapes: an immersed boundary-lattice Boltzmann approach," *Journal of Aerosol Science*, vol. 93, pp. 45–62, 2016.
- [12] K. A. Raman, R. K. Jaiman, T.-S. Lee, and H.-T. Low, "Lattice Boltzmann study on the dynamics of successive droplets impact on a solid surface," *Chemical Engineering Science*, vol. 145, pp. 181–195, 2016.
- [13] H. Rastgou and S. Saedodin, "Numerical simulation of an axisymmetric separated and reattached flow over a longitudinal blunt circular cylinder," *Journal of Fluids and Structures*, vol. 42, pp. 13–24, 2013.
- [14] X. Jiang, Y. Andreopoulos, T. Lee, and Z. Wang, "Numerical investigations on the vortex-induced vibration of moving square cylinder by using incompressible lattice Boltzmann method," *Computers & Fluids*, vol. 124, pp. 270–277, 2016.
- [15] H. Li, X.-H. Jin, H.-S. Deng, and Y.-B. Lai, "Experimental investigation on the outlet flow field structure and the influence of Reynolds number on the outlet flow field for a bladeless fan," *Applied Thermal Engineering*, vol. 100, pp. 972–978, 2016.
- [16] V.-T. Nguyen and H. H. Nguyen, "Detached eddy simulations of flow induced vibrations of circular cylinders at high Reynolds numbers," *Journal of Fluids and Structures*, vol. 63, pp. 103–119, 2016.